DAMPING AT EVERY TURN: MANEUVERS AND STABILITY IN THE FREE FLIGHT OF HAWKMOTH *MANDUCA SEXTA*

Jeremy Stuart Michael Greeter

A dissertation submitted to the faculty at the University of North Carolina at Chapel Hill in partial fulfillment of the requirements for the degree of Doctor of Philosophy in the Department of Biology.

Chapel Hill
2017

Approved by:

Tyson L. Hedrick

William M. Kier

Kenneth J. Lohmann

Laura A. Miller

Gregory S. Sawicki

ABSTRACT

Jeremy Stuart Michael Greeter: Damping at Every Turn: Maneuvers and Stability in the Free Flight of Hawkmoth *Manduca sexta*
(Under the direction of Tyson L. Hedrick)

Here I identify novel stability features in flapping flight. Implications may shift the current scientific consensus that flying animals, particularly insects, must actively monitor and respond to even slight perturbations to maintain control in pitch and roll, and allow engineers to recreate these capabilities in flying robots. Results are consistent with co-directional inertial and viscous effects working together to damp rotations. This could explain flight stability across a broad range of body sizes, speeds, and flapping frequencies.

I propose a previously undescribed, likely ubiquitous class of passive “inertio-viscous” damping. Flapping wings move, so rotational perturbations on the time scale of halfstrokes manifest as wing position/orientation changes later in the flapping cycle. My novel results show these (at least partially) passive (inertia-based) kinematic responses push on the air to produce torques that oppose the initial perturbation. I then identify key design elements which future flapping-wing micro air vehicles could employ to exploit these stability effects.

This emerges from a series of three experiments exploring roll and pitch dynamics in hawkmoth *Manduca sexta*. In the first, I coaxed moths to follow a light and described their lateral maneuver mechanics. I concluded roll is heavily damped, and positive coupling between roll and lateral acceleration, negative coupling between roll and lateral velocity, and countertorque from wing motion around the roll axis, are relevant (viscous/velocity) damping factors.

In the second, I launched miniature cannonballs at moths and described their pitch recovery mechanics. I concluded inertial (and viscous) resistance of wing stroke plane to the pitch impulse (and rotational velocity) helps create pendular stability in mid-air. Gyroscopic (and viscous) reactions to pitch impulses (and rotational velocity) manifest as deviations to wing kinematics that further damp pitch, indicating reinforcing roles for inertia and drag in flapping flight stability.

In the third, I glued T-bars on moths to create weight imbalances during hover. Results reinforce my conclusions about damping and roll/pitch-associated wing kinematics, show flexibility helps compensate for off-axis loads, and associate a novel wing kinematic with roll torque that suggests gyroscopic and pendular damping mechanisms also complement viscous/velocity-based damping in roll.

To my father. I hope you've enjoyed our many adventures as much as I have.
To my mother. Thank you for pushing me to succeed.

ACKNOWLEDGEMENTS

I thank my close family, my good friends, and my strict teachers.

I thank: My father, Stuart, who taught me how to love science and nature and learning and to always question the world around me, and also for his heavy-handed algebra lessons at the kitchen table. My mother, Dorothy, who pushed me to succeed in school, taught me to hold myself to a standard of success based on my own capabilities rather than those of others, taught me how to read, and tried very hard (but to no avail) to teach me good organizational habits. My sister, Stacy, who provided me with wisdom and emotional support, a yardstick with which to measure my personal growth, countless creative adventures in imaginary lands, and a safe haven from our mother and father! Most importantly, my noble canine companion Stinky—with his boundless enthusiasm—for teaching me loyalty and love and patience and how to live in the moment.

I also thank: My friends, among them Evan Kriminger, Sarah Shapiro, Sean Sherry, and Zach Lucy, for moral support, outrageous adventures, and for indulging in my company despite my many idiosyncrasies. My close colleagues, especially Brenna Hansen and Jonathan Rader, for always providing a sympathetic ear. My congenial roommates for putting up with my talkativeness and messiness.

I thank: My advisor Tyson Hedrick—without whom this work would simply not exist—for his thoughtful criticism, intimidating work ethic, and patience while I plodded my way through my PhD, matured professionally, and explored non-academic career options. My committee for providing suggestions throughout my graduate studies. Funding agencies for believing in my ability at various points in my scientific career, among them the Department of Defense (*via* the National Defense Science and Engineering Graduate Fellowship administered by the American Society for Engineering Education), NASA (*via* the Research and Education Awards Project administered by the South Carolina Space Grant Consortium), and the University of North Carolina Department of Biology (*via* the Evolution, Ecology, and Organismal Biology program).

And finally, for making learning engaging and challenging, I would like to thank every science, engineering, and math teacher and teaching assistant I ever had.

TABLE OF CONTENTS

LIST OF TABLES

LIST OF FIGURES

LIST OF SYMBOLS AND ABBREVIATIONS

Abbreviations

AOA	Angle Of Attack; represents the angle at which the wing encounters the air.
AICc	corrected Akaike Information Criterion—evaluates model predictive quality while penalizing for model complexity.
BIC	Bayesian Information Criterion, (or Schwartz criterion), an criterion for model selection among a finite set of models that is based on the likelihood function.
BRF	Body Reference Frame: reference frame from the perspective of the moth's COM, in which the moth's anatomical landmarks and canonical hover orientation determine x, y, and z.
COM	Center Of Mass: point where the sum of the product of individual units of mass and their distance away from that point equal zero.
COP	Center Of Pressure: net sum of force production by the wings, time-averaged over the course of a stroke cycle
DLT	Direct Linear Transformation: A method for extrapolating positions in space from pixels marked on captured frames from non-collinear camera views
FCF	Flapping Counter Force: Idea that linear translation of flapping wings creates differential drag and thrust which damps the translation. First described for sideslips.
FCT	Flapping Counter Torque: idea that rotations change the velocity of wings flapping in that rotational plane, damping the rotation. First shown for yaw.
GRF	Global Reference Frame: reference frame from the perspective of the cameras or a non-accelerating outside observer; based on the camera calibration (world view or lab frame).
MGRF	Modified Global Reference Frame: reference frame in which x/y coordinates have been rotated about the z-axis (in yaw) sot so that the x-axis is in line with the longitudinal axis of the moth.
RML	Restricted Maximum Likelihood.
RMSE	Root Mean Squared Error; RMSE values came from (data-relative) residuals.
PD, PI	Proportional-Derivative or Proportional-Integrative controller (as in control theory). Note the "PD" controllers described here are similar to the "PI" controller of Whitehead *et al.*, (2015).
SRF	Standard Reference Frame: frame where GRF points are rotated about the z-, then x-, and then the y-axis such that, in the new SRF: 1) the wing base points and the abdomen point lie on a shared x-y plane, 2) the x-z plane includes the abdomen point and a (0,0,0) that is the midpoint of a line connecting the two wing base points 3) the y-z plane is perpendicular to the first two planes and intercepts the same (0,0,0) point.

Operators, Annotations, Subscripts, and Constants

$\times$; $\lvert\ \rvert$; $\sum$	"by" or cross-product; absolute value or magnitude of; sum of
$\in$; $\bullet$; $/\!/$	constrained to within; dot product; parallel with
Δ; $\approx$; $\propto$; $\tilde{\propto}$	change in; approximately equal/congruent to; proportional to; approximately proportional to
$\stackrel{\text{def}}{=}$; $\sim$; $\sim$	equal to by definition; on the order or in the vicinity of; on the order or in the vicinity of
$\dot{}$, $\ddot{}$	first and second time derivatives of the attendant variable, respectively
$_{\Delta}$	a subscript which indicates that mid-upstroke and mid-downstroke pre-collision midstroke means for the whole data set have been subtracted (Chapter 3); a subscript which indicates the given wing kinematic variable has been mean-centered by subtracting (separate upstroke and downstroke) means measured for that variable in the control trial; for body angles (*i.e.* roll and pitch), upstrokes and downstrokes were averaged together (Chapter 4)
$_{\Delta 0}$	a subscript which indicates that the zero-reference point is the hand-chosen pre-collision canonical frame (with no special treatment for midstrokes)
$\vec{}$; $\overrightarrow{}$; $\hat{a}$; $\overleftrightarrow{}$; $\bar{}$; $\bar{a}$; $\underline{}$;	accents respectively indicate the variable underneath is a vector; the magnitude of the vector for direction $\hat{a}$ (directional unit vector); a line; a plane or indicates variable underneath is the average for the left and right wing combined (Chapter 2)
$_{ab}$	a subscript which indicates the antecedent is a coefficient relating b to a
$_{c}$	variable has been centered by subtracting its mean value for the entire data set
$_{D}$	a subscript which indicates the mechanism is related to drag
g	griavitational acceleration (980.665 $cm\ s^{-2}$)
$_{i}$	the wing ipsilateral to the direction of moth lateral velocity
I_{yy}	rotational (pitch) inertia about a Body Reference Frame (BRF) y-axis through the moth's estimated COM
K	any coefficient estimated by regression or mixed model
$_{L}$	a subscript which indicates the mechanism is related to lift
$_{LR}$	differences in a kinematic measurement between the left and right side of a moth; *i.e.* left minus right
$_{p}$	peak-to-peak amplitude of the antecedent variable
m	average moth mass at time of experiment (Chapters 1-3); moth plus pin average mass from measurements before, between, and after treatments (Chapter 4)
p	p-value (when alone, not as a subscript).
Q	multiplier that is -1 for upstrokes and +1 for downstrokes

$r^2{}_a$	adjusted r^2; calculated for linear models
$r^2{}_c$	conditional r^2; calculated for linear mixed models

Wing and Body Characteristics

$\overrightarrow{(0, \dot{y}, \dot{z})}$	3D vector with moth horizontal and vertical velocity as its only nonzero components
α; $\overline{\alpha_c}$; α_{LR}	(Chapter 2) wing pitch angle, angle a projection of $\overrightarrow{R_3}$ onto the BRF x/z plane makes relative to the BRF x/y plane; α averaged for the left and right wings, then centered to overall data mean; instantaneous difference in α between the left and right wings
α_ζ; α_{ζ_Δ}; $\alpha_{\zeta_{LR\Delta}}$	wing pitch angle: α_ζ (likely affects AOA, and COP to a lesser extent) is the angle the (x, z) components of the vector connecting the hindwing tip to the forewing tip makes relative to the stroke plane; α_{ζ_Δ} is change relative to control (Chapter 4), average (Chapter 3), or pre-collision average (Chapter 2) α_ζ; $\alpha_{\zeta_{LR\Delta}}$ is left-right asymmetry in α_{ζ_Δ}
β; $\dot{\beta}$; β_Δ	moth whole-body roll angle relative to the horizontal plane; first time derivative of whole-body roll angle; roll angle measured relative midstroke-average roll angle (Chapter 2), or pre-collision midstroke-average roll angle (Chapter 3), or to control (Chapter 4)
ζ; ζ_Δ; $\zeta_{LR\Delta}$	stroke plane inclination angle: ζ is the angle of the stroke plane relative to the BRF horizontal plane; ζ_Δ is change relative to control ζ; $\zeta_{LR\Delta}$ is left-right asymmetry in ζ_Δ
θ; θ_p; $\overline{\theta_{pc}}$; $\theta_{p_{LR}}$; $\theta_{LR\Delta}$; θ_{LR}; θ_i	elevation angle; the angle $\overrightarrow{R_1}$ makes with the BRF horizontal; peak-to-peak wing elevation amplitude (Fig. 4.3), relative to control in Chapter 4; elevation angle, averaged for left and right wings, then centered to overall data mean; left-right asymmetry in θ_p relative to midstroke averages (Chapter 2); left-right asymmetry in θ_p relative to that for the control trial; instantaneous difference in midstroke elevation angular position between the left and right wings; instantaneous midstroke elevation angle for the wing ipsilateral to moth lateral velocity
ϑ_+; ϑ_-; ϑ_Δ	elevation: forewing elevation angle relative to a BRF horizontal plane through the wing base, at the end of downstroke ϑ_+; and upstroke ϑ_-; elevation offset $\vartheta = \vartheta_+ + \vartheta_-$, and ϑ_Δ is change relative to control ϑ
$\widetilde{\Phi}_p$; $\overline{\widetilde{\Phi}}_p$	(Chapter 2) peak-to-peak angular amplitude; mean peak-to-peak angular stroke amplitude for left and right wings
Φ; Φ_p; $\overline{\Phi_{pc}}$; $\Phi_{p_{LR}}$; Φ_{LR}; $\Phi_{LR\Delta}$	instantaneous sweep angle; peak-to-peak wing sweep amplitude, or the projection of $\widetilde{\Phi}_p$ onto the BRF x/y plane (see Fig. 4.3); peak-to-peak wing sweep amplitude averaged for left and right wings, then centered to overall data mean; difference in sweep amplitude between the left and right wings; instantaneous difference in midstroke sweep angular position; left-right asymmetry in θ_p relative to that for the control trial
φ_+; φ_-; φ_Δ	sweep: forewing azimuthal angle relative to a BRF vertical plane through the wing base, at the end of downstroke φ_+; and upstroke φ_-; dorsoventral sweep asymmetry $\varphi = \varphi_+ + \varphi_-$, and φ_Δ is change relative to control or midstroke-centered φ
ξ; ξ_Δ; $\xi_{\Delta LR}$	stroke plane deviation angle: ξ (related to AOA) is the angle the forewing makes at midstroke, measured perpendicular relative to the stroke plane; ξ_Δ is change relative to control ξ; $\xi_{\Delta LR}$ is left-right asymmetry in ξ

$\vec{\tau}$	estimate of COM imbalance (the cross product of the vertical force created by the sinker with a vector stretching from the visually estimated COM to the sinker position, in the BRF
$\overrightarrow{\tau_\beta}$; $\overrightarrow{\tau_{\beta 0}}$	the roll portion of $\vec{\tau}$ ($\overrightarrow{\tau_\beta}$) comes from sinker mass and lateral placement; $\overrightarrow{\tau_\beta}$ was calculated in the BRF; $\overrightarrow{\tau_{\beta 0}}$ was calculated in the SRF.
$\overrightarrow{\tau_\psi}$; $\overrightarrow{\tau_{\psi 0}}$	the pitch portion of $\vec{\tau}$ ($\overrightarrow{\tau_\psi}$) comes from sinker mass and longitudinal placement. $\overrightarrow{\tau_\psi}$ was calculated in the BRF; $\overrightarrow{\tau_{\psi 0}}$ was calculated in the SRF
ψ; ψ_Δ; $\psi_{\Delta 0}$	moth body pitch, $\vec{R}_4$ relative to the horizontal plane (Fig. 4.3); ψ_Δ is change relative to control (Chapter 4), pre-collision average (Chapter 3) or ψ; mean-centred pitch
$\dot{\psi}$; $\dot{\psi}_\Delta$; $\dot{\psi}_{\Delta 0}$	1st time derivative of pitch orientation, *i.e.* "pitch velocity;" midstroke-centred pitch velocity; mean-centred pitch velocity
$\ddot{\psi}$; $\ddot{\psi}_\Delta$ $\ddot{\psi}_{\Delta 0}$	2nd time derivative of pitch orientation, *i.e.* "pitch acceleration;" midstroke-centred pitch acceleration; mean-centred pitch acceleration
$\overrightarrow{F_{D\pm}}$; $\overrightarrow{F_{L\pm}}$; $\overrightarrow{F_{P\pm}}$; $\overrightarrow{F_{W\pm}}$	drag; lift; parasite drag; profile (wing) drag; theoretical forces depicted and explained in Fig. 3.4
$\overleftarrow{L_1}$; $\overleftarrow{L_2}$; $\bar{P}$	geometric characteristics of the stroke plane, as defined in Fig. 4.3 and its caption
r; $\vec{r}$	distance/vector between the moth's center of mass and center of pressure, ***e.g.*** in the computational model (Eq. 3.3-5), and Fig. 3.2-3
$\vec{r}$; $\vec{r}_\pm$	COM-COP vectors shown in Fig. 3.2-3
$\overrightarrow{R_1}$; $\overrightarrow{R_{1t}}$; $\overrightarrow{R_2}$; $\overrightarrow{R_3}$; $\vec{R}_4$; $\vec{R}_5$	vector which stretches from the wing base point (point 3) to the forewing tip (point 4); the $\overrightarrow{R_1}$ vector which is ipsilateral to the direction of moth lateral velocity; vector which stretches from the wing base point (point 3) to the hindwing tip (point 5); vector which stretches from the hindwing tip (point 5) to the forewing tip (point 4); vectors which stretches from the abdomen tip through the centroid of wing base and scutum reference points, forming the moth's body pitch axis; vector with an origin at the forewing tip and parallel to the stroke plane of the moth. All vectors defined in Fig. 4.3 and its caption
x; y; z	in the, +x is forwards for the moth, $+y$ is rightwards for the moth, and , $+z$ is downwards for the moth in the BRF, and $+z$ is // with gravity in the GRF and MGRF; *i.e.* front/back, lateral, and vertical (respectively) in the given reference frame
x; $\dot{x}$; $\dot{x}_\Delta$	in the BRF, +x is forwards for the moth; $\dot{x}$ is forward velocity; $\dot{x}_\Delta$ is midstroke-centered forwards velocity
x_S; z_S	x- and z- positions of T-bar center (for control treatments) or sinker center (for non-control treatments) relative to the center of the two wing bases in the MGRF. Shown in Fig. 4.3.
y; $\dot{y}$; $\ddot{y}$	in the BRF, +y is to the right for the moth; $\dot{y}$ is rightward velocity; $\ddot{y}$ is rightward acceleration
z; $\dot{z}$; $\dot{z}_\Delta$; $\ddot{z}$	in the BRF, $+z$ is downwards for the moth, (// with gravity); $\dot{z}$ is downward velocity; $\dot{z}_\Delta$ is midstroke-centered downward velocity (Chapter 4); vertical acceleration (Chapter 2)
z_A	The abdomen's z- position relative to the center of the two wing bases in the MGRF is denoted by z_A. Shown in Fig. 4.3.

Model Coefficients

$\tau_{\zeta\psi}$ time delay between $\psi_{\Delta 0}$ and ζ_{Δ} in Eq. 3.9-10

$\tau_{\xi\psi}$ time delay between $\psi_{\Delta 0}$ and $Q\xi_{\Delta}$ in Eq. 3.13

$\tau_{\varphi\psi}$ time delay between $-\psi_{\Delta 0}$ and φ in Eq. 3.14

$\tau_{\ddot{\psi}\psi}$ time delay between $-\psi_{\Delta 0}$ and $\ddot{\psi}$ in the theoretical control model (Eq. 3.16)

$\tau_{\ddot{\psi}\dot{\psi}}$ time delay between $-\dot{\psi}_{\Delta 0}$ and $\ddot{\psi}_{\Delta 0}$ in the theoretical control model (Eq. 3.16)

$K_{\dot{\beta}\alpha}$ relates α_{LR} to $\dot{\beta}$

$K_{\dot{\beta}\Phi}$ relates $\Phi_{p_{LR}}$ to $\dot{\beta}$

$K_{\dot{\beta}\theta_p}$ relates $\theta_{p_{LR}}$ to $\dot{\beta}$

$K_{\dot{\beta}\dot{y}}$ relates $\dot{y}$ to $\dot{\beta}$

$K_{\dot{\beta}\theta_i}$ relates $\overrightarrow{(0,\dot{y},\dot{z})} \times \overrightarrow{R_{1\iota}}$ to $\dot{\beta}$

$K_{\ddot{\psi}\zeta}$ relates ${I_{yy}}^{-1} mg\sin(-\zeta_{\Delta})$ to $\ddot{\psi}_{\Delta}$ in the observational pitch acceleration models (Eq. 3.6-7 & 3.2), or theoretical $(I_{yy} + mr^2)^{-1} mgr\sin(-\zeta)$ to $\ddot{\psi}$ in the computational model (Eq. 3.3-5)

$K_{\ddot{\psi}\dot{\psi}}$ relates observed $-{I_{yy}}^{-1} {\dot{\psi}_{\Delta}}^{3} / |\dot{\psi}_{\Delta}|$ in the observational pitch acceleration models (Eq. 3.6-7 & 3.1-2), or theoretical $-(I_{yy} + mr^2)^{-1} \frac{\dot{\psi}^3}{|\dot{\psi}|}$ to $\ddot{\psi}$ in the compu-tational model (Eq. 3.3-5)

$K_{\ddot{\psi}\xi_D}$ relates $-{I_{yy}}^{-1} Q\xi_{\Delta}\cos(\zeta_{\Delta})$ to $\ddot{\psi}_{\Delta}$ in the observational pitch acceleration models (Eq. 3.7 & 3.2)

$K_{\ddot{\psi}\varphi}$ relates φ_{Δ} to $\ddot{\psi}_{\Delta}$ in the observational pitch acceleration models (Eq. 3.2 & 3.1-2)

$K_{\zeta\psi}$ relates observed ψ_{Δ} to ζ_{Δ} (Eq. 3.8), or theoretical ψ to ζ in the computational model (Eq. 3.3-5)

$K_{\zeta\psi_{\tau}}$ relates time-delayed $\psi_{\Delta 0}$ to ζ_{Δ} in Eq. 3.9-10

$K_{\xi\alpha_{\zeta}}$ relates -${\alpha_{\zeta}}_{\Delta}$ to ξ_{Δ} in Eq. 3.11

$K_{\xi\psi}$ relates ψ_{Δ} to $Q\xi_{\Delta}$ in Eq. 3.12

$K_{\xi\psi_{\tau}}$ relates time-delayed $\psi_{\Delta 0}$ to $Q\xi_{\Delta}$ in Eq. 3.13

$K_{\varphi\psi_{\tau}}$ relates time-delayed $-\psi_{\Delta 0}$ to φ in Eq. 3.14

$K_{\varphi\dot{\psi}}$ relates $-\dot{\psi}_{\Delta}\cos(\zeta - \varphi)$ to $Q\varphi_{\Delta}$ in Eq. 3.15

$K_{\ddot{\psi}\psi_{\tau}}$ relates time-delayed $-\psi_{\Delta 0}$ to $\ddot{\psi}$ in the theoretical control model (Eq. 3.16)

$K_{\ddot{\psi}\dot{\psi}_{\tau}}$ relates time-delayed $-\dot{\psi}_{\Delta 0}$ to $\ddot{\psi}_{\Delta 0}$ in the theoretical control model (Eq. 3.16)

$K_{\ddot{\psi}\dot{x}}$ relates observed $-{I_{yy}}^{-1}\cos(\psi_\Delta)\,{\dot{x}_\Delta}^3/|\dot{x}_\Delta|$ or $-{I_{yy}}^{-1}\cos(\zeta_\Delta)\,{\dot{x}_\Delta}^3/|\dot{x}_\Delta|$ to $\ddot{\psi}_\Delta$ in the preliminary pitch acceleration models Eq. 3.1-13; or theoretical $-r(I_{yy}+mr^2)^{-1}\cos(\psi)\,\dot{x}^3/|\dot{x}|$ to $\ddot{\psi}$ in the computational model (Eq. 3.3-5)

$K_{\ddot{\psi}\dot{z}}$ relates observed $-{I_{yy}}^{-1}\sin(\psi_\Delta)\,{\dot{z}_\Delta}^3/|\dot{z}_\Delta|$ or $-{I_{yy}}^{-1}\sin(\zeta_\Delta)\,{\dot{z}_\Delta}^3/|\dot{z}_\Delta|$ to $\ddot{\psi}_\Delta$ in the preliminary pitch acceleration models (Eq. 3.1-2)

$K_{\ddot{\psi}\alpha_D}$ relates $Q\alpha_{\zeta_\Delta}\cos(\zeta_\Delta)$ to $\ddot{\psi}_\Delta$ in the preliminary pitch acceleration model (Eq. 3.1)

$K_{\ddot{\psi}\alpha_L}$ relates observed $\alpha_{\zeta_\Delta}\sin(-\zeta_\Delta)$ to $\ddot{\psi}_\Delta$ in the preliminary pitch acceleration model (Eq. 3.1)

$K_{\ddot{\psi}\xi}$ relates observed $-\xi_\Delta$ to $\ddot{\psi}_\Delta$ in the preliminary pitch acceleration model (Eq. 3.1)

$K_{\ddot{\psi}\vartheta}$ relates observed $Q\vartheta_\Delta$ to $\ddot{\psi}_\Delta$ in the preliminary pitch acceleration models (Eq. 3.1-2)

$K_{\ddot{\psi}\xi_L}$ relates observed $\xi_\Delta\sin(\zeta_\Delta)$ to $\ddot{\psi}_\Delta$ in the preliminary pitch acceleration model (Eq. 3.2)

$K_{\overrightarrow{\tau_{\beta 0}}\beta}$ coefficient relating β_Δ to $\overrightarrow{\tau_{\beta 0}}$

$K_{\overrightarrow{\tau_\beta}\zeta}$ coefficient relating $\zeta_{LR\Delta}$ to $\overrightarrow{\tau_\beta}$

$K_{\overrightarrow{\tau_\beta}\Phi}$ coefficient relating $\Phi_{LR\Delta}$ to $\overrightarrow{\tau_\beta}$

$K_{\overrightarrow{\tau_{\psi 0}}\psi}$ coefficient relating ψ_Δ to $\overrightarrow{\tau_{\psi 0}}$

$K_{\overrightarrow{\tau_\psi}\varphi_\Delta}$ coefficient relating ζ_Δ to $\overrightarrow{\tau_\psi}$

$K_{\overrightarrow{\tau_{\psi 0}}\zeta_\Delta}$ coefficient relating φ_Δ to $\overrightarrow{\tau_\psi}$

$K_{\ddot{x}\zeta}$ relates theoretical $g\sin(\zeta-\psi)$ to $\ddot{x}$ in the computational model (Eq. 3.3-5)

$K_{\ddot{x}\dot{x}}$ relates theoretical $\frac{\dot{x}^3}{|\dot{x}|}/m$ to $\ddot{x}$ in the computational model (Eq. 3.3-5)

$K_{\ddot{y}\beta}$ relates $g\sin(\beta)$ to $\ddot{y}$

$K_{\ddot{y}\dot{y}}$ relates $\dot{y}$ to $\ddot{y}$

$K_{\ddot{y}\Phi}$ relates $\overline{\Phi_{pc}}sign(\beta)$ to $\ddot{y}$

$K_{\ddot{y}\theta}$ relates $\overline{\theta_{pc}}sign(\beta)$ to $\ddot{y}$

$K_{\ddot{y}\alpha}$ relates $\overline{\alpha_c}sign(\beta)$ to $\ddot{y}$

$K_{\ddot{y}\theta_i}$ relates $\overrightarrow{(0,\dot{y},\dot{z})}\times\overrightarrow{R_{1i}}$ to $\ddot{y}$

$K_{\ddot{z}\beta}$ relates $g(1-\cos(\beta))$ to $\ddot{z}$

$K_{\ddot{z}\dot{z}}$ relates $\dot{z}$ to $\ddot{z}$

$K_{\ddot{z}\Phi}$ relates $\overline{\Phi_{pc}}$ to $\ddot{z}$

$K_{\ddot{z}\theta}$ relates $\overline{\theta_{pc}}$ to $\ddot{z}$

$K_{\ddot{z}\alpha}$ relates $\overline{\alpha_c}$ to $\ddot{z}$

CHAPTER 1
GENERAL INTRODUCTION

General Overview

My dissertation focuses on the flight dynamics of the hawkmoth *Manduca sexta* (Linnaeus, 1763) (Fig. 1.1), specifically their maneuverability and stability. Scientists study subjects like this to better understand the natural world and to discover basic design principles which can be translated into technological improvements.

This introductory chapter walks the reader through basic concepts in classical mechanics and insect flight. First, it explains how the concept of stability can be applied to organisms that move. Second, it covers the basics of insect flight mechanics. Third, it discusses stability and movement in the context of insect flight mechanics and gives an overview of the current state of knowledge in this specific area. Fourth and finally, it gives an introductory overview of the experiments detailed in Chapters 2-4.

Figure 1.1 Hawkmoth Manduca sexta

Hawkmoth *Manduca sexta* feeds from a flower. Hawkmoths (Sphingidae) are a cosmopolitan group adapted to high-speed flight and hover-feeding. This particular species is native to North America and starts its life cycle as eggs deposited on either tobacco (*Nicotiana*) or devil's claw (*Proboscidea louisianica*). After feeding on its host plant as a caterpillar for several months, it pupates and emerges as an adult (imago). Moths typically live as flying adults for a few weeks or less. As plant predators and pollinators, they help keep plant ecosystems balanced and diverse. As prey items themselves, they also help transmit energy from autotrophs (plants) to higher-level predators, such as birds and mammals.

Movement and Stability

Physical stability is the ability of an object to return to an initial set of conditions ("equilibrium") when subjected to perturbation (usually within a specified range of stability). In classical mechanics, the ball and valley in Fig. 1.2A is an example of a stable system. If we apply an impulse that accelerates the ball to an initial velocity of less than $\sqrt{2gh}$, it eventually settles back to the bottom of the valley between the two peaks.

Figure 1.2A: Stability

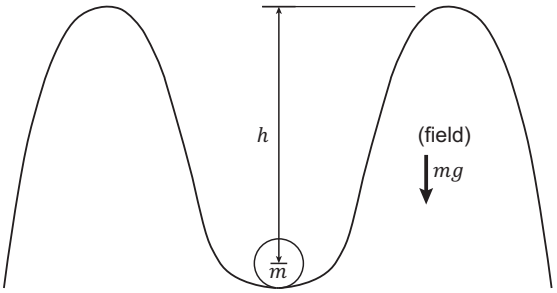

Stable ball in a valley. In classical mechanics, this ball and valley compose a stable system. If we apply an impulse that accelerates the ball to an initial velocity of less than $\sqrt{2gh}$, it eventually settles back to the bottom of the valley between the two peaks.

Fig. 1.2B shows a pendulum, another example of a stable system. When subjected to perturbation, the pendulum will return to a stable 90° orientation due to the passive effects of gravity, and the motion-damping effect of friction in its pivot. And so it is with a hypothetical tree subjected to a small gust of wind; the mechanical design of the system naturally returns it to its original state over time (in this case, after a finite number of decreasing oscillations). Even a powered pendulum, like that of a grandfather clock, will eventually return to its original, cyclical state if perturbed. This powered pendulum is an example of a stable *process*, even though its position is not fixed over time. When a system like this regularly returns to its original state after perturbation because of mechanical rules, without active outside interference, it is exhibiting "passive" stability.

Figure 1.2B: Stability of cyclical processes

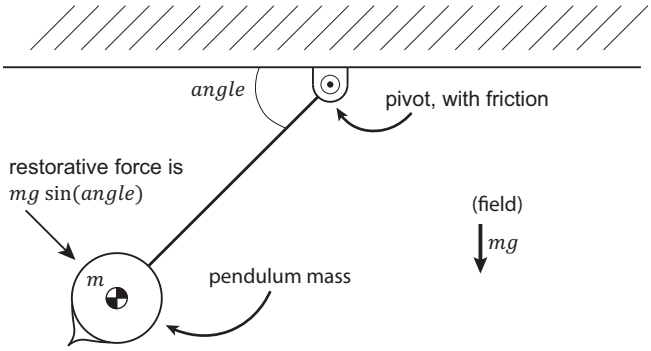

Stable pendulum. Whether *i)* regularly swung in a small arc like the pendulum in a grandfather clock, or *ii)* allowed to swing freely, this pendulum represents a classically stable system. After a perturbation, gravity and friction in the pivot will eventually return this swinging mass eventually return to its *i)* original pattern of motion or *ii)* its at-rest stable orientation with angle = 90°.

Passive vs active stability

Fig. 1.2C shows an instance of "active" stability, where a sea lion balances a ball on the tip of its nose. Here, instead of gravity creating forces that push the ball back to its original at-rest condition as in Fig. 1.2A-1.2B, the sea lion provides these restorative forces. To maintain stability during locomotion, animals use a combination of passive stability (arising from their mechanical design) and active stability (arising from their neural and musculoskeletal responses) to mitigate perturbations.

Figure 1.2C: Active stability

Sea lion uses active stability to balance a ball. Here a sea lion balances a ball on the tip of its nose. If the sea lion were a stone statue but the ball were real, this system would be considered unstable; a small perturbation of the ball would send it toppling to the ground. However, a real sea lion uses its senses (such as touch, sight, and equilibrium) to measure slight perturbations of the ball and then react with opposing forces that keep the ball balanced on its nose. This restores stability to the system, though this is considered "active" stability since sea lion must use senses, processing power, energy, and reactions to maintain the ball's position. Compare this to Fig. **1.2A)** and Fig. **1.2B)**, where gravity and the configuration of the system is enough to maintain *i)* the position of the ball or *ii)* the position or regular cyclical pattern of the swinging mass. Creatures that move typically rely on a combination of both passive and active reactions to maintain stability as they navigate through their environment in search of resources and mates.

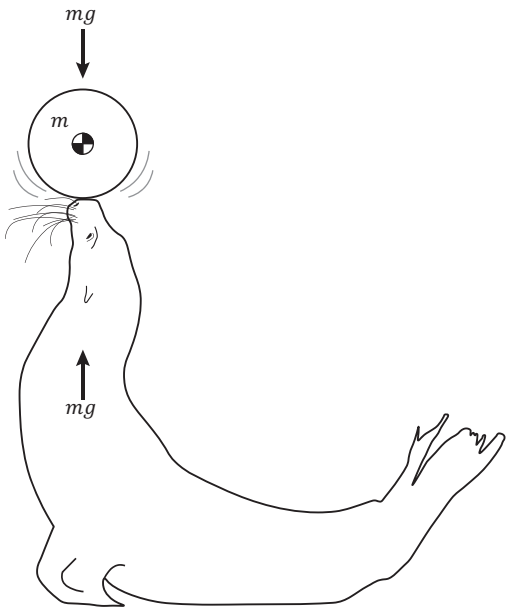

Stability in legged locomotion

Walking, swimming, and flying are all cyclical processes that stabilize against perturbations using both passive and active responses. Of these cyclical locomotor modes, human walking is probably the best understood. In human walking, the upper body functions as an inverted pendulum, rotating about pivot points created by each foot as they alternately touch ground (Dickinson *et al.*, 2000). Each successive step allows the weight of the pendulum to fall forward and the cycle to continue (Cavagna *et al.*, 1977). The process is similar even for multi-legged animals (Full and Koditschek, 1999). In humans, central pattern generators in our spinal cord initiate this ambulatory cycle, and the cycle is mechanically stable against slight imperfections in the walking surface. Larger imperfections require active reflexes also mediated by the spinal cord (Harkema *et al.*, 1997). These reflexes, though we may not be consciously aware of them, involve neural control circuits that trigger muscles to create amelioratory responses (Zehr and Stein, 1999). Larger perturbations may require further active responses mediated by the supraspinal locomotor network in the midbrain, cerebrum, and cerebellum (Jahn *et al.*, 2008;Qiao and Jindrich, 2014).

Stability in flight (see *Flight stability*) and swimming is less well-understood. Nevertheless, the same basic rules, including cyclical energy storage, central pattern generators, physical stability against small perturbations to the cycle, and neural responses to large perturbations, exist in these locomotor modes as well (Alexander and Bennet-Clark, 1977;Biewener and Daley, 2007;Dickinson *et al.*, 2000;Full *et al.*, 2002;Marder and Calabrese, 1996;Orlovskiĭ *et al.*, 1999).

What is a maneuver?

An animal engaged in a maneuver intentionally creates nonzero net torque or force in order to change its orientation, speed, or position in some way. Goal-directed maneuvers must be controlled, and thus it is generally advantageous for the animal to maintain stability throughout; except perhaps in cases of predator avoidance [*e.g.* moths falling out of the air to avoid bats (Miller and Surlykke, 2001)] or dispersal [*e.g.* young spiders floating on silk (Bell *et al.*, 2005;Lister, 1678; Lister *et al.*, 1993)]. To change direction while walking, bipedal animals typically place a foot distal from their center of mass, thus creating an off-center ground reaction force that results in a net rotational torque (Jindrich and Qiao, 2009). Meanwhile, counterbalancing tension in stabilizing muscle groups and connective tissue ensure the internal and

external structure of the walker follows the chosen path without falling over. In flying animals, the mechanisms that initiate maneuvers and create stability mid-air are much less well-understood. These topics are discussed in *Flight stability* and *Flight maneuvers*.

Flight in Animals

Powered flight has proven to be a particularly successful locomotion strategy. In addition to the millions of species of flying insects (Chin and Lentink, 2016;Dudley, 2002a), untold numbers of bats and birds and pterosaurs have also populated Earth's skies. After ~350 million years of evolution (Engel and Grimaldi, 2004;Knecht *et al.*, 2011), flying insects display capabilities our most sophisticated unmanned aerial vehicles currently lack, in a self-healing, self-fueling package that is a fraction of the size with a fraction of the processing power. For this reason, studying insect flight allows us to explore new concepts in biology that we can then directly apply to improve engineering designs.

How insect wings create lift

Insects flap their wings back and forth to create the forces necessary for flight (Weis-Fogh, 1973). When oriented effectively, wings redirect incoming air both forwards and downwards, creating a net reaction force approximately perpendicular to the orientation of the wing (or "airfoil," Fig. 1.3A). In a forward-flying insect, the portion of the force antiparallel to gravity is "lift," and the rest is either "drag" or "thrust" (Azuma, 2012). Note that these definitions of lift and drag differ from the classical fluids directions of lift being perpendicular to the flow direction and drag parallel to it. Referencing lift and drag to gravity simplifies stability and weight support analysis and is therefore common in the insect flight literature. Because these forces are the net of air pressure on the wing, various fluid flow structures that interact with the airfoil will alter lift and drag. For example, quasi-stable leading-edge-vortices (LEVs) increase lift (Fig. 1.3A; Srygley and Thomas, 2002;Birch *et al.*, 2004;Ellington *et al.*, 1996;van den Berg and Ellington, 1997), and cycling wings can intercept previously shed vortices to extract kinetic energy (Birch and Dickinson, 2003).

Figure 1.3A: Airfoils create lift and drag

Airfoils redirect incoming air to create lift. Wings redirect incoming air both forwards and downwards. This creates net reaction force ($\overrightarrow{F_{Net}}$, black), which has both vertical ($\overrightarrow{F_L}$, orange) and horizontal ($\overrightarrow{F_D}$, green) components. A specific wing will produce different ratios of vertical (lift) to horizontal (drag) force depending on its "angle of attack" (α, red) relative to the incomcing wind (light purple). Other variables that affect this relationship include hysteresis in unsteady flows (such as flapping wings in transition), viscosity, velocity, Reynolds number, and wing size, shape, area, composition, camber. The swirl at the front of the wing is created by interaction with the wing's leading edge, and is called the leading edge vortex (LEV). On the size and speed scales typical of flying insects, LEVs enhance lift and are ubiquitous (Sane, 2003).

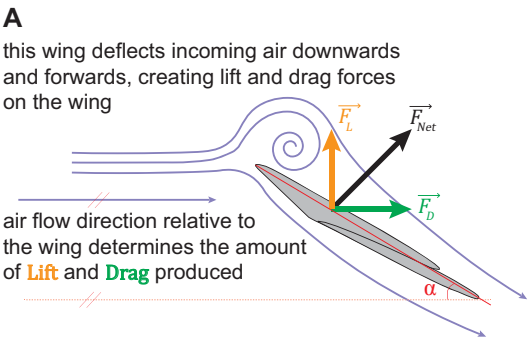

Figure 1.3B-C: Insects flap their wings to create aerodynamic forces

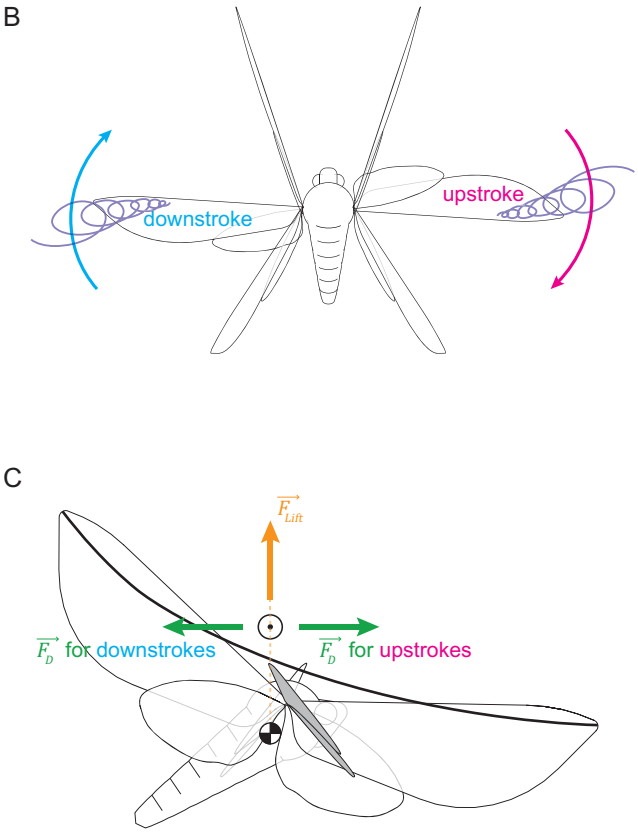

Insects flap their wings in a cycle, along a stroke path. B&C) During hover, insects like hawkmoths rotate their wings forwards and backwards in a cycle. Both up- and downstroke create lift. During hover, upstroke and downstroke create equal and opposite drag (so the moth does not move forwards or backward). In (male) hawkmoths, the front and back wings are attached and generally function as a single unit (Dudley, 2002a). As a general rule for animals with effectively two flapping airfoils, wing movement is (approximately) bilaterally symmetric. **B&C** show up- and downstroke in the same image solely for purposes of visualization. **B)** also shows LEVs (light purple) spiraling distally to be shed on the outside of each wing. **C)** shows that the center of pressure (COP, circle with a dot) lies directly vertical to the center of mass (COM, circle split into four sections) during stable hover. *Cet. par.*, variation from this arrangement causes rotation. If the magnitude of lift $|\overrightarrow{F_L}|$ is not equal to the moth's mass times gravity mg, this causes vertical acceleration. Longitudinally imbalanced drag induces longitudinal motion and pitch. Laterally imbalanced lift induces roll. Laterally imbalanced drag induces yaw.

During hover, insects like hawkmoths rotate their wings forwards and backwards in a cycle to create lift and counterbalancing drag/thrust during upstrokes and downstrokes, respectively. For hawkmoths, this

process is bilaterally symmetric during hover (Fig. 1.3B-1.3C show upstroke and downstroke in the same image solely for purposes of visualization). The amount of lift or drag produced by a wing can be roughly approximated by $\rho A u^2/2$ times the coefficient of lift or drag (C_L or C_D), where ρ is air density, A is the wing area, and u is wind speed (where Re > 1). The angle a wing makes relative to incoming air is known as the angle of attack (α in Fig. 1.3A). C_L and C_D vary with angle of attack, and are typically determined experimentally for a given set of initial conditions (Fig. 1.3D).

Figure 1.3D: Coefficients of lift and drag

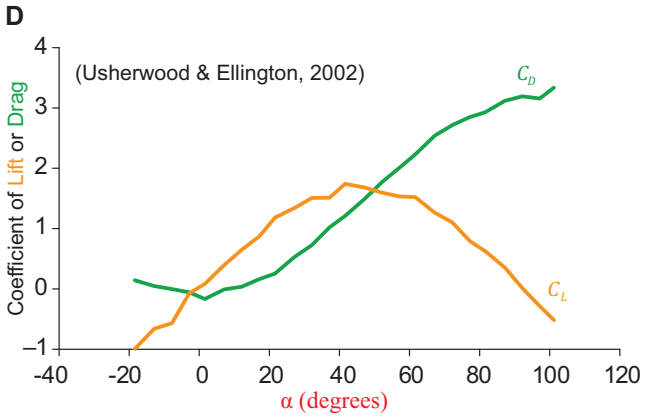

Coefficients of lift and drag depend on angle of attack. In Fig. 1.3D, the amount of lift or drag produced by a wing can be approximated by $\rho A u^2/2$ times the coefficient of lift or drag (C_L or C_D), where ρ is air density, A is the wing area, and u is wind velocity. The angle a wing makes relative to incoming air is known as the angle of attack (α in Fig. 1.2A). C_L and C_D vary with angle of attack, and are typically determined experimentally for a given set of initial conditions. With permission from (Usherwood and Ellington, 2002).

Fluids and size

Viscous forces are relatively less important in larger and faster animals. So, flight strategies change with size and speed. Essentially, viscous forces (*i.e.* forces exerted by surrounding fluids) scale with surface area, while inertia (*e.g.* the force it takes to accelerate a body or wing) scale with mass and speed. If an animal increases in size isometrically, the mass will scale faster than its surface area, (one being length squared and the other being length cubed), and fewer body-lengths-per-second will correspond to the same absolute speeds. So, there is a larger ratio of inertial to viscous fluid forces for animals of larger size. Larger animals experience less resistance to motion relative to their body size, so the medium "feels" thinner. This basic fluids principle, known as Reynolds number (Re), dictates the physical mechanisms which animals can use to effectively create lift and thrust. Disregarding factors like buoyant force and focusing on this effect only, the smallest flying insects (*e.g.* thrips or parasitoid wasps) swim through air like

a human through honey (Delvare, 1993;Jones *et al.*, 2015;Santhanakrishnan *et al.*, 2014); hawkmoths flap in air "thicker" than water to you or I; and the largest whales glide through water with lower relative resistance than air to a jumbo jet (Sane, 2003;Usherwood and Ellington, 2002;Vogel, 2008). Paddle-like hovering flight strategies are commonly seen at lower Re; while airplane-like forward gliding is commonly seen at higher Re.

Stability and Maneuvers in Flapping Flight

In the case of flight, stability involves the return of the animal's body to a stable orientation and the return of the wings to a stable flapping cycle. Velocity is controlled and maneuvers are purposeful. An unwelcome perturbation may cause an animal to deviate from its ideal path or diverge from its ideal orientation. An animal is considered to be stable in response to a perturbation if it returns to its original orientation and flapping dynamic within a reasonable period of time, and without falling/crashing. The quicker and less violent the return, the more stable is the animal to that particular type of perturbation. For purposeful maneuvers, I expect flying animals to use various reorientation strategies covered later in this section.

Flight maneuvers

The location of net forces relative to an object's center of mass (COM) determines the net torque. For example, if a building's center of mass is not directly above the center of its ground reaction forces, it experiences nonzero net-torque, and begins to topple/lean (Fig. 1.4A). In flying animals, forces are the result of air pressure, and the net center of reaction forces is known as the center of pressure (COP). So, for stable flight, the COP must be positioned directly over the COM (Fig. 1.3C). If a flying animal displaces its COM away from this position by extending or flapping an appendage, it will experience net torque and begin to rotate (Dudley, 2002b).

Figure 1.4: Net torque causes rotation

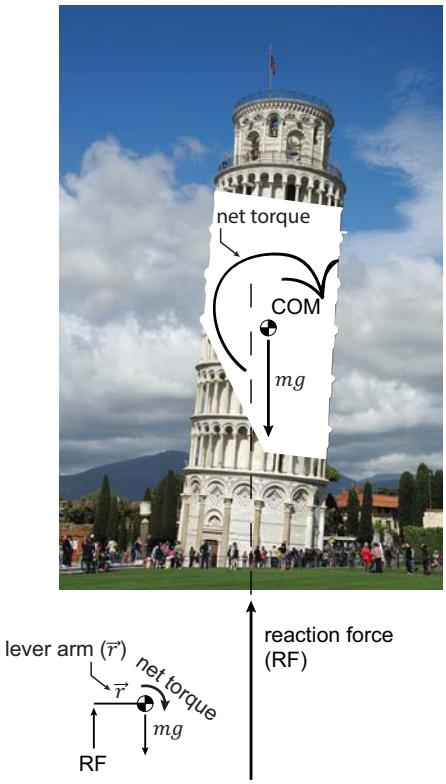

Nonzero net torque creates rotational acceleration. The location of net forces relative to an object's center of mass (COM) determines net torque. For example, if a building's center of mass is not directly above the center of its ground reaction forces, it experiences nonzero net-torque, and begins to topple/lean. Without human intervention, the more this building leans, the more displaced the COM will become, which will increase the lever arm length (r) and thus increase net torque (increasing the rate of rotational acceleration). Thus, the more it leans, the faster it will topple. In real life, the COM of the Leaning Tower of Pisa has been re-centered above its ground reaction force by adding a large amount of lead weights to the tower on the left side of this image.

There is one other option for reorientation. Flying (or falling!) animals can also reorient by leveraging the inertia of individual moving parts against one another (Frohlich, 1980). This is called "inertial" reorientation, and has been shown previously in larger flying animals at low speeds, such as bats and birds, (Bergou *et al.*, 2011;Bergou *et al.*, 2015;Hedrick *et al.*, 2007;Iriate-Díaz *et al.*, 2011;Meadows, 2015;Warrick and Dial, 1998; but see Ros *et al.*, 2015) but not insects. Insects are relatively smaller (lower Re) and have fewer hinged, heavy parts with which they might attempt inertial reorientation. A prominent, at least indirect role for inertia in the reorientation of insects is still conceivable, however, since large, rapidly-flapping insect wings are effectively gyroscopes, albeit counter-rotating ones (Chapters 3 & 5; Dickerson *et al.*, 2014;Eberle *et al.*, 2015;Jankauski and Shen, 2016;Jenkins, 2016), and because insect bodies are jointed and flexible (Chapter 4; Dhyr *et al.* 2013;Hinterwirth *et al.* 2010).

Prior to my work, much research had been conducted on free-flight maneuvers in birds (*e.g.* (Hedrick and Biewener, 2007;Tobalske *et al.*, 2007)) but relatively little on free-flying (untethered) insects (excepting Fry *et al.*, 2003). Much has been done since then, (*e.g.* (Beatus *et al.*, 2015; Ristroph *et al.* 2009; Ristroph *et al.* 2013)), and it is with these recent studies that I am best able to compare and contrast my own conclusions.

Flight stability

Researchers have only recently developed the theoretical framework that enables them to ask probing questions about stability in flapping flight. First, the basic mechanisms of lift and thrust creation in insect-scale flight needed to be understood (*e.g.* (Ellington, 1984;Weis-Fogh, 1956)). Next, questions were asked about how these animals physically create free-flight maneuvers (*e.g.* (Fry *et al.*, 2003)), and how their neural systems work (*e.g.* (Daniel and Tu, 1999;Gray *et al.*, 2002;Nishikawa *et al.*, 2007;Springthorpe *et al.*, 2012)).

The most recent step, the one which I have worked hardest to move forward, is understanding how animals maintain stability in flight. Stability has proven the most challenging of these subject areas because it necessitates a previous understanding of flight forces, maneuver methods, and neural processing systems.

Prior to 2009 when my research began, there were few free-flight studies (*i.e.* ones in which the animal is not connected to a fixed surface) on animal flight stability. Work existed on the responses of various tethered insects to simulated rotations (Fry *et al.*, 2008;Lehmann and m, 1998;Sherman and Dickinson, 2003;Taylor and Thomas, 2003). Recent work also includes the response of hummingbirds, bees, and hawkmoths responding to unsteady flow (Combes and Dudley, 2009;Ortega-Jimenez *et al.*, 2013;Ravi *et al.*, 2013;Vance *et al.*, 2013;Vandenberghe *et al.*, 2004). Computational fluid dynamic (CFD) and physical (*i.e.* robotic) modeling studies have also been conducted. However, these models necessitate (sometimes non-obvious) simplifications that, if incorrect, may result in substantial differences between model and real-world flight dynamics (Chapters 3 & 5; Chin and Lentink, 2016;Taha *et al.*, 2015).

Notable work has also been done on passive damping of rotation about the vertical (Bergou *et al.*, 2010;Hedrick *et al.*, 2009), longitudinal (Beatus *et al.*, 2015;Ristroph *et al.*, 2009), and lateral (Cheng *et al.*, 2011;Ristroph *et al.*, 2013;Whitehead *et al.*, 2015) axes (*i.e.* yaw, roll, and pitch, respectively; Fig. 1.6A-C). Key passive damping mechanisms that have been identified include flapping countertorque, or “FCT” [rotations change the velocity of wings flapping in that rotational plane, damping the rotation (Fig. 1.6; Hedrick *et al.*, 2009)], and air drag [specifically for high-drag, smaller flying insects (Ristroph *et al.*, 2013)]. When flapping frequency is slow or nonexistent, such as during gliding, these flapping-related damping factors are supplemented by many of the same stability factors seen in fixed wing aircraft (Azuma, 2012).

These passive damping factors (those identified in previous work) are almost all global reference frame (GRF) velocity effects, where rotations are damped solely by changes to wing velocity or orientation in the reference frame of a stationary observer. This is distinct from the gyroscopic/inertio-viscous passive damping factors I identify in Chapters 3-5, where torque impulses change wing kinematics relative to the flapping animal itself (*i.e.* in the "BRF," or body reference frame, like that of a passenger sitting inside of a turning airplane). These deviations from the normal flapping cycle in the BRF of the moth match those which create roll (Chapters 2, 4, 5), and pitch (Chapter 3) torque in the opposite direction of the initial torque impulse; this is the novel class of inertio-viscous damping I propose in this dissertation (Fig. 3.7, 5.2, 5.5). Since inertio-viscous damping factors complement GRF velocity (viscous) damping factors previously discussed, flapping stability could scale across a range of sizes and speeds.

Figure 1.5: FCT in yaw is an example of damping from viscous GRF wing velocity changes

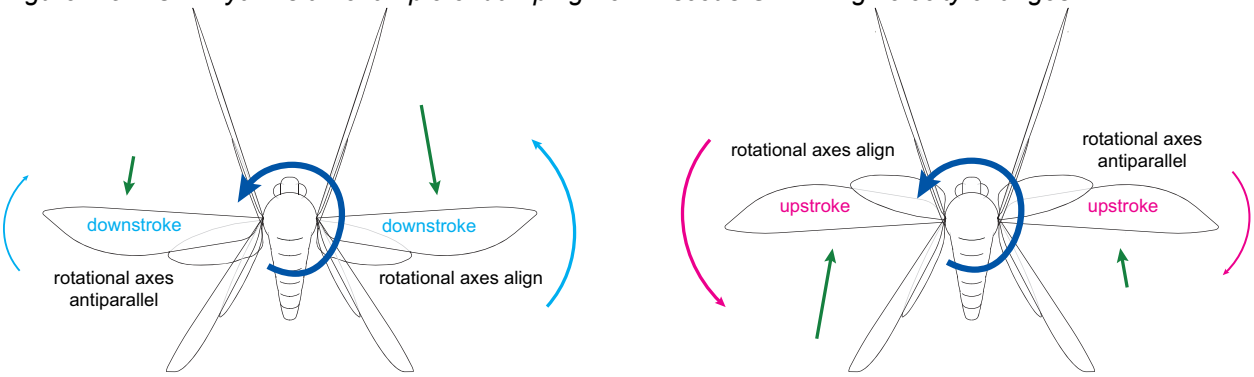

Flapping flight is damped by world reference frame velocity effects. During a leftwards yaw rotation, if the wings move at (approximately) the same speed in reference to the rotating moth (in the body reference frame, or BRF), then in the world reference frame (global reference frame, or GRF), the right wing flaps faster in downstroke and the right faster in upstroke. Research has found this type of velocity effect damps yaw in flapping flight (Hedrick *et al.*, 2009;Hedrick and Robinson, 2010), roll in hawkmoths and cockatoos (Greeter and Hedrick, 2016;Hedrick *et al.* 2007), and sideslip in fruit flies and hawkmoths (Faruque and Humbert, 2010b;Greeter and Hedrick, 2016). If the asymmetric misalignment of rotational axes with the wings were to (*via* inertia) introduce asymmetries in wing movement from the perspective of the moth, and these flapping asymmetries interacted with the air so as to create yaw countertorque, that would instead be an example of an "inertio-viscous" damping effect. A damping effect like this has not (yet) been shown to be the case for yaw rotations, though my dissertation describes such damping effects for roll and pitch.

Figure 1.6A-C: Flapping flight wing and body kinematics

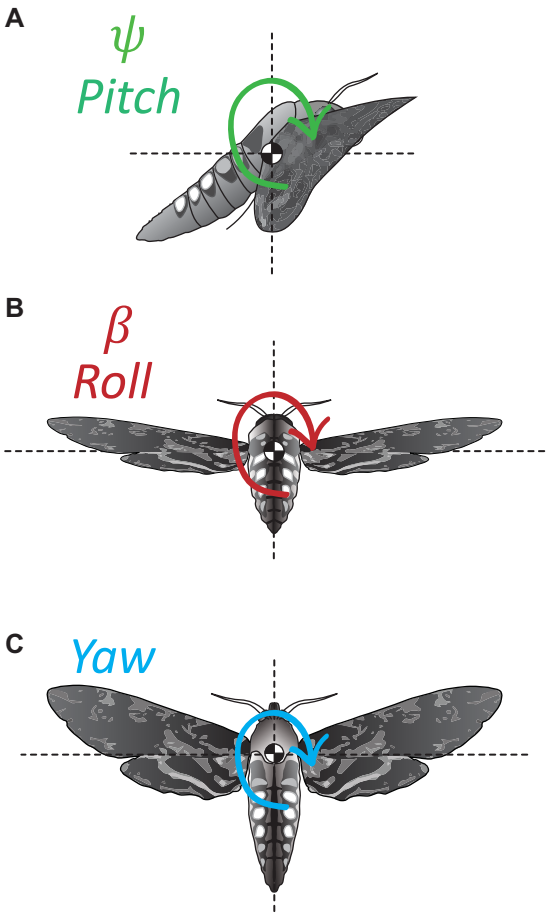

Pitch, roll, and yaw. It is convenient to break down whole-body kinematics into the six familiar degrees of freedom: up/down, left/right, fore/aft, yaw, pitch, and roll. A) Pitch (green) is rotation about the lateral (left/right) axis, B) roll (red) is rotation about the longitudinal (fore/aft) axis, and C) yaw (cyan) is rotation around the vertical (up/down) axis.

Quantifying wing and body dynamics

In *M. sexta*, as in most flying animals, the majority of reorientation forces come from the wings. Thus, it is useful to define basic wing kinematics to establish a foundation for the rest of this dissertation.

Figure 1.6 defines the chief characteristics of body (A-C) and wing (D-E) kinematics as applied in this dissertation. It is convenient to break down whole-body kinematics into the six familiar degrees of freedom: up/down, left/right, fore/aft, yaw, pitch, and roll. Yaw is rotation around the vertical (up/down) axis, pitch is rotation about the lateral (left/right) axis, and roll is rotation about the longitudinal (fore/aft) axis (Fig. 1.6A-C). Wing sweep, wing elevation, wing stroke plane, and stroke plane deviation angle are all basic kinematic measures of wing motion (Fig. 1.6D). Since angle of attack (α, Fig. 1.3B) is dynamic, it is also useful to define a "wing pitch angle" relative to some consistent geographical benchmark, such as stroke plane angle (Fig. 1.6E) or the body reference frame (BRF) horizontal axis. Fig. 4.3 (in Chapter 4) provides a more complete diagram and a detailed description of the wing and body kinematics I used throughout my research.

Figure 1.6D-E: Flapping flight wing and body kinematics

Body pitch and wing stroke path, stroke plane, sweep, elevation, and deviation. D) Wing sweep, elevation, stroke plane, and deviation angle are all basic kinematic measures of wing motion. Sweep and elevation (longitudinal and vertical wing position relative to the wing base) are typically measured as either an instantaneous position or as an amplitude for a given quarter- or halfstroke. Stroke plane is typically measured over the course of a given halfstroke, and wing deviation perpendicular to this line is stroke plane deviation angle (measured at midstroke in my work). Some publications use "wing deviation," "elevation," and "stroke plane deviation" interchangeably; however, mine do not. **E)** Since angle of attack (α, Fig. 1.2B) is dynamic, it is also common to define a "wing pitch angle" relative to some consistent geographical benchmark, such as stroke plane angle (as shown in this figure) or the BRF horizontal axis (though **E** depicts only the former convention). When fitting trends to models in my work, I typically isolate wing pitch angle at midstroke.

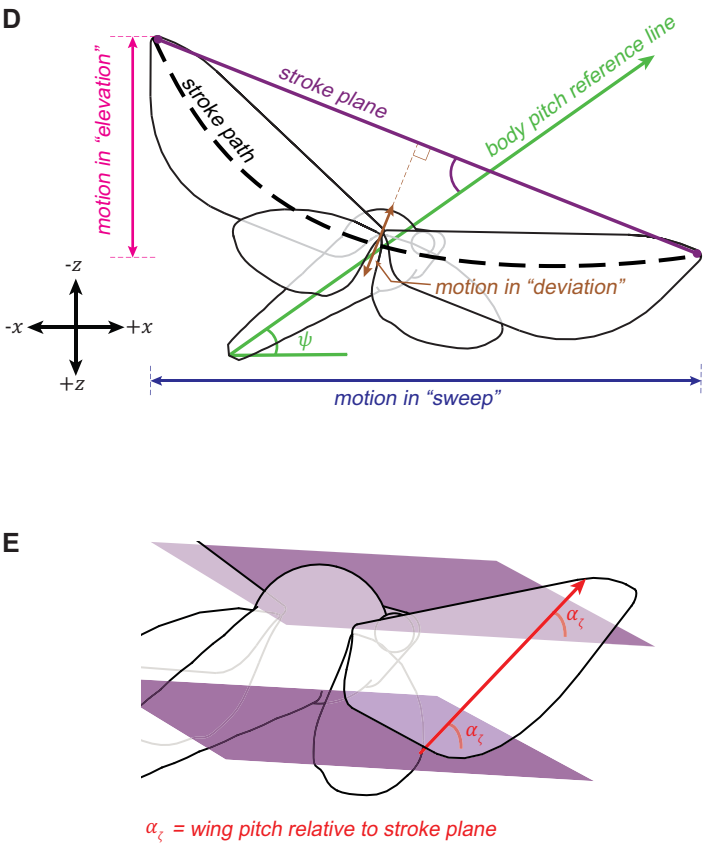

Summary of Chapters 2-4

My dissertation consists of five chapters that describe three main experiments. All three experiments look at both stability and maneuverability in the hawkmoth species *Manduca sexta* (henceforth, simply "hawkmoths"). They examine *M. sexta* roll and pitch in three distinct contexts: 1) goal-directed lateral and roll maneuvers, 2) stabilization of pitch in response to an impulse perturbation, and 3) compensation for center of mass (COM) dislocation. Despite their different approaches, all three experimental results are in close agreement. This consistency supports my conclusions about how hawkmoths maneuver and stabilize.

Chapter 2 summary

Chapter 2 describes direct lateral maneuvers and roll maneuvers in hawkmoths. In this experiment, I coaxed moths to follow a handheld oscillating light in the dark. First, results demonstrate hawkmoths reorient their net lift vector to create direct lateral maneuvers (*i.e.* "sideslips"). Second, results demonstrate hawkmoths use left-right asymmetries in wing pitch angle and sweep to generate asymmetries in lift. This asymmetry creates the net torque that initiates the roll maneuver.

Relative to previous and concurrent work, this study confirms the same basic wing mechanisms for roll torque creation, (Beatus and Cohen, 2015;Beatus *et al.*, 2015), but shows greater than expected passive damping in roll. The damping is so severe that changes to wing kinematics correlated to the first, rather than the second, derivative of roll orientation.

In this first study, we concluded that viscous interactions from global reference frame (GRF) effects are a major factor in roll damping. Recall from Fig. 1.6 that, when rotated in space (in the GRF), wings may be flapping at the same speed in the reference frame of the moth (the BRF), but experience unequal velocities that lead to viscous damping. Thus, just as in yaw, when a moth begins to roll about its longitudinal axis, global reference frame asymmetries in wing velocity damp the rotation (Fig. 5.1A). Because roll creates sideslip, the lateral motion from sideslip further enhances this effect (Fig. 5.1B). In this way, lateral motion itself damps roll.

In a similar global reference frame effects, it is likely that moths are also roll-damped by well-known velocity-based effects also present in fixed-wing aircraft, such as dihedral angle and induced angle of attack (AOA; the angle at which wings hit incoming air; Fig. 1.3A & 1.3D) asymmetry. These specific damping effects are likely small when velocity is also low (Cheng and Deng 2011; Cheng *et al.*, 2009; Elzinga *et. al*, 2014), but not when velocities are high.

Moths seemed to employ two active damping countermeasures during the maneuvers. First, the angle of attack asymmetries moths used to induce roll are opposite those which expected to create roll damping (known for fixed-wing case; Cheng *et al.*, 2011). Second, hawkmoths employ lateral asymmetry in elevation amplitude to counter roll damping. Results show roll damping is about four times as strong during upstrokes (upwards movement of the wing); which indicates global reference frame asymmetries in wing velocity about the roll axis during sideslip (Fig. 5.1A-C) are a major source of roll-damping in *M. sexta.*

Chapter 3 summary

Chapter 3 describes *M. sexta* response to impulse pitch perturbations. In this experiment, I fired a small (~.2 g) clay projectile from toy cannon at hawkmoths while they hovered in mid-air, striking them in the abdomen or thorax and perturbing them in pitch. First, it shows that hawkmoths are unexpectedly capable of stabilizing against quite large (>90°) pitch perturbations. Second, it shows this stabilization response can be (and likely is) mediated by *passive* changes to stroke plane angle and angle of attack, (and possibly passive changes to fore-aft/dorsoventral sweep amplitude as well). The implications of my results could contrast with long-standing scientific consensus, as they indicate there could be much greater passive damping in pitch than currently believed (Maeda *et al.*, 2010;Noda *et al.*, 2013;Ristroph *et al.*, 2013;Sun *et al.*, 2007;Taha *et al.*, 2015), and that wing inertia/momentum likely plays an important role in creating stability in flapping flight (*e.g.* (Cheng *et al.* 2009)).

When pitched by an impulse, both drag and inertia cause the wings to resist rotation more strongly than the body, so they continue to flap in a similar plane within the global reference frame (GRF), even as the body oscillates. This restores a measure of pendular stability to the flight of insects, with the center of pressure (COP; Fig. 1.3C) serving as a quasi-fixed point above the damped (but oscillating) center of mass (COM; Fig. 1.3C & 3.4). Because rapidly flapping wings are essentially gyroscopes, pitch torque at the wing base manifests as stroke plane deviation angle changes at midstroke. Careful examination of directionality and the data suggests these changes are reinforced by the aerodynamic forces of pitch rotation, and also help passively restore stability. Stroke plane deviation angle changes are essentially roll perturbations to the wings themselves; these changes may interact with the rotational momentum of flipping wings to create dorsoventral sweep asymmetries which also damp pitch.

Recent/concurrent research on insect flight shows both aerodynamic (Hedrick, 2011;Hedrick *et al.*, 2009;Hedrick and Robinson, 2010) and inertial (Eberle *et al.*, 2015) forces damp world frame (GRF) rotations of flapping wings. In this context, the results of Chapter 3 strongly suggest that pitch-damping in insect-scale flapping flight is the result of the sum of viscous and inertial forces. Wings of insects are thus massive vibrating structures that experience high drag, and these two effects work together to automatically resist and correct for rotations. Wing movements are *not* perfectly coupled to the body.

Since the wing kinematics that passively resist pitch rotation seem to arise from both inertial (in this case gyroscopic/accelerative) and viscous (air drag/velocity) sources, this strongly suggests a general effect that is not strictly dependent on Reynolds number alone, or possibly even the time scale of the perturbation. If inertial and aerodynamic effects are additive and create pitch stability in hawkmoths, this may be the case for flying animals across a wide variety of size scales and flapping frequencies, and in other degrees of freedom, as well. Thus this could be an important theoretical step in the study of stability in flapping flight.

Chapter 4 summary

Chapter 4 describes *M. sexta* response to the manipulation of its center of mass (COM). In these experiments, moths fed from a flower with an off-axis fishing sinker attached to a T-bar on their dorsal surface, which required them to continually create torque to maintain hover orientation.

First, the results show moths alter their orientation (their COM) position to partially adapt to the applied torque. They pitch their bodies down, increase their intra-abdominal angle, and roll their entire body to reduce the effective COM displacement. Because this does not completely correct for the COM offset, they also use their wings to create continuous pitch and roll torque, described below.

To counter the pitch-down COM offset that remains after adjusting their body pitch angle and intra-abdominal angle, moths make their stroke planes more acute, and sweep their wings farther forward relative to a control trial. They also increase angle of attack (AOA) in downstrokes. To counter the roll COM offset that remains after adjusting their body roll angle, moths increase the sweep of the sinker-ipsilateral wing pair relative to that of the sinker-contralateral wing pair. They also increase/decrease downstroke/upstroke stroke plane angle in the sinker-ipsilateral wing pair relative to the control.

Wing kinematic results were consistent with the theoretical framework I established in previous chapters. However, unlike previous chapters, I did not find a significant relationship between angle of attack (AOA) and roll; and the relationship between AOA and pitch was statistically weak (and only present for downstrokes). Furthermore, there was no significant relationship between elevation amplitude and roll. These results are consistent with my conclusion that roll is heavily damped in *M. sexta*, and that the changes

they make to angle of attack and elevation amplitude during sideslip are targeted at reducing velocity-related (world-frame/GRF) roll-damping effects.

REFERENCES

Alexander, R. M. and Bennet-Clark, H. C. (1977). Storage of elastic strain energy in muscle and other tissues. *Nature* **265,** 114-117.

Azuma, A. (2012). *The biokinetics of flying and swimming*: Springer Science & Business Media.

Beatus, T. and Cohen, I. (2015). Wing-pitch modulation in maneuvering fruit flies is explained by an interplay between aerodynamics and a torsional spring. *Phys. Rev. E* **92,** 022712.

Beatus, T., Guckenheimer, J. M. and Cohen, I. (2015). Controlling roll perturbations in fruit flies. *J. R. Soc. Interface* **12,** 10.1098/rsif.2015.0075.

Bell, J., Bohan, D., Shaw, E. and Weyman, G. (2005). Ballooning dispersal using silk: world fauna, phylogenies, genetics and models. *Bull. Entomol. Res.* **95,** 69-114.

Bergou, A. J., Swartz, S. M., Vejdani, H., Riskin, D. K., Reimnitz, L., Taubin, G. and Breuer, K. S. (2015). Falling with style: bats perform complex aerial rotations by adjusting wing inertia. *PLoS Biol.* **13,** e1002297.

Bergou, A. J., Swartz, S., Breuer, K. and Taubin, G. (2011). 3D Reconstruction and analysis of bat flight maneuvers from sparse multiple view video. 1-2.

Bergou, A. J., Ristroph, L., Guckenheimer, J., Cohen, I. and Wang, Z. J. (2010). Fruit Flies Modulate Passive Wing Pitching to Generate In-Flight Turns. *Phys. Rev. Lett.* **104,** 148101.

Biewener, A. A. and Daley, M. A. (2007). Unsteady locomotion: integrating muscle function with whole body dynamics and neuromuscular control. *J. Exp. Biol.* **210,** 2949-2960.

Birch, J. M. and Dickinson, M. H. (2003). The influence of wing-wake interactions on the production of aerodynamic forces in flapping flight. *J. Exp. Biol.* **206,** 2257-2272.

Birch, J. M., Dickson, W. B. and Dickinson, M. H. (2004). Force production and flow structure of the leading edge vortex on flapping wings at high and low Reynolds numbers. *J. Exp. Biol.* **207,** 1063-1072.

Cavagna, G. A., Heglund, N. C. and Taylor, C. R. (1977). Mechanical work in terrestrial locomotion: two basic mechanisms for minimizing energy expenditure. *Am. J. Physiol.* **233,** R243-61.

Cheng, B., and Deng, X. (2011). Translational and rotational damping of flapping flight and its dynamics and stability at hovering. *IEEE Trans. Robotics* **27.5,** 849-864.

Cheng, B., Deng, X. and Hedrick, T. L. (2011). The mechanics and control of pitching manoeuvres in a freely flying hawkmoth (Manduca sexta). *J. Exp. Biol.* **214,** 4092-4106.

Cheng, B., Fry, S. N., Huang, Q., Dickson, W. B., Dickinson, M. H., & Deng, X. (2009). Turning dynamics and passive damping in flapping flight. *IEEE Int. Conf. Robotics and Automation.* 1889-1896

Chin, D. D. and Lentink, D. (2016). Flapping wing aerodynamics: from insects to vertebrates. *J. Exp. Biol.* **219,** 920-932.

Combes, S. A. and Dudley, R. (2009). Turbulence-driven instabilities limit insect flight performance. *Proc. Natl. Acad. Sci. U.S.A.* **106,** 9105-9108.

Daniel, T. L. and Tu, M. S. (1999). Animal movement, mechanical tuning and coupled systems. *J. Exp. Biol.* **202,** 3415-3421.

Delvare, G. (1993). On the Megaphragma of Guadeloupe with the description of a new species (Hymenoptera, Trichogrammatidae). *Revue française d'Entomologie* **15,** 149-152.

Dyhr, J. P., Morgansen, K. A., Daniel, T. L. and Cowan, N. J. (2013). Flexible strategies for flight control: an active role for the abdomen. *J. Exp. Biol.* **216,** 1523-1536.

Dickerson, B. H., Aldworth, Z. N. and Daniel, T. L. (2014). Control of moth flight posture is mediated by wing mechanosensory feedback. *J. Exp. Biol.* **217,** 2301-2308.

Dickinson, M. H., Farley, C. T., Full, R. J., Koehl, M. A. R., Kram, R. and Lehman, S. (2000). How Animals Move: An Integrative View. *Science* **288,** 100-106.

Dudley, R. (2002a). *The biomechanics of insect flight: form, function, evolution*: Princeton University Press.

Dudley, R. (2002b). Mechanisms and implications of animal flight maneuverability. *Integr. Comp. Biol.* **42,** 135-140.

Eberle, A. L., Dickerson, B. H., Reinhall, P. G. and Daniel, T. L. (2015). A new twist on gyroscopic sensing: body rotations lead to torsion in flapping, flexing insect wings. *J. R. Soc. Interface* **12,** 20141088.

Ellington, C. P., van den Berg, C., Willmott, A. P. and Thomas, A. L. (1996). Leading-edge vortices in insect flight. *Nature* **384.6610,** 626-630

Ellington, C. P. (1984). The aerodynamics of hovering insect flight. VI. Lift and power requirements. *Phil. Trans. R. Soc. Lon. B Biol. Sci.* **305,** 145-181.

Elzinga, M. J., Floris B. v., and Dickinson, M. H. (2014). Strategies for the stabilization of longitudinal forward flapping flight revealed using a dynamically-scaled robotic fly. *Bioinsp. Biomim.* **9.2,** 025001.

Engel, M. S. and Grimaldi, D. A. (2004). New light shed on the oldest insect. *Nature* **427,** 627-630.

Faruque, I. and Humbert, J. S. (2010). Dipteran insect flight dynamics. Part 2: Lateral–directional motion about hover. *J. Theor. Biol.* **265,** 306-313.

Frohlich, C. (1980). The physics of somersaulting and twisting. *Sci. Am.* **242**, 154-165.

Fry, S. N., Rohrseitz, N., Straw, A. D. and Dickinson, M. H. (2008). TrackFly: virtual reality for a behavioral system analysis in free-flying fruit flies. *J. Neurosci. Methods* **171,** 110-117.

Fry, S. N., Sayaman, R. and Dickinson, M. H. (2003). The aerodynamics of free-flight maneuvers in Drosophila. *Science* **300,** 495-498.

Full, R. J., Kubow, T., Schmitt, J., Holmes, P. and Koditschek, D. (2002). Quantifying Dynamic Stability and Maneuverability in Legged Locomotion1. *Integr. Comp. Biol.* **42,** 149-157.

Full, R. J. and Koditschek, D. E. (1999). Templates and anchors: neuromechanical hypotheses of legged locomotion on land. *J. Exp. Biol.* **202,** 3325-3332.

Greeter, J. S. M., and Hedrick, T. L. (2016). Direct lateral maneuvers in hawkmoths. *Biol. Open*, bio-012922

Gray, J. R., Pawlowski, V. and Willis, M. A. (2002). A method for recording behavior and multineuronal CNS activity from tethered insects flying in virtual space. *J. Neurosci. Methods* **120,** 211-223.

Harkema, S. J., Hurley, S. L., Patel, U. K., Requejo, P. S., Dobkin, B. H. and Edgerton, V. R. (1997). Human lumbosacral spinal cord interprets loading during stepping. *J. Neurophysiol.* **77,** 797-811.

Hedrick, T. L. (2011). Damping in flapping flight and its implications for manoeuvring, scaling and evolution. *J. Exp. Biol.* **214,** 4073-4081.

Hedrick, T. L. and Biewener, A. A. (2007). Low speed maneuvering flight of the rose-breasted cockatoo (*Eolophus roseicapillus*). I. Kinematic and neuromuscular control of turning. *J. Exp. Biol.* **210,** 1897-1911.

Hedrick, T., Usherwood, J. and Biewener, A. (2007). Low speed maneuvering flight of the rose-breasted cockatoo (*Eolophus roseicapillus*). II. Inertial and aerodynamic reorientation. *J. Exp. Biol.* **210,** 1912-1924.

Hedrick, T. L., Cheng, B. and Deng, X. (2009). Wingbeat Time and the Scaling of Passive Rotational Damping in Flapping Flight. *Science* **324,** 252-255.

Hedrick, T. L. and Robinson, A. K. (2010). Within-wingbeat damping: dynamics of continuous free-flight yaw turns in Manduca sexta. *Biology Letters* **6,** 422-425.

Hinterwirth, A. J. and Daniel, T. L. (2010). Antennae in the hawkmoth *Manduca sexta* (Lepidoptera, Sphingidae) mediate abdominal flexion in response to mechanical stimuli. *J. Comp. Physiol. A* **196,** 947-956.

Iriarte-Díaz, J., Riskin, D. K., Willis, D. J., Breuer, K. S., & Swartz, S. M. (2011). Whole-body kinematics of a fruit bat reveal the influence of wing inertia on body accelerations. *J. Exp. Biol.* **214.9,** 1546-1553.

Jahn, K., Deutschländer, A., Stephan, T., Kalla, R., Hüfner, K., Wagner, J., Strupp, M. and Brandt, T. (2008). Supraspinal locomotor control in quadrupeds and humans. *Prog. Brain Res.* **171,** 353-362.

Jankauski, M. and Shen, I. (2016). Experimental studies of an inertial-elastic rotating wing in air and vacuum. *Int. J. Micro Air Veh.* **8,** 53-63.

Jindrich, D. L. and Qiao, M. (2009). Maneuvers during legged locomotion. *Chaos* **19,** 026105.

Jones, S., Laurenza, R., Hedrick, T. L., Griffith, B. E. and Miller, L. A. (2015). Lift vs. drag based mechanisms for vertical force production in the smallest flying insects. *J. Theor. Biol.* **384,** 105-120.

Knecht, R. J., Engel, M. S. and Benner, J. S. (2011). Late Carboniferous paleoichnology reveals the oldest full-body impression of a flying insect. *Proc. Natl. Acad. Sci. USA* **108,** 6515-6519.

Lehmann, F. O. and Dickinson, M. H. (1998). The control of wing kinematics and flight forces in fruit flies (Drosophila spp.). *J. Exp. Biol.* **201,** 385-401.

Linnaeus, C. v. (1763). Centuria insectorum rariorum. *Amoenitates Academicae* **6,** 384-415.

Lister, M. (1638). *Historiae animalium Angliae: tres tractatus.* Regiae Societatis Typographum Londini.

Lister, M., Davies, M., Harley, B., Parker, J. and Findlen, P. (1993). Martin Lister's English Spiders 1678. *ISIS-International Review Devoted to the History of Science and its Cultural Influence* **84,** 801-801.

Maeda, M., Gao, N., Nishihashi, N. and Liu, H. (2010). A free-flight simulation of insect flapping flight. *J. Aero Aqua Bio-mechanisms* **1,** 71-79.

Marder, E. and Calabrese, R. L. (1996). Principles of rhythmic motor pattern generation. *Physiol. Rev.* **76,** 687-717.

Meadows, R. (2015). How bats land upside down. *PLoS Biol.* **13,** e1002298.

Miller, L. A. and Surlykke, A. (2001). How Some Insects Detect and Avoid Being Eaten by Bats: Tactics and Countertactics of Prey and Predator Evolutionarily speaking, insects have responded to selective pressure from bats with new evasive mechanisms, and these very responses in turn put pressure on bats to “improve” their tactics. *Bioscience* **51,** 570-581.

Nishikawa, K., Biewener, A. A., Aerts, P., Ahn, A. N., Chiel, H. J., Daley, M. A., Daniel, T. L., Full, R. J., Hale, M. E., Hedrick, T. L. *et al.* (2007). Neuromechanics: an integrative approach for understanding motor control. *Integr. Comp. Biol.* **47,** 16-54.

Noda, R., Maeda, M. and Liu, H. (2013). Effect of Passive Body Deformation of Hawkmoth [*sic.*] on Flight Stability. *Intelligent Autonomous Systems 12*, pp. 835-842: Springer.

Orlovskiĭ, G. N., Deliagina, T. and Grillner, S. (1999). *Neuronal control of locomotion: from mollusc to man*. Oxford University Press.

Ortega-Jimenez, V. M., Greeter, J. S., Mittal, R. and Hedrick, T. L. (2013). Hawkmoth flight stability in turbulent vortex streets. *J. Exp. Biol.* **216,** 4567-4579.

Qiao, M. and Jindrich, D. L. (2014). Compensations during Unsteady Locomotion. *Integr. Comp. Biol.* **54,** 1109-1121.

Ravi, S., Crall, J. D., Fisher, A. and Combes, S. A. (2013). Rolling with the flow: bumblebees flying in unsteady wakes. *J. Exp. Biol.* **216,** 4299-4309.

Ristroph, L., Berman, G. J., Bergou, A. J., Wang, Z. J. and Cohen, I. (2009). Automated hull reconstruction motion tracking (HRMT) applied to sideways maneuvers of free-flying insects. *J. Exp. Biol.* **212,** 1324-1335.

Ristroph, L., Ristroph, G., Morozova, S., Bergou, A. J., Chang, S., Guckenheimer, J., Wang, Z. J. and Cohen, I. (2013). Active and passive stabilization of body pitch in insect flight. *J. R. Soc. Interface* **10,** 20130237.

Ros, I. G., Bassman, L. C., Badger, M. A., Pierson, A. N. and Biewener, A. A. (2011). Pigeons steer like helicopters and generate down- and upstroke lift during low speed turns. *Proc. Natl. Acad. Sci. USA* **108,** 19990-19995.

Sane, S. P. (2003). The aerodynamics of insect flight. *J. Exp. Biol.* **206,** 4191-4208.

Santhanakrishnan, A., Robinson, A. K., Jones, S., Low, A. A., Gadi, S., Hedrick, T. L. and Miller, L. A. (2014). Clap and fling mechanism with interacting porous wings in tiny insect flight. *J. Exp. Biol.* **217,** 3898-3909.

Sherman, A. and Dickinson, M. H. (2003). A comparison of visual and haltere-mediated equilibrium reflexes in the fruit fly Drosophila melanogaster. *J. Exp. Biol.* **206,** 295-302.

Springthorpe, D., Fernández, M. J. and Hedrick, T. L. (2012). Neuromuscular control of free-flight yaw turns in the hawkmoth Manduca sexta. *J. Exp. Biol.* **215,** 1766-1774.

Srygley, R. B., and Thomas, A. L. R. (2002). Unconventional lift-generating mechanisms in free-flying butterflies. *Nature* ***420*****.6916,** 660-664.

Sun, M., Wang, J. and Xiong, Y. (2007). Dynamic flight stability of hovering insects. *Acta Mechanica Sinica* **23,** 231-246.

Taha, H. E., Tahmasian, S., Woolsey, C. A., Nayfeh, A. H. and Hajj, M. R. (2015). The need for higher-order averaging in the stability analysis of hovering, flapping-wing flight. *Bioinsp. Biomim.* **10,** 016002.

Taylor, G. K. and Thomas, A. L. R. (2003). Dynamic flight stability in the desert locust *Schistocerca gregaria*. *J. Exp. Biol.* **206,** 2803-2829.

Tobalske, B. W., Warrick, D. R., Clark, C. J., Powers, D. R., Hedrick, T. L., Hyder, G. A. and Biewener, A. A. (2007). Three-dimensional kinematics of hummingbird flight. *J. Exp. Biol.* **210,** 2368-2382.

Usherwood, J. R. and Ellington, C. P. (2002). The aerodynamics of revolving wings I. Model hawkmoth wings. *J. Exp. Biol.* **205,** 1547-1564.

van den Berg, C. and Ellington, C. P. (1997). The three–dimensional leading–edge vortex of a 'hovering'model hawkmoth. *Phil. Trans. R. Soc. Lond. B Biol. Sci.* **352,** 329-340.

Vance, J., Faruque, I. and Humbert, J. (2013). Kinematic strategies for mitigating gust perturbations in insects. *Bioinsp. Biomim.* **8,** 016004.

Vandenberghe, N., Zhang, J. and Childress, S. (2004). Symmetry breaking leads to forward flapping flight. *J. Fluid Mech.* **506,** 147-155.

Vogel, S. (2008). Modes and scaling in aquatic locomotion. *Integr. Comp. Biol.* **48,** 702-712.

Warrick, D. R. and Dial, K. P. (1998). Kinematic, aerodynamic and anatomical mechanisms in the slow, maneuvering flight of pigeons. *J. Exp. Biol.* **201,** 655672.

Weis-Fogh, T. (1956). Biology and physics of locust flight. II. Flight performance of the desert locust (Schistocerca gregaria). *Phil. Trans. R. Soc. B: Biol. Sci.* **239,** 459-510.

Weis-Fogh, T. (1973). Quick Estimates of Flight Fitness in Hovering Animals, Including Novel Mechanisms for Lift Production. *J. Exp. Biol.* **59,** 169-230.

Whitehead, S. C., Beatus, T., Canale, L. and Cohen, I. (2015). Pitch perfect: how fruit flies control their body pitch angle. *J. Exp. Biol.* **218,** 3508-3519.

Zehr, E. P. and Stein, R. B. (1999). What functions do reflexes serve during human locomotion? *Prog. Neurobiol.* **58,** 185-205.

CHAPTER 2
DIRECT LATERAL MANEUVERS IN *MANDUCA SEXTA*

This chapter was published in Biology Open in 2016. DOI: 10.1242/bio.012922

Summary

We used videography to investigate direct lateral maneuvers, *i.e.* "sideslips," of the hawkmoth *Manduca sexta*. *M. sexta* sideslip by rolling their entire body and wings to reorient their net force vector. During sideslip they increase net aerodynamic force by flapping with greater amplitude, (in both wing elevation and sweep), allowing them to continue to support body weight while rolled. To execute the roll maneuver we observed in sideslips, they use an asymmetric wing stroke, increasing the pitch of the roll-contralateral wing pair, while decreasing that of the roll-ipsilateral pair. They also increase the wing sweep amplitude of, and decrease the elevation amplitude of, the contralateral wing pair relative to the ipsilateral pair. The roll maneuver unfolds in a stairstep manner, with orientation changing more during downstroke than upstroke. This is due to smaller upstroke wing pitch angle asymmetries as well as increased upstroke flapping countertorque from left-right differences in global reference frame wing velocity about the moth's roll axis. Rolls are also opposed by stabilizing aerodynamic moments from lateral motion, such that rightward roll velocity will be opposed by rightward motion. Computational modeling using blade-element approaches confirm the plausibility of a causal linkage between the previously mentioned wing kinematics and roll/sideslip. Model results also predict high degrees of axial and lateral damping. On the time scale of whole and half wing strokes, left-right wing pair asymmetries directly relate to the first, but not second, derivative of roll. Collectively, these results strongly support a roll-based sideslip with a high degree of roll damping in *M. sexta*.

Key Words

free flight, maneuver, flight control, *Manduca sexta*, lateral maneuvers, sideslip, side-slip, dodge, banked turning, roll, flapping countertorque

Introduction

Flying animals must maneuver and stabilize to navigate obstacles and avoid predators when seeking resources and mates. Moths of the Sphingidae family provide a ready model system for investigating animal flight maneuverability and stability due to their aerial agility, ease of care/training, large body size, cosmopolitan distribution, and economic significance as agricultural pests. Member species oscillate horizontally while hover-feeding, and rapidly maneuver away if visually startled; such flight behavior may have evolved to avoid ambush predators at flowers (Waaserthal, 1992;Cheng *et al.*, 2011). Previous studies have probed a multitude of sphingid characteristics, including escape flight maneuvers, in detail, but not direct lateral maneuvers, or "sideslips." Here we investigate sideslip kinematics in the sphingid *Manduca sexta* (Linnaeus, 1763).

Our first hypothesis was that *M. sexta* sideslip, at least partially, by creating direct lateral force *via* asynchrony in wing pitch angle, as described in fruit flies (Ristroph *et al.*, 2009). Ristroph *et al.* (2009) first observed that sideslipping *Drosophila melanogaster* display left-right phase asymmetry in wing pitch rotation. They showed a difference in the wing pitch angle near the end of *Drosophila*'s ≈155° halfstrokes (stroke reversal), where wing trajectories are almost lateral, that may create net lateral force that accounts for about half of sideslip acceleration. *M. sexta* wings have similarly quasi-lateral trajectories near the end of their ≈100° halfstrokes, where forces are also high (Bomphrey *et al.*, 2005).

Our alternative hypothesis was that *M. sexta* sideslip solely by rolling to reorient their net aerodynamic force vector. Apparently roll-based, roughly lateral maneuvers during insect hover have been observed, (Ellington, 1984a;Ristroph *et al.*, 2009;Muijres *et al.*, 2015); and recent work on *Aedes aegypti* showed mosquitoes perform direct lateral maneuvers *via* a simple roll-based rotation of their stroke plane (Iams, 2012). However, *A. aegypti*'s particularly low flapping amplitude of ≈45° may not permit sideslip *via* wing pitch asynchrony as described in the first hypothesis, since their wings do not achieve roughly opposing lateral trajectories near the ends of strokes like those of fruit flies and hawkmoths.

In this study we found strong agreement between videographic analysis of *M. sexta* lateral maneuvers and a first-principle model of our second, roll-only sideslip hypothesis. In further support of this result, we also identified changes to wing kinematics that more fully explain the observed lateral and vertical

accelerations. We calculated passive damping time constants for lateral and vertical acceleration based on our fitted equations, and compared them to time constants estimated from computational models.

Further exploring sideslip maneuvers, we next identified wing kinematics associated with roll, added possible passive sources of damping to this model, then tested it against the first and second time derivatives of observed roll orientation. These predictions came from qualitative observations of roll maneuvers, general principles of flapping flight, or previous animal flight maneuvering studies. For all models, we used the corrected Akaike information criterion (AICc), to select the best sets of predictor variables, and p-values from our full-parameter test model to confirm coefficient significance.

Results

Overview

Our results show that moths use roll to redirect their net force vector and thus initiate lateral maneuvers. They use sweep and elevation amplitude to amplify the force they create, and a mixture of various wing asymmetries to initiate roll. Linear movement is resisted by passive drag, and roll itself is highly damped.

Sideslips were roll-based and largely unidirectional. The average sideslip maneuver, as defined in **Methods**, lasted ≈0.2s. The overall average magnitudes for the first derivatives of yaw, pitch, and roll can be seen in Table 2.S1. During many sideslips, moths experienced brief yaw (and sometimes pitch) rotations, which they later corrected with rotational acceleration in the opposite direction. This explains the relatively high average absolute value for yaw and pitch velocity despite the ideally unidirectional nature of whole-body sideslip maneuvers. Models for vertical and lateral acceleration ($\ddot{z}$ and $\ddot{y}$) show a relationship consistent with a roll-based lateral acceleration hypothesis. Increases to $\dot{z}$ and $\dot{y}$ reduce collinear acceleration ($\ddot{z}$ and $\ddot{y}$). Bilateral increases in sweep and elevation amplitude (Φ_p and θ_p) increase vertical and horizontal force production and thus acceleration. These angles, Φ_p and θ_p, are the *peak-to-peak* angular amplitudes of the wing paths, measured respectively in the horizontal and vertical body reference planes (BRF) for each halfstroke.

Mixed models for $\dot{\beta}$ (roll velocity) show wing asymmetries affect roll velocity, primarily wing pitch angle (α), but also asymmetries in Φ_p and θ_p. Figure 2.1 shows the results for $\ddot{y}$, $\ddot{z}$, and $\dot{\beta}$, and highlights

select relevant factors for these position and orientation derivatives. Figure 2.2 shows kinematics for an example trial segment.

Figure 2.1: Model results

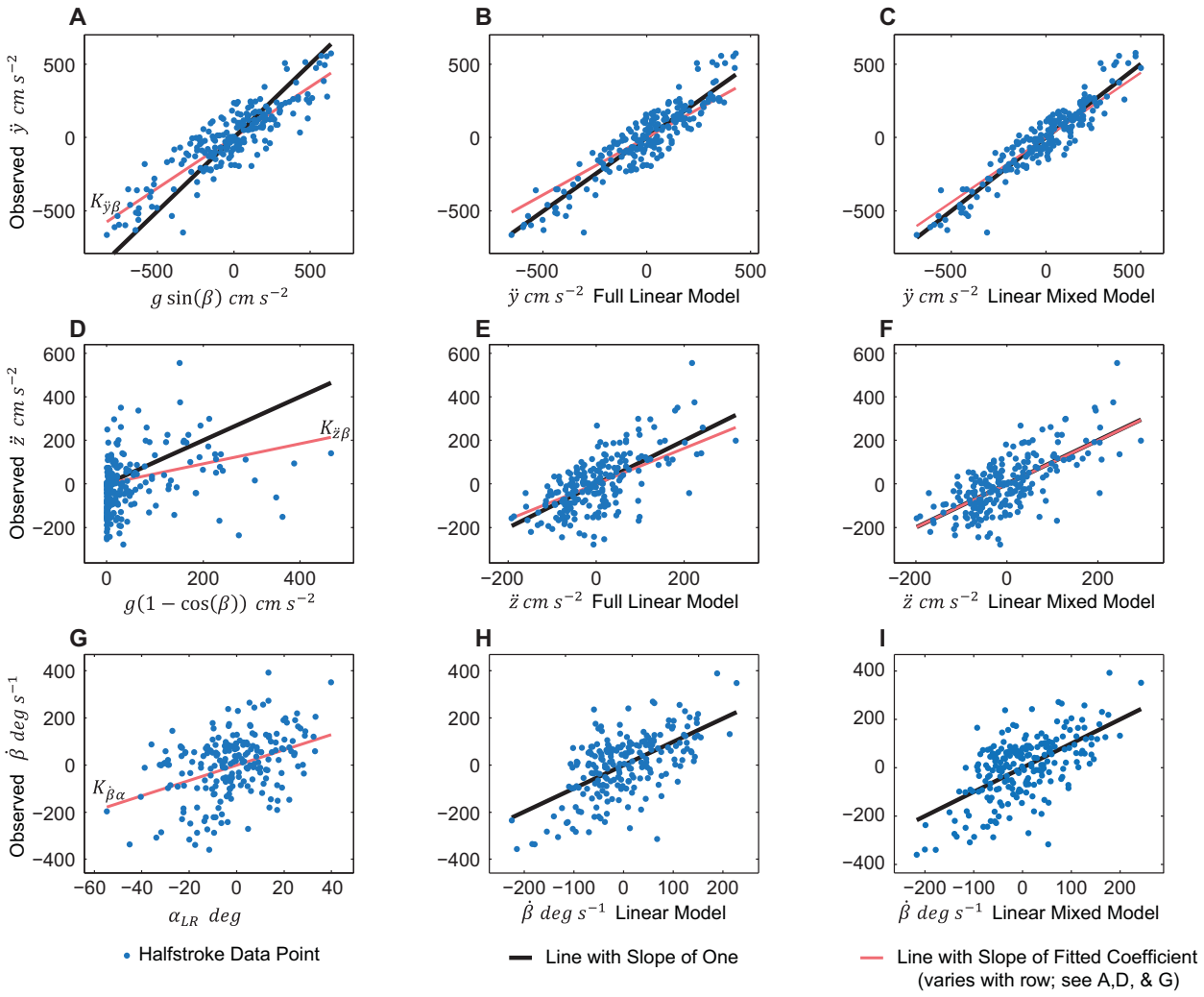

Three major moth body position and orientation derivative models. In descending vertical order, rows 1-3 show data for $\ddot{y}$, $\ddot{z}$, and $\dot{\beta}$. The thin salmon line has an intercept of zero and a slope equal to the value of the fitted coefficient, ($K_{\ddot{y}\beta}$, $K_{\ddot{z}\beta}$, and $K_{\dot{\beta}\alpha}$ respectively by row). The thicker black line has an intercept of zero and a slope of one. In the first column, we fit $\ddot{y}$ and $\ddot{z}$ to the *a priori* constant dorsally-directed force production model, and $\dot{\beta}$ to α_{LR} (the wing asymmetry that contributed the most to roll velocity). In the second column, we fit $\ddot{y}$, $\ddot{z}$, and $\dot{\beta}$ to the complete linear models that resulted from the variable selection process (Eq. 2.6-8). In **C** and **F** of the third column, we fit $\ddot{y}$ and $\ddot{z}$ to the full linear mixed models; they differ from column two only by the addition of a random intercept for each moth (which resulted in lower AICc values than the models without this adjustment). Panel **H** of the second column is the linear model for $\dot{\beta}$, which includes α_{LR}, Φ_{LR}, and $\dot{y}$. Panel **I** of the third column shows the full linear mixed model for $\dot{\beta}$ which differs from panel **H** by the addition of separate up- and downstroke coefficient estimates for elevation angle. It is important to note that, while we do present this data, panel **H** scored better than panel **I** in AICc analysis. n = 218 halfstrokes from 19 maneuvers from 4 moths. For p-values see Tables 2.1 & 2.3.

Figure 2.2: Example trial

(Caption is on the next page)

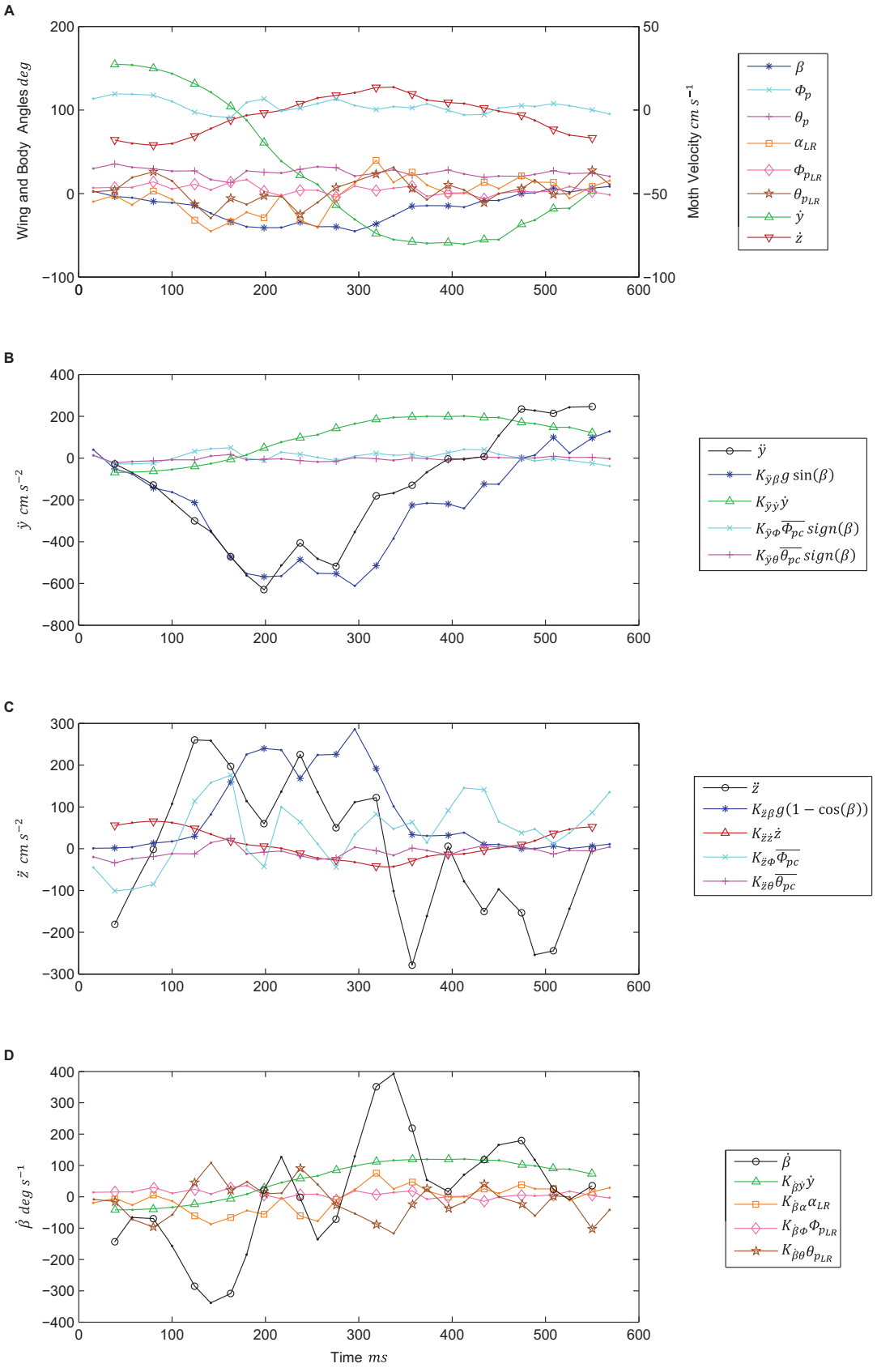

Example trial segment. Figure 2.2 (*on the previous page*) depicts a ≈580ms (14.5 wingbeat) segment of midstroke body and wing kinematic data from a representative trial segment. **A** This segment begins with a lateral deceleration followed by an acceleration in the opposite direction. Panels **B-D** depict the estimated contribution of moth wing and body kinematics to $\ddot{y}$, $\ddot{z}$, and $\dot{\beta}$, respectively. Panels **B-D** show $\ddot{y}$, $\dot{\beta}$, and $\ddot{z}$ in bold black, plotted against the independent variables from Eq. 2.1-3 after they are first multiplied by the estimated coefficients from the best linear mixed model of each orientation derivative. These coefficients are the same as those in Tables 2.1-2, and estimated from the entire data set. The plots show data at only midstrokes. Upstrokes are denoted by plain dots, while downstrokes are denoted by a different character for each measured variable.

AICc analysis results

Most predicted kinematics turned out to be significant. We subjected the mathematical models built to test our hypotheses to a variable selection process, as explained in **Methods**. Stepwise regression and AICc analysis for Eq. 2.6-8 (lateral acceleration, vertical acceleration, and roll velocity) reveals the highest quality models include the following variables (Eq. 2.1-3):

$$\ddot{y} = K_{\ddot{y}\beta} g \sin(\beta) + \left(K_{\ddot{y}\Phi}\overline{\Phi_{pc}} + K_{\ddot{y}\theta}\overline{\theta_{pc}}\right) sgn(\beta) + K_{\ddot{y}\dot{y}}\dot{y} \quad (2.1),$$

$$\ddot{z} = K_{\ddot{z}\beta} g(1 - \cos(\beta)) + K_{\ddot{z}\Phi}\overline{\Phi_{pc}} + K_{\ddot{z}\theta}\overline{\theta_{pc}} + K_{\ddot{z}\dot{z}}\dot{z} \quad (2.2),$$

$$\dot{\beta} = K_{\dot{\beta}\alpha}\alpha_{LR} + K_{\dot{\beta}\Phi}\Phi_{p_{LR}} + K_{\dot{\beta}\theta_p}\theta_{p_{LR}} + K_{\dot{\beta}\dot{y}}\dot{y} \quad (2.3),$$

where each K is a linear coefficient relating the second subscript (the independent variable) to the first (dependent variable), g = 980.665$cm\ s^{-2}$, and $sgn(\beta)$ is ± 1 according to the sign of roll orientation. Figure 2.3 shows how we define our reference frames and angles. In the above equations, wing pitch angle is α, elevation amplitude is θ_p, and sweep amplitude is Φ_p. Throughout this paper, we use $\bar{}$, $\vec{}$, $\dot{}$, $\ddot{}$, $_p$, $_i$, $_c$ and $_{LR}$ to represent left+right wing pair means, vectors, first derivatives, second derivatives, peak-to-peak amplitude, the wing ipsilateral to moth lateral velocity, mean-centered data (mean of entire data set subtracted), and the left minus right orientation or amplitude difference, respectively.

In our data, the AICc variable selection process does not eliminate any predictor variables from Eq. 2.6-8. The addition of a random intercept for each moth does decrease the minimum AICc value for both lateral and vertical acceleration models, and also brings $K_{\ddot{z}\beta}$ closer to its expected value of one. With the exception of $K_{\dot{\beta}\theta_p}$, the coefficient relating elevation amplitude to roll velocity, all signs and magnitudes matched *a priori* expectations.

Figure 2.3: Angle and point designations

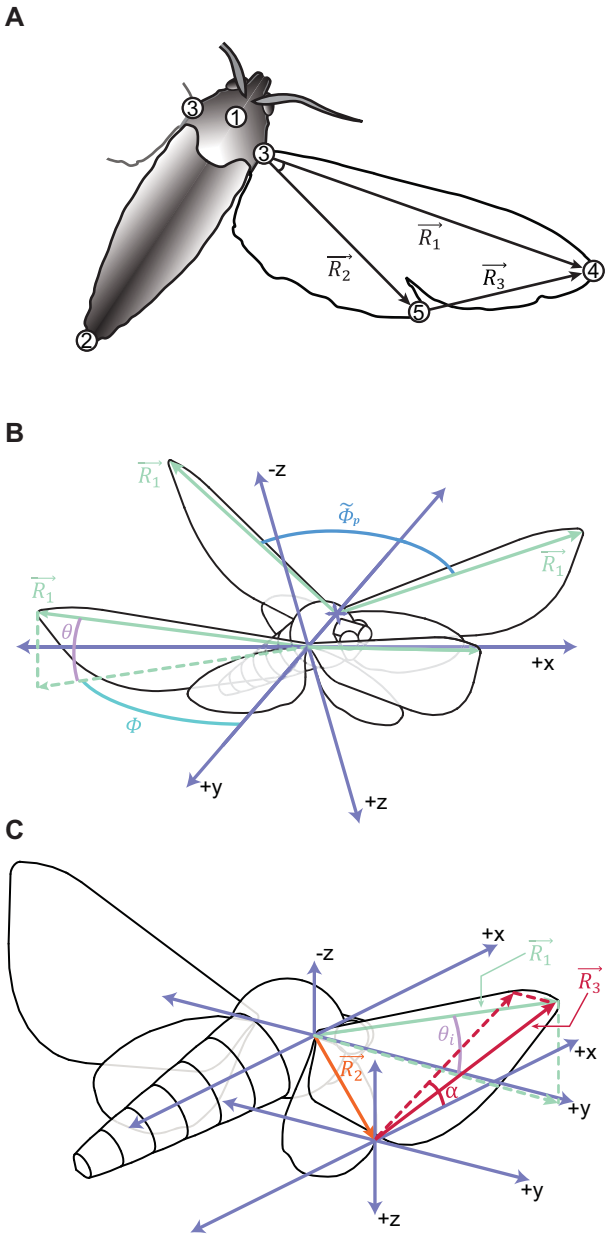

Digitization and wing angle calculation scheme. Panel **A)** shows the digitized points and resulting vectors used in wing position and orientation calculations. Only the body and right wing are shown in this image, but we marked points with bilateral symmetry on both sides of the sagittal plane. Point 1 was marked in an anterior portion of the scutum, point 2 at the tip of the abdomen, and point(s) 3 at the wing bases(s). We used points 1-3, measured in the GRF, to calculate yaw, pitch, and roll. These angles were then used to compute body point positions in the moth's BRF (Stengel 2004). We next constructed an MGRF in which *z* remained vertical, but the *x*/*y* plane was rotated in yaw so that *x* was parallel with a vector running from the distal tip of the abdomen (point 2) to the geometric centroid of points 1-3, projected onto the GRF horizontal. In the MGRF, positive *x* movement is forwards for the moth, positive *z* movement is parallel with gravity (downwards), and positive *y* movement is to the moth's right. $\overrightarrow{R_1}$ is the vector that stretches from the wing base point (3) to the forewing tip (4). $\overrightarrow{R_2}$ is the vector that stretches from the wing base point (3) to the hindwing tip (5), and $\overrightarrow{R_3}$ stretches from (5) to (4). To compute wing pitch angle (α), we projected $\overrightarrow{R_3}$ onto the BRF x/z plane and took α as the angle between this projected vector and the BRF horizontal. Midstroke wing pitch angles are all positive; we measured downstroke α relative to the positive moth BRF x-axis and upstroke α relative to the negative moth BRF x-axis. θ is the angle $\overrightarrow{R_1}$ makes with the BRF horizontal. At midstroke, when measured ipsilateral to the direction of roll, we call it θ_i. Peak-to-peak amplitude $\widetilde{\Phi}_p$ is the angle between $\overrightarrow{R_1}$'s BRF position at the top of upstroke and the end of downstroke, and *v.v.* for the following halfstroke. Sweep amplitude, Φ_p, is the projection of $\widetilde{\Phi}_p$ onto the BRF x/y plane, while θ_p (not shown) is the projection of $\widetilde{\Phi}_p$ onto the BRF x/z plane.

Lateral and vertical acceleration

Basic gravitational predictions are highly significant; wing asymmetry predictions are also significant, but less so. In order of significance, the lowest AICc lateral acceleration model (Eq. 2.1) includes $\sin(\beta)$, $\dot{y}$, $\overline{\Phi_{pc}}sgn(\beta)$, and $\overline{\theta_{pc}}sgn(\beta)$, while the lowest AICc vertical acceleration model (Eq. 2.1) includes $\overline{\Phi_{pc}}$, $1-\cos(\beta)$, θ_{pc}, and $\dot{z}$. The best fit models for $\ddot{y}$ and $\ddot{z}$ are linear mixed models (*i.e.* they contain

corrections for individual moth effects), while the best AICc model for $\dot{\beta}$ is a linear model. See Table 2.1 for the coefficients estimated for the best fit models as well as coefficients and p-values for full variable linear models *prior* to variable selection. For all of these independent variables, coefficient signs and magnitudes match expectations as outlined in **Methods**. We also calculated angular stroke amplitude ($\widetilde{\Phi}_p$) as the relative angle between the wingtip at the end of each halfstroke in the BRF. We compared the AICc and p-values of Eq. 2.6-7 against modified versions where we replaced $\overline{\Phi_p}$ and/or $\overline{\theta_{pc}}$ with $\bar{\bar{\Phi}}$. The results of these comparisons show better AICc values for $\overline{\Phi_{pc}}$ alone, as well as $\overline{\Phi_{pc}}$ and $\overline{\theta_{pc}}$ together as a unit, than equations with $\bar{\bar{\Phi}}$. The significance of $K_{\ddot{y}\Phi}$ and $K_{\ddot{y}\theta}$ is not a result of their $sgn(\beta)$ multiplier; if we attempt to fit $\ddot{y} = K_{\ddot{y}\beta} g \sin(\beta) + Ksgn(\beta)$, the p-value for K is not significant. Mixed models improve the most when we subtract the mean $\overline{\Phi_p}$ and $\overline{\theta_p}$ for the entire data set, rather than for each individual moth or trial. See Table 2.2 for a comparison of the contribution of each of these effects relative to one another.

Table 2.1: Lateral and vertical acceleration model results

	$\ddot{y}$ Linear Models					$\ddot{z}$ Linear Models				
	$\ddot{y}$	Best AICc Model $r^2{}_c \approx 0.90$	Best LM $r^2{}_a \approx 0.82$	Full Initial Variable Linear Regression		$\ddot{z}$	Best AICc Model $r^2{}_c \approx 0.79$	Best LM $r^2{}_a \approx 0.42$	Full Initial Variable Linear Regression	
$Units$	Coef.	Coef. Value	Coef. Value	Coef. Value	p	Coef.	Coef. Value	Coef. Value	Coef. Value	p
None	$K_{\ddot{y}\beta}$	0.88	0.78	0.79	<2E-16	$K_{\ddot{z}\beta}$	1.00	0.82	0.82	5.51E-14
s^{-1}	$K_{\ddot{y}\dot{y}}$	-2.51	-1.66	-1.79	1.01E-11	$K_{\ddot{z}\dot{z}}$	-3.11	-4.64	-4.64	4.85E-8
$cm\ s^{-2}\ rad^{-1}$	$K_{\ddot{y}\Phi}$	158.13	105.83	128.23	1.53 E-2	$K_{\ddot{z}\Phi}$	-560.57	-538.43	-538.56	<2E-16
$cm\ s^{-2}\ rad^{-1}$	$K_{\ddot{y}\theta}$	102.14	120.89	127.71	8.51E-5	$K_{\ddot{z}\theta}$	-148.68	-262.42	-262.77	6.19E-12
$cm\ s^{-2}$	$Icpt.$	-29.15*	--	--	--	$Icpt.$	-106.67*	-53.29	-56.73	1.51E-2

**Average moth ID random intercept*

Table 2.2: Comparison of best AIC models for $\ddot{y}$, $\ddot{x}$, and $\dot{\beta}$

Best AICc $\ddot{y}$ Linear Model		Best AICc $\ddot{x}$ Linear Model		Best AICc $\dot{\beta}$ Model	
	% Contrib.		% Contrib.		% Contrib.
$\sin(\beta)$	65.77	$1-\cos(\beta)$	30.48	α_{LR}	20.68
$\dot{y}$	22.01	$\dot{z}$	13.69	$\dot{y}$	23.56
$\Phi sign(\beta)$	5.89	Φ	38.77	$\Phi_{p_{LR}}$	21.86
$\theta sign(\beta)$	6.33	θ	17.06	$\theta_{p_{LR}}$	33.91
$Icpt.$	*Excluded*	$Icpt.$	*Excluded*	$Icpt.$	0 (set)

Roll velocity

For reasons detailed in **Methods**, we present model results for roll velocity rather than roll acceleration. The best AICc model for roll velocity (Eq. 2.3) includes α_{LR}, $\Phi_{p_{LR}}$, $\theta_{p_{LR}}$, and $\dot{y}$; the signs of $K_{\dot{\beta}\alpha}$, $K_{\dot{\beta}\Phi}$, and $K_{\dot{\beta}\dot{y}}$ match *a priori* expectations (see **Methods**), but the sign of $K_{\dot{\beta}\theta_p}$ does not. See Table 2.3 for these coefficients and Table 2.2 for a comparison of the contribution of each of these effects relative to one another. Instantaneous left-right wing position differences at midstroke separately correlate with roll velocity; however, such wing position differences do not appear in the best AICc models—likely because they simply recapitulate $\Phi_{p_{LR}}$, $\theta_{p_{LR}}$, and α_{LR}, (possibly with additional noise).

Moths show a stair-step pattern in roll at endstrokes; they reorient more in the overall direction of roll during downstroke and less during upstroke (Fig. 2.S1). In fact, roll in the overall direction of motion is often lost in upstroke rather than gained. This stair-step pattern corresponds to periodicity in α_{LR} (Fig. 2.S2-3). Autocorrelations show α_{LR} typically holds the same sign for consecutive wingbeats but displays periodicity in magnitude (Fig. 2.S3). Average downstroke $|\overline{\alpha_{LR}}|$ is 1.57 times upstroke $|\overline{\alpha_{LR}}|$, and downstroke α is 1.30 times upstroke α. Conversely, Φ_p, $\Phi_{p_{LR}}$, θ_p, and $\theta_{p_{LR}}$ are about the same magnitude and hold consistent sign for consecutive half and whole wingbeats.

Table 2.3: Roll model results

	$\dot{\beta}$	Best AICc Model $r^2_a \approx 0.34$	Separate Up- and Downstroke $K_{\dot{\beta}\theta_p}$ model $r^2_c \approx 0.38$		Full Initial Variable Linear Regression	
$Units$	Coef.	Coef. Value	Coef. Value		Coef. Value	p
s^{-1}	$K_{\dot{\beta}\alpha}$	1.92	2.24		1.84	2.83E-4
$rad\ s^{-1}$	$K_{\dot{\beta}\dot{y}}$	-2.64E-2	-2.58E-2		2.66E-2	5.03E-11
s^{-1}	$K_{\dot{\beta}\Phi}$	2.20	2.10		2.11	3.50E-5
s^{-1}	$K_{\dot{\beta}\theta_p}$	-3.71	Up	Down	-3.59	2.57E-4
			-4.89	-1.22		
rad	$Icpt.$	0 (*set*)				

Computational model results

Blade element model (Hedrick and Daniel, 2006) results mostly match observed trends. Velocity decay half-lives (*i.e.* time constants), estimated from the differential solutions to Eq. 2.1-2, are similar to those extracted from two computational models of passive theoretical *M. sexta* (Hedrick and Daniel,

2006;Kim and Han, 2014). Coefficients values from observed data and the blade element model also agree (Tables 2.S2-3). Unfortunately, the model is not sufficiently accurate to test whether the wing kinematic changes we observed fully create the body movements we observed. However, it was useful in interpreting whether the approximate wing kinematic changes selected in the experiments create the same general movements in the model as they appear to in actual moths.

Discussion

Summary

M. sexta can sideslip, and they do so by rolling their body to reorient their net force vector. They augment the net force they produce during sideslips to prevent sinking by increasing flapping amplitude, and encounter decelerative/damping drag proportional to their lateral and vertical velocity. Roll maneuvers are multifactorial and involve a high degree of damping.

These moths create roll torque *via* left-right asymmetries in sweep amplitude, elevation amplitude, and most importantly, midstroke wing pitch angle. Because moths are heavily roll-damped, asymmetries in flapping kinematics at the half-wingbeat timescale relate linearly to the first, rather than second, derivative of roll (when roll is measured at that same timescale). In addition to flapping countertorque (FCT), this damping torque is likely due in part to induced angle of attack asymmetries—a well-known effect in rolling fixed-wing aircraft. Moths roll more in the direction of net reorientation during downstroke than upstroke by modulating the wing pitch angle difference in each halfstroke, and potentially due to larger upstroke FCT since wing pitch angles and their left-right differences are smaller in upstroke.

Lateral and vertical acceleration

Our models of lateral and vertical acceleration indicate *M. sexta* roll to redirect their net force vector and thus create lateral acceleration. The most significant relationship between independent and dependent variables in the entire study is that between lateral acceleration and the moth's whole-body roll angle ($g\sin(\beta)$ and $\ddot{y}$). The relationship between roll orientation and vertical acceleration ($g(1-\cos(\beta))$ and $\ddot{z}$) is also highly significant. The coefficient for this latter relationship ($K_{\ddot{z}\beta}$) is positive because -z in our coordinate system is antiparallel with gravity (upwards). The magnitudes of $K_{\ddot{y}\beta}$ and $K_{\ddot{z}\beta}$ are both very

close to one, as expected. These relationships were also predicted by *a priori* hypotheses and further supported by visual inspection. The strong match between the roll-based sideslip hypothesis and the lateral acceleration data indicates that any additional effects such as direct lateral force production via left-right asymmetries in flap timing produce only marginal forces if they are present at all. Our linear mixed model based on roll only accounts for roughly 90% (based on $r^2{}_c$) of the observed lateral acceleration. We did consider that our use of a moving light source positioned above the moth may have enhanced the roll response in these recordings compared to self-motivated sideslips, cueing the moths to rotate their body and head to maintain a constant visual angle to the light source. However, we consider this unlikely since head stabilization is evident in our videos, and from a digital comparison of antennae position relative body orientation.

On the time scale of half wingstrokes and over the airspeed range we observed, *M. sexta* behaves as a physical system in which we can model damping opposite the direction of lateral and vertical motion as approximately proportional to collinear velocity. Comparisons between coefficients and time constants estimated from mathematical models and observed data (Tables 2.S2-3) show that this resistance probably comes from passive drag, though some resistance could conceivably come from active steering by the moth in an attempt to limit acceleration.

Finally, our linear acceleration results show that moths flap with greater amplitude to increase net maneuver force and maintain altitude during sideslips. This is opposed to alternative possibilities of bilaterally increased wing pitch angle or flapping frequency; neither of which significantly relate to increased acceleration. Increased wing pitch angle may present a problem for hawkmoths, since they already use high effective angles of attack while hovering, (Ellington, 1984a;Ellington, 1984b;Ellington *et al.*, 1996), and even higher angles when they use wing pitch asymmetry to create roll torque (Table 2.S4). Moths have shown small (~2 Hz) increases to flapping frequency in response to wing clipping (Fernandez *et al.*, 2012), though in the absence of wing area alteration, their flapping frequency (~26 Hz) may be close to some physiological limit; unclipped moths show insignificant increases in flapping frequency when maneuvering at speed (Ortega-Jimenez *et al.*, 2013).

Roll velocity

The most important contributor to roll initiation we identified in this study is wing pitch angle, a relationship estimated by coefficient $K_{\dot{\beta}\alpha}$ (Eq. 2.3). The positive signs of $K_{\dot{\beta}\Phi}$ and $K_{\dot{\beta}\alpha}$ show that greater wing pitch angle and sweep amplitude on one side of the moth relative to the other creates roll torque away from that wing pair (contralateral roll). Since airfoil velocity and angle of attack affect lift force, is consistent with established theory. Based on AICc results comparing models that used wing pitch angle calculated in several different ways, we believe the way we measure α (Fig. 2.3) is the best way to represent the kinematic relationship with the data we have. One discarded alternate wing pitch angle measurement was based on a wing "chord" stretching from the hindwing tip to a perpendicular intersection with $\overrightarrow{R_1}$ ($\overrightarrow{R_1}$ is shown in Fig. 2.3). A precise estimate of actual effective angle of attack for *M. sexta* would have been preferable; unfortunately such estimates suffer from a number of confounding factors, such as increased noise, variations in wing curvature, and the complexity of *M. sexta* wing air flow dynamics, (Ellington *et al.*, 1996;Bomphrey *et al.*, 2005;Zheng *et al.*, 2009).

We examined single-wing kinematics in greater detail to determine precisely how hawkmoths create the wing asymmetries that create roll. To create the wing pitch asymmetry, a moth rolling to the right alters the left and right wing pair α by about the same amount but in opposite directions; increasing the left while decreasing the right (Table 2.S4). Instantaneous midstroke asymmetries in sweep and elevation angular position (Φ_{LR} and θ_{LR}) also correlate strongly and positively with roll velocity, as expected if amplitude asymmetries are unevenly distributed about the midline. A positive correlation between instantaneous midstroke sweep angle and roll velocity suggests that, to create sweep amplitude asymmetries, a moth rolling to the right decreases $\Phi_{p_{LR}}$ primarily by extending its right wing pair relatively less far forward in comparison to its left wing pair. Meanwhile, the positive correlation between instantaneous midstroke elevation angle and roll velocity is more ambiguous, since the measurement of midstroke θ_{LR} is linked to changes in α_{LR}. Binned average values (Table 2.S4) imply it is possible moths bilaterally adjust both sweep and elevation angle amplitude much as they do wing pitch angle, but t-test results for this are not significant.

We observe oscillation in both $\dot{\beta}$ (in the form of a stair-step pattern) and α_{LR} for up- *vs* downstrokes (Fig. 2.S3). Thus, we here report results for mixed models which separate up- and downstroke coefficient

estimations. All derivatives depend on stroke-to-stroke changes rather than instantaneous measures so this halfstroke-frequency stair-step pattern did not interfere with how we calculated coefficients. Models where we introduced separate $K_{\dot{\beta}\alpha}$ $K_{\dot{\beta}\Phi}$, and/or $K_{\dot{\beta}\theta_p}$ for up- and downstrokes are not better according to AICc. Note α_{LR} is higher for downstrokes but $K_{\dot{\beta}\alpha}$ remains the same. This strongly suggests moths create more roll torque in the target direction of movement in downstrokes rather than upstrokes, at least in part, by adjusting the magnitude of α_{LR}. A further plausible explanation for the stair-step pattern in roll comes from key kinematic differences between up- and downstroke which likely result in greater upstroke damping, as discussed next.

Roll damping and FCT

The results reported here compliment wing velocity mediated roll damping described in the turning free-flight of cockatoos, (Hedrick *et al.*, 2007), and computational studies that predict heavily damped roll in *M. sexta* (Kim and Han, 2014). Effective angle of attack asymmetry induced by rolls, as in fixed-wing aircraft, likely damps movement in moths as well. Our results further support FCT effects. The velocity of the wings about the roll axis is additive with velocity created by overall body and wing reorientation in the global reference frame (GRF). This decreases lift in the wing contralateral to a roll, and increases lift on the wing ipsilateral to a roll (Hedrick and Biewener, 2007;Hedrick *et al.*, 2009). Flapping countertorque is a drag effect, where cross-sectional area of the wing relative to the rotation, in part, determines the strength of the effect. Thus, *ceteris paribus*, FCT (and thus roll damping) depends on the inverse of wing pitch angle as defined in this work. The data show wing pitch angle magnitudes and asymmetries are both smaller in upstrokes than downstrokes (Fig. 2.S2-3). We thus predict increases in elevation amplitude have a larger negative impact on roll during upstrokes. Consistent with this roll FCT explanation, linear models in which we separate up/downstroke θ_p result in a more negative upstroke $K_{\dot{\beta}\theta_p}$ (Table 2.3). Our results thus agree with this FCT explanation. They contradict our *a priori* expectation that increased roll-contralateral θ_p (relative to ipsilateral) would increase relative contralateral force and thus $K_{\dot{\beta}\theta_p}$ would be consistently positive, and presumably larger for downstrokes.

We find evidence of antagonistic coupling between roll and lateral velocity, ($\dot{\beta}$ and $\dot{y}$), where roll velocity towards a given side negatively correlates with whole-body velocity in that direction (*i.e.* rightwards roll velocity correlates negatively with rightwards linear velocity and *v.v.*). As seen in Fig. 2.2, our data include both lateral accelerations and decelerations, and the negative correlation between lateral velocity and roll velocity is significant for both cases. In lateral accelerations (sideslip initiation) the ipsilateral wing pair moves towards shed air, while the wing pair contralateral to sideslip moves away, which may increase ipsilateral wing force. In lateral decelerations, (sideslip reversal), lateral velocity may negatively correlate with roll velocity simply because moths are rolling away from their direction of sideslip in order to redirect force and slow down. As an alternative or supplementary explanation, this antagonistic coupling in lateral accelerations is also suggestive of the velocity-mediated sideslip damping first proposed by Faruque and Humbert (2010b).

Comparison to aerial maneuvers in other animals

Given previous research, we can compare the sideslip maneuvers of *M. sexta* directly to sideslips of the fruit fly *D melanogaster* and the mosquito *A. aegypti*, and indirectly with other maneuvers in birds and bats. Firstly, our results do not support a scenario in which *M. sexta* wing pitch angle timing asymmetries at the ends of halfstrokes play a prominent role in creating direct lateral force, as in *D melanogaster* (Ristroph *et al.*, 2009). Preliminary examination of videos digitized continuously through the wingbeat cycle does not show evidence of consistent timing differences. Instead our data provide strong support for the simple body roll hypothesis. Thus we conclude that moths use roll to reorient their net force vector, much like birds performing turns (Hedrick and Biewener, 2007;Hedrick *et al.*, 2007;Ros *et al.*, 2011), and mosquitoes performing sideslips (Iams, 2012). Iams (2012) measures “stroke plane roll,” the angle a line between the two wingtips makes relative to the horizontal. In our moths, a Pearson product moment correlation of body roll with stroke plane roll measured at midstroke yields 0.944, indicating high agreement between the two measures. This suggests stroke plane roll is indeed a plausible measurement to use in place of body roll to determine the direction of net force creation in the y/z plane. *D melanogaster* also uses a tilted stroke plane roll angle to create a portion of its lateral acceleration during sideslips and saccades (Ristroph *et al.*, 2009;Muijres *et al.*, 2015).

Free-flight *M. sexta* rolls are also comparable to aerial rolls in other animals. Many animals use their tail and body to perform inertial reorientation in order to right themselves in the air (Jusufi *et al.*, 2011). Despite *M. sexta* possessing a weighty "tail" in the form of a flexible abdomen, we did not observe it to have a role in roll reorientation. This contrasts with abdominal reflexes recorded in *M. sexta* in response to pitch or yaw displacement (Dickerson *et al.*, 2014;Dyhr *et al.*, 2013;Hinterwirth and Daniel, 2010), modeled effects on stability (Noda *et al.*, 2013), as well as the active aerodynamic role of the flat tails of birds and bats (Adams *et al.*, 2012;Gardiner *et al.*, 2011;Thomas, 1993). Instead, *M. sexta* appears to rely solely on the aerodynamics of its flapping wings to create roll maneuvers—and not at all on its wing inertia, which contrasts with both turning pigeons (Ros *et al.*, 2011) and reorienting bats (Bergou *et al.*, 2011;Iriate-Díaz *et al.*, 2011). To create roll torque, moths use a combination of wing stroke asymmetry, as seen in turning birds (Hedrick and Biewener, 2007;Ros *et al.*, 2011), and wing pitch asymmetry—similar to wing camber/pitch asymmetry observed during downstroke in both the aforementioned birds as well as dragonflies and hummingbirds (Wang *et al.*, 2003); but dissimilar to the wing rotation angle asymmetries that create roll torque in fruit fly saccades (Muijres *et al.*, 2015). Like our moths, Read (2015) found that the hummingbird *Calypte anna* rolls while turning to influence lateral velocity, and that they: 1) increase the mean elevation angle; 2) decrease the elevation amplitude; and 3) increase the stroke amplitude of the contralateral wing relative to the ipsilateral wing. However, unlike our moths, they showed a timing difference in wing pitch angle between the contralateral and ipsilateral wings that did not manifest as an angle difference at mid-downstroke.

The stepwise nature of roll reorientations and the significant relationship of moth wing kinematic changes with roll velocity rather than acceleration, together suggest a highly damped, roughly first order system for roll. This agrees with some prior free-flight research on both roll and yaw in flapping flight. Previous research on hawkmoth yaw turns revealed a roughly first-order control system in which imbalanced force from stroke amplitude and wing angle of attack asymmetry drives yaw rotations, and imbalanced drag on the wings induced by the yaw rotation naturally damps the physical system (Hedrick *et al.*, 2009;Ortega-Jimenez *et al.*, 2014). Since the component of *M. sexta*'s wing velocity about the roll axis that creates FCT in roll is much smaller than the component about the yaw axis that creates FCT in yaw, the existence of a first-order relationship between wing kinematics and body roll is especially

interesting. The apparent existence of a first order system in *M. sexta* in the creation of roll, supported by our live-animal data as well as computational models, in addition to yaw, suggests that first order control relationships could be the norm for body orientation control in flapping flight.

Methods

Animals

We acquired four male *M. sexta* as pupae from a domestic colony at the Duke University Department of Biology. These *M. sexta* were from a line of hawkmoths that was recently out-crossed with domesticated lines from several other universities. Following eclosure, adult moths had access to honey dissolved in water *ad libitum.* They lived in (30 x 30 x 30 cm) cubic mesh cages and were kept on an extended day, abbreviated night light cycle. Moths were between one and fifteen days *post*-eclosure at time of use. See Table 2.S5 for individual moth morphological details.

Experimental setup

We recorded moth sideslip maneuvers from hawkmoths flying in a 71 x 71 x 74 cm glass-walled arena following an oscillating light (Fig. 2.3). Two Phantom v7.1 and one Phantom v5.1 digital cameras (Vision Research Inc., Wayne, NJ, USA) used the high-intensity 680nm light from eight LEDs (Roithner LaserTechnik, GmBH, A-1040, Vienna, Austria) to capture moth maneuvers at a frame rate of 600-700Hz. We filmed trials at night inside a closed, unlit room with shuttered windows. The ambient light level in the filming room was approximately 180lx at the time of filming, and only 10lx without the high-intensity infrared LEDs, as measured with a lux meter (840006, Sper Scientific LTD, Scottsdale, AZ, USA). The time of filming generally coincided with nighttime in the moths' abbreviated night/day cycle. Most moths warmed up and flew naturally in the dark flight chamber, but some required manual stimulation with thumb and forefinger to elicit warm-up behavior. Once the moths were hovering at least one wingspan above the floor of the chamber, the light was oscillated above the moths, horizontal to the ground and roughly perpendicular to the moths' sagittal plane with an approximate frequency of 1.25Hz and peak-to-peak amplitude of 25cm. To construct the light, we mounted a 2.2cm radius cut-out of a phosphore/dialectric light (model# 11100,

115V/.03W, EI Products Inc., Maxwell, TX, USA) on the end of a 50.7cm long metal rod. The moths exhibited phototaxis and spontaneously followed the light's path.

Figure 2.4: Experimental setup

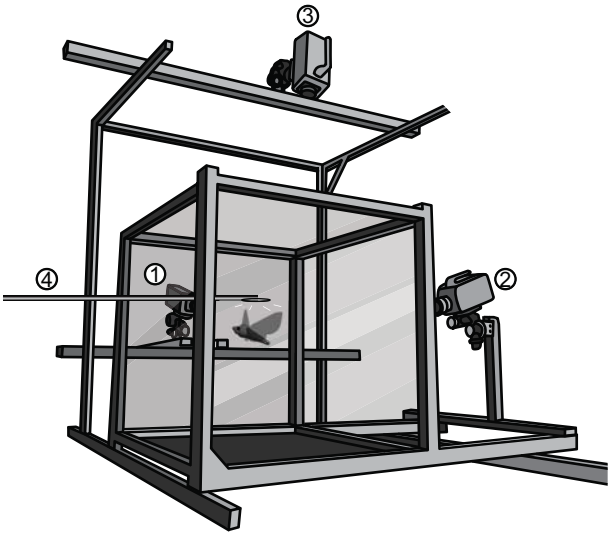

Flight chamber and cameras used in experiments. 1&2) Phantom v7.1 cameras; 3) Phantom v5.1 camera; 4) oscillating light source.

Camera calibration

We used direct linear transformation (DLT) to calibrate the cameras (Hedrick, 2008). The DLT input points were the filmed pixel positions of two light-emitting diodes situated 68.5 mm apart at the end of a wand, after we waved this wand through the filming space by hand. Three calibrations were used among the different recordings. Their pixel (*u,v,w*) Calibration Root Mean Squared Errors (RMSE) for each of the three cameras were (0.12,0.14,0.14) for trials 1-2, (0.15,0.11,0.10) for trials 3-6, and (0.13,0.14,0.15) for trial 7. See Table 2.S5 for the median RMSE of each digitized point for each trial. We based the first calibration on wand points we tracked by hand, and the second two calibrations on wand points tracked by custom software.

Video data analysis

We used qualitative observations of raw video data to select 7 trials in which the moths were sufficiently visible for manual digitization and underwent minimal yaw rotation throughout their individual sideslip maneuvers. These videos are comprised of 19 distinct lateral maneuvers; defined as lateral accelerations where the direction of acceleration is sustained for at least 0.077s, or about two 26 Hz wingbeat cycles, which is approximately the average wingbeat frequency in our trials.

Measuring wing parameters

We marked points at each of four visually-identified phases in the moths' wingstrokes: (1) end-downstroke, (2) end-upstroke, (3) mid-downstroke, and (4) mid-upstroke. This allowed us to identify key points in the stroke cycle for analysis and decreased the requisite amount of manual digitizing. In each of these four frames, we digitized 8 moth body and wing points (Fig. 2.3) using the MATLAB (r2011a, The Mathworks, Natick, MA) package DLTdv5 (Hedrick, 2008). We (rarely) excluded point 5 when visibility did not allow us to digitize it. Both the left and right wing points were marked independently on every digitized frame.

We used MATLAB to compute Euler angles and wing kinematics from the digitized points. Figure 2.3 shows wing angles and explains reference frames, including the modified global reference frame (MGRF), GRF, and BRF. To filter out regular within-wingbeat fluctuations, we calculated position and orientation derivatives from wingbeat to wingbeat changes only; we measured changes between like points in the flapping cycle rather than from each digitized frame to the next. We then averaged the resulting four derivative measurements (since there were four digitized frames per stroke) to capture both high and low frequency changes not tied to within-wingbeat oscillations. We fit x, y, z, and their derivatives, (*i.e.* whole-body position and movement), in the MGRF only. When correlating these body movements with wing kinematics, we inserted stroke amplitude values at their corresponding midstroke points. This is where we focused analysis since midstrokes are a convenient reference point where forces are either highest, or close to their highest, in the *M. sexta* stroke cycle (Bomphrey *et al.*, 2005;Zheng *et al.*, 2013). We calculated all angles using points from the BRF.

A priori *lateral and vertical acceleration models*

Here we describe the simplified models we used to analyze links between three aspects of moth movement, including lateral and vertical acceleration, as well as roll velocity. We started with the following two equations, which are based on a first principles, constant dorsally-directed force (equal to body weight) model of animal flight as follows:

$$\ddot{y} = K_{\ddot{y}\beta} g \sin(\beta) \quad (2.4),$$

$$\ddot{z} = K_{\ddot{z}\beta} g (1 - \cos(\beta)) \quad (2.5),$$

where β is measured relative to the MGRF x/y plane. Equation 2.4 tested our hypothesis that moths roll to accelerate laterally, while Eq. 2.5 tested the conjugate force model for vertical acceleration. For all equations y, z, and their derivatives are in the MGRF, *i.e.* aligned to moth sideslip motion and gravity, respectively. At no point did we attempt to separate the initiation of acceleration and its reversal; we fit the data with the same linear models regardless of the direction in which the moths were attempting to accelerate/decelerate.

Linearizing resistive forces and adding other model terms

We added to these basic equations kinematic variables that we had *a priori* reason to expect might contribute to moth directional movement, and then applied a stepwise variable elimination approach. Here, $\overrightarrow{(0,\dot{y},\dot{z})} \times \overrightarrow{R_{1\iota}}$, which is roughly equivalent to $\dot{y}\sin(\theta_i)$, represents drag on the wing ipsilateral to the directional or rotational movement. We attempted to fit this kinematic variable because the wing ipsilateral to the movement direction is exposed to both lateral velocity and roll velocity. We report the attempted fit of this measurement for completeness since we used all attempted kinematics when calculating p-values. Since we are interested in how departures from typical flapping leads to the creation of movement, we used the mean-centered versions of $\overline{\Phi_p}$ and $\overline{\theta_p}$. In Eq. 2.6, subtracting the overall mean isolates variance and thus allows us to multiply by $sign(\beta)$ to estimate coefficients. In Eq. 2.7-8, mean-centering $\overline{\Phi_p}$ and $\overline{\theta_p}$ allows us to assume a zero intercept; a significant intercept result would indicate moth-specific variation or that our model fails to represent the complete moth system maneuver dynamics.

High Reynolds number air drag is roughly proportional to velocity squared. However, the velocities moths encountered in our experiments cover a small range, over which we might expect to reasonably linearize an exponential trend. Furthermore, computational analysis of the flight of *M. sexta* suggests that, on the time scale of half wing-strokes, passive resistance to movement during horizontal and vertical movement is roughly linearly proportional to velocity rather than velocity squared for both horizontal and vertical movement terms, (Cheng and Deng, 2011;Kim and Han, 2014). Further velocity damping effects have also been proposed (Faruque and Humbert 2010). Linearizing the resistive forces and adding other model terms resulted in the following equations, (see *Expected Coefficient Values* for predictions):

$$\ddot{y} = K_{\ddot{y}\beta} g \sin(\beta) + K_{\ddot{y}\dot{y}}\dot{y} + (K_{\ddot{y}\Phi}\overline{\Phi_{pc}} + K_{\ddot{y}\theta}\overline{\theta_{pc}} + K_{\ddot{y}\alpha}\overline{\alpha_c})sgn(\beta) + K_{\ddot{y}\theta_i}\overrightarrow{(0,\dot{y},\dot{z})} \times \overrightarrow{R_{1\iota}} \quad (2.6),$$

$$\ddot{z} = K_{\ddot{z}\beta} g(1 - \cos(\beta)) + K_{\ddot{z}\dot{z}}\dot{z} + K_{\ddot{z}\Phi}\overline{\Phi_{pc}} + K_{\ddot{z}\theta}\overline{\theta_{pc}} + K_{\ddot{z}\alpha}\overline{\alpha_c} \quad (2.7).$$

Fitting roll dynamics

It quickly became clear that the data strongly supported Eq. 2.4-5, so we next investigated β (roll). Final models involve the first, rather than second, derivative of roll. Here we justify this choice.

A combination of factors led us to fit the first, rather than the second derivative of roll. Both previous and concurrent research predict strong damping in roll during flapping flight (Hedrick, 2011;Kim and Han, 2014). Trials 1-2 were continuously digitized and preliminarily analyzed; as expected, the results show accelerations that vary greatly throughout each halfstroke, and even more over the course of whole wingstrokes. Yet, the wing asymmetries that correlate with roll are largely conserved from each halfstroke to the next, and roll velocity direction is largely conserved from each whole stroke to the next (Fig. 2.S1-4). This indicates sustained intended direction of reorientation, and allows us to ignore accelerative changes on the sub-halfstroke time scale. Not only did prior kinematic analysis of *M. sexta* performing yaw turns also fit the first rather than second orientation derivative (Hedrick and Robinson 2010), but recent computational models indicate that roll on the scale of half-wingstrokes experiences heavy damping such that a linear roll-velocity model may actually be most appropriate (Cheng and Deng, 2011;Kim and Han, 2014). Regardless, we did attempt to fit roll acceleration for completeness. Linear regressions of the second derivative of roll *vs* various wing asymmetries reveal no significant trends.

We did not have a first principles prediction for the kinematics behind roll velocity. We therefore compiled a preliminary model that related various wing angle differences and body kinematics we suspected may be important to roll, and then applied the same stepwise variable elimination approach. We verified the wing angle correlations visually in several instances before adding them to the model.

$$\dot{\beta} = K_{\dot{\beta}\alpha}\alpha_{LR} + K_{\dot{\beta}\Phi}\Phi_{p_{LR}} + K_{\dot{\beta}\theta_p}\theta_{p_{LR}} + K_{\dot{\beta}\theta_i}\overline{(0,\dot{y},\dot{z})} \times \overrightarrow{R_{1i}} + K_{\dot{\beta}\dot{y}}\dot{y} \quad (2.8).$$

Expected coefficient values

In Eq. 2.6-7, we expected the values for both $K_{\ddot{y}\beta}$ and $K_{\ddot{z}\beta}$ to be close to +1. We expected $K_{\ddot{y}\dot{y}}$, $K_{\ddot{z}\dot{z}}$, and $K_{\dot{\beta}\theta_i}$ to be negative; where the component of velocity antiparallel to acceleration—or, in the cases

of $K_{\dot{\beta}\theta_i}$ and $K_{\dot{\beta}\dot{y}}\dot{y}$, ipsilateral to the moth's direction of rotation—damps motion. Since greater flapping amplitude increases force, we expected $K_{\ddot{y}\Phi}$to be positive and $K_{\ddot{z}\Phi}$ to be negative (positive *z* is down). To account for the expected nature of Φ_{pc}'s contribution to $\ddot{y}$, we multiplied $K_{\ddot{y}\Phi}$ by the sign of β before fitting $K_{\ddot{y}\Phi}$. We expected $K_{\dot{\beta}\Phi}$, $K_{\dot{\beta}\theta_p}$, and $K_{\dot{\beta}\alpha}$ to all be positive since we expected more vigorous flapping and higher angle of attack on the left side of the moth should send the moth rolling to the right, and *v.v*.

Statistics

We performed initial regressions in MATLAB, and final mixed model analysis in R (R Development Core Team, 2013). After selecting variables in the kinematic equations using stepwise variable elimination, we used AICc in conjunction with linear and linear mixed models to identify those of the best quality. To assess model quality, AICc evaluates how closely a model's predictions match observed data while penalizing for complexity. As explained later in this section, we used a cascade approach, rather than a full variable sweep, to choose and compare models.

For all models, we retroactively attempted autoregressive correlation structures with *corAR1* and *corARMA* from the *nlme* library (Pinheiro *et al.*, 2014) to evaluate the necessity of adjustment for the time series nature of the data. We used the *AICc* function from the *AICmodavg* library (Mazerolle, 2013) to evaluate the AICc values for each linear mixed model. For lateral and vertical acceleration models, all attempted autoregressive correlation structures resulted in erratic residual behavior and increased AICc, indicating reduced model quality. Since these basic autocorrelation structures did not improve fits, we did not evaluate more sophisticated techniques like vector autoregression nor apply any autoregressive correlation structures to the final chosen models.

Our cascade AICc comparison approach started with a series of linear models, using R's *lm* function from its *stats* library (R Development Core Team, 2013) with the *qr* optimizer from the *nlme* library (Pinheiro *et al.*, 2014). We started by testing the most significant identified variable against the null hypothesis of a simple intercept. For Eq. 2.1-2, we also attempted to fit a variety of intercepts, since scatter was low, and because we qualitatively observed ample variation in typical sweep and elevation amplitude among moths. In the case of roll velocity (Eq. 2.3), we did not fit an intercept since one would expect no wing kinematic asymmetries in the case of a stably hovering moth, and no roll-damping affect for zero

lateral velocity. Once the most significant variable was confirmed to decrease AICc, we added the next least significant variable to the model and tested whether it additionally improved AICc values, but also recursed/went back (at least) one step by additionally testing the model with the lone exclusion of the variable confirmed in the previous step. In this way we proceeded until we had tested that all variables identified in the stepwise variable elimination improved model quality.

Once the linear model cascade was complete, we then attempted to fit linear mixed models using *lme* with the *optim* optimizer and *REML* estimation technique, (also from *nlme*), (Pinheiro *et al.*, 2014). Here, we evaluated models of random intercepts for two possible factors in the analysis: moth and trial number in the case of lateral and vertical acceleration; and the same two intercepts as well as random coefficients for up- and downstroke in the case of roll velocity. This tested whether allowing for fixed variations between individual trials, moths, or (in the case of roll velocity) halfstrokes improved model quality. We attempted to fit random intercepts and coefficients for each possible combination of variables that had been shown to improve model quality. To limit complexity, we did not attempt nested group structures.

To correct for our initial variable selection with stepwise linear regression, we report p-values (Tables 2.1 & 2.3) for linear models in which all initially attempted independent variables are used at once, (Eq. 2.6-8), regardless of their significance. We used *summary* from the *stats* library to calculate the p-values for each coefficient. When two initially tested measurements were extremely similar in nature, however, such as wing pitch angle and estimated effective angle of attack, we only represented it once in the linear model fit which determined its p-value. We report p-values for the initially attempted models, rather than report artificially low p-values in models composed only of independent variables for which we found significant correlations with the dependent variable. We extracted adjusted r^2 ($r^2{}_a$) values directly from the output of the *lm* function, and evaluated the conditional r^2 ($r^2{}_c$) value of mixed models using the *r.squaredGLMM* function from the *MuMIn* library (Barton, 2015).

To understand in greater detail how moths alter their wing dynamics to create roll, we also compared normal flapping to that during maneuvers. We treated observed roll velocities in the bottom 25th percentile as normal flapping, and designated the rest as high roll velocity flapping. Then we used MATLAB's *ttest* (paired t-test) to compare the movements of the ipsi- and contralateral wings during high

roll velocities with wing movements during normal flapping, and *ttest2* (unpaired t-test) to compare high roll velocity ipsi- and contralateral wing movements to one another (Table 2.S6).

For both the roll velocity and linear acceleration models, we averaged the coefficient times the average absolute value of the kinematic measure and added them all together to create a reference value to determine percentage contribution as seen in Table 2.2.

Blade element model

We used a blade element model to investigate the effects of measured wing kinematics on a computationally simulated hawkmoth (Hedrick and Daniel, 2006). This model sums quasi-steady estimates of aerodynamic forces due to rotation of the wing about its spanwise axis (Sane and Dickinson, 2002), wing translation (Dickinson *et al.*, 1999), and added mass. We modified the simulation from Hedrick and Daniel (2006) to include independent kinematics for the left and right wing pairs. We used basic flapping parameters that match those of a hovering hawkmoth. We investigated the different kinematic adjustments observed in the moths by modulating either the amplitudes or, when differences were reported for mid-stroke only, by modulating the mean. We modulated the means and amplitudes since this produces wing kinematic changes without altering the relative phases of the left and right wing pairs. For example, we produced a 10 degree change in wing pitch angle at mid-stroke by increasing the average wing pitch angle of the right wing pair by 5 degrees and decreasing the wing pitch angle of the left wing pair by 5 degrees.

Analysis of methods and limitations

The methods were sufficient to test our initial hypotheses, and led to secondary hypotheses about roll that we were also able to test, but there were some shortcomings. The data size was insufficient to determine the simultaneous relevance of multiple nested random factors (*i.e.* maneuver, trial, moth number, and up- *vs* downstroke), since using *lme* with this group structure often resulted in overfit data in the form of singularities.

Several independent variables that we had little physical reason to believe should correlate with observed kinematic trends yielded significant p-values. Unlike expected independent variables that also had significant p-values, these unexpected independent variables increased minimum AICc values in the

models. This further validated our approach of using the AICc cascade approach for checking expected relationships, even though it did not eliminate any variables that survived stepwise regression variable selection.

We were unable to separate the wing kinematics of the moth's compensatory control of yaw from its intentional creation of roll. This problem is especially confounding since previous studies and computational model data indicate the wing kinematics that we show bring about roll (Hedrick *et al.*, 2009;Hedrick and Robinson, 2010;Ortega-Jimenez *et al.*, 2014) should also bring about yaw. Yet, understanding the specifics of yaw control is not a question we designed this experiment to answer; but rather one we plan to address in future research.

Funding

J.S.M.G. was supported by a National Defense Science and Engineering Graduate (NDSEG) Fellowship from the Department of Defense (DOD), administered by the American Society for Engineering Education (ASEE) during this research. Funding for this work also came from the National Science Foundation (NSF IOS-0920358 to T.L.H.).

Recognitions and Contributions

We would like to thank Dr. Eric Bair and Dr. Brandon Jackson for advice on statistics for this paper, as well as Dr. Dennis Evangelista, Pranav Khandelwal, Jonathan Rader, and the published manuscript reviewers for helpful comments.

J.S.M.G. designed and conducted the experiments, analyzed the results and authored the manuscript. T.L.H. analyzed the results, authored the manuscript and performed all operations relating to the blade-element simulation.

Data Link

Supplementary information available online at:

http://bio.biologists.org/lookup/suppl/doi:10.1242/bio.012922/-/DC1

Supplementary Materials

Table 2.S1: Mean midstroke kinematic derivatives

$Variable$	Yaw	Pitch	Roll	x	y	z
$Measure/Units$	1st Angular Derivative (rad/s)			1st Linear Derivative (cm/s)		
Abs. Value Mean ±SD	94.40±72.00	61.63±55.27	102.36 ±83.53	11.39±10.32	27.16±21.08	7.42±6.47
$Measure/Units$	2nd Angular Derivative $(rad/s^2 \times 10^3)$			2nd Linear Derivative (cm/s^2)		
Abs. Value Mean ±SD	3.67±3.35	20.02±18.55	40.35±36.90	93.07±73.78	178.63±157.11	100.39±81.98

Table 2.S1 shows the mean values and first and second derivatives of yaw, pitch, and roll; as well as the first and second derivatives of horizontal and vertical location. Here, yaw, pitch, and roll are calculated independently.

Table 2.S2: Passive $\dot{x}$ and $\dot{z}$ damping

Source	Velocity Half Life $(wingbeats)$		
	$\dot{y}$	$\dot{z}$	$\dot{\beta}$
$K_{\dot{y}\dot{y}}$, $K_{\dot{z}\dot{z}}$, and Eq. 3	7.18	5.79	≤0.25
Kim and Han 2014	17.95	7.13[a] 5.77[d]	0.68
Hedrick and Daniel, 2006	7.02	4.15[a] 2.60[d]	0.33[*]

[a] *ascending;* [d] *descending;* [†]*≤½ the $\dot{\beta}$ model sampling rate*

[*]*The roll velocity damping coefficient based on the Hedrick and Daniel (2006) model varies slightly depending on the starting roll velocity; 0.33 is for an initial roll velocity 3.5* $rad\ s^{-1}$.

Table 2.S2 compares our estimates of damping half-lives (in wingbeats) for lateral and vertical acceleration, calculated as $26ln(.5)/K$, as well as the damping half-life of roll velocity assumed from the Nyquist frequency, with those from computational models.

Table 2.S3: Observed vs *modeled damping effects*

Units	s^{-1}					$rad\ s^{-1}$
Coefficient	$K_{\dot{y}\dot{y}}$	$K_{\dot{z}\dot{z}}$	$K_{\beta\alpha}$	$K_{\beta\Phi}$	$K_{\dot{\beta}\theta_p}$	$K_{\beta\dot{y}}\dot{y}$
Observed Data Fit	-2.51	-3.11	2.24	2.10	-3.71	-2.64E-2
Computational Model	-2.35	-3.01[*]	4.96	3.44	-1.02	-9.60E-3

[*]*The model coefficient value for $K_{\dot{z}\dot{z}}$ is for downwards motion only; the estimated value was -7.75 for upwards motion.*

Table 2.S3 compares the coefficient estimates from our observed data with those estimated by the 2006 Hedrick and Daniel computational model.

Table 2.S4: Contribution of each wing kinematic change to roll

Amplitude or Angle (deg)	High Roll Velocity		Low Roll Velocity
	Ipsilateral Mean	Contralateral Mean	Bilateral Mean
α	40.34*±17.09	51.20*±15.33	46.60±14.19
Φ_p	106.88*±11.44	112.04±12.60	110.91±6.77
θ_p	21.04±9.11	18.73*±10.50	21.99±9.09

indicates significant difference from **bilateral mean value, with ≥95% confidence.*

Table 2.S4 contrasts ipsilateral with contralateral wing kinematics for rolls by presenting a mean followed by standard deviation. Note that, according to t-tests, all high roll velocity wing kinematic ipsilateral and contralateral means were different from one another with ≥95% confidence; while only some ipsilateral and contralateral means were significantly different from bilateral mean values (denoted by *). "Low Roll Velocity" includes (only) points in time where measured roll velocity was in the bottom 25th percentile, while "High Roll Velocity" includes the rest of the data set.

Table 2.S5: Moth morphological details by trial

Trial #	Date Taken	Moth ID#	Duration (s)	# of Manoeuvres	Mean Wing Length (cm)	Moth Mass (g)	DLT RMSE $(pixels)$							
							1	2	3L	3R	4L	4R	5L	5R
1	2011 11 03	1	1.22	4	5.38	1.90	0.59	0.49	0.58	0.85	0.86	0.80	0.69	0.75
2	2011 11 08	1	0.85	5	-	1.71	1.28	1.11	0.58	0.93	2.43	4.41	1.06	1.72
3	2012 08 23	2	0.15	1	5.40	1.57	0.64	0.45	0.55	0.37	0.63	0.65	0.44	0.70
4	2012 08 24	3	0.48	1	5.46	2.13	0.35	0.63	0.67	0.50	0.94	0.53	0.59	0.56
5	2012 08 26	3	0.55	2	-	1.94*	0.51	0.50	0.68	0.73	1.18	1.08	0.74	0.73
6	2012 08 26	3	0.87	4	-	1.94*	0.29	0.62	0.88	0.43	1.04	0.72	0.47	0.42
7	2012 08 30	4	0.72	2	5.48	2.24	0.71	0.59	0.81	0.58	1.39	1.14	0.76	0.67

**consecutive trials from same day with no feeding*

The left side of *Table 2.S5* shows general data collected for each video, as well as morphological details for each moth. This includes mass at time of filming and mean wing length. To the right are the RMSE values for each measured point as they are labeled in Fig. 2.4A. Here, 'L' indicates points on the left wing and 'R' the right.

Table 2.S6: Calibration residuals

Calibration Date	Trial #s	DLT RMSE by Camera $(pixels)$		
		1	2	3
2011 11 01 (hand)	1-2	0.12	0.14	0.14
2012 08 22 (auto)	3-6	0.15	0.11	0.10
2012 08 30 (auto)	7	0.13	0.14	0.15

Table 2.S6 shows the RMSE (in pixels) for each calibration used to interpret the individual camera view angles into 3D data.

Figure 2.S1: Roll angle vs time

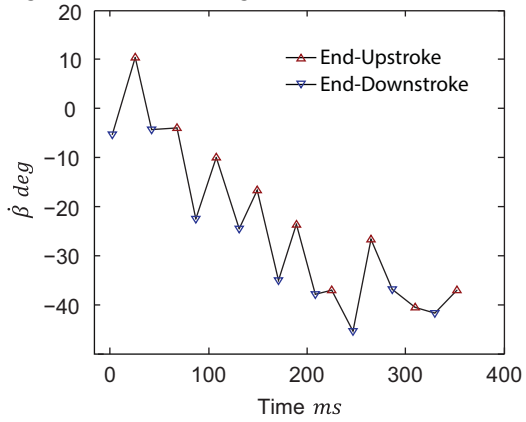

End-upstroke and end-downstroke roll orientation *vs* time from example trial. Figure 2.S1 shows the stair-step pattern of roll orientation during roll maneuvers. In this example case a moth is rolling to the left. Note that its end-upstroke roll orientation is less leftwards than its roll orientation at end-downstroke; however, the overall directional pattern of roll is still consistently leftwards from stroke to stroke. n = 18 halfstrokes from one maneuver from one moth.

Figure 2.S2: Mean wing pitch autocorrelation

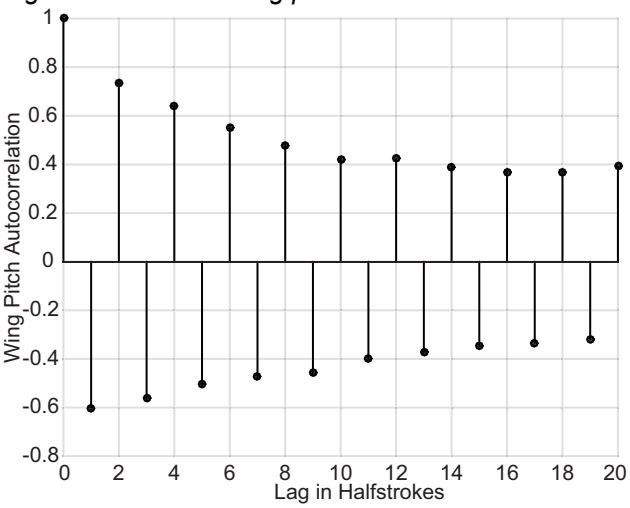

Mid-downstroke and mid-upstroke wing pitch angle autocorrelation. Figure 2.S2 shows autocorrelation of wing pitch angle where each time step is a halfstroke. Mid-downstrokes are the data points corresponding to odd numbers, and mid-upstrokes the even numbers, on the horizontal axis. Recall from Fig. 2.3 that midstroke wing pitch angles are all positive. The alternating positive-negative pattern of the autocorrelation plot shows that mean upstroke wing pitch angle is below the mean, and consistently smaller than that of downstroke. n = 218 halfstrokes from 19 maneuvers from 4 moths.

Figure 2.S3: Left-right wing pitch difference autocorrelation

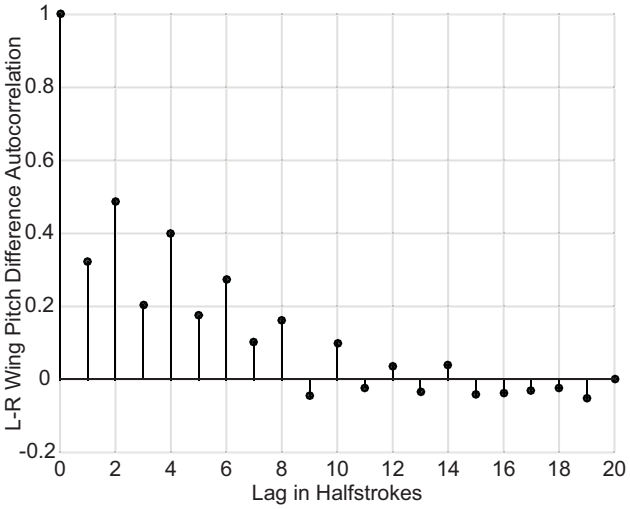

Left-Right wing pitch angle difference autocorrelation. Figure 2.S3 shows autocorrelation of left minus right wing pitch angle difference where each time step is a halfstroke. Mid-downstrokes are the data points corresponding to odd numbers, and mid-upstrokes the even numbers, on the horizontal axis. Midstroke wing pitch angle is measured as explained in Fig. 2.3. Because it is a difference, this data set includes both positive and negative numbers. The pattern shows that the sign and magnitude of left-right wing pitch angle difference is largely consistent from each halfstroke to the next, but that it is smaller in upstrokes than downstrokes. n = 218 half-strokes from 19 maneuvers from 4 moths.

Chapter 2 Symbols and Abbreviations

Box 2.1: Abbreviations

AICc	corrected Akaike Information Criterion—evaluates model predictive quality while penalizing for model complexity
BRF	Body Reference Frame, where coordinates have been rotated to align with the moth's body axis such that forward movement by the moth is $+x$, rightward movement by the moth is $+y$, and upward movement by the moth is $-z$
DLT	Direct Linear Transformation: A method for extrapolating positions in space from pixels marked on captured frames from non-collinear camera views
FCT	Flapping Counter Torque: idea that rotations change the velocity of wings flapping in that rotational plane, damping the rotation. First shown for yaw.
GRF	Global Reference Frame: unchanged coordinates from direct linear transformation and alignment with handheld global axes, where $-z$ is antiparallel with gravity
MGRF	Modified Global Reference Frame: reference frame which has been adjusted by rotating the GRF x/y plane so that the x-axis aligns with the yaw orientation of the moth
RML	Restricted Maximum Likelihood
RMSE	Root Mean Squared Error; in this study all RMSE values came from (data-relative) residuals.

Box 2.2: Variable Annotations and Constants

$\bar{}$	variable underneath is an average for the left and right wing combined
$\vec{}$	variable underneath is a vector
$\dot{}$, $\ddot{}$	first and second time derivatives of the variable underneath, respectively
$_p$	peak-to-peak amplitude of the antecedent variable
$_{LR}$	differences in a kinematic measurement between the left and right side of a moth; *i.e.* left minus right
$_c$	variable has been centered by subtracting its mean value for the entire data set
$_i$	the wing ipsilateral to the direction of moth lateral velocity
K	any coefficient estimated by regression or mixed model
g	gravity, taken as 980.665 $cm\,s^{-2}$
$r^2{}_a$	adjusted r^2; calculated for linear models
$r^2{}_c$	conditional r^2; calculated for linear mixed models

Box 2.3: Moth body kinematics

x, y, z	front/back, lateral, and vertical (respectively) in the given reference frame
$\overrightarrow{(0, \dot{y}, \dot{z})}$	3D vector with moth horizontal and vertical velocity as its only nonzero components
β	moth whole-body roll angle, measured absolute to the GRF x/y plane

Box 2.4: Moth wing kinematics

See *Fig. 2.3* for a detailed description of wing kinematics

$\overrightarrow{R_1}$	vector which stretches from the wing base point (point 3) to the forewing tip (point 4)
$\overrightarrow{R_{1\iota}}$	the $\overrightarrow{R_1}$ vector which is ipsilateral to the direction of moth lateral velocity
$\overrightarrow{R_2}$	vector which stretches from the wing base point (point 3) to the hindwing tip (point 5)
$\overrightarrow{R_3}$	vector which stretches from the hindwing tip (point 5) to the forewing tip (point 4)
$\widetilde{\Phi}_p$	peak-to-peak angular amplitude
$\overline{\widetilde{\Phi}_p}$	mean peak-to-peak angular stroke amplitude for left and right wings
Φ, Φ_p	sweep angle; the projection of $\widetilde{\Phi}_p$ onto the BRF x/y plane
$\overline{\Phi_{pc}}$	sweep amplitude averaged for left and right wings, then centered to overall data mean
$\Phi_{p_{LR}}$	difference in sweep amplitude between the left and right wings
Φ_{LR}	instantaneous difference in midstroke sweep angular position
θ	elevation angle; the angle $\overrightarrow{R_1}$ makes with the BRF horizontal
$\overline{\theta_{pc}}$	elevation angle, averaged for left and right wings, then centered to overall data mean
$\theta_{p_{LR}}$	difference in elevation amplitude between left and right wings
θ_{LR}	instantaneous difference in midstroke elevation angular position between the left and right wings
θ_i	instantaneous midstroke elevation angle for the wing ipsilateral to moth lateral velocity
α	wing pitch angle; angle a projection of $\overrightarrow{R_3}$ onto the BRF x/z plane makes relative to the BRF x/y plane
$\overline{\alpha_c}$	α averaged for the left and right wings, then centered to overall data mean
α_{LR}	instantaneous difference in α between the left and right wings

Box 2.5 Coefficients

$K_{\ddot{y}\beta}$	relates $g\sin(\beta)$ to $\ddot{y}$	$K_{\ddot{z}\Phi}$	relates $\overline{\Phi_{pc}}$ to $\ddot{z}$
$K_{\ddot{y}\dot{y}}$	relates $\dot{y}$ to $\ddot{y}$	$K_{\ddot{z}\theta}$	relates $\overline{\theta_{pc}}$ to $\ddot{z}$
$K_{\ddot{y}\Phi}$	relates $\overline{\Phi_{pc}}sign(\beta)$ to $\ddot{y}$	$K_{\ddot{z}\alpha}$	relates $\overline{\alpha_c}$ to $\ddot{z}$
$K_{\ddot{y}\theta}$	relates $\overline{\theta_{pc}}sign(\beta)$ to $\ddot{y}$	$K_{\dot{\beta}\alpha}$	relates α_{LR} to $\dot{\beta}$
$K_{\ddot{y}\alpha}$	relates $\overline{\alpha_c}sign(\beta)$ to $\ddot{y}$	$K_{\dot{\beta}\Phi}$	relates $\Phi_{p_{LR}}$ to $\dot{\beta}$
$K_{\ddot{y}\theta_i}$	relates $\overrightarrow{(0, \dot{y}, \dot{z})} \times \overrightarrow{R_{1\iota}}$ to $\ddot{y}$	$K_{\dot{\beta}\theta_p}$	relates $\theta_{p_{LR}}$ to $\dot{\beta}$
$K_{\ddot{z}\beta}$	relates $g(1-\cos(\beta))$ to $\ddot{z}$	$K_{\dot{\beta}\dot{y}}$	relates $\dot{y}$ to $\dot{\beta}$
$K_{\ddot{z}\dot{z}}$	relates $\dot{z}$ to $\ddot{z}$	$K_{\dot{\beta}\theta_i}$	relates $\overrightarrow{(0, \dot{y}, \dot{z})} \times \overrightarrow{R_{1\iota}}$ to $\dot{\beta}$

REFERENCES

Adams, R. A., Snode, E. R. and Shaw, J. B. (2012). Flapping tail membrane in bats produces potentially important thrust during horizontal takeoffs and very slow flight. *PloS One* **7,** e32074.

Altshuler, D. L., Quicazán-Rubio, E. M., Segre, P. S. and Middleton, K. M. (2012). Wingbeat kinematics and motor control of yaw turns in Anna's hummingbirds (*Calypte anna*). *J. Exp. Biol.* **215,** 4070-4084.

Barton, K. (2015). MuMIn: Multi-model inference. R package version 1.13.4. Vienna, Austria: R Foundation for Statistical Computing. http://CRAN.R-project.org/package=MuMIn.

Bergou, A. J., Swartz S., Breuer K., and Taubin G. (2011). 3D reconstruction of bat flight kinematics from sparse multiple views. *ICCV Workshops* 1618-1625.

Bomphrey, R. J., Lawson, N. J., Harding, N. J., Taylor, G.K. and Thomas, A. L. (2005). The aerodynamics of *Manduca sexta*: digital particle image velocimetry analysis of the leading-edge vortex. *J. Exp. Biol.* **208,** 1079-1094.

Cheng, B. and Deng, X. (2011). Translational and rotational damping of flapping flight and its dynamics and stability at hovering. *Robotics, IEEE Transactions* **27,** 849-864.

Cheng, B., Deng, X. and Hedrick, T. L. (2011). The mechanics and control of pitching manoeuvres in a freely flying hawkmoth (*Manduca sexta*). *J. Exp. Biol.* **214,** 4092-4106.

Dickerson, B. H., Aldworth, Z. N. and Daniel, T. L. (2014). Control of moth flight posture is mediated by wing mechanosensory feedback. *J. Exp. Biol.* **217,** 2301-2308.

Dickinson, M. H., Lehmann, F. O. and Sane, S. P. (1999). Wing rotation and the aerodynamic basis of insect flight. *Science* **284,** 1954-1960.

Dyhr, J. P., Morgansen, K. A., Daniel, T. L. and Cowan, N. J. (2013). Flexible strategies for flight control: an active role for the abdomen. *J. Exp. Biol.* **216,** 1523-1536.

Ellington, C. P., van den Berg, C., Willmott, A. P. and Thomas, A. L. (1996). Leading-edge vortices in insect flight. *Nature* **384.6610**, 626-630.

Ellington, C. P. (1984a). The aerodynamics of hovering insect flight. III. Kinematics. *Phil. Trans. R. Soc. Lon. B* **305.1122,** 41-78.

Ellington, C. P. (1984b). The aerodynamics of hovering insect flight. IV. aeorodynamic mechanisms. *Phil. Trans. R. Soc. Lon. B* **305.1122,** 79-113.

Faruque, I. and Sean Humbert, J. (2010). Dipteran insect flight dynamics. Part 2: Lateral–directional motion about hover. *J. Theor. Biol.* **265,** 306-313.

Fernandez, M. J., Springthorpe, D. and Hedrick, T. L. (2012). Neuromuscular and biomechanical compensation for wing asymmetry in insect hovering flight. *J. Exp. Biol.* **215,** 3631-3638.

Fry, S. N., Sayaman, R. and Dickinson, M. H. (2005). The aerodynamics of hovering flight in *Drosophila*. *J. Exp. Biol.* **208,** 2303-2318.

Gardiner, J. D., Dimitriadis, G., Codd, J. R. and Nudds, R. L. (2011). A potential role for bat tail membranes in flight control. *PloS One* **6,** e18214.

Hedrick, T. and Daniel, T. (2006). Flight control in the hawkmoth *Manduca sexta*: the inverse problem of hovering. *J. Exp. Biol.* **209,** 3114-3130.

Hedrick, T. L. and Biewener, A. A. (2007). Low speed maneuvering flight of the rose-breasted cockatoo (*Eolophus roseicapillus*). I. Kinematic and neuromuscular control of turning. *J. Exp. Biol.* **210,** 1897-1911.

Hedrick, T., Usherwood, J. and Biewener, A. (2007). Low speed maneuvering flight of the rose-breasted cockatoo (*Eolophus roseicapillus*). II. Inertial and aerodynamic reorientation. *J. Exp. Biol.* **210,** 1912-1924.

Hedrick, T. L. (2011). Damping in flapping flight and its implications for manoeuvring, scaling and evolution. *J. Exp. Biol.* **214,** 4073-4081.

Hedrick, T. L. (2008). Software techniques for two- and three-dimensional kinematic measurements of biological and biomimetic systems. *Bioinsp. Biomim.* **3,** 034001.

Hedrick, T. L., Cheng, B. and Deng, X. (2009). Wingbeat Time and the Scaling of Passive Rotational Damping in Flapping Flight. *Science* **324,** 252-255.

Hedrick, T. L. and Robinson, A. K. (2010). Within-wingbeat damping: dynamics of continuous free-flight yaw turns in *Manduca sexta*. *Biol. Lett.* **6,** 422-425.

Hinterwirth, A. J. and Daniel, T. L. (2010). Antennae in the hawkmoth *Manduca sexta* (Lepidoptera, Sphingidae) mediate abdominal flexion in response to mechanical stimuli. *J. Comp. Physiol. A* **196,** 947-956.

Iams, S. (2012). *Free flight of the mosquito* Aedes aegypti*.* Doctoral dissertation, Cornell University, Ithica, NY. *arXiv preprint arXiv:1205.5260*.

Iriarte-Díaz, J., Riskin, D. K., Willis, D. J., Breuer, K. S. and Swartz, S. M. (2011). Whole-body kinematics of a fruit bat reveal the influence of wing inertia on body accelerations. *J. Exp. Biol.* **214,** 1546-1553.

Jusufi, A., Zeng, Y., Full, R. J. and Dudley, R. (2011). Aerial righting reflexes in flightless animals. *Integr. Comp. Biol.* **51,** 937-943.

Kim, J. and Han, J. (2014). A multibody approach for 6-DOF flight dynamics and stability analysis of the hawkmoth *Manduca sexta*. *Bioinsp. Biomim.* **9,** 016011.

Linnaeus, C. v. (1763). Centuria insectorum rariorum. *Amoenitates Academicae* **6,** 384-415.

Mazerolle, M. J. (2013). Model selection and multimodel inference based on (Q)AIC(c). **Version 1.35.**

Muijres, F. T., Elzinga, M. J., Iwasaki, N. A. and Dickinson, M. H. (2015). Body saccades of *Drosophila* consist of stereotyped banked turns. *J. Exp. Biol.* **218,** 864-875.

Noda, R., Maeda, M. and Liu, H. (2013). Effect of Passive Body Deformation of Hawkmoth [*sic.*] on Flight Stability. *Intelligent Autonomous Systems* **12,** 835-842. Springer Berlin Heidelberg.

Ortega-Jimenez, V. M., Mittal, R. and Hedrick, T. L. (2014). Hawkmoth flight performance in tornado-like whirlwind vortices. *Bioinsp. Biomim.* **9,** 025003.

Ortega-Jimenez, V. M., Greeter, J. S., Mittal, R. and Hedrick, T. L. (2013). Hawkmoth flight stability in turbulent vortex streets. *J. Exp. Biol.* **216,** 4567-4579.

Pinheiro, J., Bates, D., DebRoy, S., Sarkar, D. and Team, R. C. (2014). *nlme: Linear and Nonlinear Mixed Effects Models*.

R Development Core Team. (2013). *R: A Language and Environment for Statistical Computing*. Vienna, Austria: R Foundation for Statistical Computing.

Read, Tyson J. G. (2015). *Hummingbirds use banking to achieve faster turns and asymmetrical wingstrokes to achieve tighter turns.* Copyrighted master's thesis, University of British Columbia, Vancouver, BC. https://open.library.ubc.ca/media/download/pdf/ 24/1.0166172/1

Ristroph, L., Berman, G. J., Bergou, A. J., Wang, Z. J. and Cohen, I. (2009). Automated hull reconstruction motion tracking (HRMT) applied to sideways maneuvers of free-flying insects. *J. Exp. Biol.* **212,** 1324-1335.

Ros, I. G., Bassman, L. C., Badger, M. A., Pierson, A. N. and Biewener, A. A. (2011). Pigeons steer like helicopters and generate down- and upstroke lift during low speed turns. *Proc. Natl. Acad. Sci. USA* **108,** 19990-19995.

Sane, S. P. and Dickinson, M. H. (2002). The aerodynamic effects of wing rotation and a revised quasi-steady model of flapping flight. *J. Exp. Biol.* **205,** 1087-1096.

Stengel R. F. (2004). *Flight dynamics*. Princeton, NJ: Princeton University Press.

Thomas, A. L. (1993). On the aerodynamics of birds' tails. *Phil. Trans. R. Soc. Lon. B* **340,** 361-380.

Waserthal, L.T. (1993). Swing-hovering combined with long toungue in hawkmoths, an antipredator adaptation during flower visits. In: *Animal-Plant Interactions in Tropical Environments* 77-87. (ed. by Barthlott *et al.*) Bonn 1992.

Wang, H., Zeng, L., Liu, H. and Yin, C. (2003). Measuring wing kinematics, flight trajectory and body attitude during forward flight and turning maneuvers in dragonflies. *J. Exp. Biol.* **206,** 745-757.

Willmott, A. P., Ellington, C. P. and Thomas, A. L. (1997). Flow visualization and unsteady aerodynamics in the flight of the hawkmoth, *Manduca sexta*. *Phil. Trans. R. Soc. Lon. B* **352,** 303-316.

Zheng, L., Hedrick, T. L. and Mittal, R. (2013). A multi-fidelity modelling approach for evaluation and optimization of wing stroke aerodynamics in flapping flight. *J. Fluid Mech.* **721,** 118-154.

Zheng, L., Wang, X., Khan, A., Vallance, R., Mittal, R. and Hedrick, T. L. (2009). A combined experimental-numerical study of the role of wing flexibility in insect flight. *47th AIAA Aerospace Science Meeting*. January 5-8, Orlando, FL. 2009-2382.

CHAPTER 3:
DRAG AND INERTIA HELP DAMP AND RESTORE PITCH IN THE FLAPPING FLIGHT OF *MANDUCA SEXTA*

This Chapter was submitted as a full-length research article to J. Exp. Biol. in 2017 for peer review. As of the writing of this dissertation, the manuscript is in the revision stages.

Summary

The inertial reactions of wings to pitch impulses reinforce velocity/drag damping reactions to pitch rotation, possibly a general feature of stability in flapping flight. Flexibility (and wing hinge elasticity) may allow these effects.

We launched projectiles to perturb hawkmoths (*Manduca sexta*) in hovering flight. These moths proved capable of recovering from large (>100°), rapid (~4 ms) pitch perturbations. Our analysis reveals two previously undescribed mechanisms that enhance pitch stability: 1) inertia and drag keep the wings flapping close to their original stroke plane in the global reference frame, and 2) passive changes to stroke plane deviation angle and effective angle of attack, (and possibly wing sweep as well), create pitch countertorque. These responses indicate flapping wings act as Coriolis vibratory gyroscopes, resisting rotational change despite reorientation of the moth's body: Nevertheless, drag also creates or reinforces both mechanisms, implying they have broad importance over a range of size scales. Abdominal movement may also amplify effect 1 in moths. Together, these changes create pitch-damping torque on a lever arm connecting the centre of pressure and centre of mass, resulting in a pendulum-like oscillatory recovery pattern. Low latency in a control model fit to observed body pitch and pitch rate, along with low latency in these two wing kinematic changes indicate these responses are nearly instantaneous and thus likely passive. Body and wing drag also instantly resist pitch rotation, but the stroke plane effect is largest and it, plus body and wing drag, together produce passive pitch stability in a computational model even without including the angle of attack or stroke plane deviation angle changes. Future investigators, modellers, and engineers should consider similar features that may benefit flying insects in general, and air vehicle design.

Key Words

Coriolis vibratory gyroscope, flapping flight, hawkmoth, passive stability, perturbation, pitch

Introduction

Despite over a century of research into animal flight and powered flight by human-designed aircraft, the elements of mechanical design and control that allow manoeuvrability and stability in flapping flight are still not fully understood. We are only beginning to answer basic questions, such as how hovering animals stabilize their orientation, or how wing movements create turns. Here, in free-flight animal experiments, we use the impact of small projectiles to perturb hovering moths *Manduca sexta* (*L.*), and then quantify their responses to better understand their ability to maintain pitch orientation.

During flight, animals and machines must respond to a range of perturbations, whether large and intermittent, or small and periodic. The underlying importance of stability to flight has inspired a range of research, including live animal experiments *e.g.* (May *et al.*, 1980;Taylor and Thomas, 2003), comparative studies (*e.g.* Hedrick *et al.*, 2009; Ristroph *et al.*, 2013), numerical simulations *e.g.* (Sun and Xiong, 2005), and control theoretic studies *e.g.* (Cheng and Deng, 2011;Liu *et al.*, 1998). Recent studies indicate stabilization engenders trade-offs such as limiting maximum flight speed in orchid bees (*Euglossini*), and hawkmoths (*Sphingidae*) flying in turbulence (Combes and Dudley, 2009;Ortega-Jimenez *et al.*, 2013) and possibly limiting manoeuvrability in hummingbirds (*Archilocus colubris*) (Ravi *et al.*, 2015).

In hawkmoths, our research has shown a high degree of passive damping stabilizes yaw and roll (Greeter and Hedrick, 2016;Hedrick *et al.*, 2009;Hedrick and Robinson, 2010), but computational and theoretical models consistently identify pitch as the angular degree of freedom with the least amount of passive stability (*e.g.* Sun *et al.*, 2007). Thus, hovering animals like *M. sexta* are expected to need sensory feedback and active control to stabilize body pitch orientation or augment a small margin of passive stability (Maeda *et al.*, 2010;Ristroph *et al.*, 2013;Taha *et al.*, 2015); but see (Noda *et al.*, 2013;Noda *et al.*, 2014).

To investigate stability in free-flying hawkmoths, we examined responses to brief, large-magnitude pitch perturbations. We shot projectiles from a spring-loaded cannon at moths in hovering flight. Each projectile collision occurred over several milliseconds. Such nearly instantaneous perturbations allow us to examine how moths react mechanically to perturbations on the time scale of halfstrokes, possibly before

their neural system registers the displacement and responds. Our experiment is similar to those on running guinea fowl (*Numida meleagris*) (Daley *et al.*, 2006), walking cockroaches (*Blaberus discoidalis*) (Jindrich and Full, 2002), and flying fruit flies (*Drosophila melanogaster*) (Beatus *et al.*, 2015;Ristroph *et al.*, 2010;Whitehead *et al.*, 2015), in that the perturbations are brief, unexpected, and mechanical in nature. However, even in those studies the impulse perturbation delivered lasts longer than a full stroke cycle. Our experiment differs from previous aerodynamic perturbation experiments on hawkmoths and bees (*Apis mellifera*) (Ortega-Jimenez *et al.*, 2014;Vance *et al.*, 2013), particularly because those perturbations were longer, primarily to the wings rather than the body, and difficult to quantify in magnitude and direction.

We predicted moth responses would incorporate both active and passive elements, but that active elements would necessarily dominate, based on previous research cited above. We first identified the wing kinematics that contributed to pitch orientation recovery by analysing high speed video of moth reactions after perturbations. We quantified these wing kinematics and combined them with *a priori* expectations based on previous research to create a nonlinear model of pitch-righting in *M. sexta*. We refined the model by applying maximum likelihood selection techniques, and applied the same approach to estimate response delays in a simple passive + active control model based on current pitch orientation and its rate of change over time. Finally, we assessed the effect of the mechanical damping identified in our analysis on flight stability using numerical simulation.

Most strikingly, our data support two novel sources of near-instantaneous passive pitch stability, neither previously considered in computational models, nor revealed in prior animal flight experiments. Overall, passive inertia and drag mechanisms dominate the initial pitch perturbation response in *M. sexta*. Combined with rotational drag (Ristroph *et al.*, 2013), these results demonstrate passive pitch stability in *M. sexta*, and its possibility in other flying animals. When a collision pitches the moth's body 1) its wings continue to flap close to their original stroke plane in the world reference frame, and 2) effective angle of attack (AOA) and stroke plane deviation angle changes that further damp pitch rotation occur near midstrokes. Since the centre of forces, or "centre of pressure" (COP) is situated above the centre of mass (COM) during normal flight, lift, drag, and gravity act on a COP-COM moment arm to create a passive pendular restorative torque. These responses indicate flapping wings act as Coriolis vibratory gyroscopes, resisting rotational change despite reorientation of the moth's body. Drag also adds to effects 1) and 2),

however, implying these novel mechanisms have broad importance over a range of body sizes because they are sourced from both inertial and viscous forces. Combined with recent work, our results also suggest flexibility at or near the wing base (Eberle *et al.*, 2015;Jankauski and Shen, 2016), and/or the abdomen (Dyhr *et al.*, 2013;Noda *et al.*, 2013;Noda *et al.*, 2014), allow such effects.

Methods

Moths came from three universities and lived in mesh cages on an extended dark:light cycle

We acquired 11 male *M. sexta* as pupae from the domestic colonies housed at the respective biology departments of UNC Chapel Hill, Duke University, and the University of Washington. UNC and UW hawkmoths were from inbred domestic colonies, while Duke moths had been recently outcrossed with several other domesticated lines. Following eclosure, moths drank water *ad libitum* in their enclosures, and fed on 1:4 solutions of sucrose or honey dissolved in tap water during recording and training. They lived in $30 \times 30 \times 30 cm$ mesh cages at ambient room temperature and humidity in a 22:2hr light:dark cycle. See Table 3.S1 for individual trial and moth details.

We trained moths to feed from man-made flowers in a recording arena

We trained food-limited *M. sexta* to feed on an artificial nectar solution while they hovered in an arena (Fig. 3.1A). The nectar was delivered *via* an artificial flower composed of a white photo paper disc attached to a nectar-filled syringe tube. Moths were trained by repeated feeding from this artificial flower in the days leading up to perturbation trials. Training times typically coincided with night or dusk in the moths' artificial extended-day, contracted-night, 24-hour light cycle. In each experimental trial, we lured the moth to approach a white paper disc that simulated our training flower but contained no nectar and did not allow for proboscis insertion. We moved this white disc completely out of contact with the moth and used a modified toy cannon to launch a small projectile at the moth (Fig. 3.1B). We used high speed cameras to record the event.

Figure 3.1: Flight chamber, cameras, and cannon

Experimental setup and cannon. We recorded pitch perturbations from hawkmoths flying in a 71 × 71 × 74cm glass-walled arena. **A)** Two Phantom v7.1 cameras and one Phantom v5.1 (Vision Research Inc., Wayne, NJ, USA) or Y4 camera (IDT Vision, Tallahassee, FL), used the high-intensity 680nm light from eight LEDs (Roithner LaserTechnik, GmBH, A-1040, Vienna Austria) to video the perturbations at 900-1200Hz. The visible light level in the arena was ~350 lx, as measured with a luxmeter *ex post facto* (840006, Sper Scientific LTD, Scottsdale, AZ, USA). We waved a wand with two red LED lights positioned 65mm apart through the filming space to calibrate the cameras (Hedrick, 2008). Labels: 1-2) Phantom v7.1 cameras; 3) Phantom v5.1 or IDT Y4 camera 4) flying moth. **B)** Spring-loaded cannon used in experiment.

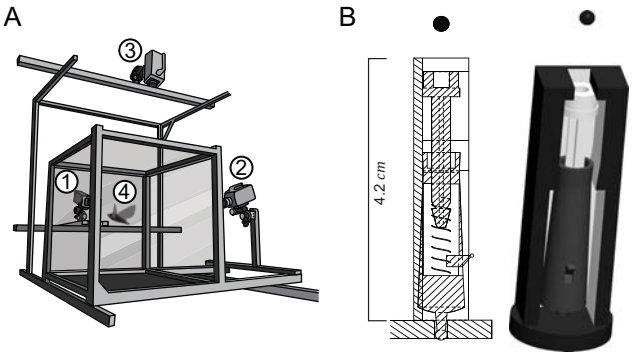

We extracted kinematics with 3D videography and MATLAB

We collected 3D kinematics using the MATLAB (2009a/2010b/2015b, The Mathworks, Natick, MA) package *DLTdv5* (Hedrick, 2008) to mark natural wing and body landmarks in every frame where they were visible. Figure 3.2 depicts marked points, calculated wing angles and the body reference frame (BRF). Our unit of comparison was the halfstroke, since both our prior work and modelling suggests average forces are sufficient for modelling basic kinematic effects in hawkmoth-scale insects (Hedrick *et al.*, 2009). When correlating these body movements with wing kinematics, we inserted halfstroke measurements at their corresponding midstroke points, since midstrokes are a convenient reference point where forces are close to their highest in the *M. sexta* stroke cycle (Bomphrey *et al.*, 2005;Zheng *et al.*, 2013). We calculated all wing angles using points from the BRF.

From the digitized points, we identified stroke cycle landmarks and wingbeat frequency. To identify endstroke points, we summed the BRF wingtip positions and marked the maximum or minimum $x + (-z)$ position near where the first time derivative of the tip's x-position changed sign. We marked midstrokes halfway between endstroke points, and used the interval between the four sets of points in each stroke cycle to calculate wingbeat frequency.

The high-frequency perturbation events of varying magnitudes complicated digital filtering; to exclude high-frequency noise but preserve near-collision data, we cleaved the signals into two parts at the frame where the projectiles first contacted the moths (Fig. 3.3). We subjected the body orientation results for the pre- and post- perturbation segments to a 25Hz low-pass digital Butterworth filter prior to analysis,

but computed wing kinematics from unsmoothed data. All final model regressions used 25Hz low-pass-filtered body orientation data (Eq. 3.1, 3.2, 3.6-8, 3.11, 3.12) except for time delay models, which used 35Hz (3.9-10, 3.13-14 & 3.16) to increase sensitivity to smaller delays.

Figure 3.2: Marked points, body angles, and wing angles

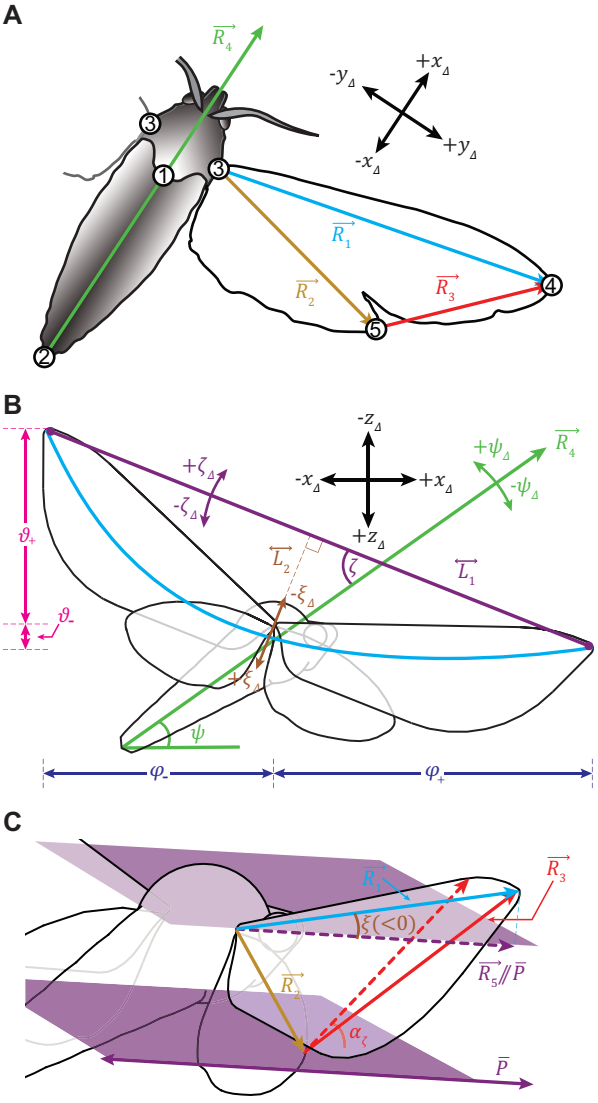

Marked points, body angles, and wing angles. We computed flapping kinematics from the time-varying 3D position of points on the moth and wings. **A)** shows the points and vectors used. The left side is not shown but was also tracked. A manually identified canonical frame provided the default position for fixed morphology of the moth. We used this to compute Euler angles (yaw, pitch, and roll) and reference frames (Stengel, 2015). In the Body Reference Frame (BRF) planes, $+x$ is forwards for the moth, $+z$ is parallel with gravity (downwards), and $+y$ is to the right. **B)** and **C)** show the body and wing angles we measured based on the points and vectors in A). We measured body pitch angle changes ψ_Δ relative to the canonical orientation of $\overrightarrow{R_4}$. The azimuthal/elevation angles of $\overrightarrow{R_1}$ relative to a BRF vertical/horizontal ($(y,z)/(x,y)$) plane through the wing base point yield wing sweep/elevation angle (φ/ϑ), at the end of downstroke (φ_+/ϑ_+) and upstroke (φ_-/ϑ_-). $\overleftrightarrow{L_1}$ connects the (x,z) forewing tip position at the end of a given up- or downstroke with its (x,z) position at the end of the previous or subsequent halfstroke. Extending $\overleftrightarrow{L_1}$ in y yields a stroke plane $\bar{P}$; during perturbation, $\bar{P}$ deviates from its average hover orientation in the BRF by "stroke plane inclination angle" ζ_Δ. Line segment $\overleftrightarrow{L_2}$ (brown) starts perpendicular to $\bar{P}$ and ends at the position of point 4 when the wing is at midstroke. The arctangent of its length over the midstroke y-position of 4 is ξ. **C)** shows an oblique view of this midstroke measurement; reflecting $\overrightarrow{R_1}$ onto $\bar{P}$ yields $\overrightarrow{R_5}$; ξ is the angle between these vectors. The difference between pre-hit average ξ and its value at a post-hit midstroke is the "stroke plane deviation angle" ξ_Δ. "Wing pitch angle" α_{ζ_Δ}, is the angle that the (x,z) components of $\overrightarrow{R_3}$ make relative to the stroke plane. To get deviation from baseline for all angles, we subtracted pre-hit midstroke averages from the measurements for each post-hit halfstroke. We averaged and subtracted upstroke and downstroke kinematics separately.

Figure 3.3: Two example trials

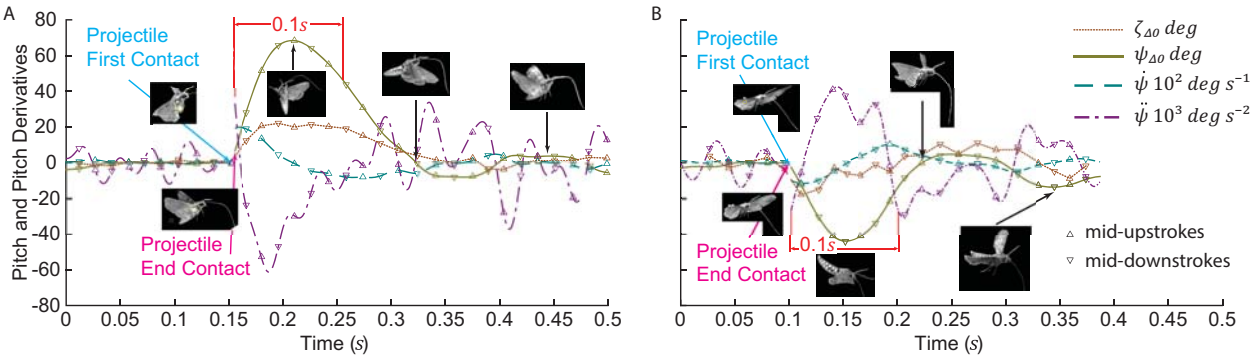

Two example trials. Here we show pitch and its time derivatives, as well as stroke plane inclination angle, for two representative trials from our data set: **A)** one pitch-up (Table 3.S1, Trial 32), and **B)** one pitch-down (Table 3.S1, Trial 56). In each figure, the cyan arrow indicates when the projectile first contacts the moth, and the magenta arrow indicates when it ends contact. Moth images show the first and last contact of the projectile, the maximum pitch deviation, initial return to zero pitch deviation, and maximum post-correction oscillation. Within the first two images, yellow circles highlight the position of the cannonball. Pitch orientation ψ_Δ, pitch velocity $\dot{\psi}_\Delta$, pitch acceleration $\ddot{\psi}_\Delta$, and stroke plane inclination angle ζ_Δ, are shown, see figure for units. The data were smoothed at $25Hz$ (see **Methods**) and mean-centered to each trial's pre-hit values. Models fit near-collision data sets of almost identical duration from each trial: this post-perturbation analysis "window" starts at the magenta arrow and ends at the nearest frame ≤$0.1s$ later.

We used a priori theory, video observations, and a stepwise approach to develop our pitch acceleration models

We first constructed a preliminary non-linear model that related various wing and body kinematics we hypothesized were important to pitch acceleration based on initial observations and *a priori* theory. The first pitch acceleration model (Eq. 3.1) included: 1) A visual observation of a mismatch between stroke plane and pitch deviations (expressed as $K_{\ddot{\psi}\zeta} mg \sin(-\zeta_\Delta)$; see *Derivation* below and also the Chapter 3 Symbols and Abbreviations); 2) A visual observation of changes to stroke plane deviation angle during perturbations ($K_{\ddot{\psi}\xi}\xi_\Delta$) 3) Wing pitch angle ($QK_{\ddot{\psi}\alpha_x}\alpha_{\zeta_\Delta}\cos(\zeta_\Delta) + K_{\ddot{\psi}\alpha_z}\alpha_{\zeta_\Delta}\sin(-\zeta_\Delta)$; see *Derivation* below) 4) Drag-based torque from longitudinal and vertical motion, ($K_{\ddot{\psi}\dot{x}}\frac{\dot{x}_\Delta{}^3}{|\dot{x}_\Delta|}\cos(\psi_\Delta) + K_{\ddot{\psi}\dot{z}}\frac{\dot{z}_\Delta{}^3}{|\dot{z}_\Delta|}\sin(\psi_\Delta)$); 5) A pitch velocity damping term ($K_{\ddot{\psi}\dot{\psi}}\frac{\dot{\psi}_\Delta{}^3}{|\dot{\psi}_\Delta|}$; see *Derivation* below) 6) Dorsoventral sweep asymmetry in lift-based torque creation ($K_{\ddot{\psi}\varphi}\varphi_\Delta$; see *Derivation* below) and, by theoretical extension 7) Drag-based torque creation from elevation angle offset ($QK_{\ddot{\psi}\vartheta}\vartheta_\Delta$):

$$\ddot{\psi}_\Delta = I_{yy}{}^{-1}\left(K_{\ddot{\psi}\zeta} mg\sin(-\zeta_\Delta) - K_{\ddot{\psi}\dot{\psi}}\frac{\dot{\psi}_\Delta{}^3}{|\dot{\psi}_\Delta|} - K_{\ddot{\psi}\dot{x}}\frac{\dot{x}_\Delta{}^3}{|\dot{x}_\Delta|}\cos(\psi_\Delta) - K_{\ddot{\psi}\dot{z}}\frac{\dot{z}_\Delta{}^3}{|\dot{z}_\Delta|}\sin(\psi_\Delta) + QK_{\ddot{\psi}\alpha_D}\alpha_{\zeta_\Delta}\cos(\zeta_\Delta) + K_{\ddot{\psi}\alpha_L}\alpha_{\zeta_\Delta}\sin(-\zeta_\Delta) - K_{\ddot{\psi}\xi}\xi_\Delta + K_{\ddot{\psi}\varphi}\varphi_\Delta + QK_{\ddot{\psi}\vartheta}\vartheta_\Delta\right), \quad (3.1)$$

where $Q = \begin{cases} +1, & downstrokes \\ -1, & upstrokes \end{cases}$, $\varphi = \varphi_+ + \varphi_-$, and $\vartheta = \vartheta_+ + \vartheta_-$, as defined in Fig. 3.2, and mechanically justified in Fig. 3.4-5. We found that ξ_Δ and α_{ζ_Δ} were negatively proportional (Fig. 3.6D), and when we treat ξ_Δ the same as α_{ζ_Δ}, ξ_Δ's statistical significance outweighs that of α_{ζ_Δ} in the model. Furthermore, while multipliers of $\cos(\psi_\Delta)$ and $\sin(\psi_\Delta)$ might be theoretically better for $K_{\ddot{\psi}\dot{x}}$ and $K_{\ddot{\psi}\dot{z}}$ terms, (as in our computational pitch model, Eq. 3.3-5), the correlation of ψ_Δ with $\ddot{\psi}_\Delta$ is both assured and non-causal; thus we replace it with ζ_Δ in an attempt to focus on causal relationships. This led us to a refined model:

$$\ddot{\psi}_\Delta = {I_{yy}}^{-1}\left(K_{\ddot{\psi}\zeta} mg \sin(-\zeta_\Delta) - K_{\ddot{\psi}\dot{\psi}}\frac{{\dot{\psi}_\Delta}^3}{|\dot{\psi}_\Delta|} - K_{\ddot{\psi}\dot{x}}\frac{{\dot{x}_\Delta}^3}{|\dot{x}_\Delta|}\cos(\zeta_\Delta) - K_{\ddot{\psi}\dot{z}}\frac{{\dot{z}_\Delta}^3}{|\dot{z}_\Delta|}\sin(\zeta_\Delta) - QK_{\ddot{\psi}\xi_D}\xi_\Delta\cos(\zeta_\Delta) + K_{\ddot{\psi}\xi_L}\xi_\Delta\sin(\zeta_\Delta) + K_{\ddot{\psi}\varphi}\varphi_\Delta + QK_{\ddot{\psi}\vartheta}\vartheta_\Delta\right) \quad (3.2)$$

Only terms which decreased BIC and had significant P-values were included in the final pitch acceleration model (Eq. 3.7).

Derivation of ${I_{yy}}^{-1}$ and r

To estimate the pitching moment of inertia I_{yy}, we reconstructed each moth body volume as a set of voxels in the 3 camera views and evenly distributed the measured body mass within that volume. Following perturbation, the moth's body rotates somewhat like a pendulum about some COR (assumed to be near the COP) a distance of r away from the COM. Thus, it is potentially reasonable to use $(I_{yy} + mr^2)$ for inertia, measure pitch about the COR, and incorporate *r* in the wing kinematics. However, *r* is unknown and a statistical estimate of it is based only on small variations in mass and rotational inertia among the 11 moths and 16 trials. Therefore, we chose to instead perform BIC-based stepwise elimination on Eq. 3.2, discarding *r*, which is estimated for the computational model from a separate nonlinear fit (Eq. 3.5).

Derivation of $K_{\ddot{\psi}\zeta} mg\, sin(-\zeta_\Delta)\, {I_{yy}}^{-1}$

In Fig. 3.4B, we show that resistance of the stroke plane angle to rotation results in pitch acceleration. We found that when a moth is pitched by ψ_Δ, its wings rotate by a lesser amount, resulting in a change in the BRF angle between the moth body and wings (ζ_Δ). This angle creates resistive torque $-mgr\sin(\zeta_\Delta)$. Since this type of resistance mimics a pendulum with a pivot at or near the COP, we divide by rotational inertia relative to the COP: ($I_{yy} + mr^2$) according to the parallel axis theorem. Once we 1) exclude r and substitute ${I_{yy}}^{-1}$ for $\left(I_{yy} + mr^2\right)^{-1}$ as justified in *Derivation of* I_{yy} *and* r, and 2) multiply by our estimated coefficient $K_{\ddot{\psi}\zeta}$, we arrive at the final term representing how resistance of the stroke plane angle to rotation creates pitch acceleration in Eq. 3.6-7 & 3.1-2: $\ddot{\psi}_\Delta = -K_{\ddot{\psi}\zeta} mg\sin(\zeta_\Delta) + \cdots$.

Derivation of $-QK_{\ddot{\psi}\xi_D}\xi_\Delta\, cos(\zeta_\Delta)\, {I_{yy}}^{-1}$

In Fig. 3.5A, we show that deviations in the AOA affect the pitch torque created by drag during upstrokes and downstrokes, similar to the dynamic described by Chen *et al.* (2017). Increased AOA leads to increased induced drag force ($\overrightarrow{F_{D_\pm}}$) with a magnitude $\propto \alpha_\zeta$. The torque on the COM is $\overrightarrow{F_{D_\pm}} \times \vec{r}$, which is thus $\propto \pm\alpha_\zeta r\cos(\zeta)$. We replace 1) α_ζ with α_{ζ_Δ} and 2) ζ with ζ_Δ because we are interested in deviations from typical pitch acceleration ($\ddot{\psi}_\Delta$); and introducing a non-"midstroke-centred" ζ term could add information to the model that is independent of how AOA affects $\ddot{\psi}_\Delta$. We then multiply $\alpha_{\zeta_\Delta} r\cos(\zeta_\Delta)$ by Q to reflect that downstroke drag $\overrightarrow{F_{D_+}}$ pitches the moth up, and upstroke drag $\overrightarrow{F_{D_-}}$ pitches the moth down. When evaluating the preliminary pitch acceleration model (Eq. 3.1), we found, however, that stroke plane deviation angle (ξ_Δ) appears to be a better measure of the way in midstroke wing angles create imbalanced drag than α_{ζ_Δ}. Since $\alpha_{\zeta_\Delta} \propto -\xi_\Delta$, (the two co-vary; Fig. 3.5B-C & 3.6D), this wing kinematic represents a combination of changes to effective AOA (α_{ζ_Δ}; Fig. 3.5A) and COP (ξ_Δ; 3.5D; Elzinga *et al.* 2014; Chen *et al.* 2017). We multiply by -1 when we substitute ξ_Δ for α_{ζ_Δ}, resulting in $-Q\xi_\Delta r\cos(\zeta_\Delta)$. Once we exclude r and divide by inertia I_{yy} (see *Derivation of* I_{yy} *and* r), and multiply by our estimated coefficient $K_{\ddot{\psi}\xi_D}$; we arrive at the final term representing how AOA and stroke plane deviation angle changes together create pitch acceleration in Eq. 3.2 & 3.7: $\ddot{\psi}_\Delta = -QK_{\ddot{\psi}\xi_D}\xi_\Delta \cos(\zeta_\Delta)\, {I_{yy}}^{-1} + \cdots$.

Derivation of $K_{\ddot{\psi}\varphi}\varphi_{\Delta}{I_{yy}}^{-1}$

In Fig. 3.5B, we show that deviation from typical dorsoventral sweep asymmetry engenders an imbalance in lift, which results in net pitch torque. During stable hover *(i)*, the cross product of dorsal $(-)$ and ventral $(+)$ lift forces $(\overrightarrow{F_{L_{\pm}}})$ and lever arms $(\overrightarrow{r_{\pm}})$ are equal so the resultant pitch torques balance; *i.e.* $\overrightarrow{F_{L_-}} \times \overrightarrow{r_-} = \overrightarrow{F_{L_+}} \times \overrightarrow{r_+}$ over the course of a whole stroke. If we assume a constant wing velocity, lift is proportional to the azimuthal angle swept by the wings; *i.e.* $\overrightarrow{F_{L_{\pm}}} \propto \varphi_{\pm}$. When the moth shortens the dorsal $(-)$ part of the stroke in the azimuthal plane *(ii)*, this asymmetry reduces $\overrightarrow{F_{L_-}} \times \overrightarrow{r_-}$ relative to $\overrightarrow{F_{L_+}} \times \overrightarrow{r_+}$. From Fig. 3.5B, we see that this reduction of φ_- rotates the lever arm $\overrightarrow{r_-}$ so that it is slightly more parallel with $\overrightarrow{F_{L_-}}$, and also reduces its length. However, we do not consider these alterations to $\overrightarrow{r_-}$ in our pitch acceleration model because they 1) are small, 2) only serve to reinforce the torque imbalance, and 3) are difficult to quantify because COP position depends on multiple factors. Thus, where *Δ* represents deviation in a measurement relative to typical flapping averages, $\left(\overrightarrow{F_{L_+}} \times \overrightarrow{r_+} - \overrightarrow{F_{L_-}} \times \overrightarrow{r_-}\right)_{\Delta} \cong (\varphi_+ - \varphi_-)_{\Delta} \stackrel{\text{def}}{\equiv} \varphi_{\Delta}$. Once we 1) exclude $|\vec{r}|$ and divide by inertia I_{yy} (see *Derivation of* I_{yy} *and* r), and 2) multiply by our estimated coefficient $K_{\ddot{\psi}\varphi}$; we arrive at the final term representing how dorsoventral sweep asymmetry creates pitch acceleration in Eq. 3.7 & 3.1-2: $\ddot{\psi}_{\Delta} = K_{\ddot{\psi}\varphi}\varphi_{\Delta}{I_{yy}}^{-1} + \cdots$.

Derivation of $K_{\ddot{\psi}\dot{\psi}}\frac{\dot{\psi}_{\Delta}{}^{3}}{|\dot{\psi}_{\Delta}|}{I_{yy}}^{-1}$

In Fig. 3.5C, we show that pitch rotation rate causes (profile) drag on the moth's wings $(\overrightarrow{F_{W_{\pm}}})$, and to a lesser extent, parasite drag on the moth's body $(\overrightarrow{F_{P_{\pm}}})$ which both result in resistive rotational damping. Parasite drag $\overrightarrow{F_{P_{\pm}}}$ acts on the moth's body, but is negligible compared to the much larger forces on the rotating wings. Again we ignore *r* and the possibility that the moth rotates around a COR different than its COM (see *Derivation of* I_{yy} *and* r), and thus divide by I_{yy}. We square the pitch velocity term $(\dot{\psi}_{\Delta})$ since drag forces are approximately proportional to $(\propto)$ the square of velocity. We perform this operation as $\dot{\psi}_{\Delta}{}^{3}/|\dot{\psi}_{\Delta}|$ so that the independent variable retains the sign of its direction of rotation. Due to stroke plane resistance to rotation, the moth's wings may rotate at approximately $K_{\psi\zeta} \approx ½$ the rate of its body (Table 3.3;

Eq. 3.8). But, $(ab)^2 = a^2b^2$ so we can disassociate this possible rate effect from the independent variable and expect to capture it within our estimate of the coefficient $\left(K_{\ddot{\psi}\dot{\psi}}\right)$, which represents how squared pitch velocity damps pitch acceleration: $\ddot{\psi}_\Delta = K_{\ddot{\psi}\dot{\psi}} \frac{\dot{\psi}_\Delta{}^3}{|\dot{\psi}_\Delta|} I_{yy}{}^{-1} + \cdots$.

Figure 3.4 New model for pitch stability in flapping flight

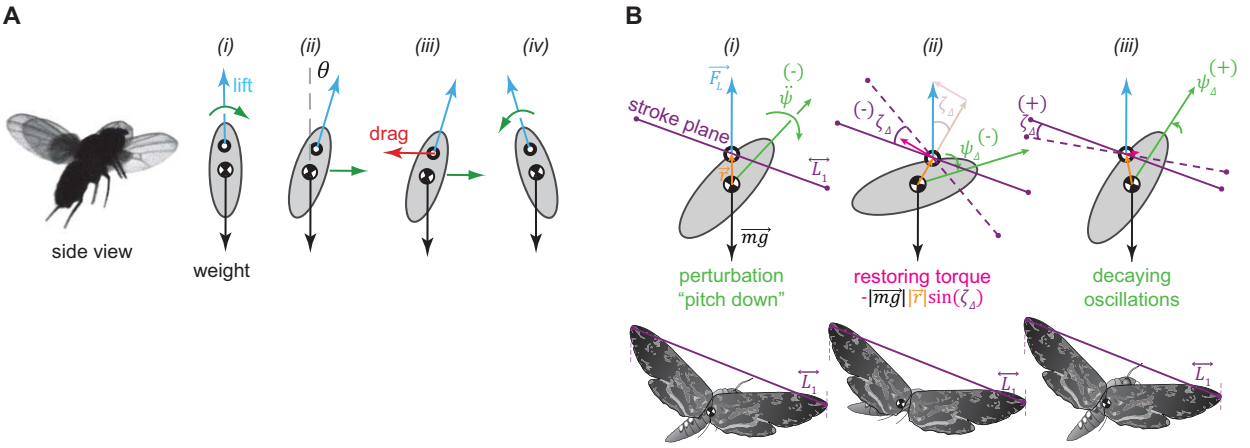

A pitch-unstable model. A) A graphical representation of the pitch instability predicted for hovering insects, reproduced with permission (Ristroph *et al.*, 2013). Here, wing motion is fixed to the body reference frame (BRF) and lift and weight are antiparallel ***(i)***. However, if pitched down **(*ii*)**, the lift vector is reoriented and is no longer antiparallel with weight, creating forward motion, **(*iii*)**. This leads to drag on the insect's wings, creating a pitch up torque. Current computational studies predict the resulting pitch-up perturbation will be larger in magnitude than the original pitch down perturbation **(*iv*)**, leading to growing oscillations. **Our stroke-plane stabilized hawkmoth result. B)** A theoretical moth, whose wings are connected to its body *via* a frictionless gimbal, experiences a pitch down perturbation; however, its wing motion remains in the original plane in the global reference frame (GRF), restoring the moth to equilibrium. In hovering **(*i*)**, the moth's lift ($\overrightarrow{F_L}$) and weight ($\overrightarrow{mg}$) vectors are equal in magnitude and antiparallel. The moth's centre of mass and centre of pressure (COP) are vertically aligned to one another and separated by $\vec{r}$. This changes when a perturbation (ψ_Δ) of -30° is applied, reorienting the moth's body and $\vec{r}$. Due to the theoretically frictionless gimbal, the stroke plane remains at a fixed orientation in the GRF **(*ii*)**. Meanwhile, the stroke plane's orientation relative to the moth's body deviates by angle ζ_Δ but lift is still directed vertically. Thus, a resultant force of $-mg\sin(\zeta_\Delta)$ acts at the COP perpendicular to $\vec{r}$, rotating the moth back toward its original orientation; *i.e.* $\overrightarrow{F_L} \times \vec{r} = -mgr\sin(\zeta_\Delta)$. In **(*iii*)**, this leads to a slight overcorrection, which is also resisted by the GRF-fixed stroke plane leading to decaying oscillations and a return to hovering equilibrium. In this theoretical case, ψ_Δ and ζ_Δ are equal to one another. In reality, friction and/or other factors cause the magnitude of ζ_Δ to be about half that of ψ_Δ over the perturbation range of -30° to 30° (Table 3.3; Eq. 3.8).

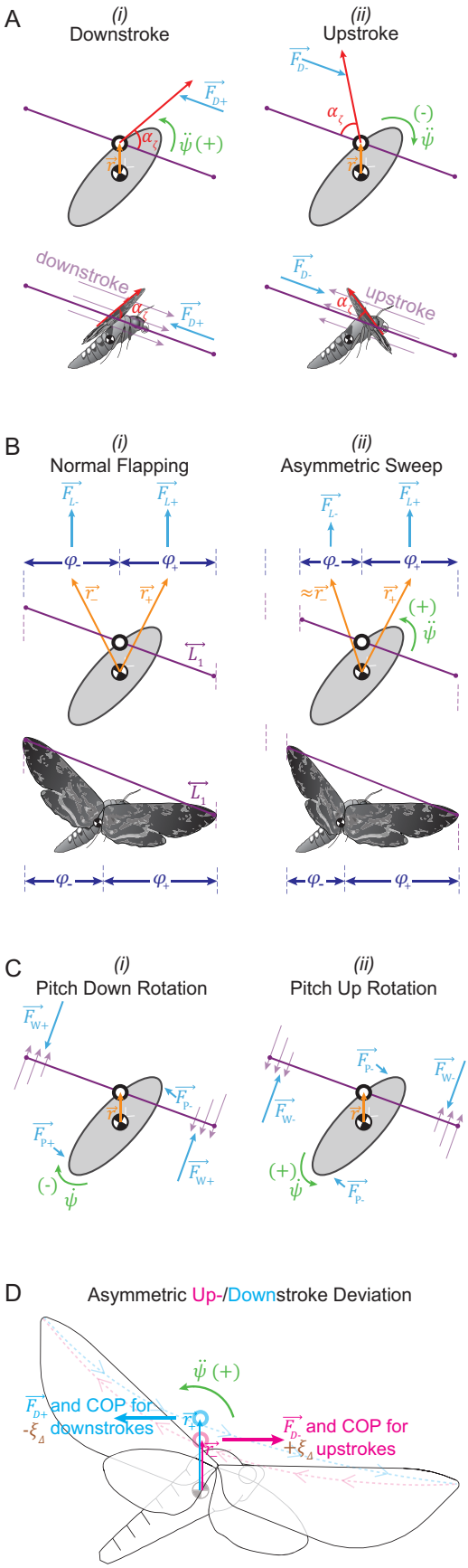

Figure 3.5: Explanation of pitch acceleration model terms

Explanation of pitch acceleration model terms which involve φ, ξ, and $\dot{\psi}$. **A)** Profile drag ($\overrightarrow{F_{D_\pm}}$) is a function of angle of attack ($\approx\alpha_\zeta$), so changes to angle of attack alter pitch torque about the COM-COP lever arm ($\vec{r}$). Increases in wing pitch may lengthen $\vec{r}$ as well, reinforcing this affect. See *Derivation of* $-QK_{\dot{\psi}\xi_D}\xi_\Delta\cos(\zeta_\Delta)\,{I_{yy}}^{-1}$ for a precise derivation of the model (Eq. 3.7) term representing how angle of attack and stroke plane deviation angle together affect pitch acceleration in downstrokes *i)* and upstrokes *(ii)*. **B)** During stable hover *(i)*, the cross product of dorsal ($-$) and ventral ($+$) lift forces ($\overrightarrow{F_{L_\pm}}$) and lever arms ($\overrightarrow{r_\pm}$) are equal so the resultant pitch torques balance; *i.e.* $\overrightarrow{F_{L_-}}\times\overrightarrow{r_-}=\overrightarrow{F_{L_+}}\times\overrightarrow{r_+}$ over the course of a whole stroke. When the moth shortens the dorsal ($-$) part of the stroke in the azimuthal plane *(ii)*, this asymmetry reduces $\overrightarrow{F_{L_-}}\times\overrightarrow{r_-}$ relative to $\overrightarrow{F_{L_+}}\times\overrightarrow{r_+}$, and creates pitch torque. See *Derivation of* ${K_{\dot{\psi}\varphi}\varphi_\Delta{I_{yy}}^{-1}}$ for a precise derivation of the model (Eq. 3.2) term representing how dorsoventral sweep asymmetry affects pitch acceleration. **C)** Pitch rotation rate causes (profile) drag on the moth's wings ($\overrightarrow{F_{W_\pm}}$), and to a lesser extent, parasite drag on the moth's body ($\overrightarrow{F_{P_\pm}}$). Together they both resist rotation. See *Derivation of* ${I_{yy}}^{-1}K_{\dot{\psi}\dot{\psi}}{\dot{\psi}_\Delta}^3/|\dot{\psi}_\Delta|$ for a precise derivation of the model (Eq. 3.2) term representing how pitch velocity damps pitch acceleration. **D)** How stroke plane deviation changes may create pitch. Concurrent work (Chen *et al.* 2017) supports that similar stroke plane deviation angle changes create pitch torque primarily by altering the COP position and net force orientation in fruit fly halfstrokes. This should complement the imbalanced drag from simultaneous wing pitch angle changes shown in **A)** and Fig. 3.6D. Stroke plane deviation angle may also alter drag, though perhaps not in a way that directly creates pitch torque; $Q\xi_\Delta$ correlated negatively with longitudinal acceleration in our data set.

Time delays between kinematics and body pitch

Equations 3.9-10 & 3.13-14 relate ζ_Δ, ξ_Δ, and φ_Δ to body kinematics from earlier instants in time, in an attempt to quantify response time lag. We shifted $\psi-\psi_0$ forward in time and compared it to ζ_Δ and ξ_Δ, and φ_Δ from the first $0.1s$ post-collision. A lag close to zero would indicate these wing kinematics passively resist rotation; a lag similar to *M. sexta*

sensorimotor response delays would indicate that the correlations come from an active response by the moth.

Previous work suggests a PD control model

The pitch acceleration control model (Eq. 3.16) tests the idea that the moths actively respond to perturbation in proportion to pitch orientation and velocity at an earlier instant in time ($t - \tau$). Time delays (τ_ψ & $\tau_{\dot{\psi}}$) are the moth's sensory + reaction time delays for response to deviations in ψ and $\dot{\psi}$, respectively. Though we call ours a PD control model, it is conceptually similar to the PI control used to model active wing kinematic responses to pitch deviation in *Drosophila* by Whitehead *et al.*, (2015).

We expected all coefficients to be positive and time delays to indicate active control

Except for Eq. 3.14-15, we expected all coefficients to be positive—where all terms represent either passive damping of pitch or active recovery by the moth. We expected $K_{\ddot{\psi}\zeta}$ to resemble COP-COM distance. Since previous studies predicted active control would dominate, we initially expected τ_ψ and $\tau_{\dot{\psi}}$ would both be greater than one wingbeat (≈33ms).

We created a simulation of $\ddot{\psi}$ based on previous work, but with variable wing hinge flexibility

Equations 3.3-5 form the basis of a simulation that tests whether a flexible connection between the wings and body during pitch perturbation can create passive stability in a theoretical moth. Equations 3.6 & 3.8 relate stroke plane inclination angle (ζ_Δ) to ψ_Δ to quantify the coefficient representing the flexibility in this connection

We created basic differential equations relating time derivatives of longitudinal position and pitch orientation and then used MATLAB's *ode45* function to solve them numerically. The equations for $\ddot{x}$ and $\ddot{\psi}$ were based on principles from our own analysis and also informed by prior work (Gao *et al.*, 2009;Hedrick and Daniel, 2006;Ristroph *et al.*, 2013;Sun *et al.*, 2007;Sun and Wang, 2007;Wu *et al.*, 2009). Our model equations are based on the following tenets: 1) First-derivative drag terms are squared; 2) Net drag torque

acts on the COP (which is stationary in the BRF); 3) Stroke plane orientation affects longitudinal acceleration; 4) Stroke plane orientation is linearly proportional to body pitch.

$$\zeta = K_{\zeta\psi}\psi \tag{3.3}$$

$$\ddot{x} = K_{\ddot{x}\zeta} g \sin(\zeta - \psi) - K_{\ddot{x}\dot{x}} \frac{\dot{x}^3}{|\dot{x}|} / m \tag{3.4}$$

$$\ddot{\psi} = \left(mgr\sin(-\zeta) - K_{\ddot{\psi}\dot{\psi}} \frac{\dot{\psi}^3}{|\dot{\psi}|} - K_{\ddot{\psi}\dot{x}} r \frac{\dot{x}^3}{|\dot{x}|} \cos(\psi) \right) / (I_{yy} + mr^2) \tag{3.5}$$

The default state of all these variables is zero; hence the exclusion of the Δ subscript in these equations. Vertical movement was not included in the model because, without a compensatory increase in vertical force production, a model moth would only lose elevation and invariably become unstable. Moths likely compensate for this predicted elevation loss by increasing flapping frequency or amplitude during perturbations (Greeter and Hedrick, 2016), but fitting such behaviour is not informative to the current study. We based our coefficient values (Table 3.S2) on estimates from a version of Eq. 3.7, but with each element multiplied by r and with an inertia of $(I + mr^2)$ as in Eq. 3.5.

Results

Overview

We analysed 8 pitch-up and 8 pitch-down perturbation trials from 11 moths. The mean downwards and upwards max post-perturbation pitch deviations were -57° and +57° [*sic.*], and the range was -78° to 106°. Average roll and yaw deviation magnitudes at the time of max pitch deviation were 9° and 13°, respectively. The mean pitch recovery time for moths that returned to less than 0.5° of their original pitch orientation within the analysed duration was $0.14s$ (6 pitch-up and 2 pitch-down trials). Qualitatively, moths in all analysed trials were in the process of recovering from the perturbation; however, some perturbations pushed moths into contact with an obstacle prior to them regaining original orientation (Table 3.S1). Videos 3.S1-2 and Fig. 3.3 & 3.S1 show typical recovery behaviour for four example trials.

Qualitatively, moths were generally able to recover from impacts with <0.5g cannonballs moving at a speed of ~$4m\,s^{-1}$. Due to targeting variation, the cannonballs collided with the moths in a variety of locations, leading to variation in perturbation magnitude and outcome. Moths that crashed (Videos 3.S3-4) often did so after suffering cannonball collisions with the wing that resulted in a mix of large pitch and roll

components, or collisions that pushed the moth into some obstacle. Moths were also likely to crash if the projectile directly struck their head. We only analysed trials in which the primary perturbation direction was pitch and the cannonball did not strike the head or wings. We terminated video analysis when the moth contacted any obstacle after the initial perturbation.

In the following section, we present our best models for pitch recovery based on our experimental observations and theoretical predictions. We used MATLAB's *stepwiselm* function with minimum-BIC (Bayesian information criterion) to eliminate insignificant terms from Eq. 3.1-2 and *fitnlm* and BIC to determine coefficients and optimal time delays for all other models. We fit data from only the first ≈6 halfstrokes post-collision, (within $0.1s$) because our interest was the immediate post-collision response (Fig. 3.8). We excluded a single outlier point, in which the moth vigorously flicked its abdomen (disrupting our pitch measurement, Fig. 3.2), from any fits that involved pitch acceleration or pitch velocity (Fig. 3.S1B).

Several wing kinematic measurements relate to pitch acceleration

After making initial modelling predictions (Eq. 3.2) based on an *a priori* set of observed and predicted relationships, (**Methods**; Fig. 3.4-5) we identified the best model relating wing and body kinematics to pitch acceleration. We first checked whether a relationship between deviations in pitch acceleration and stroke plane inclination angle were supported independent of other factors and determine that this was indeed the case (Fig. 3.6A; Eq. 3.6). Overall, we found that deviations from normal stroke plane inclination angle (ζ_Δ), stroke plane deviation angle (ξ_Δ; in concert with co-varying AOA), the sum of fore and aft wing sweep (φ_Δ), and body pitch rotation rate ($\dot{\psi}_\Delta$), were all significantly related to pitch acceleration with a coefficient of the expected sign. Variables with a Δ subscript do not represent absolute orientations, but instead quantify deviations from mean pre-collision hovering (Chapter 3 Symbols and Abbreviations; Methods). We illustrate the exact nature of wing and body kinematic measurements in Fig. 3.2. Our final model, Eq. 3.7, only includes model terms from Eq. 3.2 that reduced BIC and had significant P-values.

Figure 3.6A-B shows fit results for Eq. 3.6-7, in which I_{yy} is rotational (pitch) inertia about a Body Reference Frame (BRF) y-axis through the moth's estimated COM, m is measured moth mass in grams, g is 980.665 $cm\,s^{-2}$, Q is -1 for upstrokes and +1 for downstrokes, and K_{ab} is the coefficient relating

independent variable b to dependent variable a. See the symbols list at the end of this chapter for a description of all terms used in these two equations.

$$\ddot{\psi}_{\Delta} = {I_{yy}}^{-1} K_{\ddot{\psi}\zeta} mg\sin(-\zeta_{\Delta}) \quad (3.6),$$

$$\ddot{\psi}_{\Delta} = {I_{yy}}^{-1} (K_{\ddot{\psi}\zeta} mg\sin(-\zeta_{\Delta}) - K_{\ddot{\psi}\dot{\psi}} \frac{\dot{\psi}_{\Delta}^{\,3}}{|\dot{\psi}_{\Delta}|} - QK_{\ddot{\psi}\xi_D} \xi_{\Delta} \cos(\zeta_{\Delta}) + K_{\ddot{\psi}\varphi} \varphi_{\Delta}) \quad (3.7).$$

Figure 3.6: Correlation of pitch-related kinematic variables

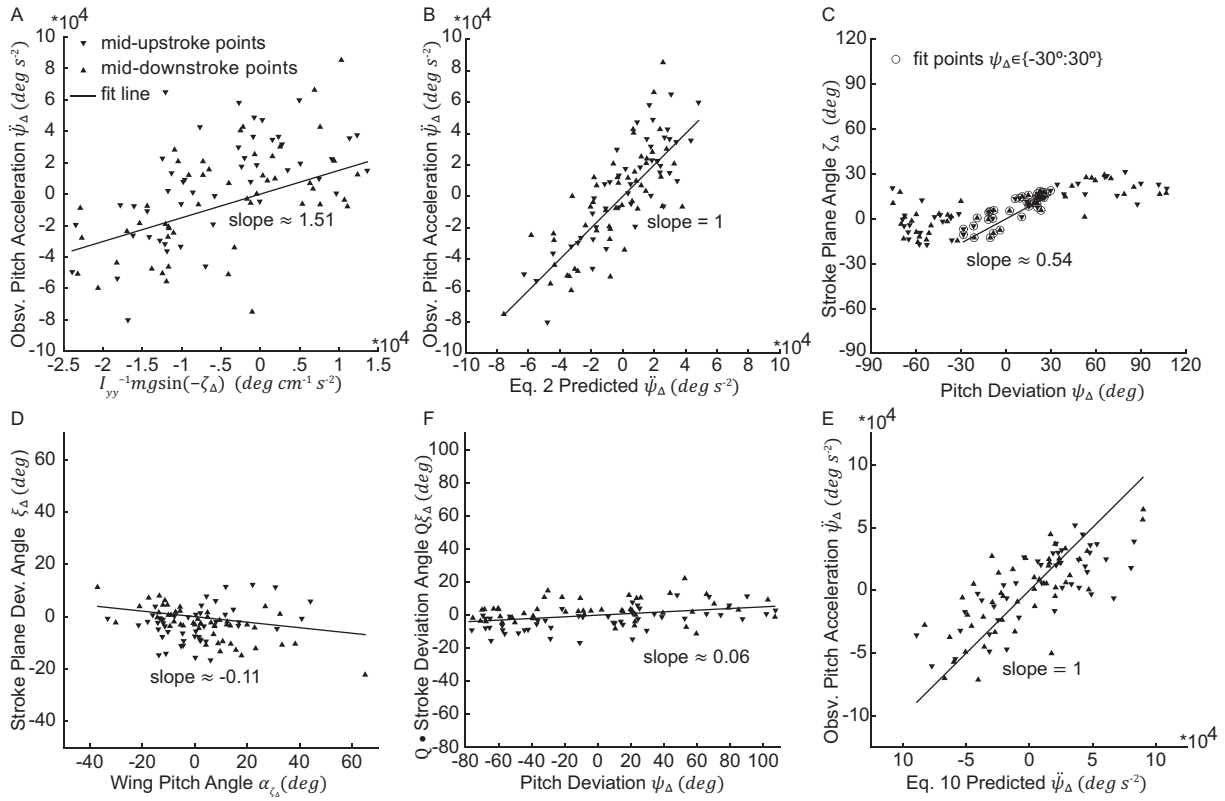

Correlation of various kinematic variables. Here, mid-upstrokes are upwards triangles, and mid-downstrokes by downwards triangles, data are from the first 0.1s post-perturbation. Fit lines either represent the slope of the only coefficient, or, when there are multiple coefficients, a line with a slope of one. Panels C-D include 48 downstrokes and 50 upstrokes, while A-B & F exclude an outlier downstroke. Table 3.3 contains the p-values, ${r^2}_a$, and coefficient values for these results. **A)** The angle between the stroke plane and body, *i.e.* "stroke plane angle" ζ_{Δ}, is closely related to pitch acceleration $\ddot{\psi}_{\Delta}$. **B)** Our full model for $\ddot{\psi}_{\Delta}$ includes stroke plane angle ζ_{Δ}, stroke plane deviation angle ξ_{Δ}, pitch rate $\dot{\psi}_{\Delta}$, and dorsoventral sweep asymmetry (φ_{Δ}). **C)** Changes in stroke plane angle track changes in body pitch; the slope of the relationship is ≈½, and it attenuates outside ±30°. **D)** Wing pitch relative to the stroke plane $\alpha_{\zeta_{\Delta}}$, and stroke plane deviation ξ_{Δ} are significantly correlated, but ξ_{Δ} is more strongly correlated with $\ddot{\psi}_{\Delta}$ in our complete model (Eq. 3.7). **E)** Stroke plane deviation ξ_{Δ} correlates significantly with pitch deviation as expected if it were effected passively by pitch rotation (Fig. 3.7; Fig. 3.S2). **F)** The best-BIC proportional-derivative $\ddot{\psi}_{\Delta}$ control model fit to time-delayed body pitch and pitch rate ($\psi_{\Delta}(t - \tau_{\ddot{\psi}\psi})$ & $\dot{\psi}_{\Delta}(t - \tau_{\ddot{\psi}\dot{\psi}})$) shows an low-latency response (≈6.7ms for $\dot{\psi}_{\Delta}$ and ≈23.3ms for ψ_{Δ}) best characterizes their correlation with pitch acceleration $\ddot{\psi}_{\Delta}$.

Table 3.1 shows the fit results of Eq. 3.6, and Table 3.2 shows the relative importance of these different terms to the modelled pitch acceleration.

Table 3.1: Eq. 3.6 fit results

Fit of Eq. 3.6			$r^2{}_a$ = 0.24
Coef.	Estimate	Units	p
$K_{\ddot{\psi}\zeta}$	1.51	cm	2.24E-7
Fit of Eq. 7			$r^2{}_a$ = 0.61
Coef.	Estimate	Units	p
$K_{\ddot{\psi}\zeta}$	1.17	cm	9.97E-7
$K_{\ddot{\psi}\dot{\psi}}$	8.37E-1	$g\ cm^2$	1.11E-7
$K_{\ddot{\psi}\xi}$	3.30E3	$g\ cm^2\ s^{-2}$	1.23E-6
$K_{\ddot{\psi}\varphi}$	2.25E3	$g\ cm^2\ s^{-2}$	6.84E-5

Table 3.2: Relative contribution of wing kinematics to pitch

Terms from Eq. 3.7	#	Interpretation	Mean of Abs. Value $deg\ s^{-2}$	Median of Abs. Value $deg\ s^{-2}$	Median for Pitch-Up $deg\ s^{-2}$	Median for Pitch-Down $deg\ s^{-2}$	Mean % relative to ∑ of Term #s 1-4	Median % relative to ∑ of Term #s 1-4	Median % relative to ∑ of Term #s 1-4 Pitch-Up	Median % relative to ∑ of Term #s 1-4 Pitch-Down
$I_{yy}{}^{-1}K_{\ddot{\psi}\zeta}mg\sin(\zeta_\Delta)$	1	stroke plane resists rotation	1.06E4	1.08E4	-2.46E2	3.22E1	29.3%	40.7%	90.9%	17.0%
$I_{yy}{}^{-1}K_{\ddot{\psi}\dot{\psi}}\dot{\psi}_\Delta{}^3/\lvert\dot{\psi}_\Delta\rvert$	2	rotational drag	7.45E3	2.44E3	-6.17E-1	4.28E0	20.6%	9.17%	<1%	2.25%
$I_{yy}{}^{-1}K_{\ddot{\psi}\xi_D}\xi_\Delta\cos(\zeta_\Delta)$	3	angle of attack	9.99E3	6.27E3	-6.98E1	4.89E1	27.7%	23.6%	25.8%	25.7%
$I_{yy}{}^{-1}K_{\ddot{\psi}\varphi}\varphi_\Delta$	4	sweep asymmetry	8.09E3	7.07E3	4.57E1*	1.05E2	22.4%	26.6%	-16.9%	55.1%
∑ of Term #s 1-4	-	predicted pitch acceleration	3.61E4	2.66E4	-1.55E-4	1.09E4	100%	100%	100%	100%
$\ddot{\psi}_\Delta$	-	observed pitch acceleration	2.64E4	2.25E4	-2.27E4	2.07E4	73.2%	84.6%	146%	190%

*there is no change in sign of $K_{\ddot{\psi}\varphi}$ for upstrokes *vs.* downstrokes, which does not match *a priori* theoretical predictions.

Stroke plane inclination angle ζ correlates with pitch and pitch acceleration

During flight, moths flap their wings back and forth along a curve (Fig. 3.2B), whose endpoints form the stroke plane. During perturbation recovery, BRF stroke plane inclination angle ζ (Fig. 3.2B), deviates from its value during hover in proportion to ψ_Δ (Fig. 3.2B & 3.4B), the moth body's deviation from its normal pitch orientation (Table 3.3, Eq. 3.8). After the moth is pitched by the cannonball, its wing pairs continue flapping closer to their original trajectory in the global reference frame (GRF) than would be expected if the wings were rigidly connected to the body (Fig. 3.3, 3.4B, 3.6C, 3.S1). The direction of stroke plane deviation during perturbations (the sign of $K_{\ddot{\psi}\zeta}$ and $K_{\zeta\psi}$) is as expected from passive inertia- and drag-based resistance to pitch perturbation (Fig 3.7E). The response is linearly proportional over a pitch range of -30° to 30°, beyond which it saturates (Fig. 3.6C). The best-fit time delay between deviations in stroke plane inclination angle and pitch orientation is <0.05 wingbeats, (Table 3.3, Eq. 3.9-5). We hypothesized that

deviation in ζ creates torque on the COP-COM vector, (Fig. 3.4B) and thus used $I_{yy}{}^{-1}K_{\ddot{\psi}\zeta}mg\sin(-\zeta_{\Delta})$ to represent how it creates pitch acceleration in Eq. 3.6-7.

Stroke plane deviation angle ξ represents mixed angle of attack and COP effects, and correlates with both pitch and pitch acceleration

During flapping, moths rotate their wings about the root to tip axis to alter the angle at which those wings interact with the air. This angle is termed the "effective angle of attack" (AOA). We expected AOA deviations would affect drag at the COP above the COM, creating pitch torque (Fig 3.5A; Chen *et al.*, 2017). Yet, in our final pitch acceleration model, only "stroke plane deviation angle" ξ_{Δ} (Fig. 3.2B) remains and not AOA. The inclusion of a $Q\xi_{\Delta}$ term in our pitch acceleration model removes the statistical significance of other terms related to AOA, including wing pitch angle relative to the stroke plane (Fig. 3.2C, $\alpha_{\zeta_{\Delta}}$). Thus, while measured ξ_{Δ} is significantly negatively proportional to $\alpha_{\zeta_{\Delta}}$ (Table 3.3, Eq. 3.11; Fig. 3.6D), it contains additional model-relevant information. Since stroke plane deviation angle changes correlate negatively with wing pitch changes of the wings during perturbation recovery (Fig. 3.6D), and with net COP location of a given halfstroke (Fig 3.5D; Elzinga *et al.* 2014; Chen *et al.*, 2017), $K_{\ddot{\psi}\xi_{D}}$ is positive. This agrees with the hypothesis that stroke plane deviation and AOA changes combine to create pitch torques that oppose rotation.

Like stroke plane angle ζ_{Δ}, stroke plane deviation angle ξ_{Δ} correlates with pitch orientation as one would expect were it a passive response (Table 3.3, Eqns. 3.8,3.12; Fig. 3.6E). Pitch-up rotations that passively alter AOA because of rotational drag and gyroscopic/inertial effects should lead to negative upstroke ξ_{Δ} and positive downstroke ξ_{Δ}; with an opposite sign association for ξ_{Δ} and halfstroke direction during pitch-down rotations (Fig. 3.7A-D). Model results agree (Table 3.3, Eq. 3.12), and the time delay is brief (Table 3.3, Eq. 3.13; Fig. 3.S2).

Fore/Aft imbalance in wing sweep correlates with pitch acceleration

Body pitch acceleration $\ddot{\psi}$ also correlates with changes in the sum of fore and aft wing sweep φ_{Δ}, *i.e.* "dorsoventral sweep asymmetry." This variable (φ_{Δ}) measures how far forward or backward a moth extends its wings during a given halfstroke (Fig. 3.2B). Thus, φ_{Δ} attempts to estimate how much lift-based

pitch torque the wings produce in front of or behind the moth's COM (Fig. 3.5B). In the final model, (Table 3.3, Eq. 3.14), abbreviated upstroke sweep correlates with pitch-up acceleration, and abbreviated downstroke sweep correlates with pitch-down acceleration. This pattern agrees with the lift-based dorsoventral sweep asymmetry observed in actively pitching fruit flies (Whitehead *et al.*, 2015) and hawkmoths (Wang *et al.*, 2008). *M. sexta* shows decreases to sweep amplitude, however, that are more pronounced in the rearward/dorsal/aft half of each halfstroke (Fig. 3.S3). This is consistent with a larger role for φ_Δ in pitch-down than pitch-up perturbations (Table 3.2, Term 4). It could be explained by greater lift production in the forwards portion of strokes, or by vertical wing movement behind the COM near the upstroke-to-downstroke transition point.

Table 3.3: Delay analysis shows passive wing kinematics

Eq.	Eq.	Filter Frequency (Hz)	Coef.	Coef. Estimate*	p	Delay Coef.	Delay Coef. Estimate (30Hz wingbeats)	$r^2{}_a$
3.8	$\zeta_\Delta = K_{\zeta\psi}\psi_\Delta$ $\psi_\Delta \in \{-30°:30°\}$	25	$K_{\zeta\psi}$	5.39E-1	6.42E-12	-	-	0.59
3.9	$\zeta_\Delta = K_{\zeta\psi_\tau}\psi_{\Delta 0}(t-\tau_{\zeta\psi})$ $\psi_\Delta \in \{-30°:30°\}$	35	$K_{\zeta\psi}$	5.47E-1	1.97E-10	$\tau_{\zeta\psi}$	<0.05	0.50
3.10	$\zeta_\Delta = K_{\zeta\psi_\tau}\psi_{\Delta 0}(t-\tau_{\zeta\psi})$	35	$K_{\zeta\psi_\tau}$	1.72E-1	1.69E-11	$\tau_{\zeta\psi}$	<0.05	0.19
3.11	$\xi_\Delta = -K_{\xi\alpha_\zeta}\alpha_{\zeta_\Delta}$	25	$K_{\xi\alpha_\zeta}$	1.06E-1	1.28E-2	-	-	-0.11
3.12	$Q\xi_\Delta = K_{\xi\psi}\psi_\Delta$	25	$K_{\xi\psi}$	5.02E-2	3.06E-4	-	-	0.13
3.13	$Q\xi_\Delta = K_{\xi\psi_\tau}\psi_{\Delta 0}(t-\tau_{\xi\psi})$	35	$K_{\xi\psi_\tau}$	5.65E-2	6.24E-5	$\tau_{\xi\psi}$	0.25	0.15
3.14	$\varphi_\Delta = K_{\varphi\psi_\tau}\psi_{\Delta 0}(t-\tau_{\varphi\psi})$	35	$K_{\varphi\psi_\tau}$	-5.96E-2+ -4.78E-1+	8.90E-5 7.97E-4	$\tau_{\varphi\psi}$	<0.05 4.6	-0.09 -.142
3.15	$Q\varphi_\Delta = -K_{\varphi\psi}\dot{\psi}\cos(\zeta-\psi_{GRF})$ $\psi_\Delta \in \{-30°:30°\}$	25	$K_{\varphi\psi}$	-2.00E-3+	1.99E-1**	-	-	0.19+

Equations are structured such that the expected sign of the coefficient, if it comes from passive effects, is positive. All coefficients are unitless, except $K_{\varphi\psi}$, which has units of s^{-1}.

+*The negative sign of these coefficients indicates a non-passive effect.*

**Nota bene: *this p-value is insignificant.*

Sensory inputs also relate to pitch acceleration

Like other insects, moths use sensorimotor control systems to correct perturbations (Dickerson *et al.*, 2014;Sane *et al.*, 2007). We attempted to identify the sensory inputs upon which moths base the active portion of their pitch-righting response by correlating time-delayed deviation in the zeroth and first time derivatives of pitch orientation (ψ_Δ and $\dot{\psi}_\Delta$) to an output for pitch control: deviation from normal pitch acceleration ($\ddot{\psi}_\Delta$) at midstrokes. We chose to assume this Proportional-Derivative (PD) control model because hawkmoths have sensory organs that readily detect such information, and previous research on

pitch correction predicts PD-like control (Whitehead *et al.*, 2015;Windsor *et al.*, 2013) . The best BIC time delay model shows a time delay of ≈0.023s for changes to pitch, ≈0.0067s for changes to pitch velocity, (Fig. 3.6F; Table 3.4; Eq. 3.16).

$$\ddot{\psi} = {I_{yy}}^{-1}\left(-K_{\ddot{\psi}\psi_\tau}\psi_{\Delta 0}\left(t-\tau_{\ddot{\psi}\psi}\right) - K_{\ddot{\psi}\dot{\psi}_\tau}\dot{\psi}\left(t-\tau_{\ddot{\psi}\dot{\psi}}\right)\right) \quad (11).$$

Table 3.4: Fit results for Eq. 3.11

Eq. 3.11: $\ddot{\psi} = {I_{yy}}^{-1}\left(-K_{\ddot{\psi}\psi_\tau}\psi_{\Delta 0}\left(t-\tau_\psi\right) - K_{\ddot{\psi}\dot{\psi}_\tau}\dot{\psi}\left(t-\tau_{\dot{\psi}}\right)\right)$						${r^2}_a$ = 0.55
Coef.	Estimate	Units	Coef. p-value	Delay Coef.	Delay Coef. Estimate	Units
$K_{\ddot{\psi}\psi_\tau}$	3.11E2	$g\ cm\ s^{-2}$	1.27E-6	τ_ψ	0.7	30 Hz wingbeats
$K_{\ddot{\psi}\dot{\psi}_\tau}$	2.50E1	$g\ cm\ s^{-1}$	1.80E-15	$\tau_{\dot{\psi}}$	0.2	

Modelling pitch perturbation responses

After fitting our model, we created a simple computational implementation of pitch perturbation response based on the theoretically passive contributors to pitch stability: $K_{\zeta\psi}$, $K_{\ddot{\psi}\dot{\psi}}$ and $K_{\ddot{\psi}\dot{x}}$. The model (see **Methods**) is based on drag terms from the literature as well as the passive relationship we measured between ζ_Δ and ψ_Δ (but does not include that between ξ_Δ and ψ_Δ). We analysed the response of the model to two basic levels of simultaneous perturbation to ψ_Δ and $\dot{\psi}_\Delta$, based on: 1) The average cannonball perturbation from this study, and 2) The largest recorded deviations in pre-perturbation hover. This fully passive moth model produces growing oscillations in pitch when the stroke plane is rigidly attached to the body (*i.e.* $K_{\zeta\psi} = 0$), but rapidly decaying oscillations in response to even a small degree of flexibility in body-to-stroke-plane coupling ($K_{\zeta\psi}$ > 0.1). Recovery is approached within the sample window (0.25-0.5*s* post-perturbation) when $K_{\zeta\psi}$ nears the value estimated in our study, (≈0.5, Table 3.3; Fig. 3.S4).

Discussion

Summary

M. sexta recover from large, sudden perturbations to pitch. The response latencies and modelled physical stability mechanisms indicate the response is initially passive with later active components. In the experiments conducted here, the passive effects are more important. Passive responses arise because 1) the wings are partially isolated from body rotations, 2) the wings resist rotation because of both drag and

gyroscopic/inertial effects, and 3) the COP lies above the COM (Fig. 3.4-5 & 3.7). A computational model shows that even a small degree of isolation or flexibility between rotation of the insect's body and its stroke plane greatly enhances stability in pitch.

Our discussion also covers several related ideas. First, stroke plane resistance to rotation and COP-COM arrangement likely also damp slight deviations during hover and aerodynamic as well as mechanical perturbations. Second, abdominal and wing base flexibility are plausible reasons for the different pitch-up and pitch-down perturbation responses. Third and finally, it is useful to consider insect wings as vibrational gyroscopes that also experience high drag. Since drag and inertia work together to create the stability mechanisms we observed, these same mechanisms could passively stabilize pitch in flight for animals across a wide range of size and speed.

We found two unexpected, and one expected, passive sources of pitch stability

In the immediate aftermath of a perturbation, drag and inertial resistance of the wings to rotation alter stroke plane angle; this reorients the net lift vector in the BRF, which in turn acts on the COP-COM lever arm to restore pitch orientation (Fig. 3.4B & 3.S4), passively stabilizing the moth. In a second previously-undescribed stability mechanism, gyroscopic/inertial effects and rotational drag on the wings alter stroke plane deviation angle. Changes to stroke plane deviation angle are complemented by wing pitch angle changes, and together they alter COP and create differential drag for upstrokes and downstrokes, further counteracting rotation. Independent work shows both gyroscopic/inertial effects, and drag to a lesser extent, modify wing position in pitch rotations (Eberle *et al.*, 2015;Jankauski and Shen, 2016). Third, rotational velocity and the associated drag on the body and wings is an expected source of passive pitch damping.

The significance of stroke plane inclination ζ_{Δ} and stroke plane deviation ξ_{Δ} in the model despite the presence of a pitch velocity term ($\dot{\psi}_{\Delta}$) indicates they are not simply statistical proxies for body and wing drag. The tight correlation of ζ_{Δ} with ψ_{Δ}, the (in hindsight) intuitive theoretical explanation for these results, and small estimated time delays (see *PD control…* below) all indicate that these wing angle changes are mostly passive in nature, and not due to the moth first sensing a change in pitch state and then producing a response that changes stroke plane inclination.

These passive sources of pitch stability are important to flight stability: Our computational model indicates that resistance of the stroke plane to rotation drastically reduces the degree of active response required for pitch perturbation recovery. They are also consistent with prior research that indicates insects sense wing kinematics, and that some aspects of wing kinematics may be passively mediated. For example, *M. sexta* sense wing rotations that would change ζ and ξ, and respond to these BRF wing kinematic changes even more strongly than they respond to visually simulated GRF pitch rotations (Dickerson *et al.*, 2014;Hinson and Morgansen, 2015;Hinterwirth and Daniel, 2010). Prior studies also show wing pitch angle may be passively maintained in insect flight (Beatus and Cohen 2015; Bergou *et al.*, 2007;Bergou *et al.*, 2010;Ishihara *et al.*, 2009a;Ishihara *et al.*, 2009b;Norberg, 1972;Whitney and Wood, 2010).

Figure 3.7: Inertia and drag work together to create passive countertorque in flapping wings

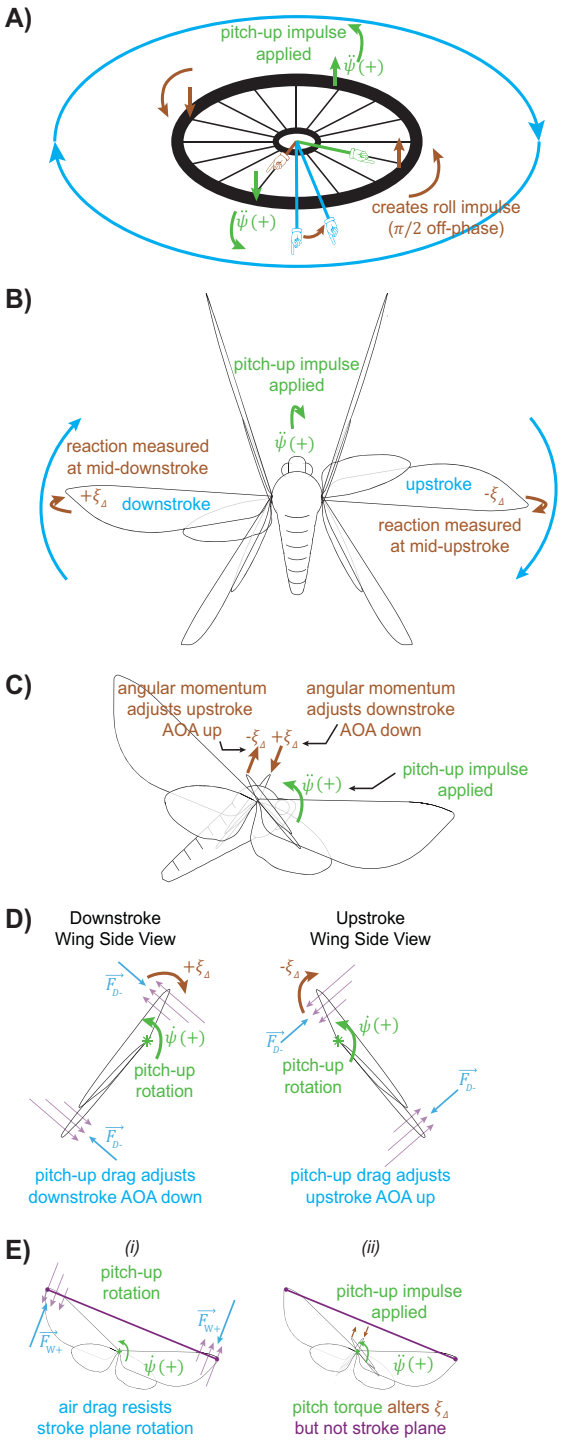

Inertia and drag work together to create passive pitch countertorque in flapping wings. A) When a pitch-up impulse is applied to this right-spinning wheel, the new angular momentum moves the spin axis (cyan) towards the axis of the applied impulse and the wheel rolls left. **B)** Flapping moth wings—mechanically-isolated, rapidly vibrating biological structures—experience similar effects. **B)** shows both wings at end-downstroke and end-upstroke, the left wing at mid-downstroke, and the right wing at mid-upstroke. A pitch-up impulse applied to the mid-stroke wings produces gyroscopic inertial effects that push the left wing down and the right wing up. This helps explain why, in the downstrokes of pitch-up-perturbed moths, we measure a decreased angle of attack (AOA), and an increased stroke plane deviation angle (ξ). **C)** This side view also showing how gyroscopic effects change AOA and stroke plane deviation angle; the moth's wings flap along a curved path and changes to that path and/or to the angle of the wing alter AOA and COP location (Fig. 3.5D). **D)** Drag adjusts AOA in the same direction as gyroscopic effects. As the moth wing rotates with pitch, it experiences drag that increases upstroke AOA and decreases downstroke AOA. Thus, inertial **(A-C)** and drag **(D)** effects influence AOA in similar ways during perturbation. **E)** Drag and inertia work together to keep stroke plane inclination angle close to its original orientation. In ***(i)*** drag on the wings during a pitch-up rotation creates a pitch-down torque. In ***(ii)*** wing inertia resists rotation when torque is applied. The resulting deviation in the stroke plane inclination angle (and lift vector) relative to the body reference frame creates a restoring torque (Fig. 3.4B). It is interesting to conjecture that inertial resistance of the wings to flipping may influence effect **D)**, since wings oscillate rapidly in wing pitch during flapping flight, (and torsional/flipping inertial resistance likely influences roll dynamics; 5.2C-D). Note that it is also possible wing deviation angle changes interact with the angular momentum of flipping wings to (passively) create a pitch-restoring dorsoventral sweep asymmetry response like the one observed in this data set, but this figure does not depict such an effect.

The positive sign of the fit coefficient $K_{\ddot{\psi}\xi_D}$ is consistent with drag from pitch rotational velocity and inertial effects passively modifying ξ and AOA (Fig. 3.7). When wings sweep along a curved path, wingtip deviation strongly influences the angle at which they encounter the air (Fig. 3.5A), and also the location of

the net of forces for the halfstroke (Fig. 3.5D). We tested two different wing kinematic approximations of these effects, which co-varied in the data: α_{ζ_Δ} and ξ_Δ. We used ξ_Δ in the final model because using only this wing kinematic was better according to BIC. It is also based only on tip position, wing base, and body orientation, which are straightforward reference points to discern in a number of different experimental situations, which we hope will facilitate broad comparisons among different experiments and organisms.

Not just for collisions; generality of stroke plane (and AOA/stroke plane deviation) damping

Although we perturbed the moth artificially, our computational model demonstrates that the underlying decoupling between body orientation and stroke plane will also effectively stabilize smaller mechanical perturbations (Fig. 3.S4) on the time scale of halfstrokes. If our conclusions are valid, in an aerodynamically (rather than mechanically) perturbed moth, the stroke plane itself will still resist rotation because of drag and inertia, bringing the body back toward its original orientation, aside from pendular oscillations due to its incomplete resistance to rotation.

Furthermore, since *M. sexta* wing movement is dominated by inertia (Jankauski and Shen, 2016), as is turning flight in general (Fry *et al.*, 2003), aerodynamic perturbation of the wings across size scales likely also results in $\pi/2$ off-phase Coriolis reactions similar to the pitch-restorative stroke plane deviation angle changes we witnessed (this chapter) and AOA changes we predict (Fig. 5.3). The amplitude and subsidence rate of the gyroscopic reactions will be determined by the viscoelasticity/viscosity of the involved body joints and surrounding air (drag effects). Since wing hinges are extremely elastic (Weis-Fogh, 1960), since wing movement is dominated by inertia (Combes *et al.* 2003; Eberle *et al.*, 2015; Jankauski and Shen, 2016), and since (as this study showed) wing movement is flexible relative to the moth's body frame, this subsidence rate is likely slow. Thus, elasticity and flexibility may allow the passive changes to wing kinematics in impulse perturbations to manifest as equal and opposite changes to wing kinematics during subsequent halfstrokes that also help restore orientation. This suggests evolution, and future engineers of micro-air vehicles (MAVs), can tune these features for increased stability (see *Passive* vs. *active stability…air vehicle design*).

As discussed in the final section of this discussion, these inertial damping effects will scale with size and speed, as will the changes to wing kinematics and stroke plane angle that arise from pitch rotational velocity (Fig. 3.7).

Changes to sweep help correct pitch, and may be mostly active

Dorsoventral sweep asymmetry φ_Δ also correlated with pitch acceleration in a way that is similar to *D. melanogaster* (Whitehead *et al.*, 2015) and another hawkmoth species (Wang et. al. 2008). While φ_Δ had a small best-fit time delay, models with longer time delays were within the same statistical range (Table 3.3, Eq. 3.14; Fig. 3.S2). Indeed, coefficient signs are inconsistent with a passive response to either pitch or pitch velocity. If drag created fore-aft wing sweep deviations, (φ_Δ), pitch-up/down rotations would curtail the second half of up/downstroke, but the coefficient is significantly negative (Table 3.3, Eq. 3.14), especially for pitch-down perturbations (not shown). If stroke plane changes bring about φ_Δ (since the BRF stroke plane becomes more/less horizontal over the course of pitch-down/up rotations) we would expect $Q\varphi_\Delta = -K_{\varphi\psi}\dot{\psi}_\Delta \cos(\zeta - \psi)$, at least when $\psi_\Delta \in \{-30°{:}\,30°\}$, but, the opposite is true (Table 3.3, Eq. 3.15). Nevertheless, one final explanation exists that could passively create the observed sweep asymmetries. Since the passively induced stroke plane deviation angle changes are essentially roll perturbations to the wings themselves, these could interact with the gyroscopic nature of wing flipping/pitching during strokes to create the observed sweep asymmetries.

PD control model results further support that M. sexta pitch response is passive

Our best-fit time-delay active control model predicts that *M. sexta* pitch stability is a combination of passive and active responses. Previous research shows that a PD controller would be sufficient for active-only stability in *M. sexta* given sufficiently small response delays (Ristroph *et al.*, 2013;Whitehead *et al.*, 2015). Nevertheless, moths might only have the opportunity to alter wing kinematics at halfstrokes (Fernandez *et al.*, 2012;Springthorpe *et al.*, 2012) due to the intrinsically discrete nature of flight muscle activations. In fact, tethered moths respond to visual/tactile flower movements and visually simulated pitch with a delay of ≈40-80ms (Dickerson *et al.*, 2014;Hinterwirth and Daniel, 2010;Sponberg *et al.*, 2015;Windsor *et al.*, 2013). Thus, prior evidence indicates moths may not be able to detect and then

respond to state changes within 0.2-0.7 wingbeats (7-23ms). Indeed, our PD-controller time delays (Table 3.4, Eq. 3.16) indicate that the *M. sexta* pitch perturbation response includes passive components. The post-perturbation steady-state reached in our computational model suggests that the hawkmoth's passive response greatly reduces the necessary active response magnitude. Thus, it is not surprising that a combination of passive and active responses results in a control system for *M. sexta* that can stabilize pitch perturbation of >100° as we recorded.

COP-COM arrangement and wing resistance to movement creates pendulum-like pitch stability

The wing kinematic changes we measured can produce restoring torque only because the moth's centre of aerodynamic forces (COP) lies well above its COM (Ellington, 1984). This arrangement results in a pendulum-like stability effect when body pitch deviates from equilibrium (the pendulum swings) and stroke plane does not deviate to the same extent (the pivot remains semi-fixed) (Ristroph et. al, 2013). The expected perturbation response of our computational model further supports these hypotheses. If, as in our computational model, we assume a centre of rotation (COR) located near the COP, passive restorative pitch acceleration would be inversely proportional to stroke plane deviation once r (COP-COM distance) becomes very large (Fig. 3.S5). However, the r estimated from Eq. 3.5 lies within the theoretical range where r is still directly proportional to restorative pitch acceleration.

The arrangement of COP above COM also magnifies the passive restoring pitch torque that changes to AOA and stroke plane deviation angle generate (Fig. 3.5A & 3.5D).

Abdominal or wing joint flexibility differences may explain pitch-up and pitch-down perturbation differences

Pitch-down perturbations produce a smaller passive stroke plane inclination response (ζ_Δ) and a greater (potentially active) sweep response (φ_Δ) than pitch-up ones (Table 3.2). This would be explained if 1) the wing joint or nearby wing portion is more pliable in response to pitch-up than pitch-down torsion, and/or 2) the decoupling of the stroke plane from the rotating body arises in part from abdominal bending, and the abdomen is more readily flexed than extended. The abdomen is relatively massive, so when a cannonball pitches the moth up by hitting its thorax, inertia flexes it forward relative to the COP, creating

pitch-down torque (Fig. 3.4B; Noda *et al.*, 2013; Noda *et al.* 2014), within a time range that is relevant to our perturbations (Dyhr *et al.*, 2013).

Passive vs. *active stability in flapping flight and air vehicle design*

Prior computational and physical flight models predict two basic unstable modes for insect flight, for anything but the smallest perturbation range (Humbert and Faruque, 2011;Maeda *et al.*, 2010;Noda *et al.*, 2013;Ristroph *et al.*, 2013;Taha *et al.*, 2015): one in pitch coupled with longitudinal motion (Kim *et al.*, 2014;Kim *et al.*, 2015;Sun *et al.*, 2007;Windsor *et al.*, 2013;Zhang and Sun, 2010); and one in roll coupled with sideslip (Liang and Sun, 2013;Windsor *et al.*, 2013;Zhang and Sun, 2010;Zhang *et al.*, 2012). Our recent observational study of sideslip (Greeter and Hedrick, 2016) and a recent physical model (Kim *et al.*, 2016) provide evidence that roll coupled with sideslip is in fact heavily damped in *M. sexta*. Here, our updated empirical model of pitch provides evidence that pitch coupled with longitudinal motion is also more stable than widely believed. Since yaw (Hedrick *et al.*, 2009;Hedrick and Robinson, 2010), roll (Greeter and Hedrick, 2016;Kim *et al.*, 2015), and pitch (this study) are all heavily damped in *M. sexta*, active control appears to supplement existing passive stability and may not be strictly necessary in flapping flight.

We can apply these insights to the design of small autonomous flying vehicles, whose biomimetic design might one day react to pitch much like *M. sexta*. Micro-air vehicles (MAVs) are at the cutting edge of flight design research, and effective stability solutions remain a design hurdle of intense focus (Karásek *et al.*, 2014;Koopmans *et al.*, 2015;Ma *et al.*, 2013;Orlowski and Girard, 2012;Pratt and Qin, 2016). To replicate *M. sexta* pitch stability, air vehicles might include an elastic, flexible “gimbal” at the wing base that allows the airframe to pitch independently, or consider a flexible or jointed airframe whose COM changes passively in reaction to physical perturbation. Instead of designing MAV wings that minimize weight or maximize force production (Bluman and Kang, 2016; Stewart *et al.*, 2016), new designs should consider sturdier wings with greater inertia to enhance stability, and with an elastic base that allows for independent stroke plane rotation, even as it reduces energy requirements (Alexander and Bennet-Clark, 1977;Andersen and Weis-Fogh, 1964).

In this way, the concepts we described here could affect every level of optimal MAV design, from body configuration (with the consideration of COP-COM distance and the insertion of flexible joints), body

material design (body and wing base flexibility), and wing size and shape (inertia- and drag-based stability effects that depend on Reynolds number).

These effects likely scale across the large size range of flying animals

Our key finding is that inertia and drag work together to create passive stability in flapping flight. The stroke plane inclination response (ζ_{Δ}), the stroke plane deviation response (ξ_{Δ}), and the drag on and inertia of the moth's body itself, are all examples of inertia and drag working together, and in the same direction, to passively stabilize pitch orientation.

Creatures that fly operate at a range of Reynolds numbers. In *M. sexta*, inertial forces dominate wing bending mechanics (Combes and Daniel, 2003; Jankauski and Shen, 2016). For smaller fliers, drag is more important. Based on our results, we predict pendulum-like passive pitch stability (and possibly passive stability in other degrees of freedom as well), to be important across the extremes of this grand biological scale, producing similar stability mechanics from fundamentally different mechanisms (drag *vs.* inertia).

See Chapter 5, ***Advancement 6*** *for further discussion.*

Chapter 3 Symbols and Abbreviations

Box 3.1: Abbreviations

AOA	effective Angle Of Attack: represents the angle at which the wing encounters the air	COP	Centre Of Pressure: net sum of force production by the wings, time-averaged over the course of a stroke cycle
BIC	Bayesian Information Criterion, (or Schwartz criterion), an criterion for model selection among a finite set of models that is based on the likelihood function.	FCT	Flapping Counter Torque: idea that rotations change the velocity of wings flapping in that rotational plane, damping the rotation. First shown for yaw.
BRF	Body Reference Frame: reference frame from the perspective of the moth's COM, in which the moth's anatomical landmarks and canonical hover orientation determine x, y, and z.	GRF	Global Reference Frame: based on the camera calibration (world view frame)
COM	Centre Of Mass: point where the sum of the product of individual units of mass and their distance away from that point equal zero.	PD, PI	Proportional-Derivative or Proportional-Integrative controller (as in control theory). Note our "PD" controller is similar to the "PI" controller of Whitehead *et al.*, (2015)

Box 3.2: Annotations, Subscripts, Constants, and Mathematical Symbols

$\times$; $\lvert\ \rvert$; $\sum$; $\in$; $\bullet$; $/\!/$; Δ; $\approx$; $\propto$; $\bar{\propto}$; $\stackrel{\text{def}}{=}$	"by" or cross-product; absolute value or magnitude of; sum of; constrained to within; dot product; parallel; change in; about equal to or approximately congruent to; proportional to; approximately proportional to; equal to by definition
$\vec{\ }$; $\overleftrightarrow{\ }$; $\bar{\ }$	accents respectively indicate the attendant variable is a vector; line; and plane
$\dot{\ }$; $\ddot{\ }$	accent indicates the first and second time derivative of the attendant variable
$_{ab}$	a subscript which indicates the antecedent is a coefficient relating b to a
$_{D}$	a subscript which indicates the mechanism is related to drag
g	gravitational acceleration (980.665 $cm\ s^{-2}$)
I_{yy}	rotational (pitch) inertia about a Body Reference Frame (BRF) y-axis through the moth's estimated COM
$_{L}$	a subscript which indicates the mechanism is related to lift
m	moth mass measured at time of the experiment
Q	multiplier that is -1 for upstrokes and +1 for downstrokes
r; $\vec{r}$	distance/vector between the moth's centre of mass and centre of pressure, ***e.g.*** in the computational model (Eq. 3.3-5), or Fig. 3.2-3
$r^2{}_a$	adjusted r^2; calculated for linear models
$_{\Delta}$	a subscript which indicates that mid-upstroke and mid-downstroke pre-collision means for the whole data set have been subtracted (midstrokes only)
$_{\Delta 0}$	a subscript which indicates that the zero-reference point is the hand-chosen pre-collision canonical frame (with no special treatment for midstrokes)
	lack of subscript on a kinematic variable indicates that we made no attempt to mean-centre/adjust the variable

Box 3.3: Geometric Characteristics of M. sexta

$\overrightarrow{F_{D\pm}}$; $\overrightarrow{F_{L\pm}}$; $\overrightarrow{F_{P\pm}}$; $\overrightarrow{F_{W\pm}}$	drag; lift; parasite drag; profile (wing) drag; theoretical forces explained in Fig. 3.4
$\overleftrightarrow{L_1}$; $\overleftrightarrow{L_2}$; $\bar{P}$	geometric characteristics of the stroke plane as defined in Fig. 3.2 and its caption
$\vec{r}$; $\vec{r}_{\pm}$	COM-COP vectors shown in Fig. 3.2-3
$\vec{R}_1$; $\vec{R}_2$; $\vec{R}_3$; $\vec{R}_4$; $\vec{R}_5$	vectors connecting digitized moth points as defined in Fig. 3.2 and its caption

Box 3.4: Wing and Body Angles

x; $\dot{x}$; $\dot{x}_{\Delta}$	in the BRF, $+x$ is forwards for the moth; $\dot{x}$ is forward velocity; $\dot{x}_{\Delta}$ is midstroke-centred forwards velocity
y	in the BRF, $+y$ is rightwards for the moth
z; $\dot{z}$; $\dot{z}_{\Delta}$	in the BRF, $+z$ is downwards for the moth, ($/\!/$ with gravity); $\dot{z}$ is downward velocity; $\dot{z}_{\Delta}$ is midstroke-centred downward velocity
α_{ζ}; $\alpha_{\zeta_{\Delta}}$	wing pitch angle: α_{ζ} (likely affects AOA, and COP to a lesser extent) is the angle the (x,z) components of the vector connecting the hindwing tip to the forewing tip makes relative to the stroke plane; $\alpha_{\zeta_{\Delta}}$ is midstroke-centred α_{ζ}
ζ; ζ_{Δ}	stroke plane inclination angle: ζ is the angle of the stroke plane relative to the BRF horizontal plane; ζ_{Δ} is midstroke-centred ζ
φ_+; φ_-	sweep: forewing azimuthal angle relative to a BRF vertical plane through the wing base, at the end of downstroke φ_+; and upstroke φ_-
φ_{Δ}	dorsoventral sweep asymmetry $\varphi = \varphi_+ + \varphi_-$, and φ_{Δ} is midstroke-centred φ
ξ; ξ_{Δ}	stroke plane deviation angle: ξ (likely affects COP, and AOA to a lesser extent) is the angle the forewing makes at midstroke, measured perpendicular relative to the stroke plane; ξ_{Δ} is midstroke-centred ξ
ψ; ψ_{Δ}; $\psi_{\Delta 0}$	moth body pitch, $\vec{R}_4$ relative to the horizontal plane (Fig. 3.2); midstroke-centred pitch; mean-centred pitch
$\dot{\psi}$; $\dot{\psi}_{\Delta}$; $\dot{\psi}_{\Delta 0}$	1st time derivative of pitch orientation, *i.e.* "pitch velocity;" midstroke-centred pitch velocity; mean-centred pitch velocity

ϑ_+; ϑ_- elevation: forewing elevation angle relative to a BRF horizontal plane through the wing base, at the end of downstroke ϑ_+; and upstroke ϑ_-

ϑ_Δ elevation offset $\vartheta = \vartheta_+ + \vartheta_-$, and ϑ_Δ is midstroke-centred ϑ

$\ddot{\psi}$; $\ddot{\psi}_\Delta$ $\ddot{\psi}_{\Delta 0}$ 2nd time derivative of pitch orientation, *i.e.* "pitch acceleration;" midstroke-centred pitch acceleration; mean-centred pitch acceleration

Box 3.5: Coefficients and Time Delays in Order of Appearance

$K_{\ddot{\psi}\zeta}$ relates ${I_{yy}}^{-1} mg\sin(-\zeta_\Delta)$ to $\ddot{\psi}_\Delta$ in the observational pitch acceleration models (Eq. 3.6-7 & 3.2), or theoretical $(I_{yy} + mr^2)^{-1} mgr\sin(-\zeta)$ to $\ddot{\psi}$ in the computational model (Eq. 3.3-5)

$K_{\ddot{\psi}\dot{\psi}}$ relates observed $-{I_{yy}}^{-1} {\dot{\psi}_\Delta}^3/|\dot{\psi}_\Delta|$ in the observational pitch acceleration models (Eq. 3.6-7 & 3.1-2), or theoretical $-(I_{yy} + mr^2)^{-1} \frac{\dot{\psi}^3}{|\dot{\psi}|}$ to $\ddot{\psi}$ in the computational model (Eq. 3.3-5)

$K_{\ddot{\psi}\xi_D}$ relates $-{I_{yy}}^{-1} Q\xi_\Delta \cos(\zeta_\Delta)$ to $\ddot{\psi}_\Delta$ in the observational pitch acceleration models (Eq. 3.7 & 3.2)

$K_{\ddot{\psi}\varphi}$ relates φ_Δ to $\ddot{\psi}_\Delta$ in the observational pitch acceleration models (Eq. 3.2 & 3.1-2)

$K_{\zeta\psi}$ relates observed ψ_Δ to ζ_Δ (Eq. 3.8), or theoretical ψ to ζ in the computational model (Eq. 3.3-5)

$K_{\zeta\psi_\tau}$ relates time-delayed $\psi_{\Delta 0}$ to ζ_Δ in Eq. 3.9-10

$\tau_{\zeta\psi}$ time delay between $\psi_{\Delta 0}$ and ζ_Δ in Eq. 3.9-10

$K_{\xi\alpha_\zeta}$ relates -${\alpha_\zeta}_\Delta$ to ξ_Δ in Eq. 3.11

$K_{\xi\psi}$ relates ψ_Δ to $Q\xi_\Delta$ in Eq. 3.12

$K_{\xi\psi_\tau}$ relates time-delayed $\psi_{\Delta 0}$ to $Q\xi_\Delta$ in Eq. 3.13

$\tau_{\xi\psi}$ time delay between $\psi_{\Delta 0}$ and $Q\xi_\Delta$ in Eq. 3.13

$K_{\varphi\psi_\tau}$ relates time-delayed $-\psi_{\Delta 0}$ to φ in Eq. 3.14

$\tau_{\varphi\psi}$ time delay between $-\psi_{\Delta 0}$ and φ in Eq. 3.14

$K_{\varphi\dot{\psi}}$ relates $-\dot{\psi}_\Delta \cos(\zeta - \varphi)$ to $Q\varphi_\Delta$ in Eq. 3.15

$K_{\ddot{\psi}\psi_\tau}$ relates time-delayed $-\psi_{\Delta 0}$ to $\ddot{\psi}$ in the theoretical control model (Eq. 3.16)

$\tau_{\ddot{\psi}\psi}$ time delay between $-\psi_{\Delta 0}$ and $\ddot{\psi}$ in the theoretical control model (Eq. 3.16)

$K_{\ddot{\psi}\dot{\psi}_\tau}$ relates time-delayed $-\dot{\psi}_{\Delta 0}$ to $\ddot{\psi}_{\Delta 0}$ in the theoretical control model (Eq. 3.16)

$\tau_{\ddot{\psi}\dot{\psi}}$ time delay between $-\dot{\psi}_{\Delta 0}$ and $\ddot{\psi}_{\Delta 0}$ in the theoretical control model (Eq. 3.16)

$K_{\ddot{\psi}\dot{x}}$ relates observed $-{I_{yy}}^{-1} \cos(\psi_\Delta) {\dot{x}_\Delta}^3/|\dot{x}_\Delta|$ or $-{I_{yy}}^{-1} \cos(\zeta_\Delta)$ ${\dot{x}_\Delta}^3/|\dot{x}_\Delta|$ to $\ddot{\psi}_\Delta$ in the preliminary pitch acceleration models Eq. 3.1-13; or theoretical $-r(I_{yy} + mr^2)^{-1} \cos(\psi)\, \dot{x}^3/|\dot{x}|$ to $\ddot{\psi}$ in the computational model (Eq. 3.3-5)

$K_{\ddot{\psi}\dot{z}}$ relates observed $-{I_{yy}}^{-1} \sin(\psi_\Delta) {\dot{z}_\Delta}^3/|\dot{z}_\Delta|$ or $-{I_{yy}}^{-1} \sin(\zeta_\Delta)$ ${\dot{z}_\Delta}^3/|\dot{z}_\Delta|$ to $\ddot{\psi}_\Delta$ in the preliminary pitch acceleration models (Eq. 3.1-2)

$K_{\ddot{\psi}\alpha_D}$ relates $Q{\alpha_\zeta}_\Delta \cos(\zeta_\Delta)$ to $\ddot{\psi}_\Delta$ in the preliminary pitch acceleration model (Eq. 3.1)

$K_{\ddot{\psi}\alpha_L}$ relates observed ${\alpha_\zeta}_\Delta \sin(-\zeta_\Delta)$ to $\ddot{\psi}_\Delta$ in the preliminary pitch acceleration model (Eq. 3.1)

$K_{\ddot{\psi}\xi}$ relates observed $-\xi_\Delta$ to $\ddot{\psi}_\Delta$ in the preliminary pitch acceleration model (Eq. 3.1)

$K_{\ddot{\psi}\vartheta}$ relates observed $Q\vartheta_\Delta$ to $\ddot{\psi}_\Delta$ in the preliminary pitch acceleration models (Eq. 3.1-2)

$K_{\ddot{\psi}\xi_L}$ relates observed $\xi_\Delta \sin(\zeta_\Delta)$ to $\ddot{\psi}_\Delta$ in the preliminary pitch acceleration model (Eq. 3.2)

$K_{\ddot{x}\zeta}$ relates theoretical $g\sin(\zeta - \psi)$ to $\ddot{x}$ in the computational model (Eq. 3.3-5)

$K_{\ddot{x}\dot{x}}$ relates theoretical $\frac{\dot{x}^3}{|\dot{x}|}/m$ to $\ddot{x}$ in the computational model (Eq. 3.3-5)

Recognitions and Contributions

The authors would like to thank TJ Tcakik for helping hand-digitize the moth videos, Rikki Schroeder for designing the cannon modifications, and the labs of Drs. Frederik Nijhout, Thomas Daniel, and Joel Kingsolver for providing moth pupae.

Both J.S.M.G. and T.L.H. designed and performed the experiments, and contributed to data analysis. J.S.M.G. identified data trends and prepared the manuscript; at all steps, T.L.H. provided oversight, edits, and advice.

Funding

J.S.M.G. was supported by a National Defense Science and Engineering Graduate (NDSEG) Fellowship from the Department of Defense (DOD), administered by the American Society for Engineering Education (ASEE) during a portion of this research. Funding for this work also came from the National Science Foundation (NSF IOS-0920358 to T.L.H.).

Data Link

At time of writing, raw data and supplementary videos are currently housed on the Hedrick Lab Server and available upon request.

Table 3.S1 Individual Trial Details

Video ID	Video Date yyyymmdd	Frame-rate (Hz)	Amount Digitized (ms)		Ball Mass (g)	Ball GRF $(\Delta V)_{ms}$ (cm s^{-1})	≈ Impact Duration (ms)	Impact Distance from COM (cm)	Max Pitch Deviation (deg)	Initial Pitch Velocity (10^2 deg s^{-1})	Time to Recovery (ms)	Moth ID	Moth Mass (g)	Abdomen Length (cm) xx	Body Pitch Inertia About COM (g cm^2)	Wing Length (cm)		Wing Frequency	
			Pre Impact	Post Impact												L	R	Pre Impact	≤0.1s Post Impact
21.1	20100407	1200	53	122	0.20	314	2.50	1.33	88.57	42.68	-[I]	1	1.30	2.77	1.73	4.55	4.18	30.42	31.86
26	20100413	1200	211	298	0.20	427	7.50	0.66	46.27	20.28	119	1	1.10	2.68	1.36	4.07	3.95	30.76	30.90
32	20100413	1200	152	359	0.20	242	2.50	1.30	68.37	32.71	169	2	1.13	2.59	1.27	3.88	3.74	32.21	31.57
33	20100415	1200	191	342	0.10	438	0.83	0.83	19.37	17.82	200	2	0.83	2.62	0.93	4.09	3.75	28.39	30.46
40	20100618	1000	186	378	0.20	372	1.00	1.14	77.72	36.41	138	3	1.02	3.20	1.35	4.40	4.37	29.14	29.62
42	20100621	1000	96	117	0.20	246	6.00	2.32	-60.84	-28.17	-[II]	4	1.20	2.84	1.46	4.61	4.73	28.94	31.38
48	20100629	1000	212	99	0.40	264	1.00	0.80	105.77	52.52	-[III]	5	1.59	2.82	2.18	4.28	4.29	30.60	32.58
56	20100715	1000	99	288	0.10	340	1.00	2.13	-43.94	-17.10	123	6	1.31	2.82	1.49	4.34	4.36	28.50	32.75
57	20100715	1000	119	278	0.10	534	3.00	0.96	24.82	15.42	114	7	1.33	2.73	1.80	4.76	4.67	27.09	28.07
61	20100716	1000	178	220	0.20	174	1.00	2.63	-47.48	-28.68	161	7	1.32	2.61	1.79	4.65	4.62	28.18	30.50
62	20100716	1000	163	402	0.20	463	5.00	1.09	24.54	2.13	98	7	1.78	2.57	2.41	4.56	4.65	31.43	30.83
72	20101019	1000	33	101	0.30	359	6.00	1.63	-14.42	-15.91	-[IV]	8	2.16	3.40	3.79	4.94	4.96	-[IX]	28.98
73	20101019	1000	43	194	0.30	345	6.00	2.37	-72.61	-42.53	-[V]	8	2.13	3.31	3.74	5.10	5.06	-[IX]	30.92
78	20101022	1200	180	226	0.29	294	7.50	1.77	-70.67	-42.33	-[VI]	9	1.66	2.90	2.26	5.16	5.07	27.16	30.21
86	20110319	1000	193	176	0.48	275	11.00	1.07	-78.17	-32.37	-[VII]	10	1.22	3.12	1.92	4.81	4.76	26.01	30.47
87	20110828	900	52	278	0.24	184	3.33	2.68	-69.57	-34.29	-[VIII]	11	1.46	3.37	2.49	4.78	4.77	27.27	28.45

I Well on its way to recovering but does not do so before exiting viewframe.

II Trial ends because proboscis impacted flower; moth eventually completey recovers within viewframe.

III Slowing and pitching back down, well on its way to recovery, but then impacts the rear wall of the filming arena, after which it rolls and appears to be headed for a second collision with the floor of the arena; but then the video ends.

IV This moth seemed to stabilize but seems to voluntarily yaw and fly off before completely regaining initial pitch orientation.

VI Moth is almost fully recovered, but then impacts some flowers in the filming arena with its proboscis, some time after the initial collision, before regaining initial pitch orientation.

VII Moth is gradually recovering from this exceptionally large pitch-down perturbation, but leaves viewframe before he is anywhere near original pitch orientation.

VIII Moth is quickly recovering, but leaves viewframe (flying longitudinally) before regaining original pitch orientation.

IX For these two trials, pre-hit data is too short to calculate wingbeat frequency.

Table 3.S2 Coefficient Estimates for Computational Model Eq. 3.3-3.5

Coef.	Fixed Value	Units	Coef.	Fixed Value	Units	Coef.	Eq. 3-5 Fit Estimate	Units
g	980.665	$cm\ s^{-2}$	$K_{\zeta\psi}$	$\in \{0{:}.05{:}1\}$	*none*	r	8.85E-1	cm
m	1.40	g	$K_{\dot{x}\zeta}$	1.00	*none*	$K_{\dot{x}\dot{x}}$	2.10E-2	$g\ cm^{-1}\ s^{-2}$
I	1.97	$g\ cm^2$	$K_{\ddot{\psi}\dot{\psi}}$	8.35E-1	$g\ cm^2\ rad^{-1}$	$K_{\ddot{\psi}\dot{x}}$	7.98E-2	$g\ rad\ s^{-2}$

3.S1

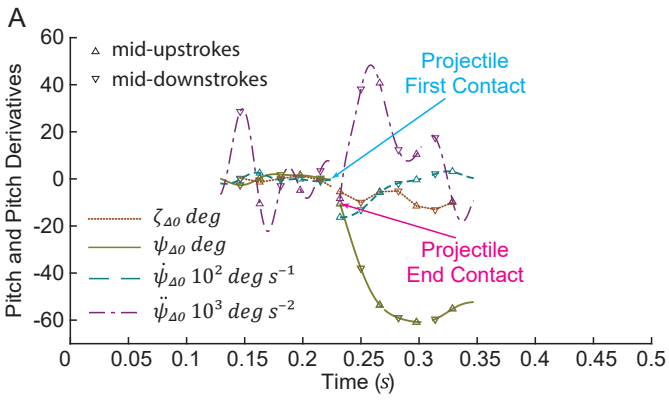

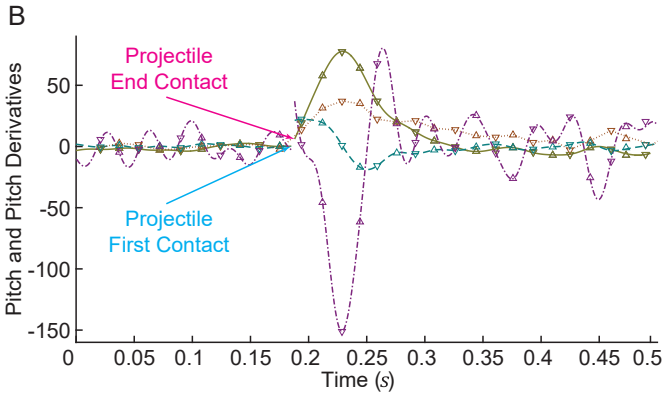

These two graphs correspond to Supplementary Videos 1-2.

A) Supplementary Video 1, (Trial 42 in Table 3.S1), shows a pitch-down perturbation. In this trial, the pitch-down perturbation pushed the moth forward and into proboscis contact with the artifical flower. We did not continue to digitize moth position after that point in time.

B) Supplementary Video 2, (Trial 40 in Table 3.S2) shows a pitch-up perturbation. The moth is first pitched by the cannonball, moving backwards and away from the impact, but recovers within frame. An abrupt stop to the rotation of the abdomen caused an extreme pitch acceleration minima visible in the graph, which we labeled as an outlier and excluded from analysis. Because it contains a large proportion of *M. sexta* mass, a role for the abdomen in pitch-righting is likely (Dhyr et al, 2013); however, we did not investiage that in this study because its impact with the cannonball would be a strong confounding factor.

Supplementary Videos 3-4 show moths crashing after perturbation.

C) Supplementary Video 4 shows a crash following a large pitch-down perturbation with a particularly large cannonball (0.48*g*). Even after this ~145deg perturbation, the moth seems to be decellerating and thus on track to recover; however, it does not manage to do so before colliding with the ground.

D) Supplementary Video 3, (which we did not analyze for the data set) shows a crash following a slight pitch-up perturbation to one wing of the moth. Moths were especially likely to crash if cannonballs contacted the wings. We also did not analyze trials where balls touched the moths on the wing or head, or on any part of the body after the initial collision.

3.S2

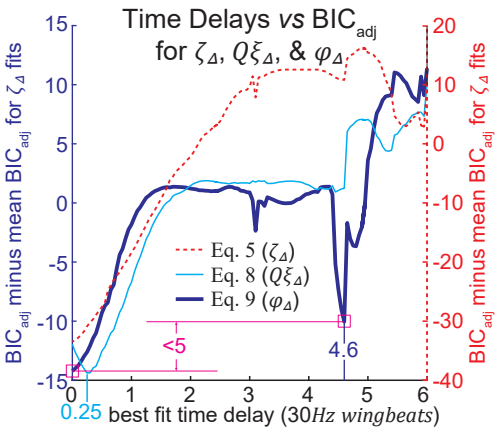

Figure 3.S2: Best-fit time delays between wing kinematics and pitch deviation. This figure plots sample-size adjusted BIC vs. time delay for Eq. 3.10 & 3.13-3.14. The vertical axes are BIC$_{adj}$ minus mean BIC$_{adj}$ for all attempted delays for a given equation. The solid blue left axis pertains to Eq. 3.13 & 3.14 ($Q\xi_\Delta$ & φ_Δ; thin cyan & thick true blue) and the dashed red right axis pertains to the Eq. 3.10 (ζ_Δ; dashed red). The best BIC$_{adj}$ time delays for ζ_Δ, $Q\xi_\Delta$, & φ_Δ are 0, 0.25, and 0 wingbeats. The low time delays for ζ_Δ & $Q\xi_\Delta$ agree with our predictions of a passive wing kinematic response, but a zero time delay for φ_Δ does not. However, as we see in this graph, there is a second loocal minima BIC$_{adj}$ for φ_Δ within 5 of the first. Though a varied sample size and other factors may influence the fidelity of comparing sample-size adjusted BIC among fits, we can see in this graph that such a local minima is not mirrored in the other equations. This agrees with other study results which together all point to an active φ_Δ response, (and in contrast, passive $Q\xi_\Delta$ & ζ_Δ responses), as expected.

3.S3

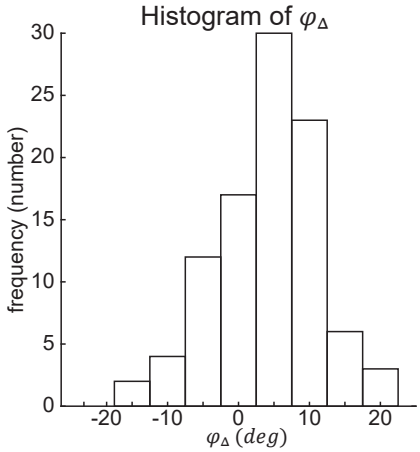

Figure 3.S3: Histogram of observed post-perturbation dorso-ventral sweep asymmetry (φ_Δ). A histogram shows φ_Δ measurements are skewed right (mean φ_Δ is positive). Since abridged quarter-strokes create sweep asymmetry, this histogram indicates the active sweep response of M. sexta to pitch perturbations arises chiefly from shortening the dorsal portion of the halfstroke. This suggests the active sweep response is more important in the case of pitch-down perturbations than it is for pitch-up perturbations.

3.S4

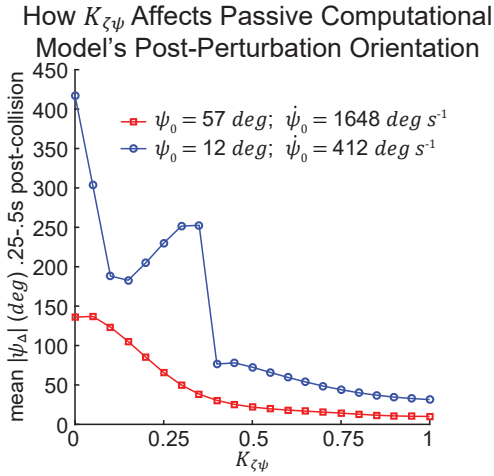

Figure 3.S4: Immediate response of computational *M. sexta* pitch model to medium and large levels of perturbation. The blue line (with decagons) is the response of the model to a pitch-up perturbation with initial pitch and pitch velocity deviations of the same magnitude as our data set's mean. The red line (with squares) is the response of the model to a pitch-up perturbation with initial values set at the maximum pitch deviation and maximum pitch velocity measured in our entire pre-perturbation dataset. Resistance of the stroke plane inclination angle and rotational damping are the only two passive pitch countertorques included in this computational model. Along the horizontal axis, we vary the value of $K_{\zeta\psi}$--the coefficient wich determines the level of resistance of the stroke plane inclination angle to rotation. The vertical values of points along each line come from the model's average pitch position from 0.25-to-0.5s post-perturbation.

3.S5

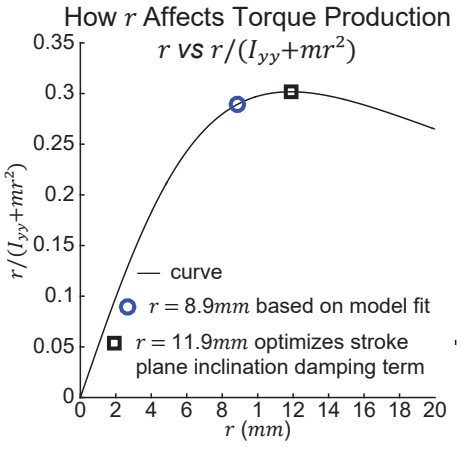

Figure 3.S5: How changes in COP-COM distance (r) alters the affect of lift orientation on stroke-plane-based countertorque. If the net effect of the suite of M. sexta pitch countertorque features cause it to rotate much like a pendulum about a quasi-fixed Center Of Rotation (COR) close to its COP (Center Of Pressure), its rotational inertia crossed with the lever of action is $r/(I_{yy}+mr^2)$. We use this multiplier for the first term of our computational pitch model. Higher values of this multiplier result in higher pitch countertorque from a rotation-resistant stroke plane inclination angle. The blue decagon shows the estimate of r based on a fit of Eq. 3.5 to observed data, and the nearby black square shows which value of r would maximize this particular passive stability effect.

REFERENCES

Alexander, R.M. and Bennet-Clark, H. C. (1977). Storage of elastic strain energy in muscle and other tissues. *Nature* **265,** 114-117.

Beatus, T. and Cohen, I. (2015). Wing-pitch modulation in maneuvering fruit flies is explained by an interplay between aerodynamics and a torsional spring. *Phys. Rev. E* **92,** 022712.

Bergou, A.J., Xu, S. and Wang, Z.J. (2007). Passive wing pitch reversal in insect flight. *J. Fluid Mech.* **591,** 321-337.

Bergou, A. J., Ristroph, L., Guckenheimer, J., Cohen, I. and Wang, Z. J. (2010). Fruit Flies Modulate Passive Wing Pitching to Generate In-Flight Turns. *Phys. Rev. Lett.* **104,** 148101.

Bluman, J. E. and Kang, C. (2016). Balancing the Efficiency and Stability of the Coupled Dynamics and Aerodynamics of a Flapping Flyer. 4009.

Bomphrey, R.J., Lawson, N. J., Harding, N. J., Taylor, G. K. and Thomas, A. L. (2005). The aerodynamics of Manduca sexta: digital particle image velocimetry analysis of the leading-edge vortex. *J. Exp. Biol.* **208,** 1079-1094.

Chang, S. and Wang, Z. J. (2014). Predicting fruit fly's sensing rate with insect flight simulations. *Proc. Natl. Acad. Sci. U.S.A.* **111,** 11246-11251.

Chen, M. W., Jiang H. W., and Sun, M. (2017). Generation of the pitch moment during the controlled flight after takeoff of fruitflies. *PloS One* **12.3,** e0173481.

Cheng, B. and Deng, X. (2011). Translational and rotational damping of flapping flight and its dynamics and stability at hovering. *IEEE Trans. Robotics* **27,** 849-864.

Cheng, B., Deng, X. and Hedrick, T. L. (2011). The mechanics and control of pitching manoeuvres in a freely flying hawkmoth (Manduca sexta). *J. Exp. Biol.* **214,** 4092-4106.

Coleman, D., Benedict, M. and Chopra, I. (2015). Design, Development and Flight-Testing of a Robotic Hummingbird. *American Helicopter Society 71st Annual Forum*, May 2015. Virginia Beach, VA.

Combes, S. A. and Daniel, T. L. (2003). Into thin air: Contributions of aerodynamic and inertial-elastic forces to wing bending in the hawkmoth Manduca sexta. *J. Exp. Biol.* **206,** 2999-3006.

Combes, S. A. and Dudley, R. (2009). Turbulence-driven instabilities limit insect flight performance. *Proc. Natl. Acad. Sci. USA* **106,** 9105-9108.

Daley, M. A., Usherwood, J. R., Felix, G. and Biewener, A. A. (2006). Running over rough terrain: guinea fowl maintain dynamic stability despite a large unexpected change in substrate height. *J. Exp. Biol.* **209,** 171-187.

Daniel, T. L. and Tu, M. S. (1999). Animal movement, mechanical tuning and coupled systems. *J. Exp. Biol.* **202,** 3415-3421.

Delvare, G. (1993). On the Megaphragma of Guadeloupe with the description of a new species (Hymenoptera, Trichogrammatidae). *Revue française d'Entomologie* **15,** 149-152.

Dickerson, B. H., Aldworth, Z. N. and Daniel, T. L. (2014). Control of moth flight posture is mediated by wing mechanosensory feedback. *J. Exp. Biol.* **217,** 2301-2308.

Dickinson, M. H., Lehmann, F. O. and Sane, S. P. (1999). Wing rotation and the aerodynamic basis of insect flight. *Science* **284,** 1954-1960.

Dyhr, J. P., Morgansen, K. A., Daniel, T. L. and Cowan, N. J. (2013). Flexible strategies for flight control: an active role for the abdomen. *J. Exp. Biol.* **216,** 1523-1536.

Eberle, A. L., Dickerson, B. H., Reinhall, P. G. and Daniel, T. L. (2015). A new twist on gyroscopic sensing: body rotations lead to torsion in flapping, flexing insect wings. *J. R. Soc. Interface* **12,** 20141088.

Ellington, C. P. (1984). The Aerodynamics of hovering insect flight. III. Kinematics. *Phil. Trans. R. Soc. B.* **305,** 41-78.

Elzinga, M. J., Floris B. v., and Dickinson, M. H. (2014). Strategies for the stabilization of longitudinal forward flapping flight revealed using a dynamically-scaled robotic fly. *Bioinsp. Biomim.* **9.2,** 025001.

Ennos, A. R. (1988). The inertial cause of wing rotation in Diptera. *J. Exp. Biol.* **140,** 161-169.

Fernandez, M. J., Springthorpe, D. and Hedrick, T. L. (2012). Neuromuscular and biomechanical compensation for wing asymmetry in insect hovering flight. *J. Exp. Biol.* **215,** 3631-3638.

Fry, S. N., Sayaman, R. and Dickinson, M. H. (2003). The aerodynamics of free-flight maneuvers in Drosophila. *Science* **300,** 495-498.

Gao, N., Aono, H. and Liu, H. (2009). A numerical analysis of dynamic flight stability of hawkmoth hovering. *J. of Biomechanical Science and Engineering* **4,** 105-116.

Greenewalt, C. H. (1962). Dimensional relationships for flying animals. *Smith. Misc. Col.* **144,** 1-46.

Greeter, J. S. M. and Hedrick, T. L. (2016). Direct lateral maneuvers in hawkmoths. *Biol. Open*, bio. 012922.

Greeter, J. S. M. and Hedrick, T. (2010). Pitch perturbation recovery in free-flying hawkmoths. *Integr. Comp. Biol.* **50,** e1-e157.

Hedrick, T.L. and Daniel, T. (2006). Flight control in the hawkmoth Manduca sexta: the inverse problem of hovering. *J. Exp. Biol.* **209,** 3114-3130.

Hedrick, T. L. and Greeter, J.S.M. (2011). Impulse perturbation and recovery in a free flying insect. *American Physical Society, 64th Annual Meeting of the APS Division of Fluid Dynamics*, November 20-22, 2011, Baltimore MD.

Hedrick, T. L. (2008). Software techniques for two- and three-dimensional kinematic measurements of biological and biomimetic systems. *Bioinsp. Biomim.* **3,** 034001.

Hedrick, T. L., Cheng, B. and Deng, X. (2009). Wingbeat Time and the Scaling of Passive Rotational Damping in Flapping Flight. *Science* **324,** 252-255.

Hedrick, T. L. and Robinson, A.K. (2010). Within-wingbeat damping: dynamics of continuous free-flight yaw turns in Manduca sexta. *Biol. Letters* **6,** 422-425.

Hinson, B. T. and Morgansen, K. A. (2015). Gyroscopic sensing in the wings of the hawkmoth Manduca sexta: the role of sensor location and directional sensitivity. *Bioinsp. Biomim.* **10,** 056013.

Hinterwirth, A. J. and Daniel, T. L. (2010). Antennae in the hawkmoth Manduca sexta (Lepidoptera, Sphingidae) mediate abdominal flexion in response to mechanical stimuli. *J. Comp. Physiol. A* **196,** 947-956.

Humbert, J. S. and Faruque, I. (2011). Analysis of insect-inspired wingstroke kinematic perturbations for longitudinal control. *J. Guidance, Control, and Dynamics* **34,** 618-623.

Ishihara, D., Horie, T. and Denda, M. (2009a). A two-dimensional computational study on the fluid-structure interaction cause of wing pitch changes in dipteran flapping flight. *J. Exp. Biol.* **212,** 1-10.

Ishihara, D., Yamashita, Y., Horie, T., Yoshida, S. and Niho, T. (2009b). Passive maintenance of high angle of attack and its lift generation during flapping translation in crane fly wing. *J. Exp. Biol.* **212,** 3882-3891.

Jankauski, M. and Shen, I. (2016). Experimental studies of an inertial-elastic rotating wing in air and vacuum. *Int. J. Micro Air Veh.* **8,** 53-63.

Jindrich, D. L. and Full, R. J. (2002). Dynamic stabilization of rapid hexapedal locomotion. *J. Exp. Biol.* **205,** 2803-2823.

Karásek, M., Hua, A., Nan, Y., Lalami, M. and Preumont, A. (2014). Pitch and roll control mechanism for a hovering flapping wing MAV. *Int. J. Micro Air Veh.* **6,** 253-264.

Kim, J., Han, J., Kim, H. and Han, J. (2014). Longitudinal flight dynamic modeling and stability analysis of flapping-wing micro air vehicles. *J. Institute of Control, Robotics and Systems.* **205** 1-6.

Kim, J., Han, J., Choi, S. and Han, J. (2016). Dynamic Stability of a Hawkmoth-scale Flapping-wing Micro Air Vehicle during Forward Flight. *AIAA Atmospheric Flight Mechanics Conference*, AIAA SciTech, San Diego, CA.

Kim, J., Han, J., Lee, J. and Han, J. (2015). Hovering and forward flight of the hawkmoth Manduca sexta: trim search and 6-DOF dynamic stability characterization. *Bioinsp. Biomim.* **10,** 056012.

Koopmans, J., Tijmons, S., De Wagter, C. and de Croon, G. (2015). Passively Stable Flapping Flight From Hover to Fast Forward Through Shift in Wing Position. *Int. J. Micro Air Veh.* **7,** 407-418.

LaCroix, B.W. and Ifju, P.G. (2016). Aeroelastic Model for Macrofiber Composite Actuators on Micro Air Vehicles. *J. Aircr.*, 1-10.

Lehmann, F. O., Gorb, S., Nasir, N. and Schutzner, P. (2011). Elastic deformation and energy loss of flapping fly wings. *J. Exp. Biol.* **214,** 2949-2961.

Liang, B. and Sun, M. (2013). Nonlinear flight dynamics and stability of hovering model insects. *J. R. Soc. Interface* **10,** 20130269.

Liu, B., Ristroph, L., Weathers, A., Childress, S. and Zhang, J. (2012). Intrinsic Stability of a Body Hovering in an Oscillating Airflow. *Phys. Rev. Lett.* **108,** 068103.

Liu, H., Ellington, C., Kawachi, K. and c. (1998). A computational fluid dynamic study of hawkmoth hovering. *J. Exp. Biol.* **201 (Pt 4),** 461-477.

Ma, K. Y., Chirarattananon, P., Fuller, S. B. and Wood, R. J. (2013). Controlled flight of a biologically inspired, insect-scale robot. *Science* **340,** 603-607.

Maeda, M., Gao, N., Nishihashi, N. and Liu, H. (2010). A free-flight simulation of insect flapping flight. *J. Aero Aqua Bio-mechanisms* **1,** 71-79.

May, M. L., Wilkin, P. J., Heath, J. E. and Williams, B. A. (1980). Flight performance of the moth, Manduca sexta, at variable gravity. *J. Insect Physiol.* **26,** 257-265.

Miller, L. A. and Peskin, C. S. (2009). Flexible clap and fling in tiny insect flight. *J. Exp. Biol.* **212,** 3076-3090.

Nakata, T. and Liu, H. (2012). Aerodynamic performance of a hovering hawkmoth with flexible wings: a computational approach. *Proc. Biol. Sci.* **279,** 722-731.

Noda, R., Maeda, M. and Liu, H. (2013). Effect of Passive Body Deformation of Hawkmoth [*sic.*] on Flight Stability. *Intelligent Autonomous Systems 12*, pp. 835-842: Springer.

Norberg, R. Å. (1972). The pterostigma of insect wings an inertial regulator of wing pitch. *J. Comp. Physiol.* **81,** 9-22.

Orlowski, C. T. and Girard, A. R. (2012). Dynamics, stability, and control analyses of flapping wing micro-air vehicles. *Prog. Aerospace Sci.* **51,** 18-30.

Pratt, T. and Qin, N. (2016). Vortex Generators for Increased Maximum Lift and Enhanced High-α Stability of a Zimmerman-Wing MAV at Low Reynolds Number. *2016 Applied Aerodynamics Conference*, R. Aeronaut. Soc., Bristol, ENG.

Ortega-Jimenez, V. M., Mittal, R. and Hedrick, T. L. (2014). Hawkmoth flight performance in tornado-like whirlwind vortices. *Bioinsp. Biomim.* **9,** 025003.

Ortega-Jimenez, V. M., Greeter, J. S., Mittal, R. and Hedrick, T. L. (2013). Hawkmoth flight stability in turbulent vortex streets. *J. Exp. Biol.* **216,** 4567-4579.

Polilov, A. A. (2012). The smallest insects evolve anucleate neurons. *Arthropod Structure & Development* **41,** 29-34.

Ravi, S., Crall, J. D., McNeilly, L., Gagliardi, S. F., Biewener, A. A. and Combes, S. A. (2015). Hummingbird flight stability and control in freestream turbulent winds. *J. Exp. Biol.* **218,** 1444-1452.

Ristroph, L., Ristroph, G., Morozova, S., Bergou, A. J., Chang, S., Guckenheimer, J., Wang, Z. J. and Cohen, I. (2013). Active and passive stabilization of body pitch in insect flight. *J. R. Soc. Interface* **10,** 20130237.

Ristroph, L., Bergou, A. J., Ristroph, G., Coumes, K., Berman, G. J., Guckenheimer, J., Wang, Z. J. and Cohen, I. (2010). Discovering the flight autostabilizer of fruit flies by inducing aerial stumbles. *Proc. Natl. Acad. Sci. USA* **107,** 4820-4824.

Rosen, M. H., le Pivain, G., Sahai, R., Jafferis, N. T. and Wood, R. J. (2016). Development of a 3.2 g untethered flapping-wing platform for flight energetics and control experiments. 3227-3233.

Sane, S. P., Dieudonne, A., Willis, M. A. and Daniel, T. L. (2007). Antennal mechanosensors mediate flight control in moths. *Science* **315,** 863-866.

Santhanakrishnan, A., Robinson, A. K., Jones, S., Low, A. A., Gadi, S., Hedrick, T. L. and Miller, L. A. (2014). Clap and fling mechanism with interacting porous wings in tiny insect flight. *J. Exp. Biol.* **217,** 3898-3909.

Sponberg, S., Dyhr, J. P., Hall, R. W. and Daniel, T. L. (2015). Luminance-dependent visual processing enables moth flight in low light. *Science* **348,** 1245-1248.

Springthorpe, D., Fernández, M. J. and Hedrick, T. L. (2012). Neuromuscular control of free-flight yaw turns in the hawkmoth Manduca sexta. *J. Exp. Biol.* **215,** 1766-1774.

Stengel, R. F. (2015). *Flight dynamics*: Princeton University Press.

Stewart, E. C., Patil, M. J., Canfield, R. A. and Snyder, R. D. (2016). Aeroelastic Shape Optimization of a Flapping Wing. *J. Aircr.*, 636-650.

Sun, M. (2014). Insect flight dynamics: stability and control. *Reviews of Modern Physics* **86,** 615.

Sun, M., Wang, J. and Xiong, Y. (2007). Dynamic flight stability of hovering insects. *Acta Mechanica Sinica* **23,** 231-246.

Sun, M. and Xiong, Y. (2005). Dynamic flight stability of a hovering bumblebee. *J. Exp. Biol.* **208,** 447-459.

Sun, M. and Wang, J. K. (2007). Flight stabilization control of a hovering model insect. *J. Exp. Biol.* **210,** 2714-2722.

Taha, H. E., Tahmasian, S., Woolsey, C. A., Nayfeh, A. H. and Hajj, M. R. (2015). The need for higher-order averaging in the stability analysis of hovering, flapping-wing flight. *Bioinspir. Biomim.* **10,** 016002.

Taylor, G. K. and Krapp, H. G. (2007). Sensory systems and flight stability: what do insects measure and why? *Adv. Insect Physiol.* **34,** 231-316.

Taylor, G. K. and Thomas, A. L. R. (2003). Dynamic flight stability in the desert locust Schistocerca gregaria. *J. of Exp. Biol.* **206,** 2803-2829.

Usherwood, J. R. and Ellington, C. P. (2002). The aerodynamics of revolving wings I. Model hawkmoth wings. *J. Exp. Biol.* **205,** 1547-1564.

Vance, J., Faruque, I. and Humbert, J. (2013). Kinematic strategies for mitigating gust perturbations in insects. *Bioinsp. Biomim.* **8,** 016004.

Wang, H., Ando, N. and Kanzaki, R. (2008). Active control of free flight manoeuvres in a hawkmoth, *Agrius convolvuli*. *J. Exp. Biol.* **211,** 423-432.

Weis-Fogh, T. (1960). A rubber-like protein in insect cuticle. *J. Exp. Biol.* **37.4,** 889-907.

Whitehead, S. C., Beatus, T., Canale, L. and Cohen, I. (2015). Pitch perfect: how fruit flies control their body pitch angle. *J. Exp. Biol.* **218,** 3508-3519.

Whitney, J. and Wood, R. (2010). Aeromechanics of passive rotation in flapping flight. *J. Fluid Mech.* **660,** 197-220.

Windsor, S. P., Bomphrey, R. J. and Taylor, G. K. (2013). Vision-based flight control in the hawkmoth Hyles lineata. *J. R. Soc. Interface* **11,** 20130921.

Wu, J. H., Zhang, Y. L. and Sun, M. (2009). Hovering of model insects: simulation by coupling equations of motion with Navier-Stokes equations. *J. Exp. Biol.* **212,** 3313-3329.

Xu, N. and Sun, M. (2013). Lateral dynamic flight stability of a model bumblebee in hovering and forward flight. *J. Theor. Biol.* **319,** 102-115.

Zhang, Y. and Sun, M. (2010). Dynamic flight stability of a hovering model insect: lateral motion. *Acta Mechanica Sinica* **26,** 175-190.

Zhang, Y., Wu, J. and Sun, M. (2012). Lateral dynamic flight stability of hovering insects: theory vs. numerical simulation. *Acta Mechanica Sinica* **28,** 221-231.

Zheng, L., Hedrick, T. L. and Mittal, R. (2013). A multi-fidelity modelling approach for evaluation and optimization of wing stroke aerodynamics in flapping flight. *J. Fluid Mech.* **721,** 118-154.

Zheng, L., Wang, X., Khan, A., Vallance, R., Mittal, R. and Hedrick, T. L. (2009). A combined experimental-numerical study of the role of wing flexibility in insect flight. *47th AIAA Aerospace Sciences Meeting*, Jan. 5-8 2009. Orlando, FL.

CHAPTER 4
HAWKMOTH RESPONSE TO LATERAL AND LONGITUDINAL LOADS

Summary

This study addresses pitch and roll control in *Manduca sexta* with a different challenge for the moths than that employed in Chapters 2 & 3. Rather than observe a spontaneous roll maneuver or response to impulse pitch perturbation, I examine at how *M. sexta* compensate for an off-axis weight attached to its thorax. This perturbation is different because it is continuous rather than impulsive, and involves potential rather than kinetic energy. It also affects both pitch and roll simultaneously, which is a logical next level of complexity in flight stability research.

Moths use both postural and wing kinematic changes to compensate for the attached weights. To relocate their center of mass (COM), they pitch down, roll to the side of the attached weight, and increase their intra-abdominal angle.

Roll: As in Chapter 2, moths 1) move their COP laterally to create net roll torque via changes to left *vs*. right wing sweep asymmetry. Unlike the results of Chapter 2, neither left-right wing pitch asymmetry (essentially effective angle of attack, AOA), nor left-right elevation amplitude correlate with apparent roll torque. This is consistent with my conclusion that left-right elevation amplitude asymmetries in the roll maneuver case were targeted at reducing global-reference frame (GRF) damping effects. In place of left-right wing pitch asymmetry, moths 2) use asymmetries in stroke plane angle to further move their COP laterally *via* asymmetric lift production.

Pitch: As in Chapter 3, moths 1) reorient their net force vector *via* changes to stroke plane angle, such that more acute angles correspond to net pitch-up torque. At least for downstrokes, results also (weakly) support 2) net force vector reorientation *via* lower stroke plane deviation angle (*i.e.* higher AOA). Also as in Chapter 3, moths additionally 3) move their COP forward by moving the average position of the flapping wings forward relative to the control; *i.e.* increasing fore-*vs*.-aft wing sweep asymmetry.

Here, body segment (and stroke plane) flexibility relative to the COM help compensate for the attached mass. This supports my previous (Chapter 3) conclusion that flexibility is an important factor in flapping flight stability, even in the case of active responses to continuous perturbations. Furthermore, the correlation of roll wing kinematics directly with my estimate of weight-induced roll torque support the former conclusion (Chapter 2) that roll is heavily damped in *M. sexta*.

Introduction

Experimental overview

Chapters 2-3 analyzed the mechanics of free-flying moths that experienced aerodynamic effects from the movement of their bodies through the air. In this final study, I rely on the groundwork of Chapters 1-3 to investigate the mechanics of steady perturbations induced by a mass attached to the backs of the moths, lateral or forward of their original center of mass (COM).

Experimental differences from previous chapters

When weights are attached, moths must continuously respond to a COM offset along the longitudinal axis alone, or along both the longitudinal and lateral axes simultaneously. This means they must create (either pitch, or both) pitch and roll torque continuously and simultaneously. Their net linear and angular velocity remains zero, however, so the velocity-based damping effects that were prominent in Chapters 2 and 3 should not exist here.

Previous work in roll

Taking the definition of lift as vertical and drag as horizontal in the body reference frame (BRF), my previous work showed moths produce laterally asymmetric lift to roll (Greeter and Hedrick, 2016; Chapter 2), and longitudinally asymmetric lift and drag to pitch (Chapter 3). Maneuvering moths used left-right asymmetries in wing sweep, elevation amplitude, and wing pitch (in lieu of angle of attack, AOA) to create roll torque. Work in *Drosophila melanogaster* also identified essentially the same three wing kinematic variables as likely effectors of roll (Beatus and Cohen, 2015;Ristroph *et al.*, 2009). Findings in these studies were strikingly similar, but they concluded the opposite about what these results meant for stability in roll.

Previous work in pitch

Previous research on control of pitch in hawkmoths (Chapter 3) and *Drosophila* (Ristroph *et al.*, 2013;Ristroph *et al.*, 2010) agree that pendular stability factors exist in pitch because the COM lies well below the center of pressure (COP) (Ellington, 1984;Kim and Han, 2014;Noda *et al.*, 2013). Hawkmoth wings resist rotation more strongly than their body, providing a quasi-fixed reference point, and the wing motions that arise from both gyroscopic and aerodynamic effects help passively restore pitch as well. In this case involving impulse perturbation response, hawkmoths produced asymmetric lift *via* bilaterally symmetric changes in stroke plane angle and fore-aft sweep amplitude, and longitudinally asymmetric drag by using different angles of attack (measured there as stroke plane deviation angles) in up- *vs.* downstrokes.

Chapter 3 showed moths use fore-aft wing sweep asymmetry, stroke plane angle, and up/downstroke stroke plane deviation and AOA asymmetries to pitch. Previous and concurrent work in *M. sexta* ((Cheng *et al.*, 2011;Willmott and Ellington, 1997b); Khandelwal and Hedrick, *unpublished data*) and hummingbirds (Cheng *et al.*, 2016) also support a role for stroke plane angle in active pitch maneuvers. Studies on *D. melanogaster* and hummingbirds also agree that active changes to fore-aft wing sweep asymmetry (Cheng *et al.*, 2016;Whitehead *et al.*, 2015) creates pitch torque. Chapter 3 and work in hummingbirds (Cheng *et al.*, 2016) also show a role for AOA in the creation of pitch torque. Together with other recent work on the gyroscopic nature of flapping and pendular stability in pitch (Dickerson *et al.*, 2014;Eberle *et al.*, 2015;Jankauski and Shen, 2016;Jenkins, 2016;Ristroph *et al.*, 2013), these two studies are also consistent with my conclusions about pitch stability in hawkmoth-scale flapping flight.

Expectations and hypotheses

The results of Chapters 2-3 allowed more detailed predictions about the pitch and roll wing dynamics examined here. This section describes my *a priori* expectations in a set of numbered hypotheses, both those that the results ultimately supported and those that they did not.

In this study, placement of the weight above the moth alters COM position, and thus the COM-COP vector. The torque applied here is continuous and due to an additional mass. I first predict that moths change the roll and/or pitch orientations of their thorax and abdomen to manipulate their COM and thus

compensate for the off-axis weight. Since the configuration of COM-below-COP is more stable (Chapter 3), I predict them to roll to the weight-ipsilateral side (*Hypothesis 1*). Since the COP and COM likely lie behind the wing bases (Ellington, 1984;Kim and Han, 2014;Willmott and Ellington, 1997b), I predict that moths pitch into a more horizontal hover orientation (*Hypothesis 2*). Since changes to the BRF stroke plane angle create pitch torque, I also predict compensatory changes in wing kinematics to relocate the COP more directly above the new COM in order to restore pitch stability (*Hypothesis 3)*.

Moths manipulate effective AOA to create both roll and pitch (Chapters 2-3). Since higher wing pitch angles increase both drag and lift, one might expect to see a conflict between the moth's ability to use consistent left-right wing pitch asymmetries to generate (lift-based) roll torque, but opposing up- and downstroke stroke plane deviation asymmetries to generate (drag-based) pitch torque. A moth rolling to the right increases its left wing pitch angle and decreases its right wing pitch angle by about the same amount. Since the *M. sexta* drag curve is approximately linear in this range (Usherwood and Ellington, 2002), it seems likely that an increase in longitudinal drag in the higher-pitched wing will be balanced by a decrease in longitudinal drag in the lower-pitched wing, resulting in zero net pitch torque. Since wing pitch was the most prominent identified factor in *M. sexta* roll during sideslip maneuvers, I predict wing pitch angle to be a key driver of roll torque here as well. I thus predict left-right wing pitch asymmetry will scale with my estimate of lateral COM displacement (*Hypothesis 4*). I predict this linear relationship to have similar coefficients for downstrokes and upstrokes (*Hypothesis 5*) as in Chapter 2.

Chapter 2 indicated left-right asymmetries in sweep and elevation amplitude also generate roll torque. Similar to the case with wing pitch, I do not expect the left-right wing sweep asymmetries moths use to generate roll torque *via* lateral lift imbalance (Chapter 2) to conflict with the fore-aft wing sweep asymmetries moths use to generate pitch torque *via* longitudinal lift imbalance (Chapter 3). I thus predict left-right wing sweep asymmetry will scale with my estimate of lateral COM displacement (*Hypothesis 6*). Moths used left-right wing elevation amplitude asymmetries, however, to counteract roll damping induced by rotation in the global reference frame (GRF), chiefly *via* flapping countertorque, or FCT. Left minus right elevation amplitude had a negative correlation with roll (velocity). In the stationary case, however, it is likely that moderately larger elevation amplitudes should generate moderately more lift (as is the case for sweep). Thus I predict left minus right elevation amplitude to have a *positive* correlation with roll torque, or be

insignificant (*Hypothesis 7*). In the sideslip maneuver case (Chapter 2), I concluded the lower wing pitch angles and greater upwards motion of upstroke meant greater exposure to FCT effects, so the linear coefficient was higher for upstrokes than downstrokes. Consistent with this conclusion, the coefficient relating elevation amplitude to roll velocity was ~4× higher during upstrokes than downstrokes (likely due to FCT). Since a hovering moth does not experience damping effects mediated by world reference frame rotational velocity, and net lift is higher during downstrokes than upstrokes (Bomphrey *et al.*, 2005;Liu *et al.*, 1998;Sane, 2003), here I expect the coefficient, if significant, to be *lower* for upstrokes than downstrokes.

I expect the wing kinematics for pitch torque generation to differ little from those I saw in Chapter 3. In response to positive longitudinal COM displacement, I predict moths will increase BRF stroke plane angle (*Hypothesis 8*), increase fore minus aft wing sweep amplitude asymmetry (*Hypothesis 9*), and decrease/increase downstroke/upstroke stroke plane deviation angle (*i.e.* increase AOA on downstrokes and reduce it during upstrokes; *Hypothesis 10*). Since forces are higher during downstroke, I predict coefficients for downstroke wing kinematics to be larger and/or more statistically significant than their upstroke counterparts (*Hypothesis 11*).

I expect the relationship between these wing kinematics and pitch torque generation to have approximately the same sign and magnitude as seen in Chapter 3. Damping is high for roll and arises chiefly from GRF wing velocity differences (Chapter 2). Damping is lower in pitch, and arises chiefly from gyroscopic and drag forces on the wings that manifest as the very kinematic changes (to the wings) that restore orientation (Chapter 3). Thus, I expect the coefficients relating pitch-torque-generating wing kinematics with longitudinal COM offset to be approximately equal to those from Chapter 3, which relate them to the second derivative of pitch orientation (*Hypothesis 12*). If stroke plane and stroke plane deviation angle changes indeed depend on COP being above the COM in order to create pitch torque, and our estimate of COM displacement is fully appropriate, I predict a slight reduction in these coefficients due to the high weight placement (*Hypothesis 13*). If fore-aft wing sweep asymmetry does not rely on vertical COM location, and since GRF damping effects are absent, I predict a slight increase in this coefficient (*Hypothesis 14*).

Summary of methods, results, and discussion

As in Chapters 2-3, I hand-digitized wing kinematics from high speed video to characterize the motion of each moth's body and wings. Also as in Chapters 2-3, I then used a stepwise Bayesian information criterion (BIC) approach to determine which of kinematic variables were the best predictors of pitch and roll (though here, I allowed a variable with a p>.05 to remain in the presented best-fit multivariate model). Methods were largely sufficient to test my hypotheses, and I believe the relationships I found to represent real physical effects.

The results indicate moths adjust roll and pitch body angles to compensate for the attached weights, and use both wing sweep and stroke plane adjustments to create roll and pitch torque. The directionality of these relationships agrees with the theoretical framework I presented in previous chapters.

Unlike Chapters 2-3, however, I did not find definitive evidence that supported a role for AOA in the creation of either roll torque. The results also do not show a relationship between elevation amplitude and roll torque. This is consistent with my idea that the AOA and elevation amplitude asymmetries observed in Chapter 2 may have been targeted at reducing FCT from roll and lateral velocity, further supports my conclusion that roll in hawkmoths is heavily damped. This suggests moths tailor their wing kinematic response to their specific circumstances and maneuvers, rather than using a "one-size-fits-all" approach to the generation of body torques. For AOA, moths substituted left/right, up-/downstroke asymmetries in stroke plane angle, combined with left/right sweep asymmetries seen Chapter 2, to generate roll torque.

In the case of pitch, I found strong support for the same fore-aft sweep asymmetry and stroke plane angle changes that moths exhibited in Chapter 3, and weak support for (downstroke) stroke plane deviation angle. Interestingly, moths also appear to widen their intra-abdominal angle to help compensate for the pitch challenge, as is well-known for tethered moths (Dickerson *et al.*, 2014;Dyhr *et al.*, 2013;Hinterwirth and Daniel, 2010). Moths also rolled to the side of the attached sinker, and tended to pitched down. This supports modeling and experimental results that suggest that the COP and COM are behind the wing base in *M. sexta* (Ellington, 1984;Kim and Han, 2014;Willmott and Ellington, 1997b). Thus, the results indicate physical flexibility helps create stability, not only in response to instantaneous perturbations as in Chapter 3, but here in response to continuous loading as well.

Table 4.1: Individual moth and treatment details

Trial #	Moth Mass (g)	Sinker Mass (g)				Sinker BRF or Pin Center Position (x_{BRF},z_{BRF}) Relative to Visually-Estimated COM (cm)				Sinker BRF Sinker BRF or Pin Center Position (x_{BRF},z_{BRF}) Relative to Visually-Estimated COM (cm)			
11	1.62	0.319	0.313	c	0.326	(0.89,-1.59,-2.25)	(0.98,-0.83,-2.31)	(0.90,0.06,-2.63)[a]	(0.89,0.16-2.60)	(0.85,-1.55,-0.99)	(0.94,-0.79,-0.93)	(1.06,0.13,-1.17)[a]	(1.03,0.25,-1.15)
15	1.77	0.249	0.257	0.257	c	(0.98,0.18,-2.68)	(0.73,0.87,-2.48)	(0.80,1.65,-2.53)	(0.81,0.15,-2.45)[a]	(1.16,-0.08,-1.01)	(0.86,0.89,-1.00)	(0.86,1.36,-1.01)	(1.11,-0.02,-0.94)[a]
17	1.64	0.251	0.257	0.248	c	(-0.06,-1.70,-2.54)	(0.15,-0.75,-2.64)	(0.25,-0.23,-2.66)	(0.47,-0.14,-2.86)[a]	(0.84,-1.78,-1.20)	(0.87,-0.82,-1.17)	(1.09,-0.30,-1.29)	(1.26,-0.19,-1.11)[a]
21	1.61	0.271	0.248	0.248	c	(0.07,0.08,-2.37)	(-0.07,0.74,-2.41)	(-0.80,1.43,-2.62)	(0.21-0.16,-2.35)[a]	(0.76,0.20,-1.20)	(0.89,0.82,-1.19)	(0.81,1.86,-1.82)	(0.80,-0.07,-1.01)[a]
27	1.42	0.245	0.255	0.255	c	(0.15,0.21,-3.02)	(0.27,1.16,-2.79)	(0.37,1.73,-2.86)	(0.840.01,-2.95)[a]	(1.00,-0.00,-1.81)	(0.94,0.99,-1.43	(1.05,1.53,-1.52)	(1.29,-0.15,-1.08)[a]
31	1.35	0.256	0.251	c	0.245	(0.37,-0.85,-2.00)	(0.40,-0.15,-2.14)	(0.51,-0.18,-2.27)[a]	(0.38-1.82-1.85)	(0.84,-0.83,-0.98)	(0.72,-0.00,-1.04)	(0.87,-0.04,-1.07)[a]	(0.98,-1.89,-0.89)
39	1.71	0.256	c	0.253	0.280	(-0.26,0.56,-2.66)	(-0.03,-0.11,-2.63)[a]	(-0.11,-0.25,-2.69)	(-0.24,0.50-2.55)	(0.52,0.58,-1.41)	(0.86,-0.10,-1.22)[a]	(0.86,-0.23,-1.32)	(0.45,0.52,-1.32)
35	2.19	0.270	c	0.258	0.249	(0.12,-1.45,-2.41)	(0.80,-0.82,-2.87)[a]	(0.52,-0.58,-2.70)	(0.18-2.39-2.49)	(0.40,-1.12,-0.98)	(0.79,-0.14,-1.02)[a]	(0.79,-0.16,-1.09)	0.64,-2.04,-0.85)
						slocal/MGRF Sinker Position Relative to Wing Bases (x_{sw},z_{sw}) Minus T-bar Center Position Relative to the Wing Bases in the Control Trial (cm)				MGRF Abdomen Position Relative to Wing Bases (x_{aw}) Minus Abdomen Position Relative to the Wing Bases in the Control Trial (cm)			
11						(0.05,0.31)	(0.06,0.33)	c	(-0.42,0.22)	(-0.13)	(0.09)	c	(0.82)
15						(0.08,-0.14)	(-0.16,0.14)	(-0.42,0.29)	c	(0.09)	(-0.01)	(0.36)	c
17						(-0.28,0.28)	(-0.22,0.28)	(0.01,-0.03)	c	(-0.56)	(-0.24)	(-0.44)	c
21						(0.10,-0.18)	(-0.25,-0.11)	(-0.77, 0.06)	c	(-0.74)	(-0.30)	(-0.11)	c
27						(-0.01,-0.07)	(0.13,0.11)	(0.16,-0.02)	c	(-0.56)	(-1.09)	(-0.55)	c
31						(-0.06, 0.27)	(-0.12,0.09)	c	(-0.16,0.56)	(-0.40)	(-0.05)	c	(-0.06)
39						(-0.25, 0.09)	c	(-0.01,-0.08)	(-0.14,,0.17)	(-0.40)	c	(-0.14)	(-0.16)
35						(-0.41, 0.39)	c	(-0.19,-0.02)	(-0.52,0.48)	(-0.35)	c	(0.56)	(0.17)
mean						(-0.15,0.14) (moves back and down, relative to COM)				(-0.21) (moves up relative to COM)			

c or [a] indicates a control trial (i.e. no sinker); this table only

Methods

Animals and training

I acquired 8 male *M. sexta* as pupae from the domestic colony housed at UNC Chapel Hill. Following eclosure, moths drank water *ad libitum* in their enclosures, and fed on 1:4 solutions of sucrose or honey dissolved in tap water during recording and training. They lived in $30 \times 30 \times 30 cm$ mesh cages at ambient room temperature and humidity in a 22:2hr light:dark cycle. Table 4.1 contains individual moth and treatment details.

I trained food-limited *M. sexta* to feed on an artificial nectar solution while hovering in an arena (Fig. 4.1). The nectar was delivered in an artificial flower composed of a small funnel attached to a nectar-filled syringe tube. I trained the moths by repeatedly feeding them from this artificial flower in the days leading up to perturbation trials. Training times typically coincided with night or dusk in the moths' extended-day, contracted-night light cycle.

Figure 4.1: Experimental setup

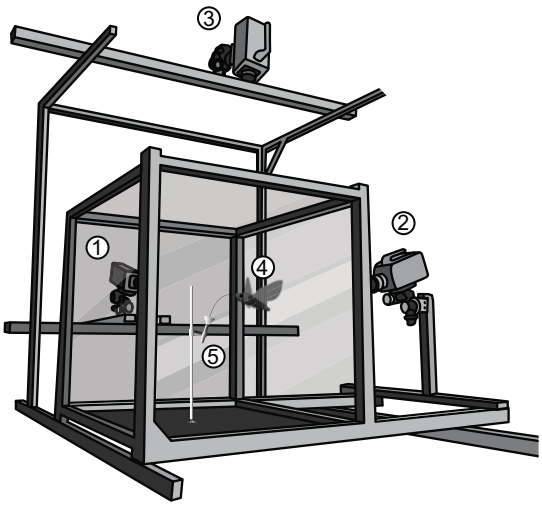

Experimental setup. 1&2) Phantom v7.1 cameras, 3) Phantom v5.1 camera, 4) hawkmoth, 5) artificial flower. Not shown: high-intensity infrared LEDs\

Experimental setup

I recorded hawkmoths feeding in a 71 x 71 x 74 cm glass-walled arena (Fig. 4.1). Two Phantom v7.1 and one Phantom v5.1 digital cameras (Vision Research Inc., Wayne, NJ, USA) used the high-intensity 680nm light from eight LEDs (Roithner LaserTechnik, GmBH, A-1040, Vienna, Austria) to capture moth feeding at a framerate of 1000Hz.

Figure 4.2: Images of moths attached to sinker and T-bar

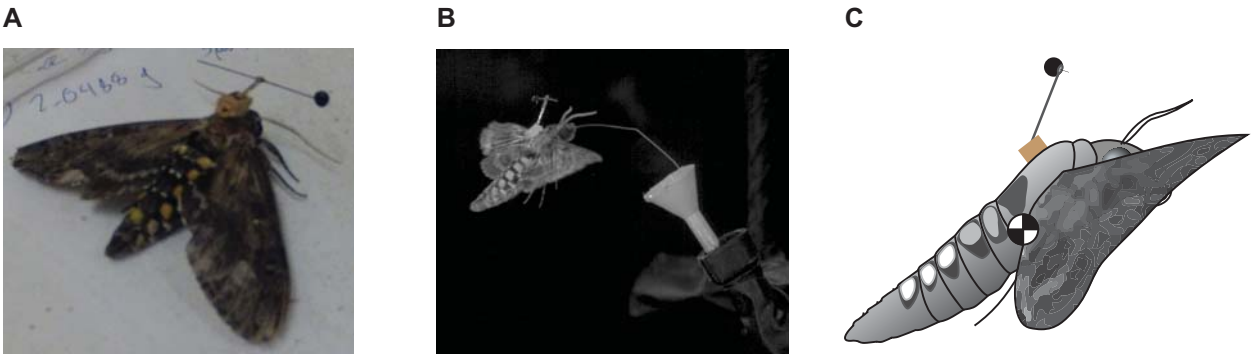

Representative moths with T-bar and sinker attached to their scuta. I glued an insect pin inside of a sewing needle to make a T-bar, and then inserted this needle into a small piece of natural cork. Successful trials involved each of four successive treatments in view of the cameras, and due to moth behavior, often with the control treatment last. **A)** Color picture of moth with T-bar and sinker attached. **B)** Freeze-frame from high-speed video showing moth with sinker attached (Trial 11, Treatment 1, Frame 36). **C)** Side-view of a moth flying with sinker attached to the T-bar.

To attach off-axis weights, I fixed an insect pin inside the eye of a needle with superglue, and then inserted that needle into a small piece of natural cork. Before each trial, I super-glued each cork to the bare scutum (scraped free of scales) of a moth and allowed it to cure (Fig. 4.2). Sinkers did not stay attached to the moths overnight, so any second attempts at acquiring successful trials were conducted with freshly-glued pins. If the attachment and initial test flight were successful, I caught the moths and adjusted the sinker position (and/or mass) in between each trial segment, henceforth often simply "treatment."

For each trial, I filmed moths feeding in a control video, and also laden with a weight in three different configurations. I filmed a control treatment with just the cork and pins attached to the moth (no sinker), and also three additional trials with the fishing sinkers attached ($0.24 - 0.33g$, EagleClaw Micro Split-Shot Assortment (Silver), ASIN: B000ALC89U, Model: #02180H-007) attached at various positions along the insect pin. I at first conducted treatments, including the control, in varying order. Nevertheless, due apparent inter-treatment behavioral variations in the moths, trials were most often successful when the control treatment came last (fourth). All but one trial consisted of the following four treatments (in random order): 1) No sinker, 2) Sinker attached at or close to the middle of the insect pin, 3) Sinker attached approximately halfway out to the end of the insect pin, 4) Sinker attached at the distal tip of the insect pin. In Trial 33, treatment 3 was accidentally repeated, but at different times (*i.e.* different attachments). See Table 4.1 for individual trial data.

Digitized points and wing angles

I analyzed the resulting data in MATLAB (r2016, The Mathworks, Natick, MA), using a digitizing and wing kinematic scheme almost identical to that of Chapters 2&3, though I did not digitize the scutum. Fig. 4.3 shows the digitizing scheme and wing angles for this experiment. I analyzed the first 100 frames from each treatment video.

Figure 4.3 Digitizing scheme and wing angles

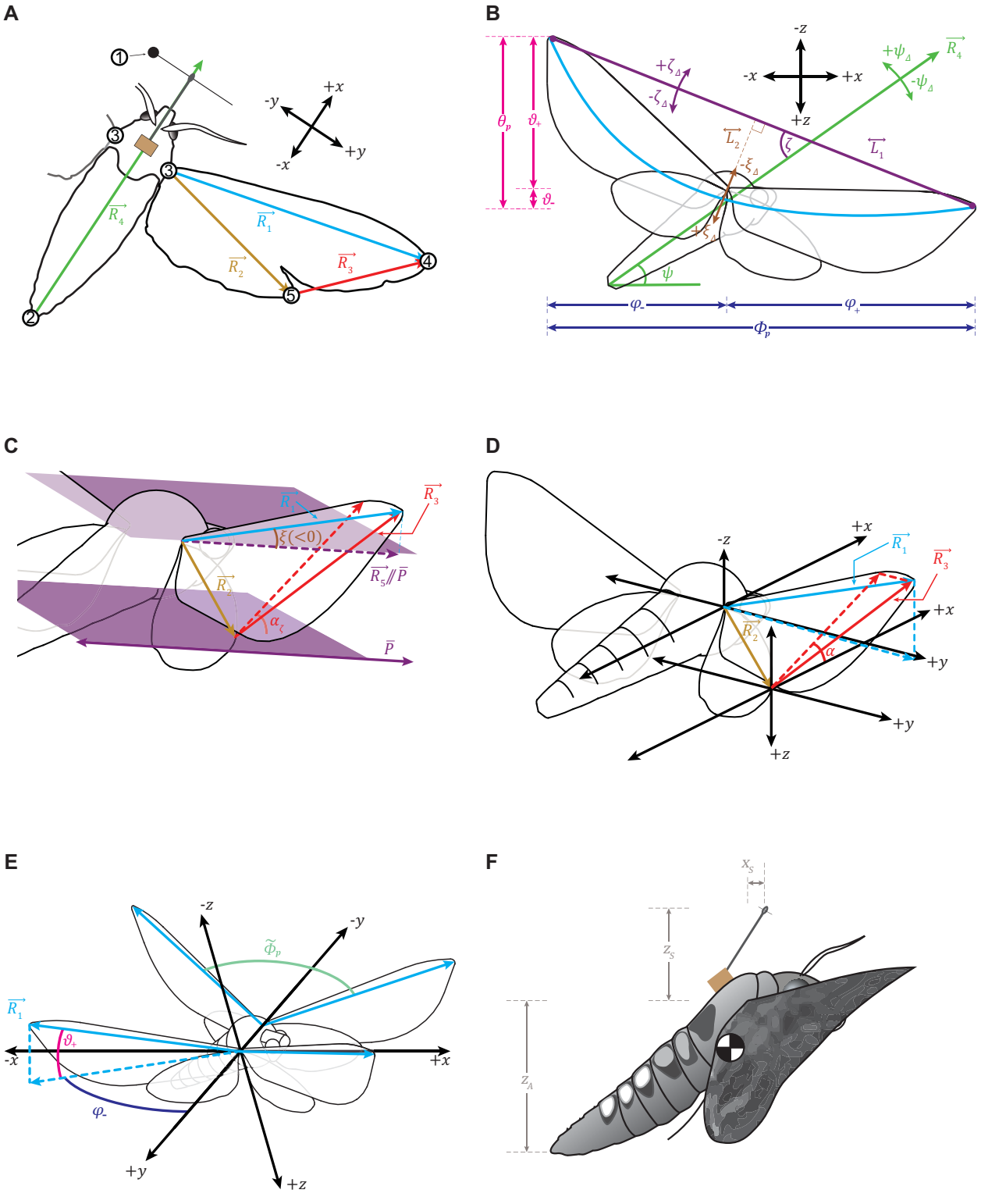

Caption next page

Marked points, body angles, and wing angles. I localized moth wing and body points in 3D space by hand from synchronized videos, allowing extraction of flight kinematics with custom MATLAB functions. **A)** shows the points I digitized (marked) on the moth, and the vectors I used in wing position and orientation calculations. **A)** only depicts the body and right wing, but I marked all points with bilateral symmetry about the sagittal plane, in every analyzed frame. I marked point 1 at the sinker location, 2 at the caudal tip of the abdomen, and 3 at both wing bases. In Chapter 3, I marked point 1 at a caudal portion of the scutum. A manually identified canonical frame provided the default position for fixed morphology of the moth. I used this to compute Euler angles (yaw, pitch, and roll) and reference frames (Stengel, 2015). In the Body Reference Frame (BRF) planes, positive x is forwards for the moth, positive z is parallel with gravity (downwards), and positive *y* is to the moth's right. $\overrightarrow{R_1}$ stretches from the wing base (3) to forewing tip (4), $\overrightarrow{R_2}$ from wing base (3) to hindwing tip (5), and $\overrightarrow{R_3}$ from hindwing tip (5) to forewing tip (4). **B)** and **C)** show the body and wing angles I measured based on the aforementioned points and vectors. I measured body pitch angle changes ψ_Δ (lime green) relative to the canonical orientation of $\overrightarrow{R_4}$, which stretches from 2 through the midpoint of a line connecting the two wing base points on any given frame. The azimuthal/elevation angles of $\overrightarrow{R_1}$ relative to a BRF vertical/horizontal ($(y,z)/(x,y)$) plane through the wing base point yields wing sweep/elevation angle (φ/ϑ), (navy blue/magenta), at the end of downstroke (φ_+/ϑ_+) and upstroke (φ_-/ϑ_-). $\overleftrightarrow{L_1}$ (purple) connects the (x,z) forewing tip position at the end of a given up- or downstroke, *i.e.* "halfstroke," with its (x,z) position at the end of the previous or subsequent halfstroke. Extending $\overleftrightarrow{L_1}$ in y yields a stroke plane $\bar{P}$; during perturbation, $\bar{P}$ deviates from its average hover orientation in the BRF by "stroke plane inclination angle" ζ_Δ (also purple). Line segment $\overleftrightarrow{L_2}$ (brown) starts perpendicular to $\bar{P}$ and ends at the position of point 4 when the wing is precisely at midstroke. The arctangent of its length over the midstroke y-position of 4 is ξ (also brown), which analysis later showed is closely related to effective angle of attack. **C)** shows an oblique view of this midstroke measurement for clarity: Reflecting $\overrightarrow{R_1}$ onto $\bar{P}$ at midstroke yields $\overrightarrow{R_5}$; ξ is the angle between these two vectors (here, negative). The difference between pre-hit average ξ and its value at a given post-hit midstroke is the "stroke plane deviation angle" ξ_Δ. To measure "wing pitch angle relative to stroke plane" α_ζ (red), also closely related to angle of attack, I measured the angle that the (x,z) components of $\overrightarrow{R_3}$ make relative to the stroke plane, and subtracted the mean hover orientation. To get deviation from the baseline for all angles, I subtracted pre-hit midstroke averages from the measurements for each post-hit halfstroke. I averaged and subtracted upstroke and downstroke kinematics separately. **D)** shows "wing pitch angle relative to BRF horizontal" (α, red), which was calculated as in Chapter 2. To compute α, I projected $\overrightarrow{R_3}$ onto the BRF x/z plane and took α as the angle between this projected vector and the BRF horizontal. Midstroke wing pitch angles are all positive; I measured downstroke α relative to the positive moth BRF x-axis and upstroke α relative to the negative moth BRF x-axis. **E)** Peak-to-peak stroke amplitude ($\widetilde{\Phi}_p$, blue-green) is the angle between $\overrightarrow{R_1}$'s BRF position at the top of upstroke and the end of downstroke, and *vv.* for the following halfstroke. It can be broken down into its BRF vertical "elevation amplitude" (θ_p, magenta) and BRF horizontal (Φ_p, navy blue) components. As seen in **B)**, θ_p & Φ_p are the same as $(\vartheta_+ + \vartheta_-)$ & $(\varphi_+ + \varphi_-)$ for any given halfstroke. Measurements ϑ, ϑ_+, ϑ_-, and $\widetilde{\Phi}_p$ were not included in the final analysis of Chapter 4 data, and are shown here strictly for illustrative purposes (since here all measurements from the dissertation are shown together in one image, and with the same color coding). **F)** The position of the pin and abdomen tip were estimated in relation to the center of the two wing bases. Here, x_S and z_S (gray) are the x- and z- positions of T-bar center (for control treatments) or sinker center (for non-control treatments) relative to the center of the two wing bases in the MGRF. The abdomen's z- position relative to the center of the two wing bases in the MGRF is denoted by z_A, (also gray).

Estimating effective "torque" from sinker position

In this experiment, the true net COM of the moths is difficult to estimate with accuracy. In place of more precise methods, I estimated the COM imbalance the moths had to compensate for ($\vec{\tau}$) using the cross product of A) a BRF vertical vector of magnitude gravity times the sinker mass, with B) a vector stretching from the visually estimated COM to the sinker position (*i.e.* $\vec{\tau} = \vec{r} \times \vec{F}$). In the absence of a better measurement for COM location, I compared wing kinematic measurements to this $\vec{\tau}$. Other estimates of BRF $\vec{\tau}$ were attempted, but did not change which factors survived the BIC model selection process. I correlated the pitch portion of $\vec{\tau}$ ($\overrightarrow{\tau_\psi}$) to wing kinematics I expected to create pitch torque, and the roll portion of $\vec{\tau}$ ($\overrightarrow{\tau_\beta}$) to wing kinematics I expected to create roll torque.

To check whether moths manipulate body orientation to compensate for the off-axis weights, I also calculated a $\overrightarrow{\tau_{\psi 0}}$ and $\overrightarrow{\tau_{\beta 0}}$ from moth and sinker points after they were rotated to a standard orientation. In this standard reference frame (SRF), I rotated GRF points about the z-, then x-, and the y-axis such that, in the new SRF: 1) the wing base points and the abdomen point lie on a shared x-y plane, 2) the x-z plane includes the abdomen point and a (0,0,0) that is the midpoint of a line connecting the two wing base points 3) the y-z plane is perpendicular to the first two planes and intercepts the same (0,0,0) point. Qualitative visual observations confirm this trend. I also constructed a modified global reference frame (MGRF) in which moth body and wing points were rotated so that the x-axis of the MGRF lies on the longitudinal axis of the moth ($\overrightarrow{R_4}$ in Fig. 4.3).

Correlating "torque" to body and wing measurements

To check whether moths adjusted their body roll and pitch to offset the additional mass, I compared the SRF $\overrightarrow{\tau_{\psi 0}}$ and $\overrightarrow{\tau_{\beta 0}}$ to body pitch (ψ_Δ) and roll (β_Δ) orientation, respectively.

I compared the BRF $\overrightarrow{\tau_\psi}$ and $\overrightarrow{\tau_\beta}$ to the wing kinematics that I identified related to pitch and roll in Chapters 2-3 to check my initial hypotheses (**Introduction**). Based on Chapter 3 results, I compared $\overrightarrow{\tau_\psi}$ to: *i*) the sine of stroke plane angle ($\sin(-\zeta_\Delta)$), *ii*) fore-aft sweep amplitude asymmetry (φ_Δ), *iii*) up-/downstroke stroke plane deviation angle ($-Q\xi_\Delta \cos(\zeta_\Delta)$), and *iv*) up-/downstroke wing pitch angle relative to the stroke plane ($Q\alpha_{\zeta_\Delta}$). I compared $\overrightarrow{\tau_\beta}$ to left-right asymmetries in: *i*) wing pitch relative to the stroke

plane ($\alpha_{\zeta_{LR\Delta}}$), *ii*) wing pitch relative to the BRF horizontal ($Q\alpha_{LR\Delta}$), *iii*) stroke plane angle ($Q\zeta_{LR\Delta}$), *iv*) stroke plane deviation angle ($\xi_{LR\Delta}$), and *v*) and *vi*) peak-to-peak sweep ($\Phi_{LR\Delta}$), and elevation ($\theta_{LR\Delta}$) amplitude. Fig. 4.3 shows these wing angles.

Wing kinematics were averages from the first 100 frames of each non-control treatment video, and I correlated elements of $\vec{\tau}$ with deviation from the control. The delta subscript indicates I subtracted from these averages corresponding up- and downstroke kinematic averages taken from the given trial's control treatment (separate averages taken for each moth). Much like the wing kinematics, the delta subscript after the body kinematic measurements ψ and β indicates I also centered these variables to the control trial's mean. Here I did not, however, calculate separate reference (control treatment) means for up- and downstroke.

When identifying best-fit models, I used a BIC-based stepwise multiple linear regression (MATLAB function *stepwiselm*) with a forced zero intercept, to identify the most informative variables. My final models only included statistically significant variables that also reduced BIC. Unlike my previous work, the perturbations in this study were consistent and stable; so, wing kinematic changes might be likely to scale equally in response to increases/decreases in perturbation magnitude. Thus I present individual data fits of separate correlations of elements of $\vec{\tau}$ to each of these kinematics, in addition to my stepwise BIC modeling results (**Results,** Tables 4.2-4.3 and Fig. 4.4-5). My ***a priori*** expectation is for all coefficients presented in **Results** Tables 4.2-3, to be positive, with the possible exception of $K_{\overrightarrow{\tau_{\psi 0}}\psi}$ for $\overrightarrow{\tau_{\psi 0}}$ *vs.* ψ_Δ (for reasons I explain in **Discussion**).

Results

Summary of observations

Tables 4.2-3 and Fig. 4.4-5 show which relationships were individually significant, as well as mixed model results. Qualitatively, moths were unable to fly when sinkers were too heavy (> ~0.4 g) and seemed to have greater difficulty responding to the weights in pitch, than in roll. No moths able to stabilize in pitch appeared unable to stabilize their flight when a sinker of the same weight was moved laterally on the insect pin. Some moths managed to fly even though their wings brushed against the insect pins during flight. Yet,

I did not attempt to record videos where that was the case, and instead adjusted or reattached the pins if possible. Many moths managed to perform for three treatments, but very few managed to perform for a fourth. Though treatment order was random, trials where the control came last seemed to be the most likely to succeed for all four consecutive treatments.

Table 4.2: Roll-related variables and models

Eq.	Interpretation	Fit Equation	Coef.	Units	Estimate	p-value	r^2
1	moths roll towards the sinker	$\overrightarrow{\tau_{\beta 0}} = -K_{\overrightarrow{\tau_{\beta 0}}\beta}\beta_{\Delta}$	$K_{\overrightarrow{\tau_{\beta 0}}\beta}$	$g\ cm^2\ s^{-2}\ rad^{-1}$	6.85E3	2.65E-2	0.193
2	higher/lower left *vs* right stroke plane angle creates rightwards roll torque in down/upstrokes	$\overrightarrow{\tau_{\beta}} = QK_{\overrightarrow{\tau_{\beta}}\zeta}\zeta_{LR\Delta}$	$K_{\overrightarrow{\tau_{\beta}}\zeta}$	$g\ cm^2\ s^{-2}\ rad^{-1}$	1.86E4	5.14E-4	0.409
3	higher left *vs* right sweep amplitude creates rightwards roll torque	$\overrightarrow{\tau_{\beta}} = K_{\overrightarrow{\tau_{\beta}}\Phi}\Phi_{LR\Delta}$	$K_{\overrightarrow{\tau_{\beta}}\Phi}$	$g\ cm^2\ s^{-2}\ rad^{-1}$	3.02E3	2.82E-2	-0.006
4	*best-BIC model* left-right stroke plane and sweep amp. asymmetries create roll torque	$\overrightarrow{\tau_{\beta}} = QK_{\overrightarrow{\tau_{\beta}}\zeta}\zeta_{LR\Delta} + K_{\overrightarrow{\tau_{\beta}}\Phi}\Phi_{LR\Delta}$	$K_{\overrightarrow{\tau_{\beta}}\zeta}$	$g\ cm^2\ s^{-2}\ rad^{-1}$	6.85E3	1.30E-2	0.489
		$\overrightarrow{\tau_{\beta}} = QK_{\overrightarrow{\tau_{\beta}}\zeta}\zeta_{LR\Delta} + K_{\overrightarrow{\tau_{\beta}}\Phi}\Phi_{LR\Delta}$	$K_{\overrightarrow{\tau_{\beta}}\Phi}$	$g\ cm^2\ s^{-2}\ rad^{-1}$	4.00E2	6.44E-2*	

*p>.05

Roll perturbation: Wing kinematic response

The roll portion of $\vec{\tau}$ in the BRF ($\overrightarrow{\tau_{\beta}}$) correlates most strongly to left-right asymmetry in stroke plane angle ($\zeta_{\Delta LR}$; Fig. 4.4B), and also weakly (p≈0.6) with left-right asymmetry in sweep amplitude ($\Phi_{\Delta LR}$; Fig. 4.4C). This estimate of lateral COM displacement does not significantly correlate with any other tested single variable. Sweep amplitude relates to $\overrightarrow{\tau_{\beta}}$ in the same way it related to the first derivative of roll velocity ($\dot{\beta}$) in Chapter 2, where moths increased left *vs.* right sweep amplitude to roll right. Stroke plane angle correlates with $\overrightarrow{\tau_{\beta}}$ in that moths increase left *vs.* right stroke plane angle during downstrokes and decrease it during upstrokes to compensate for a weight on their left side (*i.e.* to create roll-right torque). No version of left-right asymmetry in wing pitch or stroke plane deviation angle correlates significantly with $\overrightarrow{\tau_{\beta}}$.

Roll perturbation: Best-BIC multivariate linear model for roll wing kinematics

When considering up- and downstroke averages together as in Chapters 2-3, the best-BIC model includes both left-right stroke angle asymmetry $\zeta_{LR\Delta}$ and left-right sweep amplitude asymmetry $\Phi_{LR\Delta}$ (Fig. 4.4D). Note that this model's p-value for $\Phi_{LR\Delta}$ was marginally above the p<0.05 significance threshold. Including up- and downstroke averages (for non-amplitude-related variables) in the BIC-based stepwise elimination process identifies no models better than those that include both-halfstroke variables.

Figure 4.4: Roll perturbation vs. *wing and body kinematics*

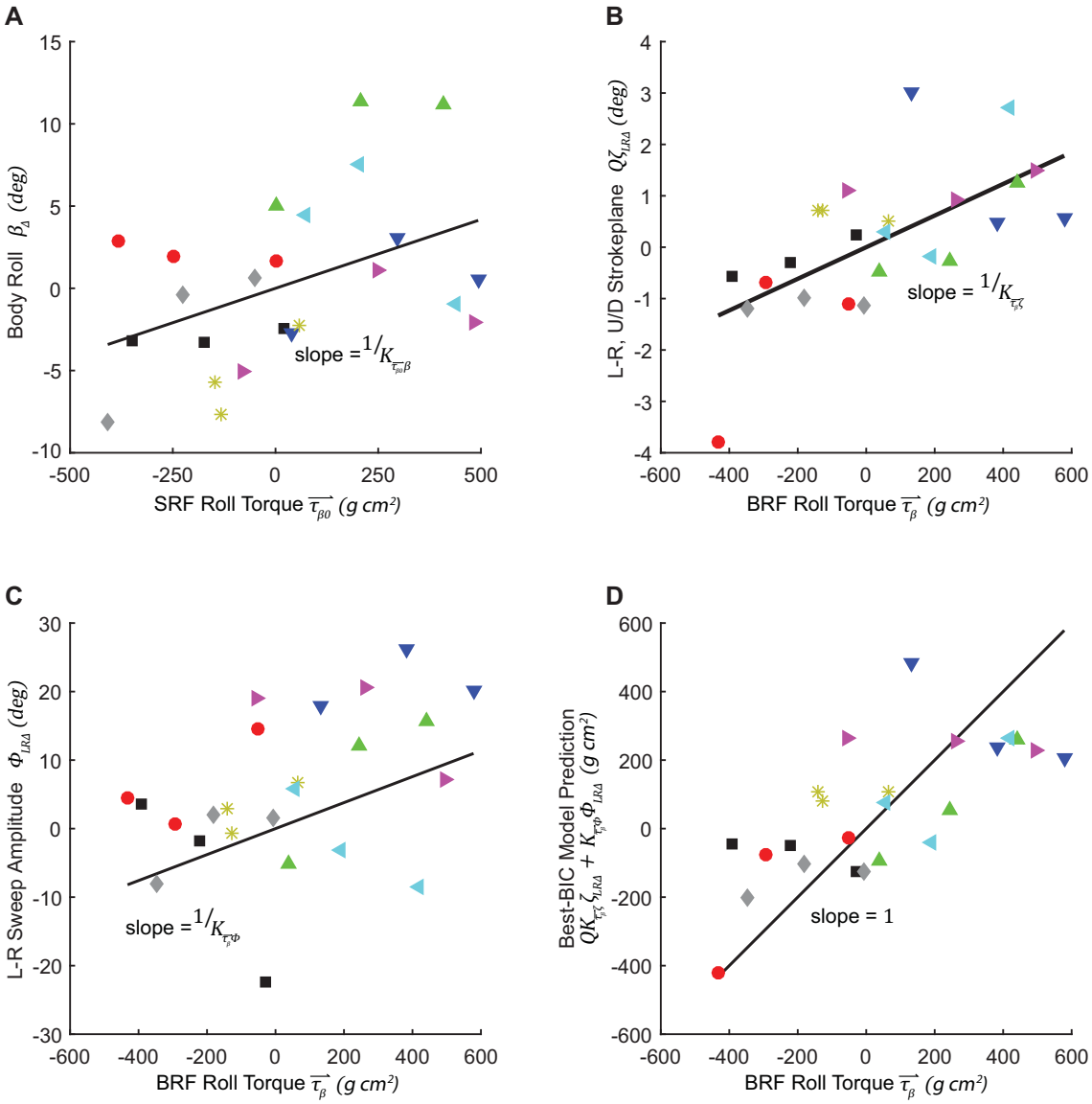

Moths use roll, and left-right asymmetries in sweep and stroke plane angle to counter weight-imposed roll torques. In these plots, each triad of points with similar color and shape corresponds to the three non-control treatments of an individual trial. Each point is the average of the given variable for the first 100 frames of a treatment, minus that variable's average for the control treatment from that trial. The magenta rightwards-pointing triangles, black squares, cyan leftwards-pointing triangles, gray rhombi, red circles, green upwards-pointing triangles, manila asterisks, and dark blue downwards-pointing triangles correspond to trials 11, 15, 17, 21, 27, 31 33, and 35 (respectively). In **A)**, larger roll deviations correlate with the estimate of weight-imposed roll torque, in a reference frame where all moths have been first computationally rotated into a standardized orientation. Moths rolled to the side ipsilateral with the fishing sinker. In **B)**, asymmetry in left-right sweep amplitude correlates with greater weight-imposed roll torque. Moths increase sweep amplitudes on the side ipsilateral with the fishing sinker. In **C)**, left-right asymmetry in stroke plane angle correlate with weight-imposed roll torque. Moths increase left-minus-right stroke plane angle in downstroke and decreased left-minus-right stroke plane angle in upstroke to create roll torque. Panel **D)** shows the best-BIC model for how moths respond to the lateral COM displacement in the BRF. The graph plots this model's predictions against the estimate of weight-imposed roll torque in the BRF.

Pitch Perturbation: Body response

Body pitch (ψ_{Δ}) does not linearly correlate with the pitch portion of $\vec{\tau}$ in the SRF ($\overrightarrow{\tau_{\psi 0}}$). They do, however, co-vary: There is a significant positive relationship between $|\psi_{\Delta}|$ and $\overrightarrow{\tau_{\psi 0}}$ (Fig. 4.5A). In other words, moths change their general body pitch orientation relative to the control trial, but choose to pitch either more down, *or* more up when exposed to stronger longitudinal COM offsets ($\overrightarrow{\tau_{\psi 0}}$ of greater magnitude; here, all negative). Results indicate moths choose to pitch their abdomens downwards (*i.e.* more horizontal; left side of the histogram in Fig. 4.6; left side of Fig. 4.7B) more often than upwards (right side of the histogram in Fig. 4.6; right side of Fig. 4.7B).

The data also indicate that the moth body response to off-axis loading is more complicated than just "pitch-up" or "pitch-down." Negative $\overrightarrow{\tau_{\psi}}$ (negative x weight positions) do not coincide with pitch-up abdomen reorientations. MGRF z abdominal position relative to the wing bases was less than that of the T-bar's center relative to the wing bases in the control trial (*i.e.* $x_{A\Delta} < 0$) (Table 4.1). This indicates the perturbed moths pitched their abdomens downwards (made their abdomens more horizontal), likely to reduce longitudinal COM displacement (Fig. 4.7C). MGRF x sinker position relative to the wing bases was less than that of the T-bar's center relative to the wing bases in the control trial (*i.e.* $x_{S\Delta} < 0$; Table 4.1). The z-position dropped slightly ($z_{S\Delta} > 0$) but likely less than one would expect given the body roll reorientations. These results indicate the perturbed moths pitched their thoraces upwards (and thus moved the sinker higher and farther back) to reduce longitudinal COM displacement (Fig. 4.7C). As explained in **Discussion**, all of the pitch reorientations mentioned here have the conceptual/theoretical potential to reduce net pitch torque $\overrightarrow{\tau_{\psi}}$ by bringing the COM longitudinally closer to the COP (Fig. 4.7B-C).

Pitch perturbation: Wing kinematic response

Fore-aft wing sweep asymmetry (φ_{Δ}) correlates significantly with $\overrightarrow{\tau_{\psi}}$ (Fig. 4.5B) in the same way it correlated to $\ddot{\psi}_{\Delta}$ in Chapter 3; more forward wing sweep is associated with the creation of pitch-up torque. Stroke plane angle (ζ_{Δ}) does not *alone* significantly correlate with the pitch portion of $\vec{\tau}$ in the BRF ($\overrightarrow{\tau_{\psi}}$; Fig. 4.5C). Yet, when both ζ_{Δ} and φ_{Δ} are included in a fit together, ζ_{Δ} does correlate with $\overrightarrow{\tau_{\psi}}$ in the same way it correlated to the second derivative of pitch ($\ddot{\psi}_{\Delta}$) in Chapter 3; more acute angles between the stroke plane

and abdomen are associated with the generation of pitch-up torque. With both-halfstroke φ_Δ included in fits, the correlation between $\sin(-\zeta_\Delta)$ and $\overrightarrow{\tau_\psi}$ is stronger for downstroke than for upstroke ζ_Δ, and stronger for downstroke ζ_Δ than for the mean of downstroke and upstroke ζ_Δ together. Halfstroke amplitudes are identical in this data set, so I did not check separate correlations for up- and downstroke φ_Δ. This is because it is unlikely that amplitudes are different over the long-term for up- and downstroke during stable state hover, at least not in ways which are not already measured by separate estimates for up- and downstroke stroke plane angle ζ_Δ. In all these cases, correlations are similar if $\overrightarrow{\tau_\psi}$ replaces $\overrightarrow{\tau_{\psi 0}}$.

Stroke plane deviation angle (ξ_Δ), it does not correlate with $\overrightarrow{\tau_\psi}$, but smaller stroke plane deviation in downstroke (recall that this would mean higher AOA) does significantly correlate with $\overrightarrow{\tau_{\psi 0}}$. Downstroke wing pitch angle relative to the stroke plane (α_{ζ_Δ}) also correlates with $\overrightarrow{\tau_{\psi 0}}$ in the same way it correlated with $\ddot{\psi}_\Delta$ in Chapter 3; higher wing pitch angles in downstroke are associated with the creation of pitch-up torque. Unlike Chapter 3, however, this correlation was stronger than that for stroke plane deviation angle ξ_Δ, and more informative according to BIC.

Pitch perturbation: Best multivariate linear model for pitch wing kinematics

When considering up- and downstroke averages together as in Chapters 2-3, the best-BIC model for $\overrightarrow{\tau_\psi}$ includes only stroke plane angle ζ_Δ and fore-aft wing sweep asymmetry φ_Δ (Eq. 8; Fig. 4.5D). I also attempted models with separate coefficients for upstroke and downstroke for non-amplitude-related variables. Downstroke-only stroke plane ($\zeta_\Delta \in downstrokes$) was a slightly (ΔBIC<2) better fit for $\overrightarrow{\tau_\psi}$ than the both-halfstroke ζ_Δ. However, this BIC difference is statistically insignificant (Kass and Raftery 1995), so I reject it in favor of the less complex, both-halfstroke model.

Figure 4.5: Pitch perturbation vs. *wing and body kinematics*

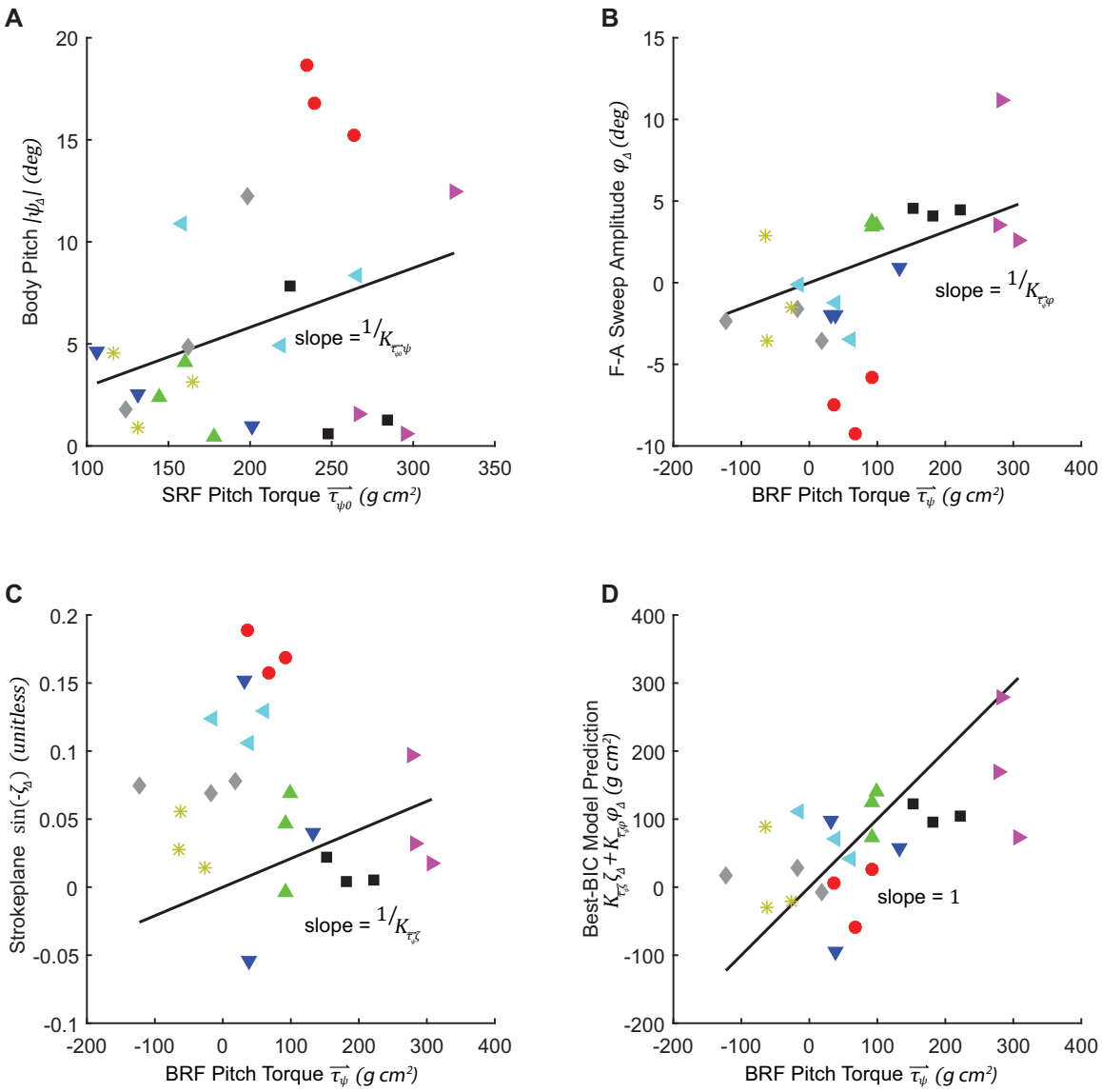

Moths use pitch, sweep, and stroke plane to counter weight-imposed pitch torques. In these plots, each set of three isochromatic/isomorphic points corresponds to each trial's triad of mean-centered treatment data points as detailed in Fig. 4.4. In **A),** larger magnitude pitch deviations correlate with estimated weight-imposed pitch torque, in a reference frame where all moths have been first computationally rotated into a standardized orientation. In **B)**, asymmetry in fore-aft sweep amplitude correlates with greater weight-imposed pitch torque. Moths increased the forward portion of sweep (relative to rearward sweep) to create pitch-up torque. In **C)**, more acute stroke plane angles correlate with greater pitch torque challenges, though this relationship is insignificant on its own, without the inclusion of a sweep amplitude asymmetry term. However, the relationship is significant on its own when compared to pitch torque estimated in the MGRF (not shown). **D)** shows the best-BIC model for how moths respond to the longitudinal COM displacement in the BRF. The graph plots this model's predictions against estimated weight-imposed pitch torque in the BRF.

Table 4.3: Pitch-related variables and models

Eq.	Interpretation	Fit Equation	Coef.	Units	Estimate	p-value	r^2
5	moths reorient in pitch to reduce the sinker's apparent pitch torque	$\overrightarrow{\tau_{\psi 0}} = K_{\overrightarrow{\tau_{\psi 0}}\psi}\lvert\psi\rvert$	$K_{\overrightarrow{\tau_{\psi 0}}\psi}$	$g\ cm^2\ s^{-2}\ rad^{-1}$	1.97E3	9.75E-6	0.092
6	higher fore *vs* aft sweep amplitude asymmetry creates pitch-up torque	$\overrightarrow{\tau_{\psi}} = K_{\overrightarrow{\tau_{\psi}}\varphi_\Delta}\varphi_\Delta$	$K_{\overrightarrow{\tau_{\psi}}\varphi_\Delta}$	$g\ cm^2\ s^{-2}\ rad^{-1}$	3.67E3	1.59E-2	0.23
7	smaller stroke plane angle relative to the body creates pitch-up torque	$\overrightarrow{\tau_{\psi}} = K_{\overrightarrow{\tau_{\psi}}\zeta_\Delta}\sin(-\zeta_\Delta)$	$K_{\overrightarrow{\tau_{\psi 0}}\zeta_\Delta}$	$g\ cm^2\ s^{-2}$	4.76E3	1.24E-1*	-1.01
8	*best-BIC model* smaller stroke plane angles and higher fore-aft sweep asymmetry together create pitch-up torque	$\overrightarrow{\tau_{\psi}} = K_{\overrightarrow{\tau_{\psi}}\varphi_\Delta}\varphi_\Delta + K_{\overrightarrow{\tau_{\psi}}\zeta_\Delta}\sin(-\zeta_\Delta)$	$K_{\overrightarrow{\tau_{\psi}}\varphi_\Delta}$	$g\ cm^2\ s^{-2}\ rad^{-1}$	1.27E3	1.38E-4	0.305
		$\overrightarrow{\tau_{\psi}} = K_{\overrightarrow{\tau_{\psi}}\varphi_\Delta}\varphi_\Delta + K_{\overrightarrow{\tau_{\psi}}\zeta_\Delta}\sin(-\zeta_\Delta)$	$K_{\overrightarrow{\tau_{\psi}}\zeta_\Delta}$	$g\ cm^2\ s^{-2}$	9.23E2	8.06E-4	

*p>.05

Figure 4.6: Histogram of body pitch response to sinker perturbation

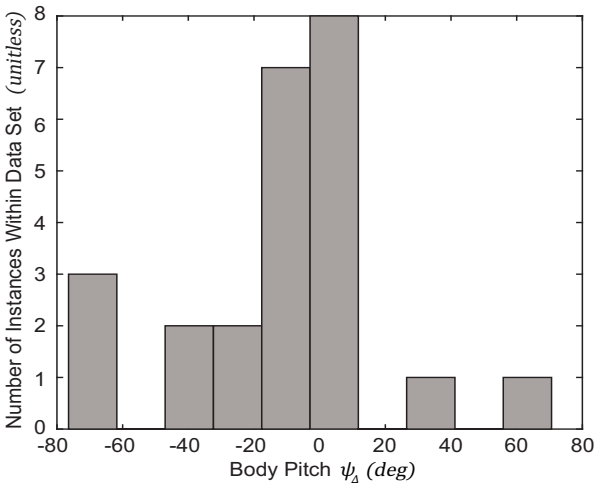

Moths pitch downwards (or upwards) in response to weight attachment. Moths pitched both downwards and upwards in response to the longitudinal COM displacement imposed by the attached weight. This histogram shows that net pitch-down responses (negative pitch; left side of the graph) were more frequent than a net pitch-up responses (positive pitch; right side of the graph).

Discussion

Overview

The observations are generally consistent with my initial hypotheses. Most predicted wing and body kinematics correlate significantly and as expected with estimates of pitch and roll torque.

The estimate of longitudinal displacement of COM used here significantly correlates with most of the kinematic variables identified as important to controlling pitch in Chapter 3, and as predicted in my introductory hypotheses. Exceptions include the weak relationship between stroke plane deviation angle and estimated pitch torque, as well as a pitch-compensatory body response that is more complicated than simple "pitch-up" or "pitch-down."

The estimate of lateral displacement of COM used here also significantly correlates with most of the kinematic variables identified as important to roll in Chapter 3, and as predicted in my introductory

hypotheses. Exceptions include the null results for a relationship between wing pitch angle and roll, as well as the predicted lack of significance in the relationship between elevation amplitude and estimated roll torque.

Moths reorient their bodies to manipulate COM
(supporting Hypothesis 1, mixed support for Hypothesis 2)

Hawkmoths change the hover orientations of both their abdomen and thorax in response to this perturbation challenge. The weights are attached to the thorax of each moth, so the observed roll and pitch reorientations change the weight's location and thus fundamentally change the nature of the applied perturbation.

Moths consistently rolled to the side ipsilateral with the fishing sinker (Fig. 4.4A & 4.7A), perhaps to simultaneously reduce weight-imposed pitch torque (in the global reference frame, GRF). This is interesting because the T-bar is approximately perpendicular to the moth's sagittal plane, so roll reorientations in both directions should reduce lateral COM displacement (as shown for pitch in Fig. 4.7B). If the net COM is displaced downwards by weight-ipsilateral roll reorientations, and upwards by weight-contralateral roll reorientations, then the consistent preference for listing to the side of the attached sinker should both enhance stability (Chapter 2; Cheng and Deng, 2011a;Cheng *et al.*, 2011;Ristroph *et al.*, 2013;Willmott *et al.*, 1997) and reduce GRF pitch torque. Since listing to the side of the attached weight helps straighten the COP-COM "pendulum" (Fig. 4.7A), this roll response is consistent with my explanation of pendular stability in flapping flight.

Based on points in the body reference frame (BRF), moths typically choose to reorient their bodies into a more-pitch down configuration to compensate for the pitch torque applied by the sinker mass, though sometimes choose a more-pitch up response (Fig. 4.6). If a moth's intra-abdominal angle stays the same, both movements might result in a reduction of COM imbalance. Upwards pitch would rotate the sinker upwards (and towards the center of the moth) and the abdomen's COM would rotate more down. Downwards pitch would rotate the sinker farther out, but the abdomen farther back as well (Fig. 4.7B). Note that the net mass of the portions of the hawkmoth that lie rearward of the wing base are likely much greater than the combined weight of the fishing sinker, forward thorax, and cephalon. Modeling studies (*e.g.* Kim

and Han, 2014;Noda *et al.*, 2013) indicate the COM and COP likely lie behind the wing bases during normal hover. This may explain why moths prefer a pitch-down orientation.

The data further indicate the moth body response to the pitch challenge presented by the weight is more nuanced than just “pitch up” or “pitch down.” On average, pitch-down-challenged moths both rotate their thoraces up (move the weight higher and farther back) and rotate their abdomens down (made their abdomens more horizontal), to modulate longitudinal COM displacement. This would make the intra-abdominal angle more obtuse, changing the pitching moment in the case of a fixed stroke plane angle (Dyhr *et al.*, 2013;Hinterwirth and Daniel, 2010). Results here also complement abdominal reorientations in other tethered insects (Baader, 1990;Camhi, 1970;Frye, 2001;Götz *et al.*, 1979). Such a reconfiguration should better longitudinally adjust COM than simple whole-body (pitch-up or) pitch-down. See Fig. 4.7C for a visual representation.

The relative pitch rotation of these two body segments likely moves the COM to a less-challenging (lower pitch) longitudinal position. However, it also displaces the COM upwards (antiparallel with gravity), and likely vertically closer to COP. This is interesting when one considers that COM locations that are farther below COP are more favorable to pitch stability, because they lengthen the effective lever arm for the production of torque *via* active changes to stroke plane angle (Chapter 3; (Cheng and Deng, 2011b;Cheng *et al.*, 2011;Ristroph *et al.*, 2013;Willmott *et al.*, 1997)). So it seems moths sacrifice some pitch stability to compensate for the attachment of the weight. This could explain why moths laden with too-heavy weights anecdotally fail only in pitch rather than roll (as described in the **Results** overview). It is also plausible that the simultaneous (weight-ipsilateral) roll reorientation helps compensate for this by moving the weight (and thus the net COM slightly) back downwards (Fig. 4.7A).

Figure 4.7: Moths reorient in roll and pitch to compensate for off-axis loads

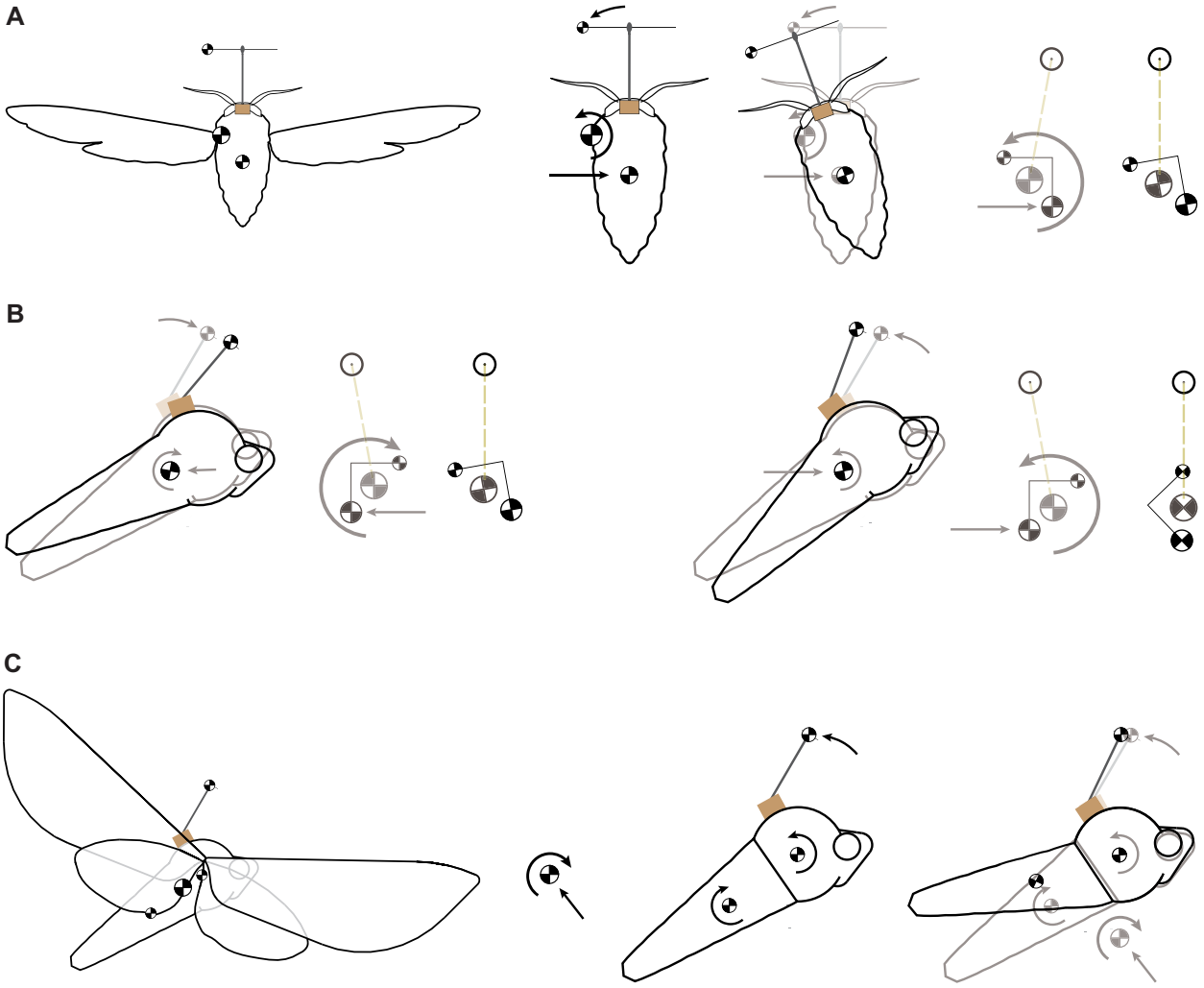

Moths reorient in roll and pitch in response to lateral and longitudinal COM displacement. In **A)**, the moth rolls to the side ipsilateral with the attached weight. Since the moth's body is much heavier than the fishing sinker, this likely shifts the net center of mass (COM) to the right, reducing weight-imposed roll torque. Because this also rotates the weight to a less vertical position, this should reduce the pitching moment as well. For both **A)** and **B)**, pendulum figures mimic the depicted reorientations. In these pendulums, the upper pivot point corresponds to a center of pressure (COP), the smallest checkered circle represents the fishing sinker's COM, the next largest checkered circle represents the moth's body COM, and the largest checkered circle represents net COM of the moth + sinker system. Note that systems are stable when the COM and COP are vertically aligned. In **B)**, both pitch-down and pitch up-movements may help reduce the pitching moment. Pitch-down moves the COM of the sinker farther forward and the COM of the moth farther back. Since the moth weighs more than the sinker, this should move the net COM backwards. Pitch-up moves the COM of the sinker backwards and the COM of the moth forwards, so that they are better vertically aligned. This may also reduce pitch torque, especially if the COP lies above the original (and new) COM. Moths chose to pitch down in response to the pitch perturbation much more often than they chose to pitch up. In **C)**, the moth pitches down, while moving its abdomen down in pitch, and its thorax up in pitch. This moves the net COM up and to the left, reducing the weight-imposed pitch torque. True measures of changes to net pitch torque would require precise COP and COM location.

Moths change wing kinematics to manipulate COP location
(supporting Hypotheses 3, 6, 9, 12)

Within the confines of this experiment, one cannot truly measure COP, but the wing kinematic measurements that correlate with roll and pitch torque indicate that Hypothesis 3 is correct. Results indicate greater fore-minus-aft wing sweep amplitude asymmetry (φ_{Δ}) moves the net COP forward to compensate for pitch-down torque, and smaller fore-minus-aft wing sweep amplitude asymmetry moves the COP backwards to compensate for pitch-up torque (supporting *Hypotheses 3,9,12*). Results also indicate lateral asymmetry in sweep ($\Phi_{LR\Delta}$) moves the net COP left or right to create roll-left or –right (supporting *Hypotheses 3,6*; though here p≈.06). In another lift-based net-COP relocation mechanism, results indicate higher/lower left *vs* right stroke plane angle creates rightwards roll torque in down/upstrokes ($Q\zeta_{LR\Delta}$) (supporting *Hypothesis 3*).

Stoke plane angle changes also create pitch torque
(supporting Hypotheses 8, 12, 14)

Unlike the wing kinematics described above, it's likely that the pitch torque from stroke plane reorientation (ζ_{Δ}) arises primarily from redirection of the net lift vector (Chapter 3; Cheng *et al.* 2011), rather than from COP relocation. More acute/obtuse stroke plane angles correlate with the creation of pitch-up/pitch-down torque, respectively (supporting *Hypotheses 8, 12*). This result is consistent with extant literature (*e.g.* (Cheng *et al.*, 2016;Cheng *et al.*, 2011;Wang *et al.*, 2008;Willmott and Ellington, 1997a)). Here, the coefficient relating ζ_{Δ} to $\overrightarrow{\tau_{\psi}}$ is slightly lower than the one that relates the second derivative of pitch to ζ_{Δ} in Chapter 3, (supporting *Hypothesis* 14). See Table 5.1 in Chapter 5 for further coefficient comparisons, and further discussion of *Hypotheses 14-15*.

More about up- vs. downstroke stroke plane angle and its role in roll

I did not initially expect $\zeta_{LR\Delta}$ to correlate with $\overrightarrow{\tau_{\psi}}$. Nevertheless, it makes sense that lower (effective) stroke plane angles in upstroke, and higher (effective) stroke plane angles in downstroke should both create more lift (upwards force). This is because the wing moves upwards in upstrokes, and downwards in downstrokes. Like most other insects, moths create lift during both halfstrokes (Weis-Fogh, 1973), but the downwards movement in downstroke enhances lift, while the upwards movement in upstroke diminishes it

(Bomphrey *et al.*, 2005;Liu *et al.*, 1998;Sane *et al.*, 2007). Thus an increase in the first and a decrease in the latter (here represented by $Q\zeta_{LR\Delta}$), should increase lift. Following this logic, when left wing $Q\zeta_{LR\Delta}$ is greater than right wing $Q\zeta_{LR\Delta}$, this should create roll-right torque (consistent with Eq. 4 and Fig. 4.4B & D, and depicted in Fig. 4.8).

Figure 4.8: Up-/downstroke stroke plane angle asymmetry changes lift, a novel roll wing kinematic

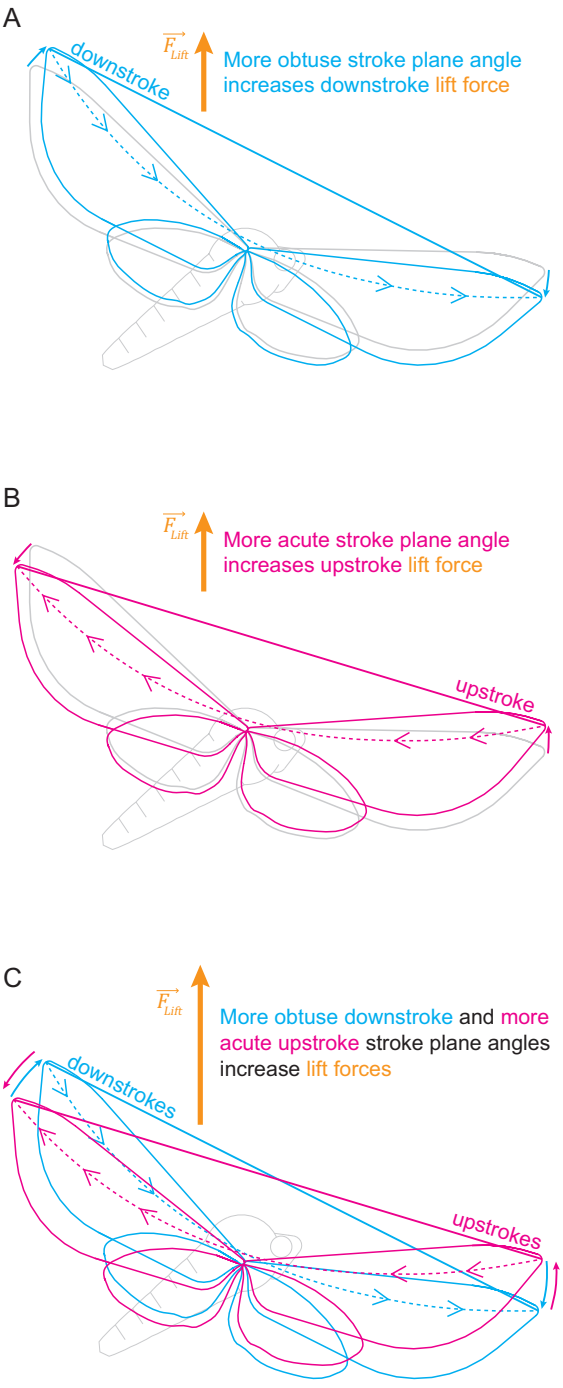

Asymmetrical lift from left-right, up-/downstroke stroke plane angle asymmetry creates roll torque. Panel **A)** shows the how changes at endstrokes alter stroke plane angle. In this explanation, higher downstroke and lower upstroke stroke plane angles enhance lift. If these endstroke changes interact with specific wing pitch timing differences, they could also (or alternatively) directly enhance lift in a manner similar to the Magnus effect, (Dickinson *et al.* 1999; Shyy *et al.* 2016; Sane and Dickinson 2002).

Upstroke and downstroke are a physically and temporally continuous cycle, so in the strictest sense, up- and downstroke stroke plane angle should be the same. However, in both this experiment and that of Chapter 3, I attempted to calculate a more kinematically/mechanically relevant stroke plane than this, since forces are highest at or just after midstroke (Bomphrey *et al.*, 2005;Liu *et al.*, 1998;Sane, 2003). Stroke plane measurements came from the majority of each halfstroke, but excluded "noise" from wing flips near the beginning and end of downstrokes. Near the beginning and end of halfstrokes, wing speed and thus forces are also low (*ibid.*). Perhaps moths use this relatively low-force endstroke time period to adjustment wing kinematics without incurring major aerodynamic penalties that would otherwise work against roll torque production). If these endstroke changes

interact with specific wing pitch timing differences and vortices, they could also (or alternatively) directly enhance lift in a manner similar to the Magnus effect (Dickinson *et al.* 1999; Shyy *et al.* 2016; Sane and Dickinson 2002).

In Chapter 2, I likely overlooked a role for left-right stroke plane asymmetry in the roll reorientations. In Chapters 3-4, I marked moth body and wing points on each analyzed video frame. In final analysis of Chapter 2 videos, I digitized only endstrokes and midstrokes, a method that precludes differentiation of up- and downstroke stroke plane angles.

Moths do not use lateral AOA asymmetry to compensate for the roll challenge (failing to support Hypotheses 4, 5)

I expected moths might use AOA asymmetries ($\alpha_{LR\Delta}$, $\alpha_{\zeta_{LR\Delta}}$, or $\xi_{LR\Delta}$) to create roll based on the results from Chapter 1. However, no version of up- or downstroke wing pitch significantly correlated with roll torque. During sideslip, both the AOA and elevation amplitude asymmetries moths use to create roll torque should decrease FCT-based roll damping (Chapter 2). Moths use a different method here, (where FCT is absent), which suggests they actively modify their wing kinematic strategies to fit specific circumstances.

Passive explanations are feasible. For example, the wing pitch angle changes I identified in Chapter 2 could be coupled with gyroscopic wing reactions to rotational perturbations applied over a larger time scale (Eberle *et al.* 2016), and/or to active endstroke adjustments (Beatus and Cohen, 2015). Here in this study, moths alter endstroke wing kinematics to create asymmetric up- and downstroke stroke planes (a novel wing kinematic change which was discussed in the previous section and illustrated in Fig. 4.8).

Hypothesis 5 followed from *Hypothesis 4*; since *Hypothesis 4* was unsupported, *Hypothesis 5* is of no practical value.

Up-/Down AOA/deviation asymmetry correlates only weakly with longitudinal COM displacement (weakly supporting Hypothesis 10)

I expected moths to increase their effective angle of attack (AOA) in downstrokes and decrease AOA in upstrokes in order to create pitch torque. In the impulsive pitch perturbations (Chapter 3), stroke plane deviation angle correlates with pitch torque in just such a manner (there, as $-Q\xi_{\Delta}\cos(\zeta_{\Delta})$), and also

with wing pitch angles that alternatively approximate effective AOA. While downstroke $-Q\xi_{\Delta}\cos(\zeta_{\Delta})$ does in fact significantly correlate with longitudinal COM displacement as one would expect for the generation of pitch-up torque, upstroke ξ_{Δ} does not. Furthermore, no computed version of AOA survives the stepwise BIC model selection process as an informative predictor for pitch torque.

Moths do not use elevation amplitude asymmetry to compensate for the roll challenge (supporting Hypothesis 7)

Since FCT damping is not a major force factor in near-hover conditions, I expected left-minus-right elevation amplitude asymmetry ($\theta_{LR\Delta}$) to have either a positive relationship with roll torque, or none at all. As expected, I did not find a statistically significant relationship between $\theta_{LR\Delta}$ and the estimate of the roll torque challenge that the moths face.

Both-halfstroke and downstroke kinematics correlate more strongly than upstroke ones (supporting Hypothesis 11)

Introducing separate up- and downstroke wing kinematics to the stepwise model selection process results in no significant (ΔBIC>5) improvements over best-BIC both-halfstroke models. Thus, both-halfstroke variables are better predictors of both roll and pitch (or in the sole case of downstroke $\sin(-\zeta_{\Delta})$ *vs.* $\overrightarrow{\tau_{\psi}}$, statistically just as good). These both-halfstrokes models agree best with my initial hypotheses and have the strongest *a priori* theoretical foundation (Chapters 2-3).

Since forces are higher during downstroke, I predicted coefficients for downstroke wing kinematics would be larger and/or more statistically significant than their upstroke counterparts. When I exclude non-amplitude both-halfstroke variables from the stepwise selection process, downstroke variables show consistently better p-values than upstroke ones, with the latter often lacking in statistical significance (p<.05). This supports *Hypothesis 11*.

I did not test separate up- and downstroke variables for amplitudes (elevation or sweep) because the moths here are in stable hover. Any increase in upstroke amplitudes would mean a simultaneous increase in downstroke amplitudes, and *vice versa*. Furthermore, I believe the separate up- and downstroke estimates of stroke plane angle and AOA-proxies (ζ, α_{Δ}, $\alpha_{\zeta_{\Delta}}$, and ξ_{Δ}) are sufficient to test the most obvious within-stroke dynamic differences.

Analysis of methods and limitations

The most severe limitation on this study was a lack of good estimates for COM and COP. True understanding of the locations of COP and COM—even during simple hover when COP & COM is net stationary over the course of the entire stroke cycle—is still relatively lacking. Here moth COM location most likely changes during the course of the trials because the moths drink sugar water from the flowers, rotate their bodies and body segments, and of course, are attached to a sinker of variable weight and location. Moth COP location also likely differs from the hover case because moths alter their flapping kinematics in response to the perturbation. Furthermore, moths may also be mechanically coupled to the feeding flower by their firmly-attached proboscis; providing a lever arm longer than their entire body length that could easily affect net torque (by altering COP location) to an unknown degree in different treatments or trials. Still, flight studies with proboscis-coupling are common-place (***e.g.*** (Sponberg ***et al.***, 2015)).

Nevertheless, flight kinematic results mostly match expectations based on previous work, and it is unlikely slight adjustments to this experiment's estimate of COM location would drastically change its results. (Increasing the size of the data set would be a better route if the goal were more statistical certainty, especially for kinematics that showed marginal statistical significance, like stroke plane deviation angle, ξ_{Δ}.) In fact, the several versions of $\vec{\tau}$ I tried, such as in the MGRF or SRF, result in the very same best-BIC models albeit with different significance levels and coefficient values. Furthermore, while the best-BIC models I identified in this study may not exhibit extremely high statistical certainty, almost all kinematics *not* included in the best-BIC models (with the exception of stroke plane deviation angle ξ_{Δ} ***vs***. pitch torque $\overrightarrow{\tau_{\psi}}$) were well outside the range of statistical significance (with p-values often as high as ~0.8). Thus I believe the relationships I identified in my best-BIC models indicate real physical effects.

Chapter 4 Symbols and Abbreviations

Box 4.1: Abbreviations

AOA	effective Angle Of Attack; represents the angle at which the wing encounters the air
BRF	Body Reference Frame: reference frame from the perspective of the moth's COM, in which the moth's anatomical landmarks and canonical hover orientation determine x, y, and z.
COM	Center Of Mass: point where the sum of the product of individual units of mass and their distance away from that point equal zero.
COP	Center Of Pressure: net sum of force production by the wings, time-averaged over the course of a stroke cycle
FCT	Flapping Counter Torque: idea that rotations change the velocity of wings flapping in that rotational plane, damping the rotation. First shown for yaw.
GRF	Global Reference Frame: based on the camera calibration (world view frame)
MGRF	Modified Global Reference Frame: world view has been rotated in yaw so that the x-axis is in line with the longitudinal axis of the moth.
SRF	Standard Reference Frame: frame where GRF points are rotated about the z-, then x-, and then the y-axis such that, in the new SRF: 1) the wing base points and the abdomen point lie on a shared x-y plane, 2) the x-z plane includes the abdomen point and a (0,0,0) that is the midpoint of a line connecting the two wing base points 3) the y-z plane is perpendicular to the first two planes and intercepts the same (0,0,0) point.

Box 4.2: Subscripts, Constants, and Mathematical Symbols

×; | |; ∈; ∥; Δ; ≈; ~	"by" or cross-product; absolute value or magnitude of; member of the given set; parallel with; change in relative to control; about equal to; on the order or in the vicinity of
$\vec{\ }$; $\overrightarrow{a}$; $\overleftrightarrow{\ }$; $\bar{\ }$	accents respectively indicate the attendant variable is a vector; the magnitude of the vector for direction $\hat{a}$ (directional unit vector); a line; and a plane
$_{ab}$	a subscript which indicates the antecedent is a coefficient relating b to a
g	gravitational acceleration (980.665 $cm\ s^{-2}$)
$_{LR}$	differences in a kinematic measurement between the left and right side of a moth; *ie* left minus right
m	moth plus pin average mass from measurements before, between, and after treatments
Q	multiplier that is -1 for upstrokes and +1 for downstrokes
$_{\Delta}$	a subscript which indicates the given wing kinematic variable has been mean-centered by subtracting (separate upstroke and downstroke) means measured for that variable in the control trial; for body angles (*i.e.* roll and pitch), upstrokes and downstrokes were averaged together.
	lack of subscript on a kinematic variable indicates that I made no attempt to mean-center/adjust the variable

Box 4.3: Geometric Characteristics of M. sexta

$\vec{L}_1; \vec{L}_2; \bar{P}$	geometric characteristics of the stroke plane as defined in Fig. 4.3 and its caption
$\vec{R}_1; \vec{R}_2; \vec{R}_3; \vec{R}_4; \vec{R}_5$	vectors connecting digitized moth points as defined in Fig. 4.3 and its caption
$x_S; z_S$	x- and z- positions of T-bar center (for control treatments) or sinker center (for non-control treatments) relative to the center of the two wing bases in the MGRF. Shown in Fig. 4.3.
z_A	The abdomen's z- position relative to the center of the two wing bases in the MGRF is denoted by z_A. Shown in Fig. 4.3.

Box 4.4: Wing and Body Kinematics

$x; y; z$	in the BRF, $+x$ is forwards for the moth, $+y$ is rightwards for the moth, and , $+z$ is downwards for the moth in the BRF, and $+z$ is // with gravity in the GRF and MGRF.
$\alpha_\zeta; \alpha_{\zeta_\Delta}; \alpha_{\zeta_{LR\Delta}}$	wing pitch angle: α_ζ (related to AOA) is the angle the (x, z) components of the vector connecting the hindwing tip to the forewing tip makes relative to the stroke plane; α_{ζ_Δ} is change relative to control α_ζ; $\alpha_{\zeta_{LR\Delta}}$ is left-right asymmetry in α_{ζ_Δ}
$\beta; \beta_\Delta$	moth whole-body roll angle relative to the horizontal plane; roll angle measured relative to control's mean roll angle
$\zeta; \zeta_\Delta; \zeta_{LR\Delta}$	stroke plane inclination angle: ζ is the angle of the stroke plane relative to the BRF horizontal plane; ζ_Δ is change relative to control ζ; $\zeta_{LR\Delta}$ is left-right asymmetry in ζ_Δ
$\theta_p; \theta_{LR\Delta}$	peak-to-peak wing elevation amplitude (see Fig. 4.3); left-right asymmetry in θ_p relative to that for the control trial
$\vartheta_+; \vartheta_-$	elevation: forewing elevation angle relative to a BRF horizontal plane through the wing base, at the end of downstroke ϑ_+; and upstroke ϑ_-
ϑ_Δ	elevation offset $\vartheta = \vartheta_+ + \vartheta_-$, and ϑ_Δ is change relative to control ϑ
$\Phi_p; \Phi_{LR\Delta}$	Peak-to-peak wing sweep amplitude (see Fig. 4.3); left-right asymmetry in θ_p relative to that for the control trial
$\varphi_+; \varphi_-$	sweep: forewing azimuthal angle relative to a BRF vertical plane through the wing base, at the end of downstroke φ_+; and upstroke φ_-
φ_Δ	dorsoventral sweep asymmetry $\varphi = \varphi_+ + \varphi_-$, and φ_Δ is change relative to control φ
$\xi; \xi_\Delta; \xi_{\Delta LR}$	stroke plane deviation angle: ξ (related to AOA) is the angle the forewing makes at midstroke, measured perpendicular relative to the stroke plane; ξ_Δ is change relative to control ξ; $\xi_{\Delta LR}$ is left-right asymmetry in ξ
$\vec{\tau}$	estimate of COM imbalance (the cross product of the vertical force created by the sinker with a vector stretching from the visually estimated COM to the sinker position, in the BRF

$\overrightarrow{\tau_\beta}; \overrightarrow{\tau_{\beta 0}}$	the roll portion of $\vec{\tau}$ ($\overrightarrow{\tau_\beta}$) comes from sinker mass and lateral placement; $\overrightarrow{\tau_\beta}$ was calculated in the BRF; $\overrightarrow{\tau_{\beta 0}}$ was calculated in the SRF.
$\overrightarrow{\tau_\psi}; \overrightarrow{\tau_{\psi 0}}$	the pitch portion of $\vec{\tau}$ ($\overrightarrow{\tau_\psi}$) comes from sinker mass and longitudinal placement. $\overrightarrow{\tau_\psi}$ was calculated in the BRF; $\overrightarrow{\tau_{\psi 0}}$ was calculated in the SRF
$\psi; \psi_\Delta$	moth body pitch, $\vec{R}_4$ relative to the horizontal plane (Fig. 4.3); ψ_Δ is change relative to control ψ

Box 4.5: Model Coefficients

$K_{\overrightarrow{\tau_{\beta 0}}\beta}$	coefficient relating β_Δ to $\overrightarrow{\tau_{\beta 0}}$	$K_{\overrightarrow{\tau_{\psi 0}}\psi}$	coefficient relating ψ_Δ to $\overrightarrow{\tau_{\psi 0}}$
$K_{\overrightarrow{\tau_\beta}\zeta}$	coefficient relating $\zeta_{LR\Delta}$ to $\overrightarrow{\tau_\beta}$	$K_{\overrightarrow{\tau_\psi}\varphi_\Delta}$	coefficient relating ζ_Δ to $\overrightarrow{\tau_\psi}$
$K_{\overrightarrow{\tau_\beta}\Phi}$	coefficient relating $\Phi_{LR\Delta}$ to $\overrightarrow{\tau_\beta}$	$K_{\overrightarrow{\tau_{\psi 0}}\zeta_\Delta}$	coefficient relating φ_Δ to $\overrightarrow{\tau_\psi}$

REFERENCES

Baader, A. (1990). The posture of the abdomen during locust flight: regulation by steering and ventilatory interneurones. *J. Exp. Biol.* **151,** 109-131.

Beatus, T. and Cohen, I. (2015). Wing-pitch modulation in maneuvering fruit flies is explained by an interplay between aerodynamics and a torsional spring. *Phys. Rev. E* **92,** 022712.

Bomphrey, R. J., Lawson, N. J., Harding, N. J., Taylor, G. K. and Thomas, A. L. (2005). The aerodynamics of Manduca sexta: digital particle image velocimetry analysis of the leading-edge vortex. *J. Exp. Biol.* **208,** 1079-1094.

Camhi, J. M. (1970). Yaw-correcting postural changes in locusts. *J. Exp. Biol.* **52,** 519-531.

Cheng, B. and Deng, X. (2011a). Translational and rotational damping of flapping flight and its dynamics and stability at hovering. *IEEE Trans. Robotics* **27,** 849-864.

Cheng, B. and Deng, X. (2011b). Translational and rotational damping of flapping flight and its dynamics and stability at hovering. *IEEE Trans. Robotics* **27,** 849-864.

Cheng, B., Tobalske, B. W., Powers, D. R., Hedrick, T. L., Wang, Y., Wethington, S. M., Chiu, G. T. and Deng, X. (2016). Flight mechanics and control of escape manoeuvres in hummingbirds. II. Aerodynamic force production, flight control and performance limitations. *J. Exp. Biol.* **219,** 3532-3543.

Cheng, B., Deng, X. and Hedrick, T. L. (2011). The mechanics and control of pitching manoeuvres in a freely flying hawkmoth (*Manduca sexta*). *J. Exp. Biol.* **214,** 4092-4106.

Dickinson, M. H., Lehmann, F. O. and Sane, S. P. (1999). Wing rotation and the aerodynamic basis of insect flight. *Science* **284,** 1954-1960.

Dickerson, B. H., Aldworth, Z. N. and Daniel, T. L. (2014). Control of moth flight posture is mediated by wing mechanosensory feedback. *J. Exp. Biol.* **217,** 2301-2308.

Dyhr, J. P., Morgansen, K. A., Daniel, T. L. and Cowan, N. J. (2013). Flexible strategies for flight control: an active role for the abdomen. *J. Exp. Biol.* **216,** 1523-1536.

Eberle, A. L., Dickerson, B. H., Reinhall, P. G. and Daniel, T. L. (2015). A new twist on gyroscopic sensing: body rotations lead to torsion in flapping, flexing insect wings. *J. R. Soc. Interface* **12,** 20141088.

Ellington, C. P. (1984). The aerodynamics of hovering insect flight. II. Morphological parameters. *Phil. Trans. R. Soc. Lon. B* **305,** 17-40.

Frye, M. A. (2001). Effects of stretch receptor ablation on the optomotor control of lift in the hawkmoth *Manduca sexta*. *J. Exp. Biol.* **204,** 3683-3691.

Götz, K. G., Hengstenberg, B. and Biesinger, R. (1979). Optomotor control of wing beat and body posture in Drosophila. *Biol. Cybern.* **35,** 101-112.

Greeter, J. S. and Hedrick, T. L. (2016). Direct lateral maneuvers in hawkmoths. *Biol. Open*, bio. 012922.

Hinterwirth, A. J. and Daniel, T. L. (2010). Antennae in the hawkmoth *Manduca sexta* (Lepidoptera, Sphingidae) mediate abdominal flexion in response to mechanical stimuli. *J. Comp. Phys. A* **196,** 947-956.

Jankauski, M. and Shen, I. (2016). Experimental studies of an inertial-elastic rotating wing in air and vacuum. *Int. J. Micro Air Veh.* **8,** 53-63.

Jenkins, A. L. (2016). *The Homogeneity of Optimal Sensor Placement Across Multiple Winged Insect Species*. Master's thesis, University of Washington.

Kass, R. E., Raftery, A. E. (1995), Bayes Factors, *J. Amer. Statistical Assoc.*, **90**.**430,** 773–795.

Kim, J. and Han, J. (2014). A multibody approach for 6-DOF flight dynamics and stability analysis of the hawkmoth Manduca sexta. *Bioinsp. Biomim.* **9,** 016011.

Liu, H., Ellington, C., Kawachi, K. and c. (1998). A computational fluid dynamic study of hawkmoth hovering. *J. Exp. Biol.* **201 (Pt 4),** 461-477.

Noda, R., Maeda, M. and Liu, H. (2013). Effect of Passive Body Deformation of Hawkmoth [*sic.*] on Flight Stability. *Intelligent Autonomous Systems 12*, pp. 835-842: Springer.

Ristroph, L., Berman, G. J., Bergou, A. J., Wang, Z. J. and Cohen, I. (2009). Automated hull reconstruction motion tracking (HRMT) applied to sideways maneuvers of free-flying insects. *J. Exp. Biol.* **212,** 1324-1335.

Ristroph, L., Ristroph, G., Morozova, S., Bergou, A. J., Chang, S., Guckenheimer, J., Wang, Z. J. and Cohen, I. (2013). Active and passive stabilization of body pitch in insect flight. *J. R. Soc. Interface* **10,** 20130237.

Ristroph, L., Bergou, A. J., Ristroph, G., Coumes, K., Berman, G. J., Guckenheimer, J., Wang, Z. J. and Cohen, I. (2010). Discovering the flight autostabilizer of fruit flies by inducing aerial stumbles. *Proc. Natl. Acad. Sci. USA* **107,** 4820-4824.

Sane, S. P. (2003). The aerodynamics of insect flight. *J. Exp. Biol.* **206,** 4191-4208.

Sane, S. P. and Dickinson, M. H. (2002). The aerodynamic effects of wing rotation and a revised quasi-steady model of flapping flight. *J. Exp. Biol.* **205,** 1087-1096.

Sane, S. P., Dieudonne, A., Willis, M. A. and Daniel, T. L. (2007). Antennal mechanosensors mediate flight control in moths. *Science* **315,** 863-866.

Sponberg, S., Dyhr, J. P., Hall, R. W. and Daniel, T. L. (2015). Luminance-dependent visual processing enables moth flight in low light. *Science* **348,** 1245-1248.

Shyy, W., Kang, C. K., Chirarattananon, P., Ravi, S., and Liu, H. (2016). Aerodynamics, sensing and control of insect-scale flapping-wing flight. *Proc. R. Soc. A* **472.2186,** 20150712.

Stengel, R. F. (2015). *Flight dynamics*: Princeton University Press.

Usherwood, J. R. and Ellington, C. P. (2002). The aerodynamics of revolving wings I. Model hawkmoth wings. *J. Exp. Biol.* **205,** 1547-1564.

Wang, H., Ando, N. and Kanzaki, R. (2008). Active control of free flight manoeuvres in a hawkmoth, Agrius convolvuli. *J. Exp. Biol.* **211,** 423-432.

Weis-Fogh, T. (1973). Quick Estimates of Flight Fitness in Hovering Animals, Including Novel Mechanisms for Lift Production. *J. Exp. Biol.* **59,** 169-230.

Whitehead, S. C., Beatus, T., Canale, L. and Cohen, I. (2015). Pitch perfect: how fruit flies control their body pitch angle. *J. Exp. Biol.* **218,** 3508-3519.

Willmott, A. P., Ellington, C. P. and Thomas, A. L. (1997). Flow visualization and unsteady aerodynamics in the flight of the hawkmoth, Manduca sexta. *Phil. Trans. R. Soc. B: Biol. Sci.* **352,** 303-316.

Willmott, A. P. and Ellington, C. P. (1997a). The mechanics of flight in the hawkmoth Manduca sexta. I. Kinematics of hovering and forward flight. *J. Exp. Biol.* **200,** 2705-2722.

Willmott, A. P. and Ellington, C. P. (1997b). The mechanics of flight in the hawkmoth Manduca sexta. II. Aerodynamic consequences of kinematic and morphological variation. *J. Exp. Biol.* **200,** 2723-2745.

CHAPTER 5
MY CONCLUSIONS IN PERSPECTIVE

Overview

This chapter puts my results and conclusions in context with recent work of others who study flight in animals. I stress the importance of my contributions, specifically identifying novel sources of stability in flapping flight, as well as identifying which wing kinematics contribute to the creation of maneuvers in real insects.

Prior State of Work

Prior to my studies, there was a significant body of work on the morphology and flight of tethered insects from the old (*e.g.* (Fraenkel, 1932;Schilstra and Hateren, 1999;Weis-Fogh, 1956)) to the new (*e.g.* (Sugiura and Dickinson, 2009)). Yet free-flight studies that focused on turning maneuvers or rotational stability in insect flight were rare (but see (Fry *et al.*, 2003;Wang *et al.*, 2008;Wang *et al.*, 2003)). Much work has been done since then, with the most notable progress on model organisms *Drosophila melanogaster* ("fruit flies") and *Manduca sexta* ("hawkmoths").

Work on *D. melanogaster* has primarily approached the problem from the *a priori* view that quick active reactions are necessary to maintain stability against small perturbations (*e.g.* (Beatus *et al.*, 2015)). Typically, computational fluid dynamic (CFD) modeling studies agree with this assessment (Sun *et al.*, 2007;Sun, 2014;Sun and Wang, 2007); although studies reaching different conclusions exist (*e.g.* (Gao *et al.*, 2011;Farque and Humbert 2010a)). My work on *M. sexta* flight maneuvers has typically approached the issue assuming that important or relevant the mechanisms for passive flight stability had yet to be identified. This view was informed by key papers that showed that yaw is passively damped across an array of flight scales, including that of fruit flies (*e.g.* (Cheng *et al.*, 2009;Hedrick *et al.*, 2009;Hesselberg and Lehmann, 2007;Sun, 2014;Warrick *et al.*, 2012), in partial disagreement with prominent work on the

matter (Fry *et al.*, 2003). Furthermore, a few CFD studies have indeed suggested hawkmoth flight has some range of natural stability in roll and/or pitch (*e.g.* (Gao *et al.*, 2009)), especially when updated with some flexibility features similar to the ones my dissertation identifies in real moths (*e.g.* (Kim *et al.*, 2016;Noda *et al.*, 2013;Noda *et al.*, 2014)). Yet a focus on the role of active responses in *M. sexta* has remained prominent (*e.g.* (Sponberg *et al.*, 2015)).

Advancement 1: How Hawkmoths Move Left & Right, Up, and How They Roll and Pitch

The most basic of my contributions is my identification of the wing kinematics that create roll, pitch, yaw, as well as lateral and upwards vertical motion, specifically in the case of free flight. As a result of my work, the rotation of hawkmoths in many basic degrees of freedom are now much better described. Though at least one free-flight insect pitch paper had been published (Wang *et al.*, 2008), prior to my work only yaw (Hedrick *et al.*, 2009) was reasonably well-understood. Concurrent advancements in flight largely identify the same wing kinematic factors as important to creating roll, yaw, pitch, sideslip, and vertical motion in insect-scale hovering flight (Beatus and Cohen, 2015;Beatus *et al.*, 2015;Cheng *et al.*, 2016;Iams, 2012;Ravi *et al.*, 2015;Read, 2015;Ristroph *et al.*, 2009;Ristroph *et al.*, 2013;Whitehead *et al.*, 2015), although many interpreted these results differently with regards to stability implications, as discussed below.

Advancement 2: Stability in Roll

Much CFD research predicts relatively small margins of stability in roll for insects across a wide range of flight scales, from fruit flies to hawkmoths (Faruque and Humbert, 2010b;Humbert and Faruque, 2011;Xu and Sun, 2013;Zhang and Sun, 2011;Zhang and Sun, 2010). These studies typically predict that roll and sideslip are linked in an unstable divergence (much like the *a priori* theory described for pitch and longitudinal motion in Chapter 3; left side of Fig. 3.4).

Nevertheless, my work indicates that roll is instead heavily damped, and, at least in hawkmoths, *inhibited* (rather than reinforced) by lateral motion (Greeter and Hedrick, 2016). In Chapter 2, hawkmoth wing kinematics correlated with the first, rather than the second, derivative of roll orientation. Active decreases in roll-contralateral elevation amplitude (relative to the ipsilateral) further indicate flapping

countertorque (FCT) is a major source of rotational damping during this movement. This result agrees with conclusions from turning cockatoos (Hedrick *et al.*, 2007), as well as conjectures that mosquito roll may be heavily damped as well (Iams, 2012).

Though the wing kinematics that create roll in *M. sexta* are surprisingly similar to those of *D. melanogaster* (Beatus and Cohen, 2015;Beatus *et al.*, 2015;Ristroph *et al.*, 2009), my conclusions differ from their assertion that rotations about the body long axis are almost exclusively actively damped (Beatus and Cohen, 2015;Beatus *et al.*, 2015). The rigid model they use to justify this conclusion does not allow for FCT effects (Hedrick *et al.*, 2009), nor gyroscopic damping effects (Chapter 3), and their theoretical framework also does not address the counter-FCT effects (Greeter and Hedrick, 2016) of the active wing kinematic changes they witnessed post-perturbation. Still, many CFD models identifying unstable roll in *D. melanogaster* roll do endeavor to include FCT. It is possible that roll stability rules are different for the tiny fruit fly [Re ~150, m ~1mg; (Fry *et al.*, 2005;Vogel, 1966)], than for the comparatively massive hawkmoth [Re ~8000, m ~1.4g (Sane, 2003;Usherwood and Ellington, 2002; Chapters 1-4)]. Stability rules are also likely different when perturbation "impulses" last longer than an entire wingstroke (Ristroph et al. 2010;Beatus and Cohen, 2015;Beatus *et al.*, 2015), rather than much less than a halfstroke (Chapter 3).

My correlation of wing kinematics with roll velocity in the active maneuvering case (Chapter 2) but roll torque in the hover case (Chapter 4), combined with the absence of wing kinematics that would reduce FCT in the latter, make a strong case for passive roll damping in *M. sexta*. Future research should investigate the scaling of roll damping with size, and should re-examine left-right stroke plane asymmetry in the active roll maneuver case (which I did not measure in Chapter 2, but found to be important in Chapter 3).

Figure 5.1: Summary of GRF velocity/viscous sources of damping during roll rotations

A *flapping countertorque works against rotations in the flapping plane*

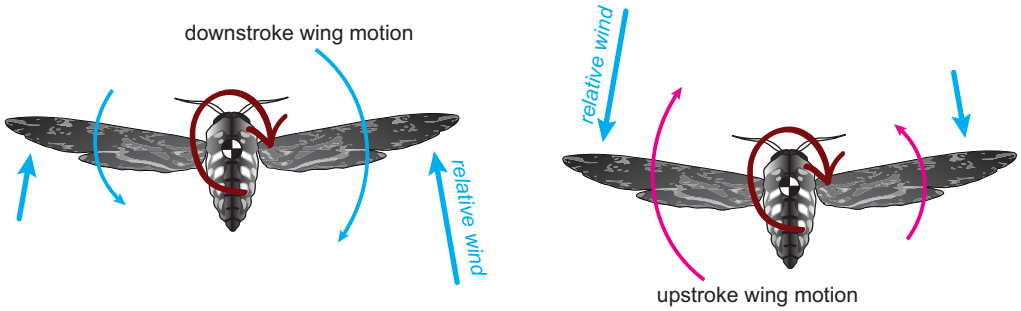

B *roll and lateral motion increase velocity (and thus magnify lift) asymmetries in upstrokes*

C *roll induces effective AOA asymmetries which create countertorque*

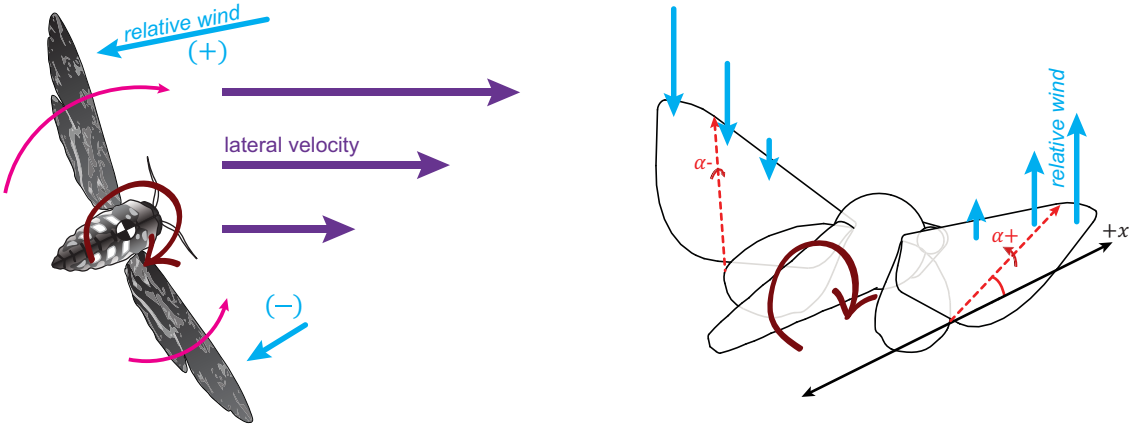

D

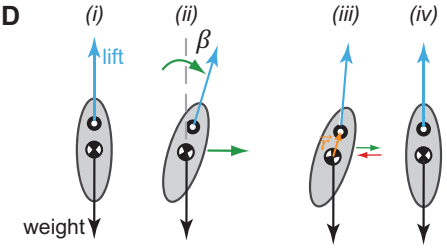

GRF Velocity/viscous sources of roll-damping. Panel **A** depicts the flapping countertorque (FCT) that arises from wing movement around the moth's roll rotational axis. Panel **B** depicts how the coupling of rightwards roll with rightwards linear movement magnifies the FCT damping effect during upstrokes by increasing the velocity on the moth's left wing over that of its right. **C** shows how a rightwards roll decreases left effective angle of attack (AOA) and increases right effective AOA. In the active roll maneuvers of Chapter 2, moths countered effects **A** and **B** with reduced left (relative to right) wing elevation amplitude and effects **A** and **C** with increased left (relative to right) wing pitch angles. **D**, in the style of Ristroph *et al.* (2009), shows the reaction of a lift-generating rigid body to a theoretical roll-right perturbation in the undamped *(i–ii)* and damped *(iii-iv)* cases. In *(iii)*, roll is damped by resistance of the "roll" stroke plane angle (implicit in **A-B**, and Fig. 5.2A-B), so lift remains more vertical than the rigid body, creating pendular countertorque. Rightwards lateral movement (green) further damps roll (β) as shown in Chapter 2. Thus roll could eventually be restored in the roll-damped case, as it is in pitch, with damping of the "pitch" stroke plane angle (Chapter 3; Fig. 3.4B). As in other figures, the checkered circle represents center of mass, and the circle with the white center represents center of pressure. Translation likely creates differential drag and thrust that directly damps flight maneuvers, especially roll-limited sideslips (Faruque and Humbert, 2010b); this is known as flapping counterforce (FCF), but is not depicted in this figure.

Figure 5.2: Inertial roll damping factors. Resistance of roll stroke plane angle, damping reactions at endstrokes, and in wing pitch

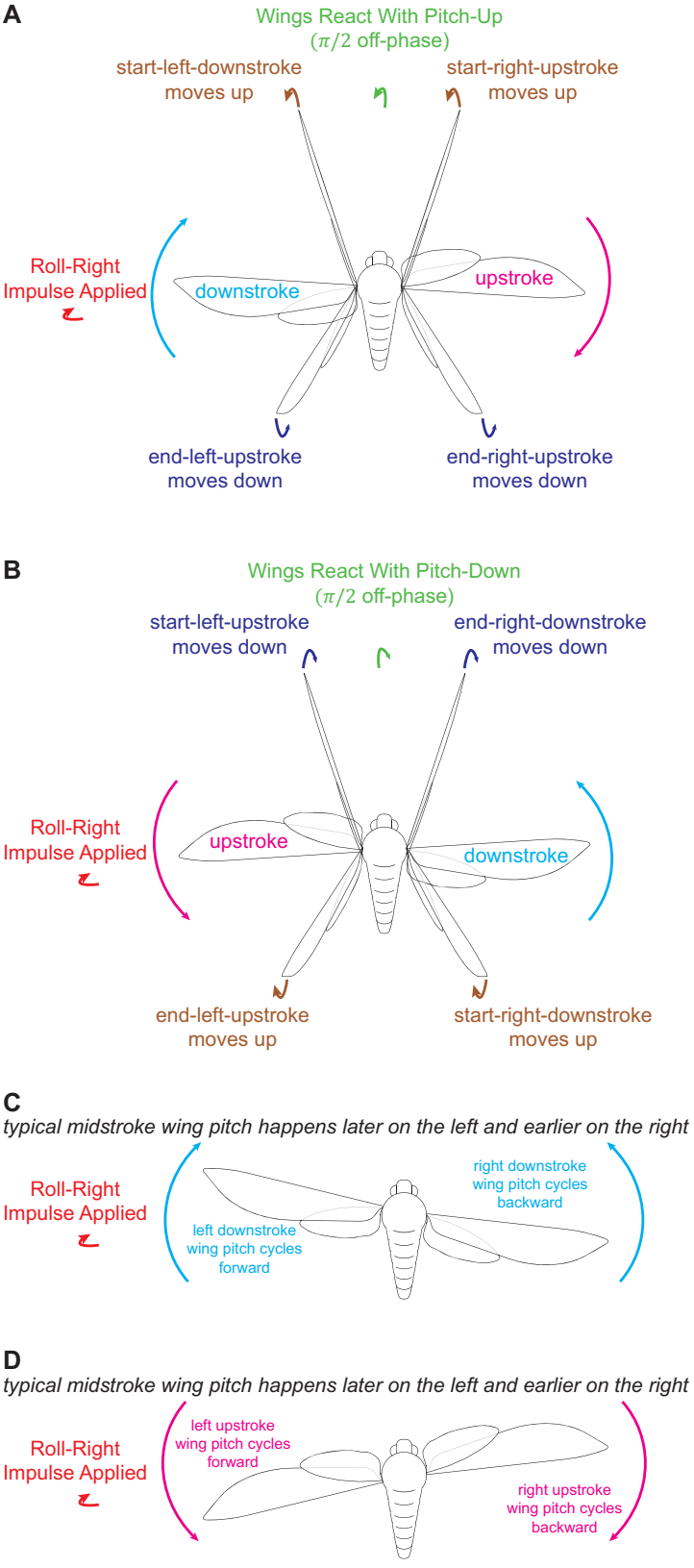

Thought experiment: Roll-right impulse creates inertio-viscous damping. In **A-B**, a roll impulse to flapping wings creates a Coriolis reaction at endstrokes. These endstroke reactions appear to match those shown in to create roll-left torque in Chapter 4. Note that resistance of the roll stroke plane to movement should create pendular stability (as shown for stroke plane and pitch in Chapter 3), and matches GRF viscous damping factors in roll (Fig. 5.1A-B & 5.1D). In **C-D**, the theoretical roll-right impulse causes left wing pitch timing to cycle forward, and right wing pitch timing to cycle backward. Slight differences in wing pitch timing, and asymmetrical midstroke wing pitch, are associated with roll torque in fruit flies (Ristroph *et al.*, 2009) and hawkmoths (Chapter 2). Intriguingly, this change would also reinforce each of the damping factors depicted in 5.1A-D.

It is likely that the gyroscopic damping I identified in the pitch case (Fig. 5.4) also damps roll (Fig. 5.2A-B). In theory, if we apply a roll-right torque to a flying moth, we should again see a gyroscopic reaction $\pi/2$ out of phase—at both endstrokes. In the left wing, this would decrease downstroke stroke plane angle, and increase upstroke stroke plane angle. In the right wing, this would increase downstroke stroke plane angle, and decrease upstroke stroke plane angle. In Chapter 4, I showed this combination of changes to stroke plane angle correlates

with roll-left torque (Fig. 4.7). Thus the stroke plane reactions of the wings induced by rotation should damp roll.

The wing pitch timing differences from a theoretical roll impulse/rotation (Fig. 5.1C-D) also match both active wing kinematic changes and passive damping factors associated with the creation of roll torque in the opposite direction from the given perturbation. In fact, the overhead view of the theoretical hawkmoth in Fig. 5.2C closely matches that of a real fruit fly seen in Ristroph *et al.* (2009), in both sweep and wing pitch timing. They proposed that, because wing pitch changes steeply near midstroke, even slight asymmetries in wing pitch timing generate relevant asymmetric forces. Based on continuous wing pitch angles from the control moths in Chapter 4 (Fig. 5.3), the similar dynamics are present in hawkmoths.

Based on this logic, a roll-right impulse would reduce left, and increase right AOA at (and just after) midstroke (for both upstrokes and downstrokes). I showed these near-midstroke wing pitch asymmetries generate roll-left torque in *M. sexta*. Rotation induced by the roll-right perturbation, and the resultant sideslip, would induce differences in the vertical flow velocity on either side of the moth (Fig. 5.3A-B) further damping roll; the more perpendicular orientation of the lower-wing-pitch left wing would further magnify this FCT effect, especially in upstrokes (Chapter 2). Thus, this inertia-induced wing asymmetry would decrease left *vs.* right force production on its own, and also complement the viscous damping factors identified in Chapter 2.

Other rotational modes also affect wing pitch gyroscopically (Eberle *et al.*, 2015). So, future research should address the role of torsional wing inertia (wing flipping inertia) in the creation of stability in other degrees of freedom as well, such as pitch or yaw.

Figure 5.3: Wing pitch angle in M. sexta

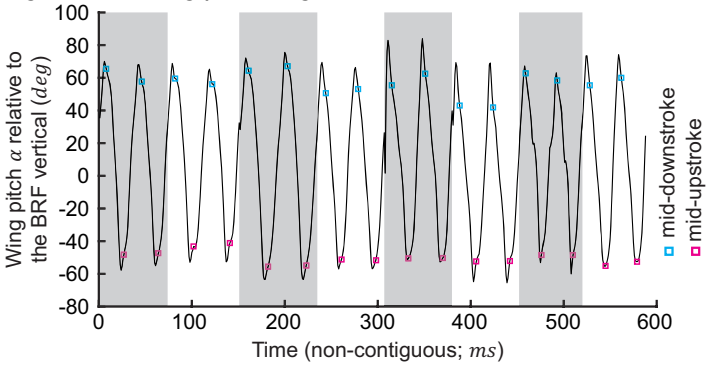

Wing pitch angle from 8 hovering moths. A concatenated time series of wing pitch angle, measured similar to Fig. 2.3C, but with a wing chord relative to the moth's *vertical* BRF plane. Excerpts are from the eight control treatments in Chapter 4. Note the sharp changes in wing pitch near midstrokes are similar to those that allow timing asymmetries to create roll in fruit flies (Ristroph *et al.*, 2009).

Advancement 3: Stability in Pitch

Figure 5.4: Inertial and viscous effects work together to stabilize pitch
Summary (reprint) of Figure 3.7. See Chapter 3 for further detail. The reaction of wings to a pitch impulse in **B)** match that of **A)** a similarly arranged spinning wheel. The **E)** same or **D)** similar wing reactions to perturbation are enhanced by rotational drag. In keeping with the discussion of wing torsion from the previous section (Fig. 5.2C-D), it is interesting to note that inertial resistance of the wings to flipping should enhance the damping factors presented in **B-D**. Note that it is possible wing deviation angle changes interact with the angular momentum of flipping wings to (passively) create a pitch-restoring dorsoventral sweep asymmetry response like the one I witnessed in Chapter 3, but this figure does not depict such an effect.

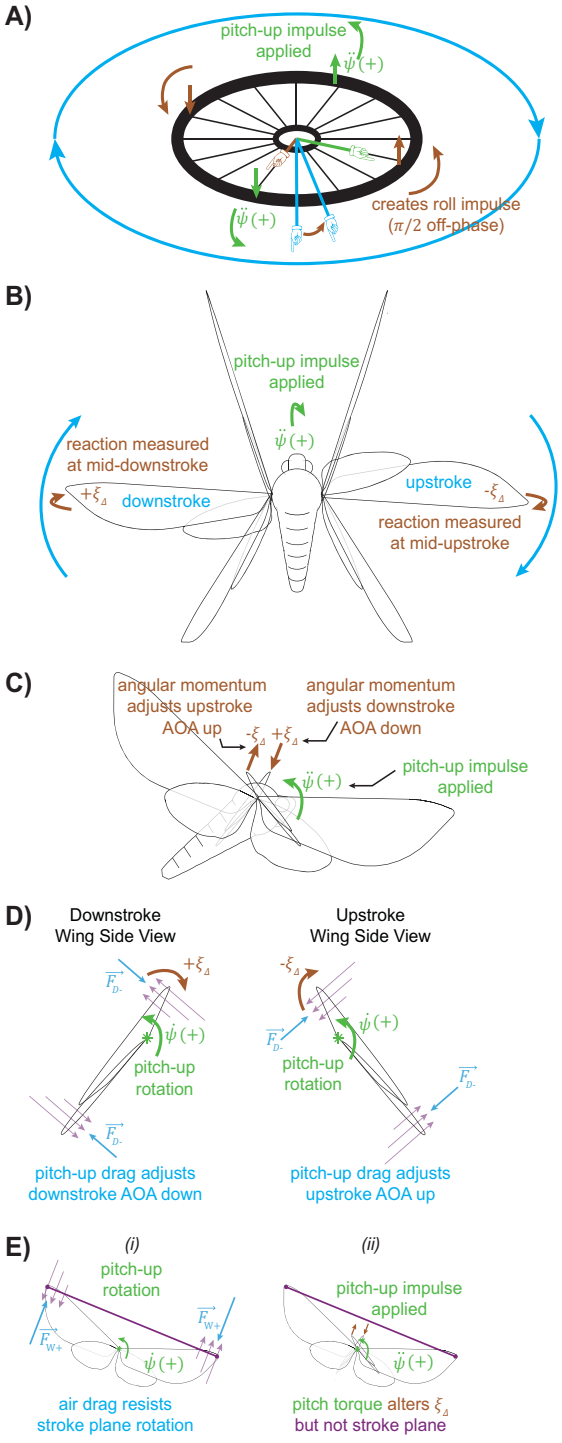

My experiments are the first to identify several passive mechanisms for pitch stability in *M. sexta*. Concurrent work had predicted pitch in flapping flight was unstable, and that *M. sexta* would rely on rapid sensory feedback and active control to stabilize body pitch orientation, or at best augment a thin margin of passive stability (Maeda *et al.*, 2010;Noda *et al.*, 2013;Ristroph *et al.*, 2013;Taha *et al.*, 2015). Besides parasite (body) drag on the most drag-affected "fluffy" insects (Ristroph *et al.*, 2013), no mechanisms for substantial margins of passive pitch stability had been proposed.

My work shows a different aspect of pitch stability. As moths pitch, the stroke plane resists rotation because it has inertia and drag. Because the wings are flapping quickly, they respond to pitch perturbations with (off-phase) deviations at *midstroke* (rather than at endstroke, which instead would mean changes to stroke plane angle). These two wing kinematic factors (stroke plane and stroke plane deviation)

correlate with pitch acceleration almost immediately following perturbation (Chapter 3), well after perturbation (Chapter 3), *and* to pitch torque in moths responding to displaced COM (Chapter 4; Table 5.1). Thus I am confident these near-instantaneous wing kinematic responses produce restorative pitch torque in *M. sexta*, damping pitch and making it more stable than previously believed.

Table 5.1: Comparing pitch-inducing wing kinematics from Chapters 3&4

	Chapter 3			Chapter 4		
Units	Coef.	Estimate	p-value	Coef.	Estimate	p-value
$g\ cm^2\ s^{-2}$	$mgK_{\ddot{\psi}\zeta}{}^{**}$	1.61E3	9.97E-7	$K_{\overrightarrow{\tau_\psi}\zeta}{}^{*}$	9.22E2	8.06E-4
$g\ cm^2$	$K_{\ddot{\psi}\dot{\psi}}{}^{**}$	8.37E-1	1.11E-7	–	–	–
$g\ cm^2\ s^{-2}$	$K_{\ddot{\psi}\xi}{}^{**}$	3.30E3	1.23E-6	$K_{\overrightarrow{\tau_{\psi 0}}\xi}{}^{+}$	1.94E3	7.81E-4
$g\ cm^2\ s^{-2}$	$K_{\ddot{\psi}\varphi}{}^{**}$	2.25E3	6.84E-5	$K_{\overrightarrow{\tau_\psi}\varphi}{}^{*}$	1.27E3	1.37E-4

Table 5.1 directly compares the coefficients that relate stroke plane angle, stroke plane deviation, and fore-aft pitch asymmetry to body movements in Chapter 3 and torque imposed by off-axis weights in Chapter 4. It also addresses *Hypotheses* 13-14 from Chapter 4. The coefficients for stroke plane asymmetry (row 1) and stroke plane deviation angle (row 3) decrease as would be expected with a reduction in COP-COM vertical distance due to moth reorientation in response to the weight. However, the coefficient for fore-aft sweep asymmetry decreases as well, when it should actually increase given that COM is moved longitudinally farther back by the majority of reorientations I measured. This weakly supports *Hypothesis 13* and does not support Hypothesis 14. It also suggests that I may have underestimated the pitch challenge in Chapter 4, perhaps by visually estimating a COM that is too far forward on the moth. Symbols and coefficients are as explained in Chapters 2 & 3: ζ_Δ is stroke plane, $\ddot{\psi}_\Delta$ is pitch acceleration, ξ_Δ is stroke plane deviation, φ_Δ is fore-minus-aft sweep amplitude, the delta Δ subscript indicates all measurements are relative to the control, and the subscripts next to each K coefficient indicate it relates the second subscript quantity (independent variable) to the first (dependent variable) in a linear model.

**From a fit to $\ddot{\psi}_\Delta = {I_{yy}}^{-1}(K_{\ddot{\psi}\zeta} mg \sin(-\zeta_\Delta) - K_{\ddot{\psi}\dot{\psi}} \frac{{\dot{\psi}_\Delta}^3}{|\dot{\psi}_\Delta|} - Q K_{\ddot{\psi}\xi_D} \xi_\Delta \cos(\zeta_\Delta) + K_{\ddot{\psi}\varphi}\varphi_\Delta)$

*From a fit to $\overrightarrow{\tau_\psi} = K_{\overrightarrow{\tau_\psi}\zeta} \sin(-\zeta_\Delta) + K_{\overrightarrow{\tau_\psi}\varphi}\varphi_\Delta$

+From a fit to $\overrightarrow{\tau_{\psi 0}} = -K_{\overrightarrow{\tau_{\psi 0}}\xi}\xi_\Delta \cos(\zeta_\Delta),\ \xi_\Delta \in \{downstroke\ measurements\ only$

Advancement 4
Flexibility Assists Flight Stability

Much prior work has focused on describing how torsional springs in the wing hinge might modulate angle of attack in insect flight (Bergou *et al.*, 2007;Bergou *et al.*, 2010;Ishihara *et al.*, 2009a;Ishihara *et al.*, 2009b;Norberg, 1972;Whitney and Wood, 2010). Mine is the first to point out how flexibility and springiness in the wing hinge might also provide body rotational stability.

The stroke plane and stroke plane deviation resistance to pitch perturbation described above (and in Chapter 3) show that flexibility of the wings relative to the COM allows moths to instantaneously and passively respond to perturbations. The abdominal flexion observed in the weight-attachment study (Chapter 4) shows that flexibility between body segments also increases stability, enhancing the rapid,

passive response to impulsive perturbations, as well as steady-state, active responses to continuous perturbations.

Animals are not rigid machines, but viscoelastic and flexible. If flexibility enhances flight stability in both of the only two cases I studied, it is likely true for other flying animals and other degrees of freedom as well. These conclusions compliment those identifying flexibility in control structures as a source of passive stability in running cockroaches (Jindrich and Full, 2002), and increased maneuverability but decreased stability in swimming cetaceans (Fish *et al.*, 2008;Fish, 2002).

Advancement 5
Maneuver and Perturbation Wing Kinematics Differ Due to Passive Damping and Active Counter-Damping

My results also show that moths use a body and wing kinematic strategy tailored to specific perturbation and maneuver scenarios; *i.e.* there is not just one "pitch" or "roll" or perturbation or maneuver response. In the GRF roll maneuver case (Chapter 1) moths reduced rotational damping with wing kinematics (asymmetries in elevation amplitude and wing pitch/AOA). Since the moths were not rotating in the weight addition experiments, it is not surprising that these wing kinematic changes did not significantly correlate with roll.

If response and maneuver strategies vary for moths depending on the specific scenario, they likely vary similarly for other animals as well. Thus, to successfully identify complete information about which wing kinematics create maneuvers, respond to perturbations, *etc.*, future researchers must be careful to avoid misguided assumptions about wing kinematics, even in the same animals creating torque about the same rotational axes.

Nevertheless, these seemingly customized wing responses could in theory arise from quite simple control strategy. For example, flying animals might be primed to sense the differences between prescribed and actual wing movements, and then respond in such a way that either enhances (in the perturbation case) or counteracts (for the maneuver case) this damping (Fig. 5.5). Visuomotor responses are "slow" in *Manduca sexta* (≈40-80ms; Dickerson *et al.*, 2014;Sponberg *et al.*, 2015;Windsor *et al.*, 2013). Nevertheless, flying insects have other rapid-response gyroscopically-mediated sensors, such as antennae (Sane et. al, 2007), halteres (Pringle, 1948), and wings (Dickerson *et al.* 2014) which may allow them to

more rapidly estimate/measure and respond to changes in state, even proportional to their displacement (*i.e.* with PD-like control; Beatus *et al.*, 2015). Thus, active reactions could rapidly reinforce the passive inertial and viscous damping responses seen in *M. sexta*.

Figure 5.5: Control implications. A simple control model for flapping flight?

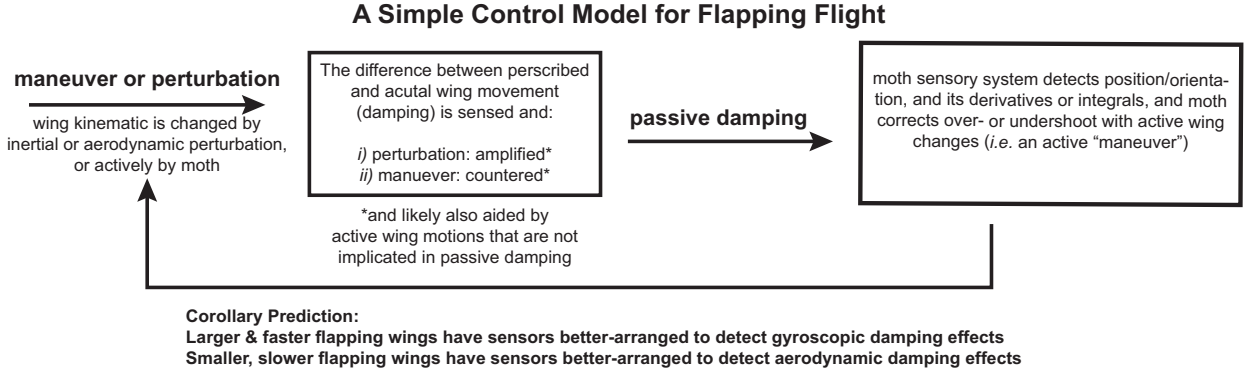

A control system based on detecting the difference between prescribed and actual wing motion. Flying animals may measure the difference between prescribed and actual wing motion, then reinforce them in the case of an active stabilizing response; and counteract them in the case of maneuvers. This could explain the active counter-damping kinematics I showed in roll maneuvers, and the match between wing kinematics which create active rotations, and those which arise passively after perturbation (as shown for pitch in Chapters 3-4 and Fig. 5.3; predicted for roll in Chapter 4 and Fig. 5.2).

Advancement 6
Reinforcing Gyroscopic and Aerodynamic Effects in Flapping Flight May Create Similar Stability and Maneuver Mechanics across Size and Speed Scales

By far the most provocative element of my dissertation describes how—at least for pitch—inertial and aerodynamic passive reactions to perturbation likely work together to create passive wing movements that resist rotations instantly. This would help explain how animals manage to maintain stability in flight.

In Chapter 3, the stroke plane inclination response (ζ_{Δ}), the stroke plane deviation response (ξ_{Δ}), and the drag on, and inertia of, the moth's body itself, are all examples of inertia and drag working together, and in the same direction, to passively stabilize pitch orientation. This novel conclusion suggests that future work should examine whether inertia and drag also work in parallel to stabilize other directions of motion, such as yaw (Eberle *et al.*, 2015;Hedrick *et al.*, 2009) or pitch (Chapter 3). In Chapters 2 & 4, they further indicate that both FCT (drag-based) and gyroscopic (inertia-based) damping also increase roll stability (Fig. 5.1-2). Largely active and direct inertial mechanisms have been shown to be important in some flapping

flight reorientations (Bergou *et al.*, 2011;Bergou *et al.*, 2015;Hedrick *et al.*, 2007;Iriate-Díaz *et al.*, 2011;Meadows, 2015), and proposed to be synergistic with wing reorientations in the banked flapping turns of birds (Warrick and Dial, 1998; but see Ros *et al.*, 2015). My conclusion here is largely different from these findings and proposals in that: 1) The effects I point out here are passive responses to perturbations, rather than arising from active changes to wing kinematics, 2) The inertial damping is indirect, or inertio-viscous, in that the inertial response of a flapping wing to rotation pushes on the air to create countertorque, rather than an active effect where angular momentum is directly transmitted from a rotating wing to other parts of the body, and, separate from this, 3) These passive changes to wing kinematics reinforce aerodynamically-induced (passive) changes to wing orientation, and together they damp rotations.

Creatures that fly vary vastly in size, and thus operate at a range of Reynolds numbers (Re; ratio of inertial to viscous forces). At Re ~8000 (Usherwood and Ellington, 2002), *M. sexta* is larger than most insects but smaller than most birds. Here, inertial forces account for >85% of wing bending mechanics (Combes and Daniel, 2003; Jankauski and Shen, 2016), but for smaller fliers, drag is more important; for *D. melanogaster*, inertia and drag contribute about equally to wing bending (Ennos, 1988;Lehmann *et al.*, 2011). Across this size range, flying animal body design remains remarkably consistent (Greenewalt, 1962), and insect wings are able to sense and respond to both gyroscopic and aerodynamic forces (Dickerson *et al.*2014; Eberle *et al.*2015). Based on these conclusions, we predict pendulum-like passive pitch stability (and possibly passive stability in other degrees of freedom as well), to be important across the extremes of this grand biological scale, producing similar stability mechanics from fundamentally different mechanisms (drag *vs.* inertia).

We now know that in insects, flapping wings do not just generate lift; they also detect rotational changes to wing motion (Dickerson *et al.*, 2014), and that those changes aid stability (Chapters 2-5). Furthermore, scale-independent sources of near-instantaneous passive damping likely simplify the developmental and evolutionary changes in body size for flying animals. These facts give us insight into the optimal design of MAVs, as well as the evolution of biological flight.

How Might My Conclusions Inform and Improve MAV Design?

Certainly if we could create an exact quantum replica of a living *M. sexta*, this equally corpulent moth would be capable of the same surprising aerial feats, such as recovery from >100 deg pitch perturbations (Chapter 3), or >5.5 $m\,s^{-1}$ flight in a wind tunnel (Tyson Hedrick, *personal communication*). But which body design features are most important to creating stability?

Mechanical engineering is informed every day by the biomechanics solutions scientists identify in nature, and flight is no exception. Specifically, micro-air vehicles (MAVs) are an area of much active design research. Effective stability solutions remain a design hurdle of intense focus (Karásek *et al.*, 2014;Koopmans *et al.*, 2015;Ma *et al.*, 2013;Orlowski and Girard, 2012;Pratt and Qin, 2016) that is often used to justify funding for research into insect-scale flapping flight in animals.

Taken as a whole, my work shows that flapping-wing MAV designs of today may neglect important sources of passive stability. Flexibility in an MAV wing hinge would help mimic the passive rotational stability mechanisms I identified. Elasticity in the wing base would help gyroscopic responses propagate to subsequent halfstrokes. Appropriate tuning of drive frequency (while considering elastic and damping mechanics) would maximize the amplitude of the stabilizing gyroscopic response, and possibly help passively mitigate the effects of wing wear. Larger, heavier, and faster flapping wings would increase gyroscopic damping effects; smaller, lighter, draggier, slower-flapping wings would increase aerodynamic damping effects. Flexibility in the wing hinge and chassis design could also help damp rotations (Chapter 3; Noda *et al.*, 2014), as well as help MAVs carry awkward loads (Chapter 4). I can also hypothesize a simple functional control model for an MAV, based on my findings in *M. sexta* (Fig. 5.5).

In short, stiffness along the leading edge of the wing, body flexibility, wing hinge flexibility and elasticity, and tuning of natural frequencies, could enhance inertial wing responses to perturbation and allow them to carry forward to subsequent halfstrokes. Given damping factors, one could tune elasticity at the wing hinge to mode-match (and thus maximize) restorative reactions of the wings to perturbation. This could also enhance the sensitivity of an active perturbation response system based on detectable wing deviations. As work progresses in this field, and biomechanics in general, researchers will likely continue to discover simple solutions to engineering problems already selected for by nature.

Chapter 5 Abbreviations

Box 5.1: Abbreviations

AOA	effective Angle Of Attack; represents the angle at which the wing encounters the air
BRF	Body Reference Frame: reference frame from the perspective of the moth's COM, in which the moth's anatomical landmarks and canonical hover orientation determine x, y, and z.
COM	Center Of Mass: point where the sum of the product of individual units of mass and their distance away from that point equal zero.
COP	Center Of Pressure: net sum of force production by the wings, time-averaged over the course of a stroke cycle
FCF	Flapping Counter Force: Idea that linear translation of flapping wings creates differential drag and thrust which damps the translation. First described for sideslips.
FCT	Flapping Counter Torque: idea that rotations change the velocity of wings flapping in that rotational plane, damping the rotation. First shown for yaw.
GRF	Global Reference Frame: based on the camera calibration (world view frame)

REFERENCES

Beatus, T., Guckenheimer, J. M. and Cohen, I. (2015). Controlling roll perturbations in fruit flies. *J. R. Soc. Interface* **12,** 10.1098/rsif.2015.0075.

Beatus, T. and Cohen, I. (2015). Wing-pitch modulation in maneuvering fruit flies is explained by an interplay between aerodynamics and a torsional spring. *Phys. Rev. E* **92,** 022712.

Bergou, A. J., Xu, S. and Wang, Z. J. (2007). Passive wing pitch reversal in insect flight. *J. Fluid Mech.* **591,** 321-337.

Bergou, A. J., Swartz, S., Breuer, K. and Taubin, G. (2011). 3D Reconstruction and analysis of bat flight maneuvers from sparse multiple view video. 1-2.

Bergou, A. J., Ristroph, L., Guckenheimer, J., Cohen, I. and Wang, Z. J. (2010). Fruit Flies Modulate Passive Wing Pitching to Generate In-Flight Turns. *Phys. Rev. Lett.* **104,** 148101.

Bergou, A. J., Swartz, S. M., Vejdani, H., Riskin, D. K., Reimnitz, L., Taubin, G. and Breuer, K. S. (2015). Falling with style: bats perform complex aerial rotations by adjusting wing inertia. *PLoS Biol.* **13,** e1002297.

Cheng, B., Fry, S. N., Huang, Q., Dickson, W. B., Dickinson, M. H. and Deng, X. (2009). Turning dynamics and passive damping in flapping flight. 1889-1896.

Cheng, B., Tobalske, B. W., Powers, D. R., Hedrick, T. L., Wang, Y., Wethington, S. M., Chiu, G. T. and Deng, X. (2016). Flight mechanics and control of escape manoeuvres in hummingbirds. II. Aerodynamic force production, flight control and performance limitations. *J. Exp. Biol.* **219,** 3532-3543.

Dickerson, B. H., Aldworth, Z. N. and Daniel, T. L. (2014). Control of moth flight posture is mediated by wing mechanosensory feedback. *J. Exp. Biol.* **217,** 2301-2308.

Eberle, A. L., Dickerson, B. H., Reinhall, P. G. and Daniel, T. L. (2015). A new twist on gyroscopic sensing: body rotations lead to torsion in flapping, flexing insect wings. *J. R. Soc. Interface* **12,** 20141088.

Ennos, A. R. (1988). The inertial cause of wing rotation in Diptera. *J. Exp. Biol.* **140,** 161-169.

Faruque, I. and Humbert, J. S. (2010a). Dipteran insect flight dynamics. Part 1: Longitudinal motion about hover. *J. Theor. Biol.* **264,** 538-552.

Faruque, I. and Humbert, J. S. (2010b). Dipteran insect flight dynamics. Part 2: Lateral–directional motion about hover. *J. Theor. Biol.* **265,** 306-313.

Fish, F. E., Howle, L. E. and Murray, M. M. (2008). Hydrodynamic flow control in marine mammals. *Integr. Comp. Biol.* **48,** 788-800.

Fish, F. E. (2002). Balancing Requirements for Stability and Maneuverability in Cetaceans. *Integr. Comp. Biol.* **42,** 85-93.

Fraenkel, G. (1932). Untersuchungen über die Koordination von Reflexen und automatisch-nervösen Rhythmen bei Insekten. *Zeitschrift für vergleichende Physiologie* **16,** 418-443.

Fry, S. N., Sayaman, R. and Dickinson, M. H. (2003). The aerodynamics of free-flight maneuvers in Drosophila. *Science* **300,** 495-498.

Fry, S. N., Sayaman, R. and Dickinson, M. H. (2005). The aerodynamics of hovering flight in Drosophila. *J. Exp. Biol.* **208,** 2303-2318.

Gao, N., Aono, H. and Liu, H. (2009). A numerical analysis of dynamic flight stability of hawkmoth hovering. *J. Biomech. Sci. Eng.* **4,** 105-116.

Gao, N., Aono, H. and Liu, H. (2011). Perturbation analysis of 6DoF flight dynamics and passive dynamic stability of hovering fruit fly *Drosophila melanogaster*. *J. Theor. Biol.* **270,** 98-111.

Greeter, J. S. M. and Hedrick, T. L. (2016). Direct lateral maneuvers in hawkmoths. *Biol. Open*, bio. 012922.

Hedrick, T., Usherwood, J. and Biewener, A. (2007). Low speed maneuvering flight of the rose-breasted cockatoo (*Eolophus roseicapillus*). II. Inertial and aerodynamic reorientation. *J. Exp. Biol.* **210,** 1912-1924.

Hedrick, T. L., Cheng, B. and Deng, X. (2009). Wingbeat Time and the Scaling of Passive Rotational Damping in Flapping Flight. *Science* **324,** 252-255.

Hesselberg, T. and Lehmann, F. O. (2007). Turning behaviour depends on frictional damping in the fruit fly Drosophila. *J. Exp. Biol.* **210,** 4319-4334.

Humbert, J. S. and Faruque, I. (2011). Analysis of Insect-Inspired Wingstroke Kinematic Perturbations for Longitudinal Control. *Journal of guidance, control, and dynamics* **34,** 618-623.

Iams, S. (2012). *Free flight of the mosquito* Aedes aegypti. Doctoral dissertation, Cornell University, Ithica, NY. *arXiv preprint arXiv:1205.5260*

Iriarte-Díaz, J., Riskin, D. K., Willis, D. J., Breuer, K. S., & Swartz, S. M. (2011). Whole-body kinematics of a fruit bat reveal the influence of wing inertia on body accelerations. *J. Exp. Biol.* **214.9,** 1546-1553.

Ishihara, D., Horie, T. and Denda, M. (2009a). A two-dimensional computational study on the fluid-structure interaction cause of wing pitch changes in dipteran flapping flight. *J. Exp. Biol.* **212,** 1-10.

Ishihara, D., Yamashita, Y., Horie, T., Yoshida, S. and Niho, T. (2009b). Passive maintenance of high angle of attack and its lift generation during flapping translation in crane fly wing. *J. Exp. Biol.* **212,** 3882-3891.

Jindrich, D. L. and Full, R. J. (2002). Dynamic stabilization of rapid hexapedal locomotion. *J. Exp. Biol.* **205,** 2803-2823.

Karásek, M., Hua, A., Nan, Y., Lalami, M. and Preumont, A. (2014). Pitch and roll control mechanism for a hovering flapping wing MAV. *Int. J. Micro Air Veh.* **6,** 253-264.

Kim, J., Han, J., Choi, S. and Han, J. (2016). Dynamic Stability of a Hawkmoth-scale Flapping-wing Micro Air Vehicle during Forward Flight. 0016.

Koopmans, J., Tijmons, S., De Wagter, C. and de Croon, G. (2015). Passively Stable Flapping Flight From Hover to Fast Forward Through Shift in Wing Position. *Int. J. Micro Air Veh.* **7,** 407-418.

Lehmann, F. O., Gorb, S., Nasir, N. and Schutzner, P. (2011). Elastic deformation and energy loss of flapping fly wings. *J. Exp. Biol.* **214,** 2949-2961.

Ma, K. Y., Chirarattananon, P., Fuller, S. B. and Wood, R. J. (2013). Controlled flight of a biologically inspired, insect-scale robot. *Science* **340,** 603-607.

Maeda, M., Gao, N., Nishihashi, N. and Liu, H. (2010). A free-flight simulation of insect flapping flight. *Journal of Aero Aqua Bio-mechanisms* **1,** 71-79.

Meadows, R. (2015). How bats land upside down. *PLoS Biol.* **13,** e1002298.

Noda, R., Maeda, M. and Liu, H. (2013). Effect of Passive Body Deformation of Hawkmoth [*sic.*] on Flight Stability. *Intelligent Autonomous Systems 12*, pp. 835-842: Springer.

Noda, R., Nakata, T. and Liu, H. (2014). Body flexion effect on the flight dynamics of a hovering hawkmoth. *J. Biomech. Sci. Eng.* **9,** 14-00409-14-00409.

Norberg, R. Å. (1972). The pterostigma of insect wings an inertial regulator of wing pitch. *J. Comp. Physiol.* **81,** 9-22.

Orlowski, C. T. and Girard, A. R. (2012). Dynamics, stability, and control analyses of flapping wing micro-air vehicles. *Prog. Aerospace Sci.* **51,** 18-30.

Pratt, T. and Qin, N. (2016). Vortex Generators for Increased Maximum Lift and Enhanced High-α Stability of a Zimmerman-Wing MAV at Low Reynolds Number. *2016 Applied Aerodynamics Conference*, R. Aeronaut. Soc., Bristol, ENG.

Pringle, J. (1948). The gyroscopic mechanism of the halteres of Diptera. *Phil. Trans. R. S. Lon. B Biol. Sci.* **233.602,** 347-384.

Ravi, S., Crall, J. D., McNeilly, L., Gagliardi, S. F., Biewener, A. A. and Combes, S. A. (2015). Hummingbird flight stability and control in freestream turbulent winds. *J. Exp. Biol.* **218,** 1444-1452.

Read, T. J. G. (2015). *Hummingbirds use banking to achieve faster turns and asymmetrical wingstrokes to achieve tighter turns*. Master's Thesis, University of California, Berkeley.

Ristroph, L., Berman, G. J., Bergou, A. J., Wang, Z. J. and Cohen, I. (2009). Automated hull reconstruction motion tracking (HRMT) applied to sideways maneuvers of free-flying insects. *J. Exp. Biol.* **212,** 1324-1335.

Ristroph, L., Bergou A. J., Ristroph, G., Coumes, K., Berman, G. J., Guckenheimer, J., Wang, Z. J., and Cohen, I. (2010). Discovering the flight autostabilizer of fruit flies by inducing aerial stumbles. *Proc. Natl. Acad. Sci.* **107.11,** 4820-4824.

Ristroph, L., Ristroph, G., Morozova, S., Bergou, A. J., Chang, S., Guckenheimer, J., Wang, Z. J. and Cohen, I. (2013). Active and passive stabilization of body pitch in insect flight. *J. R. Soc. Interface* **10,** 20130237.

Ros, I. G., Bassman, L. C., Badger, M. A., Pierson, A. N. and Biewener, A. A. (2011). Pigeons steer like helicopters and generate down- and upstroke lift during low speed turns. *Proc. Natl. Acad. Sci. USA* **108,** 19990-19995.

Sane, S. P. (2003). The aerodynamics of insect flight. *J. Exp. Biol.* **206,** 4191-4208.

Sane, S. P., Dieudonne, A., Willis, M. A. and Daniel, T. L. (2007). Antennal mechanosensors mediate flight control in moths. *Science* **315,** 863-866.

Schilstra, C. and Hateren, J. H. (1999). Blowfly flight and optic flow. I. Thorax kinematics and flight dynamics. *J. Exp. Biol.* **202 (Pt 11),** 1481-1490.

Sponberg, S., Dyhr, J. P., Hall, R. W. and Daniel, T. L. (2015). Luminance-dependent visual processing enables moth flight in low light. *Science* **348,** 1245-1248.

Sugiura, H. and Dickinson, M. H. (2009). The generation of forces and moments during visual-evoked steering maneuvers in flying Drosophila. *PLoS One* **4,** e4883.

Sun, M. (2014). Insect flight dynamics: stability and control. *Reviews of Modern Physics* **86,** 615.

Sun, M., Wang, J. and Xiong, Y. (2007). Dynamic flight stability of hovering insects. *Acta Mechanica Sinica* **23,** 231-246.

Sun, M. and Wang, J. K. (2007). Flight stabilization control of a hovering model insect. *J. Exp. Biol.* **210,** 2714-2722.

Taha, H. E., Tahmasian, S., Woolsey, C. A., Nayfeh, A. H. and Hajj, M. R. (2015). The need for higher-order averaging in the stability analysis of hovering, flapping-wing flight. *Bioinsp. Biomim.* **10,** 016002.

Usherwood, J. R. and Ellington, C. P. (2002). The aerodynamics of revolving wings I. Model hawkmoth wings. *J. Exp. Biol.* **205,** 1547-1564.

Vogel, S. (1966). Flight in Drosophila. Part I. Flight performance of tethered flies. *J. Exp. Biol.* **44,** 567-578.

Wang, H., Ando, N. and Kanzaki, R. (2008). Active control of free flight manoeuvres in a hawkmoth, *Agrius convolvuli*. *J. Exp. Biol.* **211,** 423-432.

Wang, H., Zeng, L., Liu, H. and Yin, C. (2003). Measuring wing kinematics, flight trajectory and body attitude during forward flight and turning maneuvers in dragonflies. *J. Exp. Biol.* **206,** 745-757.

Warrick, D. R. and Dial, K. P. (1998). Kinematic, aerodynamic and anatomical mechanisms in the slow, maneuvering flight of pigeons. *J. Exp. Biol.* **201,** 655672.

Warrick, D., Hedrick, T., Fernández, M. J., Tobalske, B. and Biewener, A. (2012). Hummingbird flight. *Current Biology* **22,** R472-R477.

Weis-Fogh, T. (1956). Biology and physics of locust flight. II. Flight performance of the desert locust (Schistocerca gregaria). *Phil. Trans. R. Soc. B: Biol. Sci.* **239,** 459-510.

Whitehead, S. C., Beatus, T., Canale, L. and Cohen, I. (2015). Pitch perfect: how fruit flies control their body pitch angle. *J. Exp. Biol.* **218,** 3508-3519.

Whitney, J. and Wood, R. (2010). Aeromechanics of passive rotation in flapping flight. *J. Fluid Mech.* **660,** 197-220.

Windsor, S. P., Bomphrey, R. J. and Taylor, G. K. (2013). Vision-based flight control in the hawkmoth Hyles lineata. *J. R. Soc. Interface* **11,** 20130921.

Xu, N. and Sun, M. (2013). Lateral dynamic flight stability of a model bumblebee in hovering and forward flight. *J. Theor. Biol.* **319,** 102-115.

Zhang, Y. L. and Sun, M. (2011). Control for small-speed lateral flight in a model insect. *Bioinsp. Biomim.* **6,** 036003.

Zhang, Y. and Sun, M. (2010). Dynamic flight stability of a hovering model insect: lateral motion. *Acta Mechanica Sinica* **26,** 175-190.

APPENDIX
LOW-SPEED WIND TUNNEL DESIGN

Overview

In addition to the research projects described earlier in the dissertation, I also designed a laminar-flow, low-speed wind tunnel. This wind tunnel has since been used in several flight experiments, including one that resulted in a second-author publication (Ortega-Jimenez *et. al*, 2013). In its current configuration, the maximum speed is approximately 5.5 $m\,s^{-1}$. Recently, one *M. sexta* specimen managed to fly at that speed (Tyson Hedrick 2017, *personal communication*). It is now housed in Wilson Hall at UNC Chapel Hill.

Figure A.1: Dimensioned wind tunnel side view

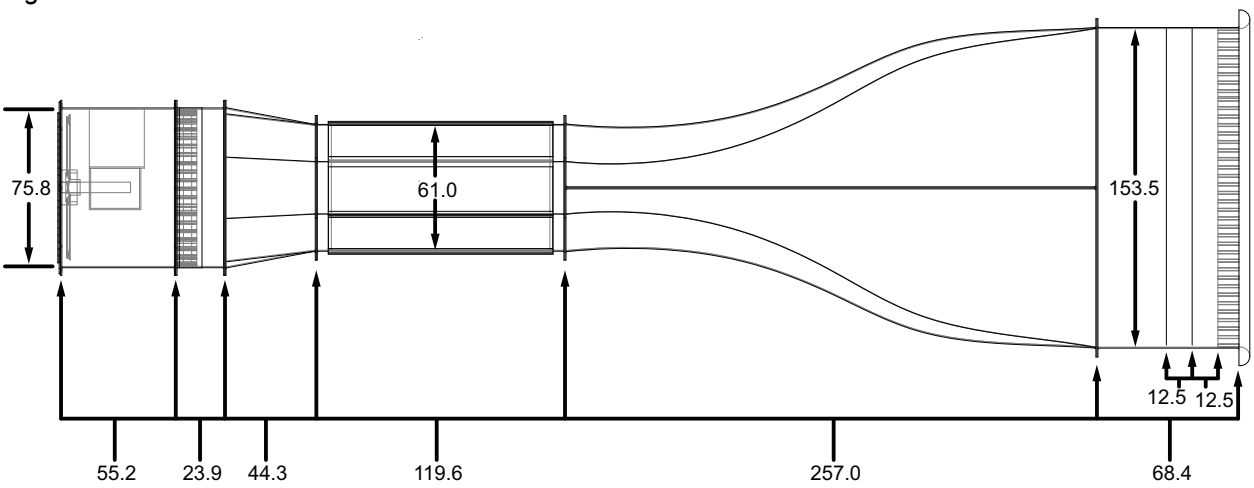

A lateral view of the wind tunnel, shown without supporting structure. This is a to-scale drawing of the wind tunnel that this document describes. Dimensions are in centimeters. Some details are intentionally excluded. Honeycomb cell size is not to scale. The support structure (not shown) for the fan and downstream half of the vibration isolator is detachable from that of the rest of the wind tunnel.

Design, Construction and Location

The low-speed wind tunnel used here (Fig. A.1) is located in Wilson Hall at UNC-CH. It was designed in-house with final design details and construction by Quate Industrial Fabrication (Durham, NC, USA). It is a suction type, open-flow wind tunnel; constructed mainly of 5 mm thick aluminum and is housed in an 8.08L × 2.53W × 3.59H m rectangular room where it is supported by a metal frame on locking wheels. With its current configuration, it has a min/max speed of 0.1 / 4 $m\,s^{-1}$. Air enters the square settling

chamber and passes through a flow collimator and two screens. Air then enters a nozzle with a square entrance and regular octagonal exit. The nozzle speeds up the air, which then passes through a plastic screen as it enters the working section. After leaving the working section, the air enters an expansion duct with an octagonal opening and circular exit. It then travels through a vibration-isolating duct which also houses a flow collimator positioned directly in front of the fan entrance. Finally, the air passes through the fan and exits the wind tunnel through a discharge guard.

Settling Chamber

In the settling chamber, a flow collimator and screens even out flow velocity where it is lowest (and thus resistance is minimal). The flow collimator chiefly parallelizes flow pathlines and reduces small-scale turbulence, while the screens chiefly create a more uniform speed profile and thin the boundary layer (Barlow *et al.*, 1999; Mehta and Bradshaw 1979). The settling chamber has interior dimensions of 153.5 × 153.5 cm. The inlet has 32.5 cm clearance with the floor and 45 cm clearance with the closest ceiling fixture (156 cm with the ceiling). The entrance to the settling chamber is curved in a circular arc. A recess in the settling chamber walls, as well as a metal grid which spans the entrance, together hold the flow collimator in place. The flow collimator is a 10.2 cm deep aluminum honeycomb (HexWeb® ACG®, Hexcel Co., Stamford, CT, USA), with >95% open area and a cell apothem of 4.75 mm. Next, the flow encounters two stainless steel woven mesh screens (Newark Wire Cloth Co., Clifton, NJ), each with 36% open area and metal wire diameters of 254 and 25.4 μm, respectively. The finer screen was placed upstream in this study, opposite their typical operational order. The settling chamber attaches to the nozzle *via* hinges and clamps to allow rotation away from the rest of the wind tunnel. The side of this chamber is removable for screen cleaning purposes.

Nozzle

After the air exits the settling chamber, it then travels through the nozzle. The nozzle contracts to increase flow velocity, reduce velocity variations to a smaller fraction of the average velocity, and induce/maintain a well-defined, thin boundary layer (Barlow *et al.*, 1999; Mehta & Bradshaw 1979; Schlichting and Gersten, 2004). The nozzle is composed of two largely identical halves, shown in the figure below. The nozzle has a contraction ratio of ~5.7. The quadrilateral nozzle entrance maximizes contraction ratio given the room shape, while four chamfers at each edge expand to give the exit a regular octagonal shape. The octagonal shape is intended to thin the boundary layer and prevent flow separation near the edges (Barlow *et al.*, 1999).

The four interior chamfer hypotenuses from $x = 1$ to 257 cm are described by:

$$hypotenuse = (-1.5365 \times 10^{-10})x^4 + (-4.3531 \times 10^{-7})x^3 + (7.6242 \times 10^{-5})x^2 + 0.11133x + 0.51218 \quad \text{(A.1)}$$

The other (horizontal and vertical) sides of the nozzle vary from

$$x \in \{1\ to\ 120\ cm: \\ side = (-4.6226 \times 10^{-7})x^4 + (8.0989 \times 10^{-5})x^3 - 0.0066144x^2 - 0.093549x + 153.2122 \quad \text{(A.2)}$$

$$x \in \{120\ to\ 257\ cm: \\ side = (1.2824 \times 10^{-7})x^4 + (-1.0414 \times 10^{-4})x^3 - 0.036188x^2 - 6.4184x + 492.50 \quad \text{(A.3)}$$

Working Section

The next destination for the flow is the working section, which is the portion of the wind tunnel designed for low-turbulence flow experiments (Fig. A.1-2). After exiting the nozzle (in the current experimental setup) the air passes through a plastic screen with open area >93% and a variable wire diameter of ~0.2-0.5 mm (1.27 cm per grid). In this experiment, this screen restricted moths to the working section, expansion duct, and vibration isolator. The octagonal, transparent design of the working section allows for viewing from eight different principle angles. It also allows for easier transition into the circular shape of the fan. The clear panels are made of Lexan® (SABIC Innovative Plastics Holding B.V., Pittsfield, MA, USA).

Figure A.2: Oblique view of wind tunnel test section

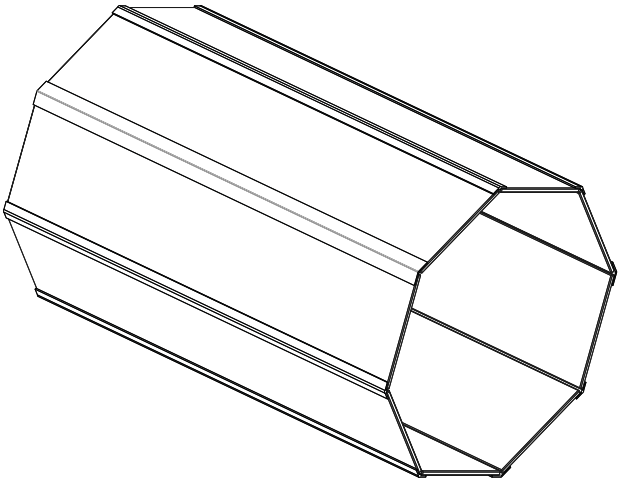

Wind tunnel test/working section oblique view. The test section is a regular octagon. Each panel is fitted with a hinge on one side and clamps on the other to allow test section access. There are many benefits to an octagonal test section. First, it allows multiple flat plane angles for video collection. Second, an octagonal cross section likely has less turbulence at corners relative to a square test section. Third, it aids the gradual transition of flow from the square settling chamber to the circular fan. Fourth, this allows us to keep the contraction ratio of the overall wind tunnel high (since starting with a square entrance allowed us to maximize its area in a square-shaped room).

Expansion Duct and Vibration Isolator

Expansion ducts and anti-twist vanes are typical wind tunnel components that decrease fan power requirements and reduce flow irregularities in upwind working sections (Barlow *et al.*, 1999). This wind tunnel also has a vibration isolator. The expansion duct, which has an expansion ratio of ~1.0870, connects the working section to the vibration isolator. Next, the vibration isolator connects the expansion duct to the fan. Due to room size constraints, this wind tunnel's expansion duct is proportionally shorter than those of most similarly-sized low-speed wind tunnels (Barlow *et al.*, 1999); the vibration isolator helps create more laminar working section flow by increasing the distance between the working section and fan blades. This vibration isolator is the same diameter as the fan, and has the appearance of a flanged pipe with the middle section removed (Fig. A1). A ~0.5 mm thick tarp encircles the gap between the two flanged halves, and pipe clamps on either side of the gap secure the tarp in place. The support structure for the fan and downstream half of the vibration isolator is detachable from that of the rest of the wind tunnel (although in (Ortega-Jimenez *et. al*, 2013), the two support structures were rigidly attached *via* metal tubing). The vibration isolator also houses a circular section of honeycomb flow collimator. This flow collimator (of the same material as previously described) is intended to damp the rotational patterns the fan introduces to the air. Thus, this collimator is intended to take the place of the anti-twist vanes more typically situated directly before fan blades in similar wind tunnels (Barlow *et al.*, 1999).

Fan and Motor

The final section of the wind tunnel is the fan. Todd Air Solutions (Salisbury, NC, USA) delivered the 736RPM, 1.49 kW, 0.165 $m^3\ s^{-1}$, belt-driven tube axial duct fan (WAF-30, Cincinnati Fan & Ventilator Co, Mason, OH, USA). Situated parallel to the flow, two large steel plate fins and a teardrop belt tube collectively support the fan bearing encasement (which is not tapered). The power supply is 200 V, 15 A. This electricity runs through a safety circuit breaker and then a variable frequency drive, (VS1MX82-2F, Baldor Electric Co., Fort Smith, AR, USA), which provides variable power to the fan motor (EM3558T-8, Baldor Electric Co.) and is controlled *via* an in-house dial-type potentiometer and switch panel. Flow finally exits the wind tunnel by passing through a concentric circle discharge guard. The fan is 1.64 m from the room exit door and has between 0.65 and 1.07 m lateral clearance with the left and right walls of the room, respectively.

REFERENCES

Barlow, J. B., Rae, W. H. and Pope, A. (1999). *Low-Speed Wind Tunnel Testing.* New York, NY: Wiley & Sons, Inc.

Mehta, R. D., and Bradshaw, P. (1979). Design rules for small low speed wind tunnels. *Aeronaut. J.* **83.827**, 443–449.

Ortega-Jimenez, V. M., Greeter, J. S. M., Mittal, R. and Hedrick, T. L. (2013). Hawkmoth flight stability in turbulent vortex streets. *J. Exp. Biol.* **216.24**, 4567-4579.

Schlichting, H. and Gersten, K. (2004). *Boundary-Layer Theory* eighth edition, translated by K. Mayes, contributions by E. Kraus and H. Oertel Jr., New York, NY: Springer Publishing Co.